SCUOLA DI DOTTORATO
UNIVERSITÀ DEGLI STUDI DI MILANO-BICOCCA

Dipartimento di / Department of

Scienza dei Materiali

Dottorato di Ricerca in / PhD program Scienza e Nanotecnologia dei Materiali Ciclo / Cycle XXXVIII

DESIGN AND CHARACTERIZATION OF DMBI-BASED N-TYPE DOPANTS FOR ORGANIC SEMICONDUCTORS AND CARBON NANOTUBES

Cognome / Surname Paoli Nome / Name Gabriele

Matricola / Registration number 873081

Tutore / Tutor: Prof. Luca Beverina

Supervisor: Prof. Mauro Sassi

Coordinatore / Coordinator: Prof. Francesco Montalenti

ANNO ACCADEMICO / ACADEMIC YEAR 2024/2025

Contents

Chapter 1 - Introduction

1. Introduction

The growing field of optoelectronic technologies now addresses innovative devices such as flexible displays, wearable sensors, organic photovoltaics (OPVs), light-emitting diodes (OLEDs), and thin-film transistors (TFTs). Moreover, thermoelectric generators (TEGs) have recently attracted attention for their ability to convert small temperature gradients into electrical power, offering a path toward autonomous devices with low consumption.[1]

All these technologies rely on semiconductor materials, whose electrical and thermal properties can be tuned through doping. While inorganic semiconductors have long dominated optoelectronics due to their excellent performance and established processing methods, their rigidity and high fabrication temperatures limit their use in flexible or large-area devices. Conversely, organic and carbon-based semiconductors (OSCs and CNTs) offer complementary features: their solution processability, chemical versatility, and mechanical flexibility enable lightweight, flexible, and scalable devices.[2,3]

However, achieving stable n-type doping remains one of the main challenges to fully exploit these materials. The issue arises firstly from the intrinsic air instability of the n-type dopants, where exposure to oxygen or moisture easily leads to degradation. A widely adopted strategy to improve stability is the use of molecular dopant precursors, which can be activated in situ by heat or light. Among them, benzimidazoline-based dopants, with N-DMBI-H as a benchmark, stand out for their processability and controlled activation.

At the same time, molecular dopants introduce their own set of challenges. In polymer semiconductors, such as N2200, they often show limited miscibility and a tendency toward phase segregation, which can alter the film microstructure and reduce the effectiveness of the doping process. In contrast, the rigid and interconnected morphology of CNT networks is less affected by such segregation effects. Here, the main limitation lies instead in their susceptibility to oxidation and dedoping under ambient conditions, which compromises long-term electrical stability.

This work develops in this context. It focuses on the design of new DMBI-based dopants capable of forming specific interactions with the semiconductor matrix, stabilizing morphology and enabling controlled doping in polymers such as N2200, or improving environmental stability in CNT networks. The goal is to contribute to the development of more stable and efficient n-type materials for future organic and carbon-based electronic applications.

Before addressing the experimental results, the next sections provide an overview of the theoretical and technological framework of this study, covering thermoelectricity, the fundamentals of organic semiconductors and carbon nanotubes, and the related molecular doping.

1.1. Properties of Semiconductors: electrical conductivity and thermoelectricity

Semiconductors are fundamental materials in several technologies, including transistors, diodes, solar cells, and thermoelectric generators. Their relevance arises from a unique set of electronic properties that can be finely determined by structural engineering. In particular, **electrical conductivity** is a central property in semiconductors, that refers to a material's ability to transport electric charge, and it is quantitatively described by the following equation:

$$\sigma = e(\mu_e n + \mu_h p) \tag{1.1}$$

where e is the elementary charge, and μ_e, μ_h, n, and p are the electron mobility, the hole mobility, the electron density, and the hole density, respectively.[4]

Since the most common form in which organic semiconductors and CNTs are processed is in thin film, we discuss of the determination of electrical conductivity of this samples in the following section. [5–9]

1.1.1. Electrical Conductivity: Two-probe method and its limitations

The most direct approach to determine the electrical conductivity of a thin film relies on the two-probe method. In this configuration, a constant current I is applied across the sample through two probes in contact with the electrodes, and the resulting voltage V is measured. Conductivity is then calculated according to

$$\sigma = \frac{L}{W t_z R} \tag{1.2}$$

with R being the measured resistance by the Kelvin setup, L the channel length, W the channel width, and t the film thickness.

However, the two-probe configuration suffers from significant limitations, as the measured resistance includes not only the intrinsic sample resistance (R_{sample}) but also the wire resistance (R_{wire}) and, most importantly, the electrode-sample contact resistance (R_{contact}). While R_{wire} is typically negligible due to the use of highly conductive metals, $R_{contact}$ can be comparable to R_{sample} and thus introduce significative error.[10,11]

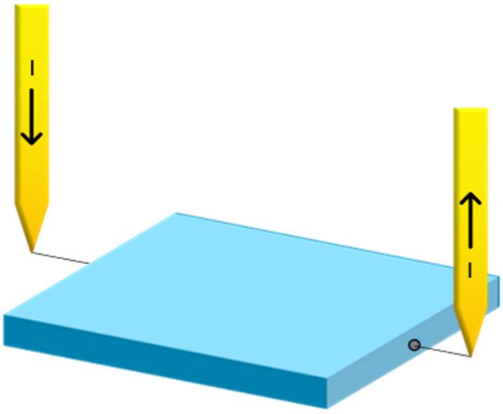

Figure 1.1
Illustration of the two probe method for conductivity measurements.

1.1.2. Conductivity: Four-probe methods

To overcome this issue, the four-probe method is widely employed. In this approach, two outer probes inject the current I across the sample, while two inner probes measure the potential drop using a high-impedance voltmeter. As no significant current flows through the voltage-sensing probes, their contact resistance becomes negligible, thus eliminating the main source of error present in the two-probe setup.

Two major configurations are commonly used in this technique: the **collinear four-point probe** and the **van der Pauw method** (Figure 1.2).

In the collinear configuration, probes are positioned equally spaced along the film surface. If the sample dimensions are much larger than the probe spacing, and the spacing is greater than half of the film thickness, the conductivity can be determined by applying a simplified analytical expression. Otherwise, correction factors accounting for sample geometry are required.[10]

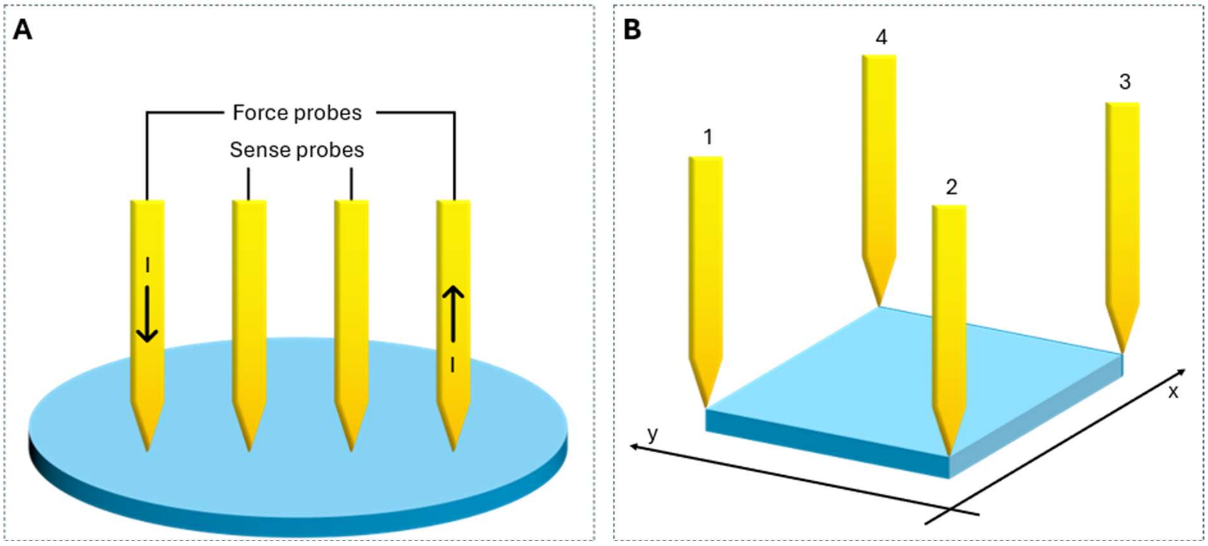

Figure 1.2
Illustration of A) the collinear four-point probe method and B) the van der Pauw method.

The van der Pauw method represents a more versatile approach for **arbitrarily shaped films.**[12,13] In this configuration, four contacts are positioned along the perimeter of the sample, which is conventionally arranged in a square geometry of side length 1 cm. Measurements are performed by alternately selecting two probes as current electrodes and the remaining two as voltage probes. For instance, $R_{12,34}$ corresponds to current driven through contacts 1-2 and voltage measured between contacts 3-4. Complementary resistances (e.g., $R_{43,21}$) are obtained by swapping current and voltage terminals. Averaging these values provides effective resistances in the x and y directions, respectively R_x and R_y (see B, Figure 2.1):

$$R_x = (R_{23,41} + R_{41,23} + R_{32,41} + R_{41,32}) \,/4 \tag{1.3}$$

$$R_y = (R_{12,34} + R_{34,12} + R_{43,21} + R_{21,43}) \,/4 \tag{1.4}$$

These resistances are related to the sheet resistance, R_s, by equation 1.5. This resistance, which is considered as the surface resistivity, is independent on the superficial area of the film and has Ω/sqr as dimensional unit.

$$e^{-\pi\frac{R_x}{R_s}} + e^{-\pi\frac{R_y}{R_s}} = 1 \tag{1.5}$$

Knowing the sheet resistance and the thickness of the sample (t_z) the electrical conductivity can be derived as

$$\sigma = \frac{1}{t_z}\frac{1}{R_s} \tag{1.6}$$

Reliable results require homogeneous films without pinholes, uniform thickness much smaller than the lateral dimensions, and relatively small contacts, often obtained with droplets of silver paste.[10,13]

1.1.3. Thermoelectricity: applications

Nowadays, the transition toward renewable energy sources is becoming increasingly significant. Among these, **thermal energy** plays an important role, as it is abundant and, unlike solar energy, **independent of day-night cycles**.[1]
To convert heat into electricity, and vice versa, **thermoelectric devices** are employed. These systems exploit temperature gradients to generate electrical energy or to provide precise temperature control through solid-state mechanisms.[14–16]

Thermoelectric devices are used across a wide range of fields: in **solar energy systems**, where they recover waste heat and enhance photovoltaic efficiency; in **industrial and IoT sensors**, enabling accurate and self-powered temperature monitoring; and in **medical technology**, where they can power implantable devices such as pacemakers and glucose monitors, or provide localized cooling for ophthalmological and dental applications.[1]

They are also integrated into **wearable electronics** for energy harvesting and personalized thermoregulation, and applied in **fire-warning systems** for automatic heat detection, without necessity of maintenance. Moreover, thermoelectric modules contribute to **AI hardware and robotics**, supporting heat management and self-powered motion recognition.

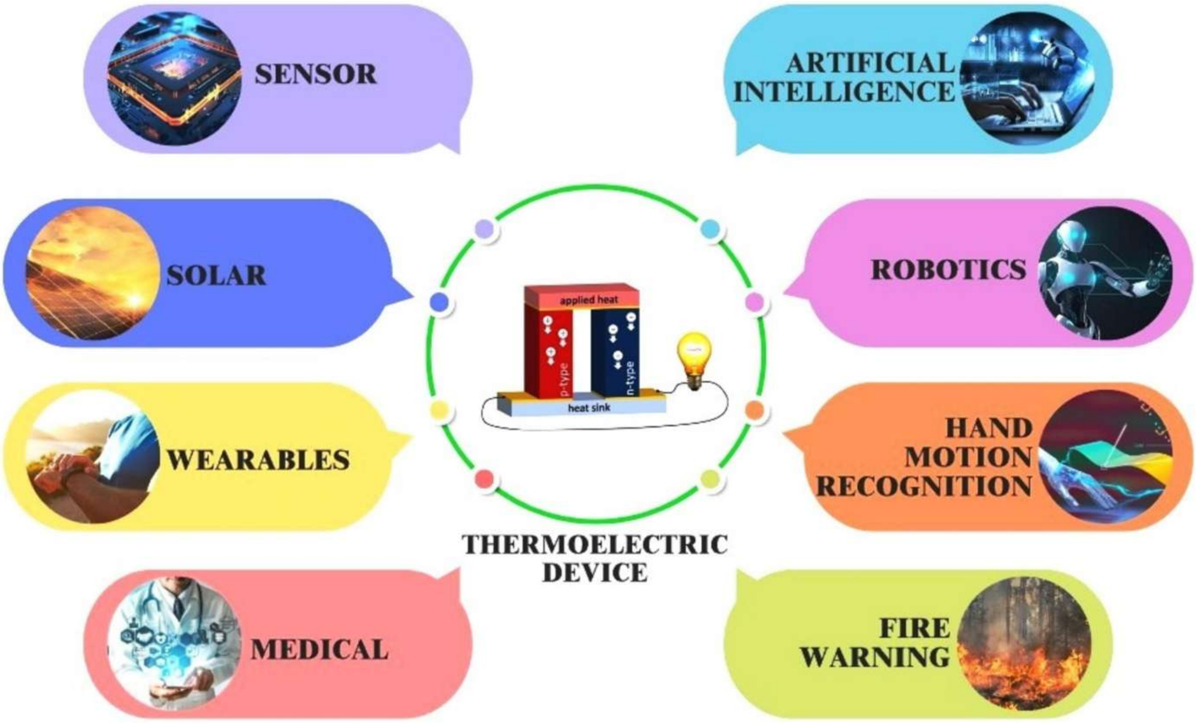

Figure 1.3
Illustration of some thermoelectric applications. Reproduced with permission (Elsevier) from the work of Baskaran and Rajasekar et al.[1]

All of this is made possible by the **thermoelectric effect**, the fundamental principle governing these devices, which will be discussed in detail in the following section.

1.1.4. Thermoelectricity: thermoelectric phenomenon

In a material subjected to a **temperature gradient** (i.e. two ends of the material are kept at different temperatures), the charge carriers tend to move from the hot side to the cold side. This charge separation leads to the generation of an electrical voltage. At the same time, when an external voltage is applied to the material, heat transfer is induced at its ends. Collectively, these phenomena are known as **thermoelectric effect**, first discovered by Thomas Seebeck in 1821.[4]

The thermoelectric effect can be divided into three distinct physical contributions:

- **Seebeck Effect**: A temperature gradient generates a voltage within the material. This phenomenon is quantified by the **Seebeck coefficient** or **thermopower** (S, typically expressed in μV/K):

$$S = \frac{\Delta V}{\Delta T} \tag{1.7}$$

where ΔV is the generated voltage and ΔT is the applied temperature difference.

- **Peltier Effect**: An externally applied electric current induces heat absorption or release at the material's ends, resulting in a temperature difference.
- **Thomson Effect**: When an electric current flows through a conductor subjected to a temperature gradient, the material may absorb or release heat depending on the relative directions of the electric current and the thermal gradient.

The efficiency of thermoelectric materials is quantified by the ratio between the electrical power generated (via the Seebeck effect) and the heat supplied to the hot side per unit time. This is described by the dimensionless **figure of merit**, zT, defined as:

$$zT = \frac{S^2\sigma}{\kappa}T \tag{1.8}$$

where S is the Seebeck coefficient, σ is the electrical conductivity, κ is the thermal conductivity, and T is the absolute temperature. The term $S^2\sigma$ is known as the **power factor** and represents the material's ability to produce electrical energy upon a thermal gradient. A high **figure of merit** corresponds to better thermoelectric performances.

Seebeck coefficient can also be defined as

$$S = \frac{8\pi^2 {k_B}^2 \sigma}{3eh^2} m^* T \left(\frac{\pi}{3n}\right)^{\frac{2}{3}} \tag{1.9}$$

where e is the elementary carrier charge, kB is Boltzmann constant, m* is the charge carrier effective mass, h is Planck's constant, and n is the charge carrier concentration.[17] Thus, S lowers with the increase of charge carrier concentration, in contrast with the behavior of electrical conductivity (equation (1.1).

Additionally, the thermal conductivity (κ) is the sum of the thermal conductivity of the charge-carrier (κ_c), as electrons and holes, and the thermal conductivity of the phonons (κ_l), thus the lattice contribution. In particular, the charge carrier contributions is related to the electrical conductivity by the **Wiedmann-Franz law:**

$$\kappa_c = L\sigma T \tag{1.10}$$

where L is the Lorentz constant, which is equal to 2.45×10^{-8} V^2 K^{-2} for metals and 1.5 10^{-8} V^2 K^{-2} for nondegenerate semiconductors,[4] and T is the absolute temperature. Therefore, the increase of electrical conductivity is accompanied by the increase of thermal conductivity.

A summary of the mutual dependences of thermoelectric parameters is reproduced in Figure 1.4.

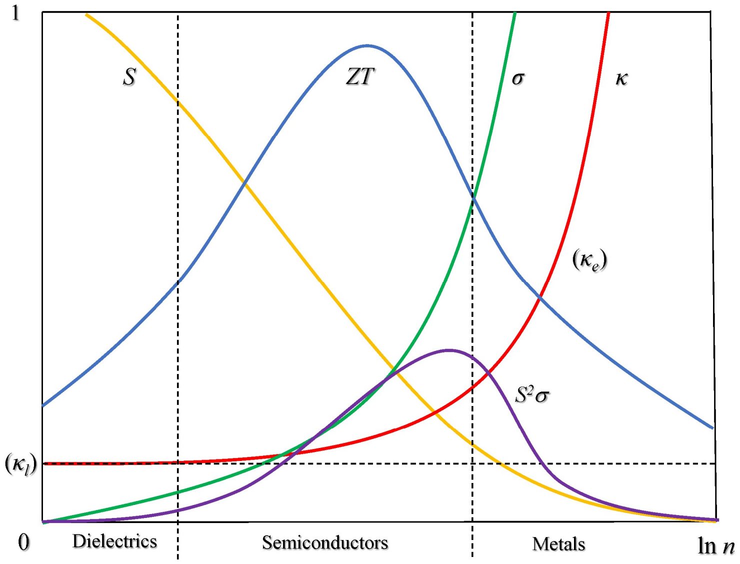

Figure 1.4
Schematic dependence of the main thermoelectric parameters, Seebeck coefficient (S), electrical conductivity (σ), thermal conductivity (ϰ), power factor ($S^2\sigma$), and figure of merit (ZT), on the charge carrier concentration (n). Reproduced from the work of Asencio-Hurtado et al.[18] License CC BY.

To achieve materials with a high figure of merit (zT), and, thus, an efficient conversion of thermal energy into electrical energy and vice versa, it is necessary to combine high electrical conductivity (σ), large Seebeck coefficient (S) with low thermal conductivity (κ). Obtaining high zT values in **metals** is particularly challenging, as they exhibit very high electrical conductivity, which is accompanied by comparably high thermal conductivity due to the Wiedemann-Franz law. Moreover, their Seebeck coefficients are typically small.[14]

On the contrary, **insulating** materials show very low thermal conductivity but insufficient electrical conductivity. Semiconductors, on the other hand, exhibit relatively high Seebeck coefficients and reduced thermal conductivity. In addition, they offer the possibility of tuning the charge carrier concentration through doping to maximize the power factor.[1,10,19,20]

This versatility makes semiconductors the most promising class of materials for thermoelectric applications.

1.2. Carbon-based and Organic Semiconductors

The transition from conventional inorganic semiconductors to organic- or carbon-based semiconductor materials is driven by the introduction of chemical and physical properties that are complementary to those of established technologies (see Table 1.1).[2,3] In this section, we will examine in detail the electronic characteristics of **organic semiconductors** (OSCs) and **carbon nanotubes** (CNTs).

Table 1.1
Comparison between the major properties that distinguish innovative semiconductors, as organic- based and carbon-based SCs, and traditional inorganic SCs.

Properties	**Organic-based and carbon-based SCs**	**Inorganic SCs**
Mechanical properties	Highly flexible and mechanically robust	Usually rigid and brittle
Density	Lightweight materials	Dense and heavy materials
Fabrication and processing conditions	Solution-processed at low temperatures	Complex fabrication steps at high temperature and high vacuum
Design freedom	High allowance of customization of their chemical structure	Properties are fixed by the crystal lattice
Application versatility	Flexible displays Wearable sensors Biomedical devices Organic solar cells OLEDs	High-power, high-frequency, and durable electronic devices

1.2.1. OSCs: electronic structure

Organic semiconductors are characterized by **conjugated π-electron systems**.[21] In these systems, carbon atoms are sp² hybridized, meaning each carbon has a $2p_z$ orbital that overlaps with the $2p_z$ orbitals of neighboring carbons. This overlap allows the π-electrons to delocalize along the molecule, which reduces the energy gap between the **highest occupied molecular orbital (HOMO)** and the **lowest unoccupied molecular orbital (LUMO)**. This energy difference is known as the **band gap (E_g).** As conjugation increases, the system approaches the limiting case in which the bonding and antibonding π-orbitals overlap, leading to the formation of a **valence band (VB)** and a **conduction band (CB)** .[22]

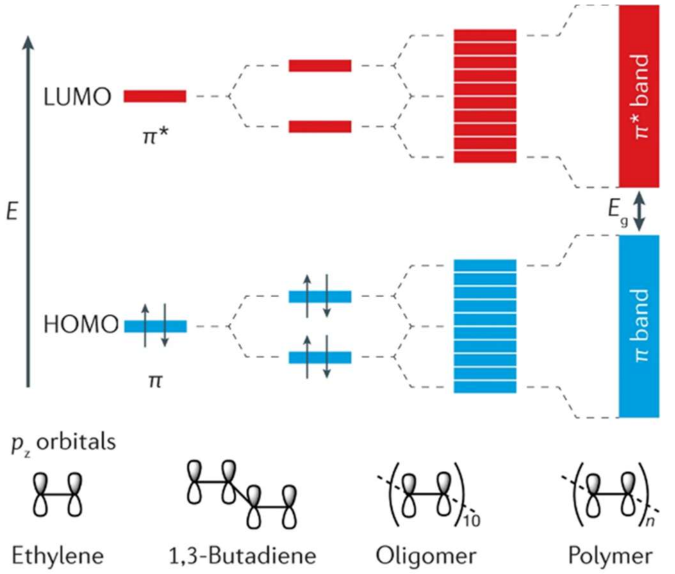

Figure 1.5
Formation of a valence band and a conduction band in conjugated π-electron systems by $2p_z$ orbital overlapping. The figure is adapted with the permission of Spinger Nature from the work of Li and coworkers.[23]

A representative example of a conjugated polymer is **poly(3-hexylthiophene)** (P3HT), one of the most studied materials in organic photovoltaic (OPV) research. However, P3HT still exhibits a relatively high band gap of about 1.9 eV, which limits its light absorption. For this reason, several strategies have been developed to further reduce the band gap of semiconducting polymers.[24] There are **three main approaches** to achieve this goal:

1. Extending the π-conjugated system;
2. Converting aromatic structures into quinoid ones;
3. Incorporating donor-acceptor (D-A) repeating units.

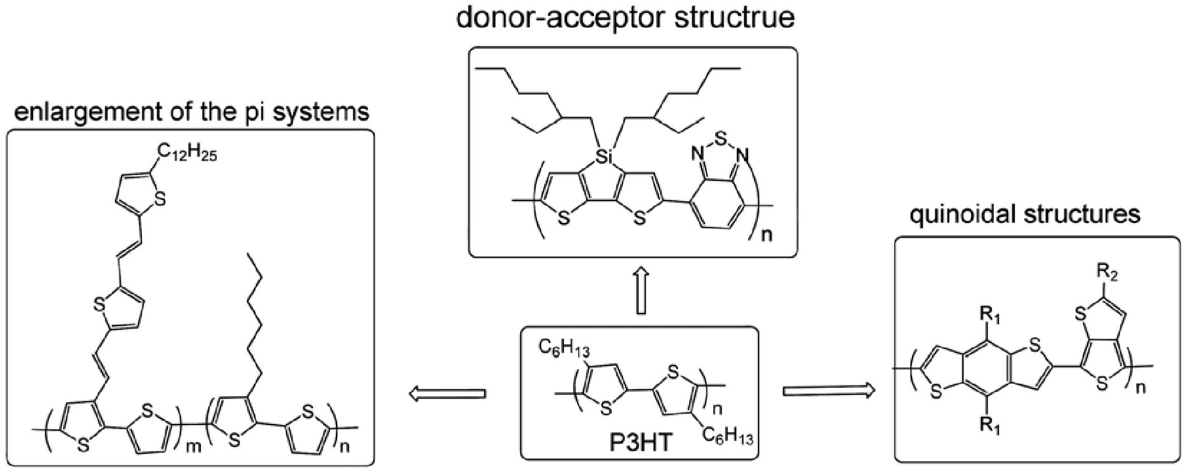

Figure 1.6
Molecular structures of semiconducting polymers designed by following the approaches to reduce the band gap, compared to the benchmark P3HT. Reproduced with permission by the Royal Society of Chemistry from the work of Zhang e Wang et al.[25]

The first two strategies are effective in narrowing the band gap, but they have the drawback of raising the HOMO energy level, which leads to a decrease in the open-circuit voltage (V_{oc}) of the device.[25,26]

This issue is not present in **D-A copolymers**. The donor-acceptor approach is currently considered the most relevant strategy to obtain low-band-gap organic semiconductors. In this case, the frontier molecular orbitals (FMOs) of the donor and acceptor units **hybridize**, furnishing a HOMO level close to the HOMO of the donor, and a LUMO that is primarily localized on the acceptor and is similar in energy to its LUMO. This configuration allows an effective reduction of the band gap without significantly affecting the open-circuit voltage.

The donor-acceptor approach is currently considered the **most relevant** strategy to obtain low-band-gap organic semiconductors.[24,27]

Generally, the band gap for pristine conjugated small molecules or polymers typically ranges from 1.5 to 3.5 eV, thus, still too high for actual implementation in optoelectronic devices.[28]

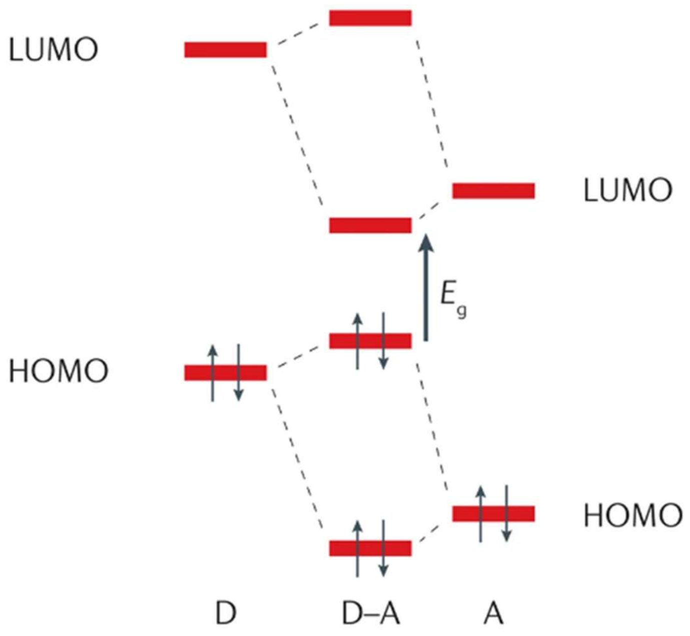

Figure 1.7
Orbital hybridization of donor (D) and acceptor (A) units, giving a smaller bandgap in donor-acceptor (D-A) polymers. The figure is adapted with the permission of Spinger Nature from the work of Li and coworkers.[23]

Organic semiconductors (OSCs) are often classified as **n-type**, where electrons are the primary charge carriers, or **p-type**, where holes dominate. However, this classification should be treated with some caution. When discussing charge transport, it is worth noting that many organic semiconductors are intrinsically **ambipolar**, and are therefore not strictly p- or n-type materials. In practice, the dominant charge carrier is typically defined at the device level, for instance through electrode selection, interface engineering, or intentional doping.

In this context, it is more appropriate to distinguish OSCs based on the position of their frontier molecular orbitals (FMOs). P-type OSCs typically exhibit high HOMO energy levels, meaning that the energy required to remove an electron and bring it to the vacuum level (**ionization energy, IE**) is relatively low. Conversely, n-type OSCs are characterized by low-lying LUMO levels, making them easier to reduce, since the energy required to add an electron from the vacuum level, defined as the **electron affinity (EA)**, is small.

1.2.2. OSCs: charge transport

The introduction of an unpaired charge into the conjugated system triggers a local lattice distortion known as a **polaron**, which corresponds to a relaxation of the molecular lattice. The formation of a polaron is accompanied by the appearance of electronic states within the band gap of the neutral molecule, referred to as **polaron states**. If a second charge of the same type is added, a bipolaron can form, whether that the energy gained from the lattice interaction exceeds the Coulombic repulsion between the two analogous charges.[29] Charge transport in organic semiconductors relies on the movement of polarons and is influenced by the electronic coupling between adjacent molecules as well as their relative spatial disposition.[30]

In the solid state, semiconducting molecules interact primarily through **weak van der Waals forces**, which limits the electronic coupling between molecules and, consequently, the extent of charge delocalization. However, in materials with highly ordered regions, significant charge delocalization can be achieved, leading to band-like conduction as observed in single-crystal solids.[31,32]

Organic materials are typically processed as thin films, whose morphology is mainly composed of an **amorphous matrix** with varying amounts of crystalline regions: semicrystalline materials contain a high percentage of ordered domains, partially ordered materials have a lower percentage of crystallinity, and amorphous materials completely lack crystallinity. The presence of an amorphous phase is characteristic of polymeric materials, and is related to their greater suitability for solution processing and flexibility compared to small molecules.[33]

As mentioned earlier, in the ordered regions charge carriers can be considered **delocalized** and “free to move”, whereas, in the amorphous regions, conduction occurs via **thermally activated hopping** of charges between adjacent molecules. The disordered molecular packing in organic semiconductors often leads to localized states within the band gap, known as **trap states**, which can hinder charge carrier mobility.[34]

The polaron distortion, combined with limited charge delocalization and morphological disorder, negatively affects the material charge mobility. Therefore, organic semiconductors typically exhibit carrier mobilities below 10 $cm^2\ V^{-1}\ s^{-1}$,[35] significantly lower than those reported for highly crystalline inorganic semiconductors (10^2 - 10^4 $cm^2\ V^{-1}s^{-1}$).[36]

Due to the poor mobility of charge carriers and the large band gap of intrinsic organic semiconductors, the electrical conductivity of these materials at room temperature is very low, ranging from 10^{-10} and 10^{-6} S cm^{-1}. Such performance is insufficient for practical device applications, and in this context, doping is employed as an effective method to enhance the properties of OSCs. On the other hand, under these conditions, the Seebeck coefficient typically exhibits relatively high absolute values, being primarily governed by the energetic distribution of transport states and the charge carrier concentration, which leads to an intrinsic trade-off between thermopower and electrical conductivity.

1.2.3. CNTs: electronic structure

Carbon nanotubes (CNTs) are nanomaterials that belong to the bigger class of carbon-based materials, thus materials that are primarily based on sp^2 carbon, such as for example graphene, graphene nanoribbons and fullerenes, among the others. Discovered in 1991 by Sumio Iijima,[37] CNTs are cylindrical nanostructures obtained by rolled-up graphene sheets, where carbon atoms are arranged in a hexagonal lattice. CNTs are classified as **single-walled carbon nanotubes (SWCNTs)**, where there is a single graphene cylinder, while they are called **multi-walled carbon nanotubes (MWCNTs)**, when composed by multiple concentric cylinders. The diameter of SWCNTs commonly ranges from 0.4 to 4 nm, whilst MWCNTs can have diameters up to 100 nm, and both with lengths extending from nanometers to micrometers.[38,39] Their geometry and the extended sp^2-hybridized carbon bonding are responsible of the exceptional properties of CNTs, making them pivotal materials in nanoelectronics, materials science, and energy storage.

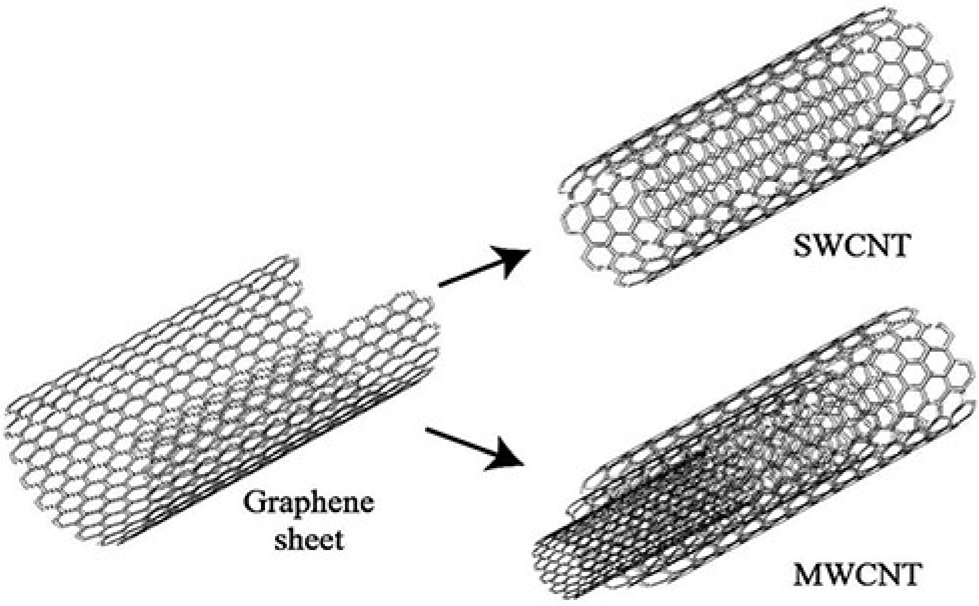

Figure 1.8
Schematic representation of the structural relationship between a graphene sheet and carbon nanotubes. Rolling up a single graphene sheet forms a single-walled carbon nanotube (SWCNT), while the concentric rolling of multiple graphene sheets results in a multi-walled carbon nanotube (MWCNT). Reproduced with permission from the work of Sheikhpour et al.[40]

To better understand the electronic structure of CNT, it is useful to discuss firstly the properties of graphene. Graphene is a lattice developed in two dimensions and constituted only by carbon sp^2

hybridized. The occupied band and the unoccupied band generated by this system cross at the **Fermi level** in a discrete and finite set of points. The Fermi level, even called charge neutrality point, is the energy level at which the probability of occupation by an electron is 50%. Due to this characteristic graphene has a zero-gap character, analogous to that of metals.

However, by passing from planar systems to rolled-up sheets, **periodic boundary conditions** are introduced. Thus, in the case of CNT the wavevectors "around" the nanotube circumference can only assume a set of discrete values, they are quantized. In the case that the allowed vectors include the Fermi level, , the CNT has a metallic behavior (m-CNT), on the contrary the system has a small band gap, and it behaves as a semiconductor (s-CNT). [41]

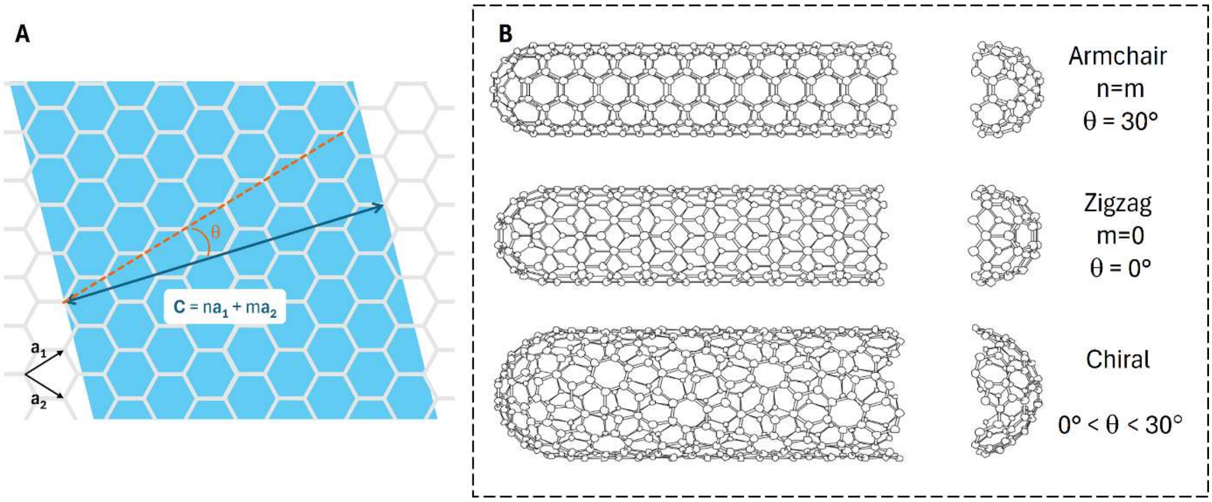

Figure 1.9
(A) Derivation of the SWNT structure from graphene, the chiral vector is highlighted. Adapted with permission by Elsevier from the work of Qian and co-workers et al.[41]
(B) Schematic models for the three possible types of single-wall carbon nanotubes. Adapted from Dresselhaus, M.S., Avouris, P. (2001). Introduction to Carbon Materials Research. In: Dresselhaus, M.S., Dresselhaus, G., Avouris, P. (eds) Carbon Nanotubes. Topics in Applied Physics, vol 80. Springer, Berlin, Heidelberg.

Chirality is defined by the chiral vector **C**, which describes how the graphene sheet is rolled. The expression of the vector is

$$C = na_1 + ma_2 \tag{1.11}$$

Where **a_1** and **a_2** are the basis versors of the graphene sheet, and the couple (n,m) is the chiral index. From the values of n and m it is possible to determine the electronic character of the CNTs. As a general rule, if the ratio (n-m)/3 results in an integer, the tubes are metallic; if not, they are semiconducting.[41–43] In addition, it is possible to specify the chirality by the angle formed between the vector **C** and the versor **a_1**, called the chiral angle θ.
Carbon nanotubes of the type n,n (where n = m, and $\theta = 30°$), that are referred to as **armchair tubes** due to the armchair pattern along the circumference, present a metallic behavior. On the contrary, **zigzag tubes** (m = 0, and $\theta = 0°$) and **chiral tubes** (n,m with $n \neq m \neq 0$, and $0° < \theta < 30°$) can be semiconducting or metallic.

In addition, the diameter of the CNT is inversely proportional to the amplitude of the band gap. In fact, an infinite large diameter recover the approximation of a graphene sheet where the band gap is zero, and, thus, the tube has a metallic behaviour.[44] Whilst, typically for semiconducting SWCNTs, the band gap ranges from 0.1 to 2 eV.
In the case of MWCNTs, the conductivity is determined by the interactions between the outermost shell and the innershell and the discrimination between semiconductor and conductor is not as obvious.[45]
Furthermore, the band gap and the resulting electronic properties of CNTs can be significantly affected by **external factors** such as structural defects,[46] doping,[47] and interactions with the surrounding environment.
These combined effects ultimately define whether a CNT behaves as a metal or a semiconductor and thus determines its suitability for specific applications.

1.2.4. CNTs: charge transport

Charge transport in **metallic carbon nanotubes** is characterized by a **weak intermolecular localization** of the charges, and the boundaries between different nanotubes act only as weak sources of disorder. In these systems, the conductivity can reach or even overcome the performance of metals, as copper.[48,49]

However, **semiconducting CNTs** behave differently.
As we have seen, a single nanotube has a defined electronic structure, but actual samples of s-CNT are polydisperse and consist in semiconducting nanotubes that differ in chirality, diameter, and length. Additionally, in every sample can vary the degree of nanotube network density, the bundling

of the CNT and the presence of defects. The conductance of a network of nanotubes depends on the density and on the connectivity of the same, and it is described by the percolation theory.

The **percolation phenomenon** is characterized by a phase transition in which a system passes from insulating to conducting as the probability of site or bond occupation increases. To describe it, Saberi et al.[50] considers a 2D hexagonal honeycomb lattice, where metallic hexagonal plaquettes are randomly placed on an insulating structure connected to a bulb. At low occupation probability, only small and disconnected metallic clusters form, so no current can pass through the lattice. As this probability increases and overpasses a critical threshold **p_c (percolation threshold)**, a bridge is formed and connects the opposite sides of the lattice, allowing current to flow and the bulb to light up.

Analogously to this image, in CNT systems, under the percolation threshold, the conductance remains negligible. However, once the critical value is reached, the conductance rises by several orders of magnitude. As the density of nanotubes continues to increase over the p_c, the general network connectivity is enhanced, resulting in multiple current pathways and, thereby, higher conductivity.[51]

In addition to the density, the factors affecting the CNT conductance for a single tube are the **intramolecular charge transport** (along the CNT) and the **length** of the CNTs. Then, if we consider a system composed by multiple nanotubes, we have to take in account the nanotube-nanotube **junctions**, the energetic landscape, which is composed of the different CNTs, **trap states** and **dipolar disorders**, scattering caused by lattice defects and field screening in bundles (Figure 1.10).

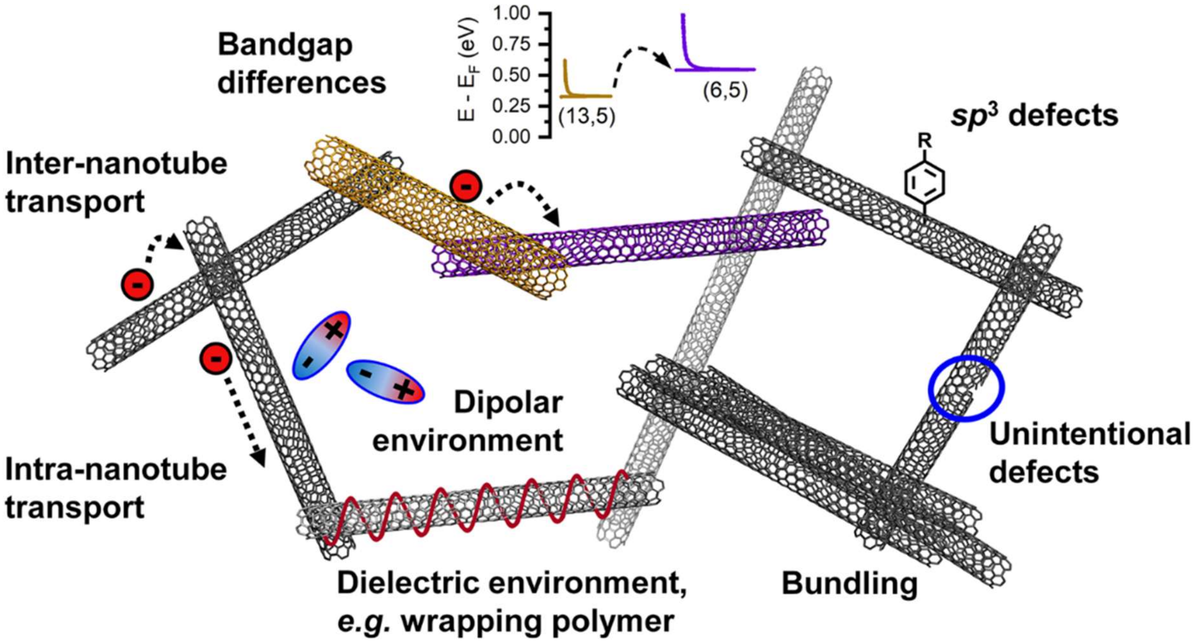

Figure 1.10
Illustration of different contributions to conductance or resistance in dense networks of purely semiconducting SWNTs. Reproduced by the work of Zorn and Zaumseil et al.[52]. License CC BY 4.0.

There is no model that considers all these parameters, but, applying some simplifications, we can still define some general trends.

Single SWCNTs, longer than the mean free path of electrons (< 1mm), are characterized by a band transport hindered by the scattering at phonons and defects. In an ideal, defect-free nanotube, the charge carrier mobility increases with the reduction of the temperature and/or with the increase of the tube diameter. This behavior follows the empirical law:

$$\mu(T,d) = \mu_0 \frac{300K}{T} T \left(\frac{d}{1\,nm}\right)^{\beta} \tag{1.12}$$

Where m_0 = 12000 $cm^2\,V^{-1}\,s^{-1}$ and b = 2.26. Accordingly, at room temperature, a single (6,5) SWCNT (d = 0.757 nm) would have a charge carrier mobility of ~6400 $cm^2\,V^{-1}\,s^{-1}$.

In SWCNT networks, the **inter-tube junctions** act as potential barriers that carriers must overcome via hopping or **tunneling.**[53] The nanotube network can be considered as a disordered system where the charges are transported across different highly conductive regions through carrier hopping. The models used to describe the hopping mechanism of such carriers converges to the fact that hopping is a **thermally activated mechanism** and, hence, the conductivity in this case increases with the temperature.[48,52]

We can conclude that, depending on the network compositions, there are different contributions to the temperature dependence: the thermally activated transport across inter-tube junctions, the inverse temperature dependence of charge transport within individual tubes, and the mobility increase with the square of the nanotube diameter.[52]

However, the **strong intermolecular π-orbital** overlap keeps the hopping energetic barriers relatively low, making the related resistance comparable to that of single molecules (10^2-10^5 kW). Sano et al.[54] evidences how such resistances are higher when the tubes interested by the transfer differ in diameter and chirality, but nevertheless they decrease as the diameters of the CNT increases. The main problem related to the junctions is actually represented by the introduction of a significant intermolecular **scattering** which can drastically reduce charge carrier mobility.[45,51,52,55] For example, as reported by Tripathy et al.[51] in 2020, the highest obtained mobilities of random SWCNT networks are only around 150 $cm^2\ V^{-1}\ s^{-1}$. Notably, this scattering can be mitigated by increasing the length of the nanotubes, as longer CNTs require fewer junctions for charge transport. Therefore, maximizing device performance calls for a combination of structural uniformity, optimized CNT length, and tailored network architecture.

Ultimately, the charge transport characteristics of semiconducting CNT networks result in moderate Seebeck coefficients, reflecting the interplay between highly conductive nanotubes and thermally activated transport across inter-tube junctions.

1.3. Doping

The Fermi level of an undoped semiconductor is located approximately at the middle of the bandgap, and, thus, the concentration of the holes and the electrons in the material are **equal**. This scenario can be modified by doping.[20] The concept of doping was first introduced in the field of inorganic semiconductors and refers to the process of increasing the charge carrier density (n), and, thereby, the electrical conductivity, of a material through the controlled introduction of impurities and their interactions with the host. These impurities can **donate electrons**, in case of n-type doping, shifting the Fermi level to higher values, or **accept electrons** for p-type doping, shifting the Fermi level to lower values (see Figure 1.11).[56,57]

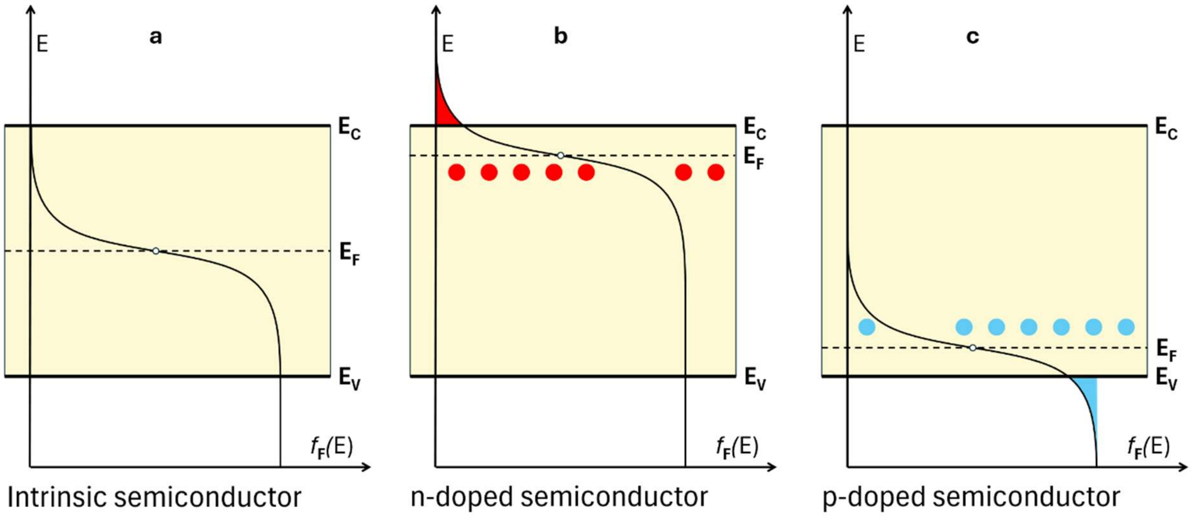

Figure 1.11
Schematic representation of the Fermi-Dirac distribution in (a) an intrinsic organic semiconductor, (b) p-type doping with acceptor states (red), and (c) n-type doping with donor states (blue). Upon the introduction of electrons (red) or holes (blue), doping shifts the Fermi level (E_F) towards the HOMO or the LUMO, respectively, modifying the occupancy of electronic states.

In the context of inorganic semiconductors, doping is usually operated through the incorporation of substitutional or interstitial atomic impurities into the crystal lattice. These atoms act as donors if they have more valence electrons, or as acceptors if they have fewer than the host atoms. For example, phosphorus and arsenic are donors for silicon and germanium, while boron and gallium are acceptors.

This doping process is extremely efficient in inorganic systems, and **each dopant atom typically**

originates one fully mobile carrier. Therefore, even extremely low doping levels, between 10^{-3} and 10^{-6} of doping ratio, are enough to significantly improve conductivity without disrupting the morphology of the host.

1.3.1. Doping in OSCs

In contrast, **organic semiconductors (OSCs)** present a different scenario due to their unique structure and electronic nature. In these systems, molecular dopants are blended with the host semiconductor and trigger doping through **oxidation (p-type)** or **reduction (n-type)** reactions, however, the practical application of this strategy is dramatically more ambitious in respect of the inorganic case.

Because OSCs are characterized by a **low intrinsic charge carrier mobility**, the concentration of dopant needed to achieve relevant electrical conductivities is very high (between 10% and 40% molar ratio in respect of the conductive unit). The introduction of such a quantity of dopant, that morphologically represents an impurity, can have a considerable influence on the microstructure of the semiconductor system. Moreover, differently from inorganic systems, where dopants are covalently bound within the lattice, the dopant interacts typically via **weak van der Waals** or Coulombic forces with semiconductor molecules. This gives the possibility to the **dopant** to diffuse, segregate, and ultimately reduces operational stability of devices over time. Consequently, reaching effective and stable doping in OSCs requires careful design and deep understanding of dopant/host interactions at the molecular level.

1.3.2. Doping in CNTs

Carbon nanotubes are intrinsically neutral/ambipolar materials, because their DOS around the Fermi level is symmetrical. However, in ambient conditions they physisorbe oxygen and become p-doped. As reported by Tey et al.[58], oxygen reduces the Fermi level of the CNT and thus improve the conductivity of the semiconductor, while complete dedoping can be operated by annealing at high temperature (900°C) reestablishing the Fermi level at its theoretical position.

In carbon nanotubes (CNTs) there are two main branches of doping: **substitutional doping** and **charge-transfer doping**.[41]
Substitutional doping involves the exchange of heteroatoms (such as nitrogen, boron, sulfur, or

phosphorus) with carbon atoms directly into the CNT lattice during synthesis. This is usually operated by chemical vapour deposition (CVD), using precursors like NH_3 (for N-doping) or B_2H_6 (for B-doping). This kind of doping is similar to the inorganic case: the introduction of impurities triggers the formation of **impurity states** into the electronic band structure that modifies the energy levels of the CNT.

In the second case, in analogy to OSCs doping, molecules dope the carbon nanotubes by redox reactions. Due to the geometry and the electronic properties of the CNTs, three main charge-transfer mechanisms are possible:[59]

- **External doping**, where dopants are adsorbed on the outer surface of the nanotubes. Although there are few examples of co-deposition of the CNT and dopant,[60] typically the CNT are obtained in film form, and in a second step the dopant is deposited on top of it, either from solution or through thermal evaporation.[61]
- **Internal doping**, which operates through the encapsulation inside the hollow core of the nanotubes. When SWCNTs are synthesized they have cap structures at their ends that are removed by annealing at 400-650°C to obtain access to the internal surface.[62,63]
  Subsequently, the dopant encapsulation can be performed by gas-phase processing techniques[64] or liquid phase processing techniques.[65]
- **Electrochemical doping**, where charge carriers are injected into the SWCNTs exploiting an external voltage.[66] The pre-formed CNTs are immersed into an ionic liquid, such as *N*-trimethyl-*N*-propylammonium bis(trifluoromethanesulfonyl)imide (TMPA-TFSI),[19,66] which acts as both the electrolyte and the source of counterions. Upon action of a voltage, charge carriers are injected into the SWCNTs, resulting in their doping.

Since the dopant molecules are introduced in pre-formed CNT network, molecular doping does **not alter the morphology** of the semiconductor.[59] Moreover, the rigid structures of the tubes is barely perturbated by insertion of charges, leading to a better delocalization in respect of the case in which a polaron is formed.

For both external and electrochemical doping, the dopants G, and the influence of counterions on the electrical properties follows similar behavior. However, when dopants are inserted inside the nanotubes (internal doping), higher doping levels and electrical conductivities have been observed though the exact reasons for this enhanced performance are still not fully understood.

1.3.3. Applications and doping relevance

When considering practical device implementation, the integration of **doped** carbon nanotubes (CNTs) and organic semiconductors (OSCs) becomes essential. Both material classes exhibit charge transport predominantly governed by hopping or percolative conduction mechanisms, as discussed in the previous sections. These mechanisms are influenced by the local electronic environment, structural disorder, and energy level alignment at material interfaces. In this context, **doping** emerges as an essential strategy for the controlled modulation of both electrical and interfacial properties.

For CNTs, chemical doping can significantly enhance electrical conductivity by increasing the free carrier density within the CNT network. This is particularly advantageous in random networks or films used in thin-film transistors (CNT-FET),[67] sensors,[68] where pristine conductivity may be insufficient for optimal device operation. Furthermore, doping enables precise tuning of the CNT Fermi level, improving alignment with electrode work functions and, thereby, facilitating more efficient charge injection or extraction.[69]

Analogously, in OSCs, doping enhances the conductivity of transport layers, reducing Ohmic losses and lowering the operating voltages in devices such as organic photovoltaics (OPVs),[23] organic light-emitting diodes (OLEDs),[70] and organic field-effect transistors (OFETs).[71] Doping can also passivate trap states within the energy gap, thus mitigating carrier recombination and increasing the effective charge-carrier mobility.[72]

One of the application domains where doping plays a particularly relevant role is in **thermoelectric devices**. These devices rely on coupling p-type and n-type semiconductors to form a complete thermoelectric circuit, typically involving the connection in series of multiple elements to achieve a significant thermoelectric voltage.[73] OSCs possess inherently low thermal conductivity, typically ranging from 0.1 to 1.0 W m^{-1} K^{-1}, due to their disordered morphology. This property is highly favorable for achieving high figures of merit (zT). However, as previously discussed, their intrinsic charge carrier concentration is extremely low, making doping essential to achieve the electrical conductivities required for practical thermoelectric performance.[74] In contrast, CNTs exhibit intrinsically high electrical conductivity even in their pristine form, but their thermal conductivity is also exceptionally high, mining the achievement of high zT values.[74] In this context, doping is used to modify the Seebeck coefficient while further enhancing electrical conductivity, enabling to obtain the best of both worlds, also, it is not uncommon to employ composite obtained by mixing CNTs and OSCs.[15]

1.3.4. Doping Efficiency

Not all molecular dopants successfully generate free charge carriers within the host. To quantify the effectiveness of a doping process, the doping efficiency (η_{eff}) is defined as the ratio between the number of free charge carriers (N_{free}) generated and the number of dopant molecules introduced (N_{dopant}):[30,75]

$$\mu_{eff} = \frac{N_{free}}{N_{dopant}} \tag{1.13}$$

The generation of mobile charge carriers typically involves two steps: the charge transfer and the dissociation of the charged species.[76]

1.3.5. Generation of Free Charge Carriers

The charge transfer, or ionization step, can occur organic semiconductors and CNTs mainly through two distinct mechanisms: ion-pair formation (IPA) and charge transfer complex (CTC) formation.[56,57,60,74,77,78]

Ion-pair formation is the most widely observed and better understood mechanism.[30] It involves an integer charge transfer between the dopant and the organic semiconductor (OSC), resulting in the formation of a cation and an anion that subsequently interact via Coulombic attraction. In this step, the thermodynamic driving force of the charge transfer reaction is crucial.[79] High ionization yields are typically observed in systems where there is a **large energy difference** between the dopant and the host semiconductor, such as a high electron affinity (EA) of the acceptor or a low ionization potential (IP) of the donor.

On the other hand, the formation of a **charge transfer complex (CTC)** occurs through the hybridization of the molecular orbitals of the OSC and the dopant, resulting in the formation of a neutral complex with distinct frontier molecular orbitals.[49] Unlike ion-pair formation, CTC formation does not necessitate a strict energy level offset, instead, charge transfer is partial and does not produce free ions or radicals. Although CTCs can undergo further ionization by transferring a full charge to or from another OSC unit in the matrix, this process typically requires thermal activation and is generally less efficient than direct integer charge transfer.

From an experimental perspective, integer charge transfer and charge-transfer complex formation can be distinguished by employing UV-Vis-NIR spectroscopy. Integer charge transfer is typically accompanied by the appearance of the characteristic absorption bands of the dopant ions. In contrast, charge-transfer complexes give rise to new low-energy absorption bands that are not present in the pristine materials. These bands originate from optical transitions between hybridized donor-acceptor electronic states and reflect a reduced effective energy gap of the complex, indicating partial rather than full charge transfer.[49]

In addition to these classical mechanisms, more recent works have highlighted a **third class of doping** mechanisms that involve chemical reactions coupled with charge transfer. These include hydride transfer, proton transfer, Lewis acid-base interactions, and nucleophilic substitution. In these systems, the dopant acts as a redox agent and, at the same time, participates in a chemical reaction with the OSC that facilitates the doping process.

After their formation, the carrier charges must separate from the counterion to become mobile and contribute to the conductivity of the system. Therefore, overall doping efficiency depends by both the ionization yield of the dopant and the degree of ion pair **dissociation**. Commonly, doping efficiencies are relatively low, ranging from 10-20% due to inefficiencies in one or both steps of the process.[80]

In particular, in certain systems, even when the dopant ionization step is almost complete, overall doping efficiencies can fall below 5% due to poor charge separation.[81] This inefficiency is primarily attributed to the intrinsically **low dielectric constants** of organic semiconductors and carbon nanotubes,[82] which hinder effective electrostatic screening. Consequently, the Coulomb binding energy between the dopant ion and the charge carrier can reach values of 0.2-0.6 eV,[83,84] a very high activation energy compared to the ambient thermal energy ($k_BT \approx 25$ meV).[81] Thus, the ion pair formed in this process acts as a **trap** for the charge carrier at the dopant site. However, this bound state can be weakened by energetic disorder within the host matrix, by overlapping Coulomb potentials,[59] or by employing bulkier dopants.

The **size** of the dopant influences the doping efficiency by different points of view.[85]

First, bulkier dopants **increase the average distance** between charge and counterion, thereby weakening the Coulomb interaction.[86] Therefore, dopant counterion of big dimensions delocalize the charge on the semiconductor in a larger segment, loosening the Coulombic interaction in the bounded ion-pair and enabling a better conductivity.[87] However, dopant molecules that are **excessively bulky** may be sterically hindered from accessing all available doping sites on the semiconductor, especially in sequential doping, resulting in inhomogeneous doping and limited charge transfer.[88]

1.4. Molecular dopants

Early strategies for doping organic semiconductors often involved the use of highly oxidizing gases, like halides (I_2, Br_2).[89,90] These dopants were found to be efficient acceptors for materials like phthalocyanines, significantly enhancing their electrical conductivity. However, due to **high diffusivity** related to their reduced molecular volume, these dopants proved to be unsuitable for applications in which long-term thermal and chemical stability are required. For example, in multilayer device architectures like p-n or p-i-n junctions, dopant migration can degrade the performance. For n-doping, the first approaches relied on elemental species such as alkali metals,[91] which are strong electron rich reductants. However, while these dopants can easily transfer charges to organic semiconductors, they often suffer from similar issues related to diffusion and instability.

To address these limitations, researchers have increasingly focused on larger and more complex dopant molecules, especially those with **aromatic** or **π-conjugated frameworks.**[92,93] Due to their bulkiness, these dopants tend to exhibit limited mobility, combined with higher solubility, ease of processing and versatile synthetic protocols, which are fundamental features for a fine-tuning of the dopant properties.

In respect of these characteristics, this project contributes to the growing field of research by further exploring the design and application of bulky molecular dopants.

1.4.1. N-type and P-type Dopants

To dope OSCs with high efficiency, plenty of studies have focused on the molecular design of dopants. To date, **modulating the energy level** has been recognized as the most efficient strategy, but before delving into this problem it is helpful to reconsider quantitively the energy levels of semiconductors.

In Figure 1.12, the energy levels of some of the most common organic semiconductors are reported. Species characterized by superficial HOMO levels, approximately between -4.5 eV and -5.5 eV,[94] are considered p-type semiconductors. While n-type OSCs have usually deep LUMO level that can be found between -3.5 eV and -5.0 eV.[35] In CNTs, the HOMO and the LUMO levels are influenced by the diameter of the tubes, but in principle the HOMO is reported to lie between -4.6 eV and -5.6 eV, while the LUMO can be found between -3.5 eV and -4.0 eV.[95,96]

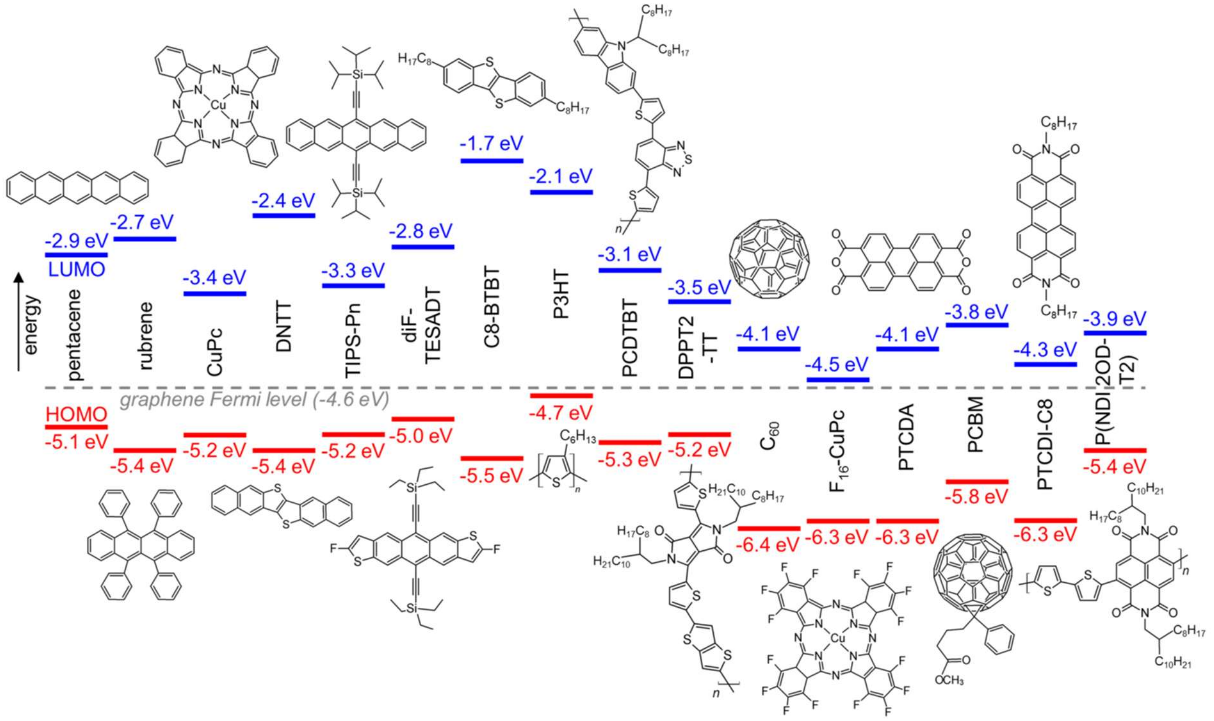

Figure 1.12
Energy level diagram of selected organic semiconductors, showing the HOMO (in red) and LUMO (in blue) energy positions relative to the vacuum level. Molecular structures are displayed alongside their corresponding energy values. The graphene Fermi level (-4.6 eV) is indicated as a reference. Reproduced with permission of the Royal Society of Chemistry from the work of Kim and Kymissis et al.[97]

To achieve effective p-type doping in a semiconductor, the electron acceptor dopant must possess a LUMO energy level lower than the HOMO of the host semiconductor. From figure 1.12, it can be noted that the acceptor's LUMO should be below approximately -4.7 eV to function efficiently as a dopant.

Among p-type dopants, tetracyanoquinodimethane (TCNQ) derivatives constitute the most extensively studied class.[74] TCNQ was first introduced in 1976 and inherently exhibits a relatively high LUMO level of about -4.3 eV. Nevertheless, through the introduction of electron-withdrawing substituents, such as fluorine atoms on the molecular core, the electron affinity increases and consequently the LUMO energy decreases. For instance, 2,3,5,6-tetrafluoro-tetracyanoquinodimethane (F4TCNQ) presents a LUMO level around -5.24 eV, enabling it to dope a broad range of organic semiconductors effectively.[98] The pioneering work of Yim et al.[99] demonstrated the efficacy of F4TCNQ doping across various polymer semiconductors, and subsequent investigations have thoroughly characterized the F4TCNQ/poly(3-hexylthiophene) (P3HT) system, which has become a benchmark in the field.[81,100–102] Scientific efforts in this direction have reported important results, like in the case of the dopant Magic Blue (tris(4-

bromophenyl)ammoniumyl hexachloroantimonate), where doping of P3HT yields conductivities on the order of 3460 S cm^{-1}, and doping of poly[2,5-bis(3-alkylthiophen-2-yl)thieno[3,2-b]thiophene] (PBTTT) results in conductivities as high as 9700 S cm^{-1}.[103]

The early rapid development of p-type doping, together with the relative ease of designing molecules, has greatly facilitated the synthesis of dopants with deep LUMO levels. These dopants also exhibit high solubility in conventional solvents commonly used for electronic device processing.[104] As a result, p-type doping has become more prominent than n-type doping.

In the realm of n-type doping for organic semiconductors, the majority of reported systems exhibit **limited electron conductivities**, typically not exceeding 10 S cm^{-1}.[105–107]
A notable exception to this general trend has been reported by Yu et al.[108], who achieved a significantly higher n-type conductivity of up to 114 S cm^{-1} in N-DMBI-doped thin films of TBDOPV-T-518, a thiophene-fused benzodifurandione oligomer of p-phenylenevinylene. Furthermore, Tang and co-workers[109] synthesized a polymer semiconductor, poly(benzodifurandione) (PBFDO), which spontaneously generates free negative charges during synthesis, effectively undergoing in situ self-doping. This material has exhibited extraordinarily high electrical conductivity exceeding 2000 S cm^{-1}.

In general, the unsatisfactory performance of n-type dopants can be attributed to several intrinsic challenges: the difficulty in **designing** molecular species that efficiently donate electrons, their limited compatibility and **miscibility** with organic semiconductor matrices, and their poor **environmental stability**.[106] In fact, n-type dopants require a HOMO level higher than -3.8 eV to effectively dope n-type semiconductors such as PCBM and P(NDI2OD-T2), which are among the top-performing n-type organic semiconductors.[110] However, dopants with HOMO levels in this energy region are susceptible to oxidation via redox reactions with water or oxygen.[35] Specifically, reduction of water to molecular hydrogen is thermodynamically favorable for energy levels above -3.7 eV, while reduction of oxygen to hydrogen peroxide or hydroxide can occur at approximately -4.4 eV and -4.9 eV, respectively. Therefore, in principle any dopant with the HOMO level located at energies > -4.9 eV is prone to oxidation. However, this outcome changes if we consider **overpotentials**, or, in other words, energy barriers that must be overcome for the reactions with water or oxygen to proceed. As a result, oxidation by oxygen generally does not occur unless the electron energy level exceeds about -4.0 eV, providing a kinetic stability window for dopants with HOMO energies below this threshold.

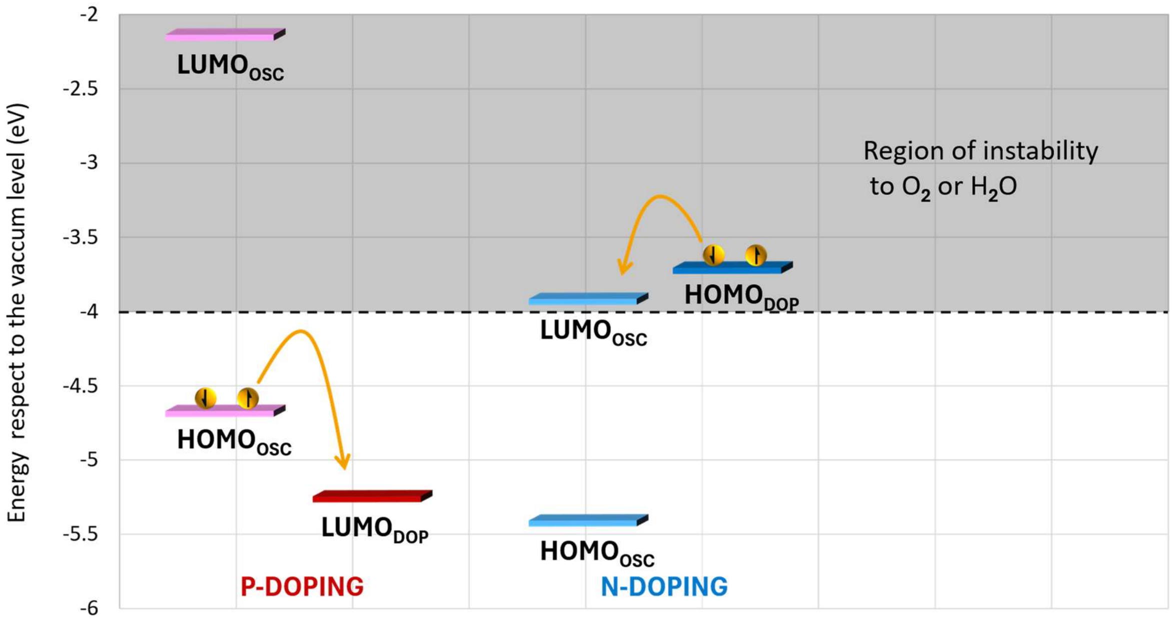

Figure 1.13
Schematic representation of the charge-transfer process that occurs during p-doping of OSCs or n-doping of OSCs. It is highlighted by the energetic region in which the species can be subjected to oxidation by ambient species.

To reduce dopant oxidation and deactivation in organic semiconductors (OSCs), several strategies have been developed. One effective approach involves modifying the **semiconductor's design.** By incorporating electron-deficient units, electron-withdrawing groups, or heteroatoms, the LUMO of the OSC can be lowered, reducing the polaron's susceptibility to oxidation.[35] Additionally, an increase in the **rigidity** and in the **planarity** of the OSC backbone enhances π–π stacking interactions, promoting the formation of highly ordered and densely packed regions. These regions facilitate charge transport while hindering the diffusion of environmental species into the matrix, thereby reducing trap sites.[111] Moreover, especially in photovoltaic devices, a common strategy involves **encapsulating** the semiconductor film with an impermeable polymer layer to prevent oxygen and moisture ingress, significantly improving environmental stability.[65,112,113] Alternatively, self-encapsulation can occur in thick and dense films where environmental species struggle to penetrate the central regions.[114]

Self-encapsulation can also be observed in carbon nanotubes (CNTs). Dörling et al.[115] reported that thicker CNT films exhibit improved air stability. However, literature often do not consider the impact of film thickness, leading to inconsistent performances comparison across studies, despite identical conditions and dopants.

For CNTs, **encapsulation** is the preferred method to achieve air stability. Surface encapsulation typically employs polymers such as polyethylene glycol (PEG) or polyethyleneimine (PEI) to isolate CNTs from atmospheric species.[116,117] A relevant contribution by Suzuki and co-workers[118] demonstrated that coating CNTs with parylene-C maintained stable doping conditions for 365 days. However, complete coverage of CNTs can significantly reduce conductivity, making encapsulation at sites prone to environmental molecule adsorption the best option.[116,117] Similarly, internal doping, where dopants are incorporated within the CNTs, enhances stability, and can be considered a form of internal encapsulation.[119] CNT coating may also involve the adsorption of oxidized dopant counterions, which exhibit strong Coulombic interactions with the CNT, limiting access to environmental species.[47,120–123]

Finally, the most widely adopted strategy for stable n-type doping involves the use of kinetically stabilized dopants, or **precursors**, which are air-stable and capable of in situ doping upon activation. This approach will be explored in detail in the following section.

1.4.2. Dopant Precursors

Molecular precursors for n-type doping are typically **stable compounds** that, upon thermal or photochemical activation, release or facilitate the transfer of electrons to the organic semiconductor (OSC) host material, thus achieving effective n-type doping. Unlike direct dopants, these precursors generally require an **external trigger** to become active, which determines enhanced stability and greater control over the doping process. An additional critical advantage of precursor dopants is their improved **compatibility** with organic solvents. This feature is especially important for solution-processing techniques, where the use of orthogonal solvents is essential to prevent the dissolution of previously deposited layers in multilayer architectures.[5,124] Several representative examples of such molecular precursors are illustrated in Figure 1.14.

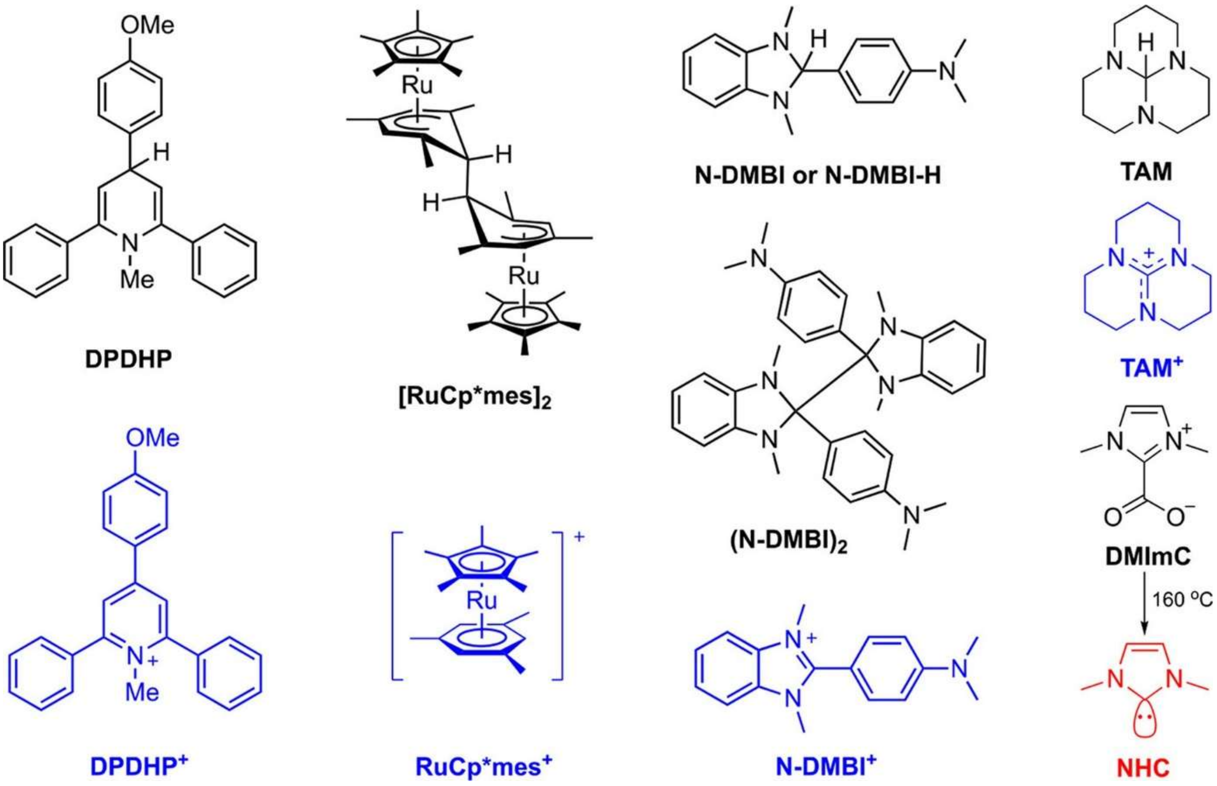

Figure 1.14
Chemical structures of solution-processable n-dopants (black), related dopant cations (blue), and active species (red). Reproduced with permission of the American Chemical Society from the work of Lu and co-workers.[125]

The first example of a solution-processable precursor dopant was reported by Bao and co-workers in 2010,[126] namely **N-DMBI-H** (4-(1,3-dimethyl-2,3-dihydro-1H-benzoimidazol-2-yl)phenyl)dimethylamine). This molecule can be activated either thermally or via photoexcitation. Although the exact activation mechanism remains not fully elucidated, it is understood to involve C-H bond cleavage and hydride transfer, effectively functioning as an active organic hydride donor.

Other notable hydride dopants include **DPDHP** (4-(4-methoxyphenyl)-1-methyl-2,6-diphenyl-1,4-dihydropyridine).[127] Both N-DMBI-H and DPDHP are relatively large molecules featuring aromatic cations that interact strongly with the substrate, thereby significantly influencing the morphology of the dopant/OSC interface.

More recently, hydride donor dopants derived from triaminomethane, commonly referred to as **TAMs**, have attracted increasing attention.[125,128] TAMs and N-DMBI-H are frequently compared within the literature due to their complementary attributes. TAMs are notably smaller and lack aromatic structures, resulting in a greater affinity for alkyl side chains attached to the OSC rather than for the aromatic domains, i.e. the regions that influence charge transport the most.

Furthermore, compared to N-DMBI-H and DPDHP, TAMs appear to possess thermodynamically favorable doping mechanisms, albeit with slower kinetics, offering enhanced control over the doping process.

Another class of molecular precursors involves **N-heterocyclic carbenes** or related carboxylate species, which activate thermally via decarboxylation to generate a reactive carbene. This carbene then dopes the substrate by forming covalent bonds, as exemplified by DMImC (see Figure 1.14).[129] The covalent bond significantly limits molecular diffusion, thereby enhancing the stability of the doped system.

Additionally, **dimeric forms** of DMBI, $(N\text{-}DMBI)_2$, serve as precursors with an activation mechanism that does not involve hydrogen release. Instead, dopant activation proceeds through thermally induced cleavage of the bond linking the two monomer units, generating two radical species capable of doping. This mechanism is analogous to that observed for dimeric organometallic precursors such as $(RuCp^*Mes)_2$, which belongs to the broader class of **sandwich compounds** widely utilized in n-type doping.[30]

Among the various n-type dopants currently available, N-DMBI-H and its derivatives remain the most extensively employed in molecular n-doping. [130]Accordingly, the following discussion will focus primarily on these molecules and will use them as a reference to discuss the molecular doping mechanism.

1.4.3. N-DMBI and Molecular Doping Process

The molecular doping process comprises **three contemporary phenomena**, all of which are thermally favored. The first is the **ionization of the dopant**, wherein the dopant donates one or more charges to the semiconductor, and has been extensively described in the previous section.

Taking N-DMBI-H as a reference, its reported HOMO level is theoretically too low in energy to directly transfer an electron from the neutral precursor to an n-type semiconductor such as the conjugated polymer N2200 (or P(NDI2OD-T2)), process that would correspond to path A in .

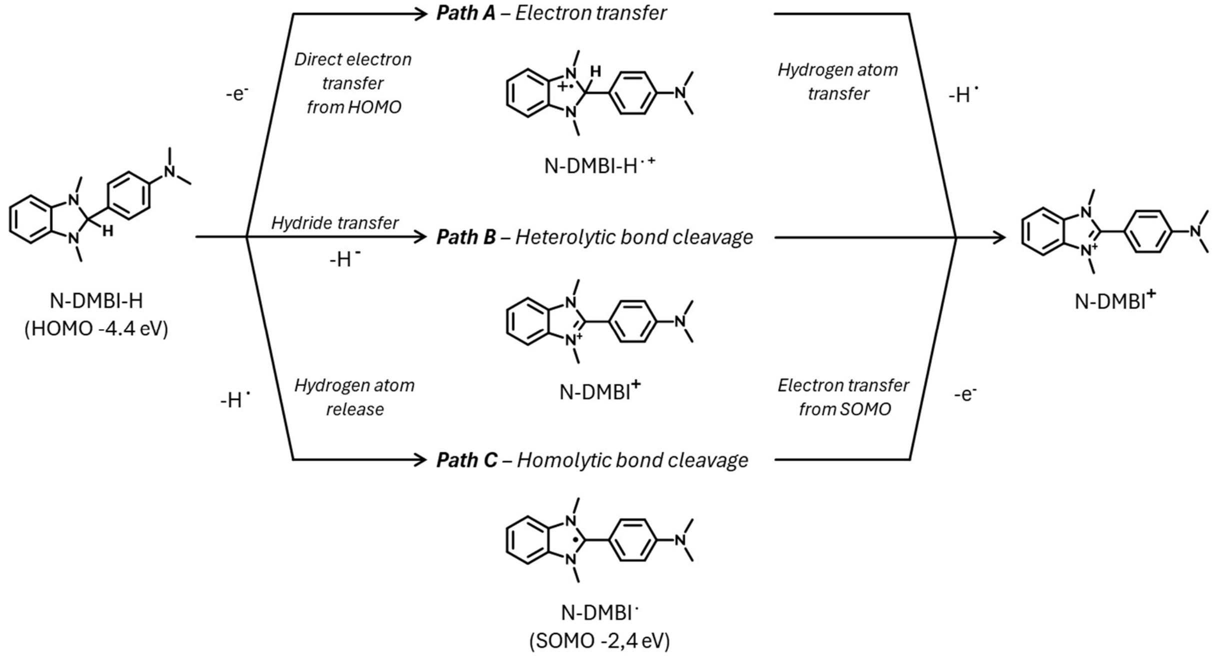

Figure 1.15
Schematic illustration of the three possible activation pathways of N-DMBI-H: (path A) direct electron transfer, (path B) heterolytic bond cleavage and (path C) homolytic cleavage leading to radical formation. Adapted with permission of AIP Publishing from the work of Bardagot and coworkers et al.[131]

Accordingly, literature indicates that the most widely supported mechanisms **do not involve direct charge transfer** from the neutral precursor (paths B and path C). [30,131,132] Where in path B, the process involves a hydride transfer from the precursor to the host, generating reduced species that subsequently act as dopants, as exemplified by the reaction with the semiconductor PCBM (Figure 1.16).

$$\text{N-DMBI-H} \xrightarrow{\text{PCBM}} \text{N-DMBI}^{+} + \text{PCBM-H}^{-} \xrightarrow{\text{PCBM}} \text{N-DMBI}^{+} + \text{PCBM}^{\bullet -} + \text{PCBM-H}^{\bullet}$$

Figure 1.16
Schematic representation of the hydride-transfer reaction steps between a fullerene derivative and N-DMBI. Represented with permission of the American Chemical Society from the work of Scaccabarozzi et al.[30]

While in path C the **homolytic cleavage** of the C-H bond generates a DMBI radical with a singly occupied molecular orbital (SOMO) level high enough to easily transfer a charge to the typical n-type semiconductors.

Simultaneously with charge transfer, a second process to consider is the **diffusion** of the dopant molecules within the semiconductor matrix. Molecular species, particularly those with small molecular sizes, exhibit high mobility in the matrix. This mobility is beneficial for doping because it enables the dopant molecules to access all the redox sites on the semiconductor. This is especially important for sequential doping methods, where the dopant is deposited after the semiconductor film and must penetrate the bulk. However, this phenomenon can also be detrimental, as it facilitates dopant aggregation, both in neutral form and after activation, leading respectively to a **decrease in doping efficiency** and **disruption** of the semiconductor's morphology. While in carbon nanotubes, due to the robustness of the network, the presence of the dopant alters barely the microstructure of the semiconductor layer,[59] in the case of OSCs the interplay between dopant and host is crucial to determine the microstructure, and, hence, the performance.[133] If the dopant has a **scarce miscibility** with the semiconductor it can aggregate in clusters, leading to phase segregation.[134,135] In such cases, only the dopant molecules present at the interface with the host matrix can activate, determining a reduction of the doping efficiency. **Phase segregation** can manifest as vertical phase segregation (blooming), where the dopant accumulates at the semiconductor film surface, or as internal clustering within the matrix, and is more relevant in presence of high doping concentration and with highly mobile dopants.

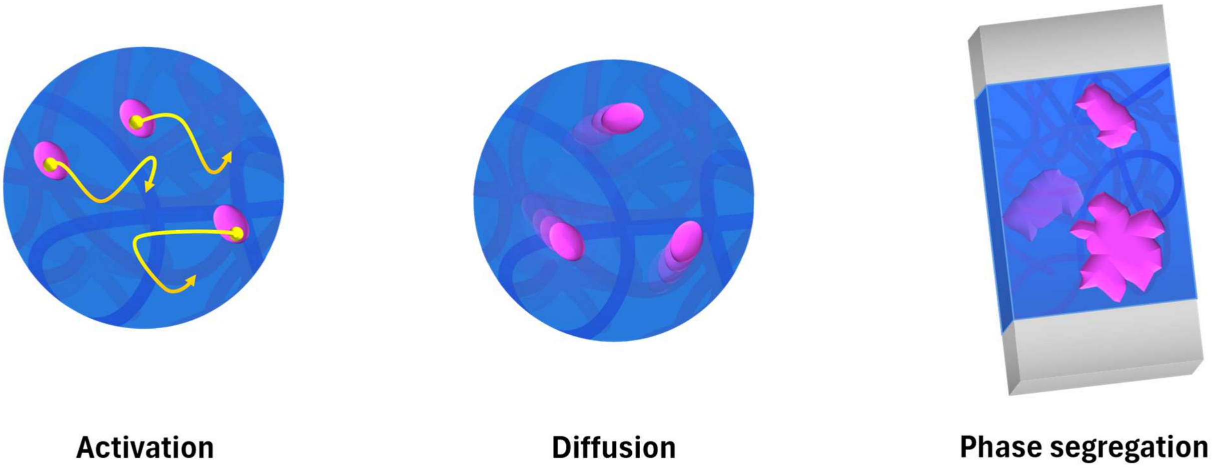

Figure 1.17
Illustration of the three phenomena that are involved in the molecular doping process.

In the case of N-DMBI-H, phase segregation represents a significant challenge. The main drawback of N-DMBI-H lies in its poor miscibility with n-dopable polymers, causing an unstable interface between the dopant and host material. The literature reports that this issue is commonly addressed by introducing **solubilizing side chains** onto the core structure of N-DMBI-H, or even on the semiconductor side chains. Although such derivatives exhibit improved miscibility with the host semiconductor, they often affect negatively charge carrier mobility, resulting in device performances that remain considerably inferior to those achieved with state-of-the-art p-type dopants. For example, one effective strategy involves the insertion of polar side chains, like polyethylene glycol (PEG) segments, into the OSC backbone.[136–138] These functional groups provide better interaction with polar dopants and increase the dielectric constant of the medium. Ultimately, Coulomb interactions between the dopant ion and the polaron are weakened, thereby promoting charge delocalization. In general, this kind of approach aims to increase **the free energy** of the system rather than introducing specific interactions between the dopant and the semiconductor.

However, the same modifications can have a negative impact on morphology. The introduction of non-conductive moieties, as well as an excessive loading of dopant, can degrade carrier mobility (μ). This is due to the formation of Coulomb scattering centers and disruption of the molecular packing within the OSC film, which is determinant in charge transport properties.[139]

In summary, while N-DMBI-H and its derivatives have emerged as effective n-type molecular precursor dopants, their performance is often limited by intrinsic drawbacks such as poor miscibility with many n-dopable polymers and a tendency toward phase segregation. Although strategies such as side-chain engineering and polarity modulation have improved miscibility and reduced Coulomb binding energies, these modifications frequently introduce trade-offs, particularly in charge carrier mobility and morphological stability. These limitations highlight the need for a **new generation of DMBI-based dopants** that can combine efficient activation pathways with tailored, specific interactions with the semiconductor matrix, enabling high doping efficiencies without compromising the microstructure or transport properties of the host material.

1.5. Aim of the Project

Building upon these considerations, this project is dedicated to the development of new benzimidazoline-based dopants that are not primarily aimed at increasing the interfacial entropy between dopants and semiconductors in a non-specific manner, but rather at introducing molecular features capable of establishing **specific interactions** with the host material. This rationale underpins the structure of the present work.

In Chapter 2, we present the different types of DMBI derivatives reported in the literature, focusing on those carrying alkyl substituents, and compare them with the monofunctional DMBI derivatives developed within our research group. The chapter gives a fundamental overview of the innovative synthetic methodologies that we have optimized to access such derivatives.

In Chapter 3, we expand on this discussion by addressing the synthesis of multifunctional dopants built on DMBI cores, with a focus on both the challenges encountered and the promising synthetic strategies identified.

Subsequently, we dedicate Chapter 4 to the characterization of doping behavior for both a newly developed monofunctional dopant and a novel dimeric dopant on the polymer N2200, the substrate that we have used as reference for our previous works.[140–142]

Finally, in Chapter 5 we perform a detailed characterization of the doping activity of the same species used in chapter 4 but using semiconducting CNTs as substrates.

The goal of this research is to advance the design of DMBI-based dopants towards molecular architectures that ensure not only efficient activation but also improved miscibility and specific interactions with the host matrix. In this way, the project seeks to overcome the limitations of current state-of-the-art n-type dopants and to establish guidelines for the rational development of the next generation of molecular doping agents.

1.6. Bibliography

(1) Baskaran, P.; Rajasekar, M. Recent Progress in Thermoelectric Devices and Applications. *Chem. Eng. J.* **2025**, *506*, 159929. https://doi.org/10.1016/j.cej.2025.159929.

(2) Riede, M.; Lüssem, B.; Leo, K. Organic Semiconductors. In *Comprehensive Semiconductor Science and Technology*; Elsevier, 2011; pp 448–507. https://doi.org/10.1016/B978-0-44-453153-7.00123-1.

(3) Dawidczyk, T. J.; Kong, H.; Katz, H. E. Organic Semiconductors (OSCs) for Electronic Chemical Sensors. In *Handbook of Organic Materials for Optical and (Opto)electronic Devices*; Elsevier, 2013; pp 577–596. https://doi.org/10.1533/9780857098764.3.577.

(4) Front Matter. In *Thermoelectricity and Advanced Thermoelectric Materials*; Elsevier, 2021; pp i–ii. https://doi.org/10.1016/b978-0-12-819984-8.09991-4.

(5) Wang, S.; Peng, L.; Sun, H.; Huang, W. The Future of Solution Processing toward Organic Semiconductor Devices: A Substrate and Integration Perspective. *J. Mater. Chem. C* **2022**, *10* (35), 12468–12486. https://doi.org/10.1039/D2TC02316D.

(6) Eslamian, M. Inorganic and Organic Solution-Processed Thin Film Devices. *Nano-Micro Lett.* **2017**, *9* (1), 3. https://doi.org/10.1007/s40820-016-0106-4.

(7) Timmermans, M. Y.; Estrada, D.; Nasibulin, A. G.; Wood, J. D.; Behnam, A.; Sun, D.; Ohno, Y.; Lyding, J. W.; Hassanien, A.; Pop, E.; Kauppinen, E. I. Effect of Carbon Nanotube Network Morphology on Thin Film Transistor Performance. *Nano Res.* **2012**, *5* (5), 307–319. https://doi.org/10.1007/s12274-012-0211-8.

(8) Sawatzki-Park, M.; Wang, S.-J.; Kleemann, H.; Leo, K. Highly Ordered Small Molecule Organic Semiconductor Thin-Films Enabling Complex, High-Performance Multi-Junction Devices. *Chem. Rev.* **2023**, *123* (13), 8232–8250. https://doi.org/10.1021/acs.chemrev.2c00844.

(9) Budida, J.; Srinivasan, K. Review of Thin Film Deposition and Techniques. *Mater. Today Proc.* **2023**, *92*, 1030–1033. https://doi.org/10.1016/j.matpr.2023.05.004.

(10) Bahk, J.-H.; Favaloro, T.; Shakouri, A. THIN FILM THERMOELECTRIC CHARACTERIZATION TECHNIQUES. *Annu. Rev. Heat Transf.* **2013**, *16* (1), 51–99. https://doi.org/10.1615/AnnualRevHeatTransfer.v16.30.

(11) Bissessur, R.; White, W.; Dahn, D. C. Electrical Characterization of Conductive Polymers and Their Intercalated Nanocomposites with Molybdenum Disulfide. *Mater. Lett.* **2006**, *60* (2), 248–251. https://doi.org/10.1016/j.matlet.2005.08.026.

(12) Oliveira, F. S.; Cipriano, R. B.; Da Silva, F. T.; Romão, E. C.; Dos Santos, C. A. M. Simple Analytical Method for Determining Electrical Resistivity and Sheet Resistance Using the van Der Pauw Procedure. *Sci. Rep.* **2020**, *10* (1), 16379. https://doi.org/10.1038/s41598-020-72097-1.

(13) Dörling, B.; Zapata-Arteaga, O.; Campoy-Quiles, M. A Setup to Measure the Seebeck Coefficient and Electrical Conductivity of Anisotropic Thin-Films on a Single Sample. *Rev. Sci. Instrum.* **2020**, *91* (10), 105111. https://doi.org/10.1063/5.0021715.

(14) Chen, G.; Dresselhaus, M. S.; Dresselhaus, G.; Fleurial, J.-P.; Caillat, T. Recent Developments in Thermoelectric Materials. *Int. Mater. Rev.* **2003**, *48* (1), 45–66. https://doi.org/10.1179/095066003225010182.

(15) Zhou, S.; Shi, X.; Li, L.; Liu, Q.; Hu, B.; Chen, W.; Zhang, C.; Liu, Q.; Chen, Z. Advances and Outlooks for Carbon Nanotube-Based Thermoelectric Materials and Devices. *Adv. Mater.* **2025**, *37* (13), 2500947. https://doi.org/10.1002/adma.202500947.

(16) Li, J.; Lei, T. Recent Progress on Addressing the Key Challenges in Organic Thermoelectrics. *Chem. – Asian J.* **2021**, *16* (12), 1508–1518. https://doi.org/10.1002/asia.202100285.

(17) Wu, T.; Kim, J.; Lim, J.-H.; Kim, M.-S.; Myung, N. V. Comprehensive Review on Thermoelectric Electrodeposits: Enhancing Thermoelectric Performance Through Nanoengineering. *Front. Chem.* **2021**, *9*, 762896. https://doi.org/10.3389/fchem.2021.762896.

(18) Ascencio-Hurtado, C. R.; Ambrosio Lázaro, R. C.; Estrada-López, J. J.; Torres Jacome, A. Review of Si-Based Thin Films and Materials for Thermoelectric Energy Harvesting and Their Integration into Electronic Devices for Energy Management Systems. *Eng* **2023**, *4* (2), 1409–1431. https://doi.org/10.3390/eng4020082.

(19) Fujii, T. Demonstration of a Thermoelectric Device Using Electric Double-Layer Gating: Simultaneous Control of the Thermoelectric Properties of p-Type and n-Type Carbon Nanotubes. *J. Appl. Phys.* **2021**, *129* (4). https://doi.org/10.1063/5.0031247.

(20) Pei, K. Recent Advances in Molecular Doping of Organic Semiconductors. *Surf. Interfaces* **2022**, *30*, 101887. https://doi.org/10.1016/j.surfin.2022.101887.

(21) Morab, S.; Sundaram, M. M.; Pivrikas, A. Review on Charge Carrier Transport in Inorganic and Organic Semiconductors. *Coatings* **2023**, *13* (9), 1657. https://doi.org/10.3390/coatings13091657.

(22) Mdluli, S. B.; Ramoroka, M. E.; Yussuf, S. T.; Modibane, K. D.; John-Denk, V. S.; Iwuoha, E. I. π-Conjugated Polymers and Their Application in Organic and Hybrid Organic-Silicon Solar Cells. *Polymers* **2022**, *14* (4), 716. https://doi.org/10.3390/polym14040716.

(23) Li, G.; Chang, W.-H.; Yang, Y. Low-Bandgap Conjugated Polymers Enabling Solution-Processable Tandem Solar Cells. *Nat. Rev. Mater.* **2017**, *2* (8). https://doi.org/10.1038/natrevmats.2017.43.

(24) Holliday, S.; Li, Y.; Luscombe, C. K. Recent Advances in High Performance Donor-Acceptor Polymers for Organic Photovoltaics. *Prog. Polym. Sci.* **2017**, *70*, 34–51. https://doi.org/10.1016/j.progpolymsci.2017.03.003.

(25) Zhang, Z.; Wang, J. Structures and Properties of Conjugated Donor–Acceptor Copolymers for Solar Cell Applications. *J. Mater. Chem.* **2012**, *22* (10), 4178. https://doi.org/10.1039/c2jm14951f.

(26) Hashemi, D.; Ma, X.; Ansari, R.; Kim, J.; Kieffer, J. Design Principles for the Energy Level Tuning in Donor/Acceptor Conjugated Polymers. *Phys. Chem. Chem. Phys.* **2019**, *21* (2), 789–799. https://doi.org/10.1039/C8CP03341B.

(27) Müllen, K.; Pisula, W. Donor–Acceptor Polymers. *J. Am. Chem. Soc.* **2015**, *137* (30), 9503–9505. https://doi.org/10.1021/jacs.5b07015.

(28) Scharber, M. C.; Sariciftci, N. S. Low Band Gap Conjugated Semiconducting Polymers. *Adv. Mater. Technol.* **2021**, *6* (4). https://doi.org/10.1002/admt.202000857.

(29) Bredas, J. L.; Street, G. B. Polarons, Bipolarons, and Solitons in Conducting Polymers. *Acc. Chem. Res.* **1985**, *18* (10), 309–315. https://doi.org/10.1021/ar00118a005.

(30) Scaccabarozzi, A. D.; Basu, A.; Aniés, F.; Liu, J.; Zapata-Arteaga, O.; Warren, R.; Firdaus, Y.; Nugraha, M. I.; Lin, Y.; Campoy-Quiles, M.; Koch, N.; Müller, C.; Tsetseris, L.; Heeney, M.;

Anthopoulos, T. D. Doping Approaches for Organic Semiconductors. *Chem. Rev.* **2022**, *122* (4), 4420–4492. https://doi.org/10.1021/acs.chemrev.1c00581.

(31) Hu, P.; He, X.; Jiang, H. Greater than 10 Cm2 V−1 S−1: A Breakthrough of Organic Semiconductors for Field-Effect Transistors. *Infomat* **2021**, *3*, 613–630. https://doi.org/10.1002/inf2.12188.

(32) *Technology and Applications of Amorphous Silicon*; Street, R. A., Ed.; Springer Series in Materials Science; Springer Berlin Heidelberg: Berlin, Heidelberg, 2000. https://doi.org/10.1007/978-3-662-04141-3.

(33) Sun, H.; Guo, X.; Facchetti, A. High-Performance n-Type Polymer Semiconductors: Applications, Recent Development, and Challenges. *Chem* **2020**, *6* (6), 1310–1326. https://doi.org/10.1016/j.chempr.2020.05.012.

(34) Haneef, H. F.; Zeidell, A. M.; Jurchescu, O. D. Charge Carrier Traps in Organic Semiconductors: A Review on the Underlying Physics and Impact on Electronic Devices. *J. Mater. Chem. C* **2020**, *8* (3), 759–787. https://doi.org/10.1039/c9tc05695e.

(35) Griggs, S.; Marks, A.; Bristow, H.; McCulloch, I. N-Type Organic Semiconducting Polymers: Stability Limitations, Design Considerations and Applications. *J. Mater. Chem. C* **2021**, *9* (26), 8099–8128. https://doi.org/10.1039/d1tc02048j.

(36) Levinshtein, M. E.; Rumyantsev, S.; Shur, M. S. *Handbook Series on Semiconductor Parameters - Volume 1*; World Scientific Publishing Company, 1999; Vol. 1.

(37) Sumio, I. Helical Microtubules of Graphitic Carbon. *Nature* **1991**, *354*, 56–58. https://doi.org/10.1038/354056a0.

(38) Chen, G.; Seki, Y.; Kimura, H.; Sakurai, S.; Yumura, M.; Hata, K.; Futaba, D. N. Diameter Control of Single-Walled Carbon Nanotube Forests from 1.3–3.0 Nm by Arc Plasma Deposition. *Sci. Rep.* **2014**, *4* (1). https://doi.org/10.1038/srep03804.

(39) Malhotra, B. D.; Srivastava, S.; Augustine, S. Biosensors for Food Toxin Detection: Carbon Nanotubes and Graphene. *MRS Proc.* **2015**, *1725*, mrsf14-1725-i05-02. https://doi.org/10.1557/opl.2015.165.

(40) Sheikhpour, M.; Naghinejad, M.; Kasaeian, A.; Lohrasbi, A.; Shahraeini, S. S.; Zomorodbakhsh, S. The Applications of Carbon Nanotubes in the Diagnosis and Treatment of Lung Cancer: A Critical Review. *Int. J. Nanomedicine* **2020**, *Volume 15*, 7063–7078. https://doi.org/10.2147/IJN.S263238.

(41) Qian, L.; Xie, Y.; Zhang, S.; Zhang, J. Band Engineering of Carbon Nanotubes for Device Applications. *Matter* **2020**, *3* (3), 664–695. https://doi.org/10.1016/j.matt.2020.06.014.

(42) Odom, T. W.; Huang, J.-L.; Kim, P.; Lieber, C. M. Structure and Electronic Properties of Carbon Nanotubes. *J. Phys. Chem. B* **2000**, *104* (13), 2794–2809. https://doi.org/10.1021/jp993592k.

(43) Venkataraman, A.; Amadi, E. V.; Chen, Y.; Papadopoulos, C. Carbon Nanotube Assembly and Integration for Applications. *Nanoscale Res. Lett.* **2019**, *14* (1), 220. https://doi.org/10.1186/s11671-019-3046-3.

(44) Charlier, J.-C.; Blase, X.; Roche, S. Electronic and Transport Properties of Nanotubes. *Rev. Mod. Phys.* **2007**, *79* (2), 677–732. https://doi.org/10.1103/revmodphys.79.677.

(45) Yang, Q.; Ma, L.; Xiao, S.; Zhang, D.; Djoulde, A.; Ye, M.; Lin, Y.; Geng, S.; Li, X.; Chen, T.; Sun, L. Electrical Conductivity of Multiwall Carbon Nanotube Bundles Contacting with Metal

Electrodes by Nano Manipulators inside SEM. *Nanomaterials* **2021**, *11* (5), 1290. https://doi.org/10.3390/nano11051290.

(46) Ahmad, S. Organic Semiconductors for Device Applications: Current Trends and Future Prospects. *J. Polym. Eng.* **2014**, *34* (4), 279–338. https://doi.org/10.1515/polyeng-2013-0267.

(47) Hu, Q.; Lu, Z.; Wang, Y.; Wang, J.; Wang, H.; Wu, Z.; Lu, G.; Zhang, H.-L.; Yu, C. Double Doping Approach for Unusually Stable and Large N-Type Thermoelectric Voltage from p-Type Multi-Walled Carbon Nanotube Mats. *J. Mater. Chem. A* **2020**, *8* (26), 13095–13105. https://doi.org/10.1039/D0TA03247F.

(48) Yanagi, K.; Udoguchi, H.; Sagitani, S.; Oshima, Y.; Takenobu, T.; Kataura, H.; Ishida, T.; Matsuda, K.; Maniwa, Y. Transport Mechanisms in Metallic and Semiconducting Single-Wall Carbon Nanotube Networks. *ACS Nano* **2010**, *4* (7), 4027–4032. https://doi.org/10.1021/nn101177n.

(49) *Carbon Nanotubes: Synthesis, Structure, Properties, and Applications*; Dresselhaus, M. S., Dresselhaus, G., Avouris, P., Eds.; Topics in applied physics; Springer: Berlin ; New York, 2001.

(50) Saberi, A. A. Recent Advances in Percolation Theory and Its Applications. *Phys. Rep.* **2015**, *578*, 1–32. https://doi.org/10.1016/j.physrep.2015.03.003.

(51) Tripathy, S.; Bose, B.; Chakrabarti, P. P.; Bhattacharyya, T. K. Resistive Analysis of Scattering-Dependent Electrical Transport in Single-Wall Carbon-Nanotube Networks. *IEEE Trans. Electron Devices* **2020**, *67* (12), 5676–5684. https://doi.org/10.1109/ted.2020.3029734.

(52) Zorn, N. F.; Zaumseil, J. Charge Transport in Semiconducting Carbon Nanotube Networks. *Appl. Phys. Rev.* **2021**, *8* (4). https://doi.org/10.1063/5.0065730.

(53) Simon, J.; André, J.-J. *Molecular Semiconductors*; Lehn, J. M., Rees, Ch. W., Eds.; Springer Berlin Heidelberg: Berlin, Heidelberg, 1985. https://doi.org/10.1007/978-3-642-70012-5.

(54) Sano, E.; Tanaka, T. A Simple Drain Current Model for Single-Walled Carbon Nanotube Network Thin-Film Transistors. *J. Appl. Phys.* **2014**, *115* (15). https://doi.org/10.1063/1.4871775.

(55) Fuhrer, M. S.; Nygird, J.; Shih, L.; Forero, M.; Yoon, Y.-C. Crossed Nanotube Junctions. **2000**, *288*.

(56) Zhang, Z.; Yan, W.; Chen, Y.; Chen, S.; Jia, G.; Sheng, J.; Zhu, S.; Xu, Z.; Zhang, X.; Li, Y. Stable Doping of Single-Walled Carbon Nanotubes for Flexible Transparent Conductive Films. *ACS Nano* **2022**, *16* (1), 1063–1071. https://doi.org/10.1021/acsnano.1c08812.

(57) Xu, J.-L.; Dai, R.-X.; Xin, Y.; Sun, Y.-L.; Li, X.; Yu, Y.-X.; Xiang, L.; Xie, D.; Wang, S.-D.; Ren, T.-L. Efficient and Reversible Electron Doping of Semiconductor-Enriched Single-Walled Carbon Nanotubes by Using Decamethylcobaltocene. *Sci. Rep.* **2017**, *7* (1). https://doi.org/10.1038/s41598-017-05967-w.

(58) Tey, J. N.; Ho, X.; Wei, J. Effect of Doping on Single-Walled Carbon Nanotubes Network of Different Metallicity. *Nanoscale Res. Lett.* **2012**, *7* (1). https://doi.org/10.1186/1556-276x-7-548.

(59) Liu, Y.; Zhao, Z.; Kang, L.; Qiu, S.; Li, Q. Molecular Doping Modulation and Applications of Structure-Sorted Single-Walled Carbon Nanotubes: A Review. *Small* **2024**, *20* (3), 2304075. https://doi.org/10.1002/smll.202304075.

(60) Stanton, N. J.; Ihly, R.; Norton-Baker, B.; Ferguson, A. J.; Blackburn, J. L. Solution-Phase *p*-Type Doping of Highly Enriched Semiconducting Single-Walled Carbon Nanotubes for Thermoelectric Thin Films. *Appl. Phys. Lett.* **2021**, *119* (2). https://doi.org/10.1063/5.0055837.

(61) Yamaguchi, R.; Ishii, T.; Matsumoto, M.; Borah, A.; Tanaka, N.; Oda, K.; Tomita, M.; Watanabe, T.; Fujigaya, T. Thermal Deposition Method for p–n Patterning of Carbon Nanotube Sheets for Planar-Type Thermoelectric Generator. *J. Mater. Chem. A* **2021**, *9* (20), 12188–12195. https://doi.org/10.1039/d1ta02206g.

(62) Hornbaker, D. J.; Kahng, S.-J.; Misra, S.; Smith, B. W.; Johnson, A. T.; Mele, E. J.; Luzzi, D. E.; Yazdani, A. Mapping the One-Dimensional Electronic States of Nanotube Peapod Structures. *Science* **2002**, *295* (5556), 828–831. https://doi.org/10.1126/science.1068133.

(63) Takenobu, T.; Takano, T.; Shiraishi, M.; Murakami, Y.; Ata, M.; Kataura, H.; Achiba, Y.; Iwasa, Y. Stable and Controlled Amphoteric Doping by Encapsulation of Organic Molecules inside Carbon Nanotubes. *Nat. Mater.* **2003**, *2* (10), 683–688. https://doi.org/10.1038/nmat976.

(64) Jordan, J. W.; Cameron, J. M.; Lowe, G. A.; Rance, G. A.; Fung, K. L. Y.; Johnson, L. R.; Walsh, D. A.; Khlobystov, A. N.; Newton, G. N. Stabilization of Polyoxometalate Charge Carriers via Redox-Driven Nanoconfinement in Single-Walled Carbon Nanotubes. *Angew. Chem. Int.* **2022**, *61*, e202115619.

(65) Lee, J.; Kim, H.; Kahng, S.-J.; Kim, G.; Son, Y.-W.; Ihm, J.; Kato, H.; Wang, Z. W.; Okazaki, T.; Shinohara, H.; Kuk, Y. Bandgap Modulation of Carbon Nanotubes by Encapsulated Metallofullerenes. *Nature* **2002**, *415* (6875), 1005–1008. https://doi.org/10.1038/4151005a.

(66) Yanagi, K.; Kanda, S.; Oshima, Y.; Kitamura, Y.; Kawai, H.; Yamamoto, T.; Takenobu, T.; Nakai, Y.; Maniwa, Y. Tuning of the Thermoelectric Properties of One-Dimensional Material Networks by Electric Double Layer Techniques Using Ionic Liquids. *Nano Lett.* **2014**, *14* (11), 6437–6442. https://doi.org/10.1021/nl502982f.

(67) Maheswaran, R.; Shanmugavel, B. P. A Critical Review of the Role of Carbon Nanotubes in the Progress of Next-Generation Electronic Applications. *J. Electron. Mater.* **2022**, *51* (6), 2786–2800. https://doi.org/10.1007/s11664-022-09516-8.

(68) Muhulet, A.; Miculescu, F.; Voicu, S. I.; Schütt, F.; Thakur, V. K.; Mishra, Y. K. Fundamentals and Scopes of Doped Carbon Nanotubes towards Energy and Biosensing Applications. *Mater. Today Energy* **2018**, *9*, 154–186. https://doi.org/10.1016/j.mtener.2018.05.002.

(69) Xue, Y.; Ratner, M. A. Electron Transport in Semiconducting Carbon Nanotubes with Hetero-Metallic Contacts. *Nanotechnology* **2005**, *16* (1), 5–9. https://doi.org/10.1088/0957-4484/16/1/002.

(70) Lüssem, B.; Riede, M.; Leo, K. Doping of Organic Semiconductors. *Phys. Status Solidi A* **2013**, *210* (1), 9–43. https://doi.org/10.1002/pssa.201228310.

(71) Gómez, P.; Cerdá, J.; Más-Montoya, M.; Georgakopoulos, S.; Da Silva, I.; García, A.; Ortí, E.; Aragó, J.; Curiel, D. Effect of Molecular Geometry and Extended Conjugation on the Performance of Hydrogen-Bonded Semiconductors in Organic Thin-Film Field-Effect Transistors. *J. Mater. Chem. C* **2021**, *9* (33), 10819–10829. https://doi.org/10.1039/d1tc01328a.

(72) Zuo, G.; Li, Z.; Andersson, O.; Abdalla, H.; Wang, E.; Kemerink, M. Molecular Doping and Trap Filling in Organic Semiconductor Host–Guest Systems. *J. Phys. Chem. C* **2017**, *121* (14), 7767–7775. https://doi.org/10.1021/acs.jpcc.7b01758.

(73) Abbasi, M. S.; Sultana, R.; Ahmed, I.; Adnan, M.; Shah, U. A.; Irshad, M. S.; Vu, H. N.; Do, L. T.; Thi Vu, H. H.; Pham, T.-D.; Nang, H. X.; Dao, V.-D. Contemporary Advances in Organic Thermoelectric Materials: Fundamentals, Properties, Optimization Strategies, and Applications. *Renew. Sustain. Energy Rev.* **2024**, *200*, 114579. https://doi.org/10.1016/j.rser.2024.114579.

(74) Zhao, W.; Ding, J.; Zou, Y.; Di, C.; Zhu, D. Chemical Doping of Organic Semiconductors for Thermoelectric Applications. *Chem. Soc. Rev.* **2020**, *49* (20), 7210–7228. https://doi.org/10.1039/D0CS00204F.

(75) Gavaza, G. M.; Yu, Z. G.; Wu, P. A Universal Theoretical Approach for Examining the Efficiency of Doping Processes in Semiconductors. *J. Appl. Phys.* **2009**, *105* (11). https://doi.org/10.1063/1.3143044.

(76) Tietze, M. L.; Benduhn, J.; Pahner, P.; Nell, B.; Schwarze, M.; Kleemann, H.; Krammer, M.; Zojer, K.; Vandewal, K.; Leo, K. Elementary Steps in Electrical Doping of Organic Semiconductors. *Nat. Commun.* **2018**, *9* (1). https://doi.org/10.1038/s41467-018-03302-z.

(77) Tanaka, N.; Yamaguchi, I.; Yamaguchi, R.; Fujigaya, T. Study of the Electron-Doping Mechanism in Single-Walled Carbon Nanotubes Using Dimethylbenzimidazole. *Faraday Discuss.* **2024**, *250*, 390–399. https://doi.org/10.1039/d3fd00128h.

(78) Yan, H.; Ma, W. Molecular Doping Efficiency in Organic Semiconductors: Fundamental Principle and Promotion Strategy. *Adv. Funct. Mater.* **2022**, *32* (12). https://doi.org/10.1002/adfm.202111351.

(79) Müller, J. S.; Comí, M.; Eisner, F.; Azzouzi, M.; Herrera Ruiz, D.; Yan, J.; Attar, S. S.; Al-Hashimi, M.; Nelson, J. Charge-Transfer State Dissociation Efficiency Can Limit Free Charge Generation in Low-Offset Organic Solar Cells. *ACS Energy Lett.* **2023**, *8* (8), 3387–3397. https://doi.org/10.1021/acsenergylett.3c00943.

(80) Lüssem, B.; Keum, C.-M.; Kasemann, D.; Naab, B.; Bao, Z.; Leo, K. Doped Organic Transistors. *Chem. Rev.* **2016**, *116* (22), 13714–13751. https://doi.org/10.1021/acs.chemrev.6b00329.

(81) Pingel, P.; Neher, D. Comprehensive Picture Ofp-Type Doping of P3HT with the Molecular Acceptor F4TCNQ. *Phys. Rev. B* **2013**, *87* (11). https://doi.org/10.1103/physrevb.87.115209.

(82) Hertel, T.; Hagen, A.; Talalaev, V.; Arnold, K.; Hennrich, F.; Kappes, M.; Rosenthal, S.; McBride, J.; Ulbricht, H.; Flahaut, E. Spectroscopy of Single- and Double-Wall Carbon Nanotubes in Different Environments. *Nano Lett.* **2005**, *5* (3), 511–514. https://doi.org/10.1021/nl050069a.

(83) Dominguez-Flores, F.; Santos, E.; Schmickler, W.; Juarez, F. Interaction between Chloride Ions Mediated by Carbon Nanotubes: A Chemical Attraction. *J. Solid State Electrochem.* **2020**, *24* (11–12), 3207–3214. https://doi.org/10.1007/s10008-020-04802-z.

(84) Gebhardt, J.; Bosch, S.; Hof, F.; Hauke, F.; Hirsch, A.; Görling, A. Selective Reduction of SWCNTs – Concepts and Insights. *J. Mater. Chem. C* **2017**, *5* (16), 3937–3947. https://doi.org/10.1039/c5tc01407g.

(85) Hermosilla-Palacios, M. A.; Martinez, M.; Doud, E. A.; Hertel, T.; Spokoyny, A. M.; Cambré, S.; Wenseleers, W.; Kim, Y.-H.; Ferguson, A. J.; Blackburn, J. L. Carrier Density and Delocalization Signatures in Doped Carbon Nanotubes from Quantitative Magnetic Resonance. *Nanoscale Horiz.* **2024**, *9* (2), 278–284. https://doi.org/10.1039/d3nh00480e.

(86) Aubry, T. J.; Axtell, J. C.; Basile, V. M.; Winchell, K. J.; Lindemuth, J. R.; Porter, T. M.; Liu, J.; Alexandrova, A. N.; Kubiak, C. P.; Tolbert, S. H.; Spokoyny, A. M.; Schwartz, B. J. Dodecaborane-Based Dopants Designed to Shield Anion Electrostatics Lead to Increased Carrier Mobility in a Doped Conjugated Polymer. *Adv. Mater.* **2019**, *31* (11). https://doi.org/10.1002/adma.201805647.

(87) Murrey, T. L.; Aubry, T. J.; Ruiz, O. L.; Thurman, K. A.; Eckstein, K. H.; Doud, E. A.; Stauber, J. M.; Spokoyny, A. M.; Schwartz, B. J.; Hertel, T.; Blackburn, J. L.; Ferguson, A. J. Tuning Counterion Chemistry to Reduce Carrier Localization in Doped Semiconducting Carbon Nanotube Networks. *Cell Rep. Phys. Sci.* **2023**, *4* (5), 101407. https://doi.org/10.1016/j.xcrp.2023.101407.

(88) Brownlie, L.; Shapter, J. Advances in Carbon Nanotube N-Type Doping: Methods, Analysis and Applications. *Carbon* **2018**, *126*, 257–270. https://doi.org/10.1016/j.carbon.2017.09.107.

(89) Minakata, T.; Nagoya, I.; Ozaki, M. Highly Ordered and Conducting Thin Film of Pentacene Doped with Iodine Vapor. *J. Appl. Phys.* **1991**, *69* (10), 7354–7356. https://doi.org/10.1063/1.347594.

(90) Chiang, C. K.; Fincher, C. R.; Park, Y. W.; Heeger, A. J.; Shirakawa, H.; Louis, E. J.; Gau, S. C.; MacDiarmid, A. G. Electrical Conductivity in Doped Polyacetylene. *Phys. Rev. Lett.* **1977**, *39* (17), 1098–1101. https://doi.org/10.1103/physrevlett.39.1098.

(91) Parthasarathy, G.; Shen, C.; Kahn, A.; Forrest, S. R. Lithium Doping of Semiconducting Organic Charge Transport Materials. *J. Appl. Phys.* **2001**, *89* (9), 4986–4992. https://doi.org/10.1063/1.1359161.

(92) Mityashin, A.; Olivier, Y.; Van Regemorter, T.; Rolin, C.; Verlaak, S.; Martinelli, N. G.; Beljonne, D.; Cornil, J.; Genoe, J.; Heremans, P. Unraveling the Mechanism of Molecular Doping in Organic Semiconductors. *Adv. Mater.* **2012**, *24* (12), 1535–1539. https://doi.org/10.1002/adma.201104269.

(93) Aziz, E. F.; Vollmer, A.; Eisebitt, S.; Eberhardt, W.; Pingel, P.; Neher, D.; Koch, N. Localized Charge Transfer in a Molecularly Doped Conducting Polymer. *Adv. Mater.* **2007**, *19* (20), 3257–3260. https://doi.org/10.1002/adma.200700926.

(94) Cagardová, D.; Lukeš, V. Molecular Orbital Analysis of Selected Organic P-Type and n-Type Conducting Small Molecules. *Acta Chim. Slovaca* **2017**, *10* (1), 6–16. https://doi.org/10.1515/acs-2017-0002.

(95) Talsma, W.; Ye, G.; Liu, Y.; Duim, H.; Dijkstra, S.; Tran, K.; Qu, J.; Song, J.; Chiechi, R. C.; Loi, M. A. Efficient Selective Sorting of Semiconducting Carbon Nanotubes Using Ultra-Narrow-Band-Gap Polymers. *ACS Appl. Mater. Interfaces* **2022**, *14* (33), 38056–38066. https://doi.org/10.1021/acsami.2c07158.

(96) Bahmanzadgan, F.; Ghaemi, A.; Qasemnazhand, M.; Molaee, M. Simulation of Gas Adsorption on Single-Walled Carbon Nanotubes. *Sci. Rep.* **2025**, *15* (1), 15595. https://doi.org/10.1038/s41598-025-99988-5.

(97) Kim, C.-H.; Kymissis, I. Graphene–Organic Hybrid Electronics. *J Mater Chem C* **2017**, *5* (19), 4598–4613. https://doi.org/10.1039/c7tc00664k.

(98) Saska, J.; Gonel, G.; Bedolla-Valdez, Z. I.; Aronow, S. D.; Shevchenko, N. E.; Dudnik, A. S.; Moulé, A. J.; Mascal, M. A Freely Soluble, High Electron Affinity Molecular Dopant for Solution Processing of Organic Semiconductors. *Chem. Mater.* **2019**, *31* (5), 1500–1506. https://doi.org/10.1021/acs.chemmater.8b04150.

(99) Yim, K.; Whiting, G. L.; Murphy, C. E.; Halls, J. J. M.; Burroughes, J. H.; Friend, R. H.; Kim, J. Controlling Electrical Properties of Conjugated Polymers via a Solution-Based p-Type Doping. *Adv. Mater.* **2008**, *20* (17), 3319–3324. https://doi.org/10.1002/adma.200800735.

(100) Zapata-Arteaga, O.; Perevedentsev, A.; Prete, M.; Busato, S.; Floris, P. S.; Asatryan, J.; Rurali, R.; Martín, J.; Campoy-Quiles, M. A Universal, Highly Stable Dopant System for

Organic Semiconductors Based on Lewis-Paired Dopant Complexes. *ACS Energy Lett.* **2024**, *9* (7), 3567–3577. https://doi.org/10.1021/acsenergylett.4c01278.

(101) Duong, D. T.; Wang, C.; Antono, E.; Toney, M. F.; Salleo, A. The Chemical and Structural Origin of Efficient P-Type Doping in P3HT. *Org. Electron.* **2013**, *14* (5), 1330–1336. https://doi.org/10.1016/j.orgel.2013.02.028.

(102) Fontana, M. T.; Stanfield, D. A.; Scholes, D. T.; Winchell, K. J.; Tolbert, S. H.; Schwartz, B. J. Evaporation vs Solution Sequential Doping of Conjugated Polymers: F_4 TCNQ Doping of Micrometer-Thick P3HT Films for Thermoelectrics. *J. Phys. Chem. C* **2019**, *123* (37), 22711–22724. https://doi.org/10.1021/acs.jpcc.9b05069.

(103) Dash, A.; Guchait, S.; Scheunemann, D.; Vijayakumar, V.; Leclerc, N.; Brinkmann, M.; Kemerink, M. Spontaneous Modulation Doping in Semi-Crystalline Conjugated Polymers Leads to High Conductivity at Low Doping Concentration. *Adv. Mater.* **2024**, *36* (13), 2311303. https://doi.org/10.1002/adma.202311303.

(104) Li, J.; Zhang, G.; Holm, D. M.; Jacobs, I. E.; Yin, B.; Stroeve, P.; Mascal, M.; Moulé, A. J. Introducing Solubility Control for Improved Organic P-Type Dopants. *Chem. Mater.* **2015**, *27* (16), 5765–5774. https://doi.org/10.1021/acs.chemmater.5b02340.

(105) Wei, H.; Cheng, Z.; Wu, T.; Liu, Y.; Guo, J.; Chen, P.; Xia, J.; Xie, H.; Qiu, X.; Liu, T.; Zhang, B.; Hui, J.; Zeng, Z.; Bai, Y.; Hu, Y. Novel Organic Superbase Dopants for Ultraefficient N-Doping of Organic Semiconductors. *Adv. Mater.* **2023**, *35* (22), 2300084. https://doi.org/10.1002/adma.202300084.

(106) Yuan, D.; Liu, W.; Zhu, X. Efficient and Air-Stable n-Type Doping in Organic Semiconductors. *Chem. Soc. Rev.* **2023**, *52* (11), 3842–3872. https://doi.org/10.1039/D2CS01027E.

(107) Perry, E. E.; Chiu, C.-Y.; Moudgil, K.; Schlitz, R. A.; Takacs, C. J.; O'Hara, K. A.; Labram, J. G.; Glaudell, A. M.; Sherman, J. B.; Barlow, S.; Hawker, C. J.; Marder, S. R.; Chabinyc, M. L. High Conductivity in a Nonplanar *n* -Doped Ambipolar Semiconducting Polymer. *Chem. Mater.* **2017**, *29* (22), 9742–9750. https://doi.org/10.1021/acs.chemmater.7b03516.

(108) Yu, Z.-D.; Lu, Y.; Wang, Z.-Y.; Un, H.-I.; Zelewski, S. J.; Cui, Y.; You, H.-Y.; Liu, Y.; Xie, K.-F.; Yao, Z.-F.; He, Y.-C.; Wang, J.-Y.; Hu, W.-B.; Sirringhaus, H.; Pei, J. High N-Type and p-Type Conductivities and Power Factors Achieved in a Single Conjugated Polymer. *Sci. Adv.* **2023**, *9* (8), eadf3495. https://doi.org/10.1126/sciadv.adf3495.

(109) Tang, H.; Liang, Y.; Liu, C.; Hu, Z.; Deng, Y.; Guo, H.; Yu, Z.; Song, A.; Zhao, H.; Zhao, D.; Zhang, Y.; Guo, X.; Pei, J.; Ma, Y.; Cao, Y.; Huang, F. A Solution-Processed n-Type Conducting Polymer with Ultrahigh Conductivity. *Nature* **2022**, *611* (7935), 271–277. https://doi.org/10.1038/s41586-022-05295-8.

(110) Kim, T. H.; Kim, J. H.; Kang, K. Molecular Doping Principles in Organic Electronics: Fundamentals and Recent Progress. *Jpn. J. Appl. Phys.* **2023**, *62* (SE), SE0803. https://doi.org/10.35848/1347-4065/acbb10.

(111) Tang, C. G.; Hou, K.; Leong, W. L. The Quest for Air Stability in Organic Semiconductors. *Chem. Mater.* **2024**, *36* (1), 28–53. https://doi.org/10.1021/acs.chemmater.3c02093.

(112) Aitola, K.; Gava Sonai, G.; Markkanen, M.; Jaqueline Kaschuk, J.; Hou, X.; Miettunen, K.; Lund, P. D. Encapsulation of Commercial and Emerging Solar Cells with Focus on Perovskite Solar Cells. *Sol. Energy* **2022**, *237*, 264–283. https://doi.org/10.1016/j.solener.2022.03.060.

(113) Fu, Y.; Tsai, F.-Y. Air-Stable Polymer Organic Thin-Film Transistors by Solution-Processed Encapsulation. *Org. Electron.* **2011**, *12* (1), 179–184. https://doi.org/10.1016/j.orgel.2010.10.021.

(114) Yang, C.-Y.; Stoeckel, M.-A.; Ruoko, T.-P.; Wu, H.-Y.; Liu, X.; Kolhe, N. B.; Wu, Z.; Puttisong, Y.; Musumeci, C.; Massetti, M.; Sun, H.; Xu, K.; Tu, D.; Chen, W. M.; Woo, H. Y.; Fahlman, M.; Jenekhe, S. A.; Berggren, M.; Fabiano, S. A High-Conductivity n-Type Polymeric Ink for Printed Electronics. *Nat. Commun.* **2021**, *12* (1), 2354. https://doi.org/10.1038/s41467-021-22528-y.

(115) Dörling, B.; Hawkey, A.; Zaumseil, J.; Campoy-Quiles, M. Strong Dependence of Air Stability on Thickness in N-Doped Carbon Nanotube Thermoelectrics. *Appl. Phys. Lett.* **2024**, *124* (11), 113302. https://doi.org/10.1063/5.0198773.

(116) Zhou, W.; Fan, Q.; Zhang, Q.; Cai, L.; Li, K.; Gu, X.; Yang, F.; Zhang, N.; Wang, Y.; Liu, H.; Zhou, W.; Xie, S. High-Performance and Compact-Designed Flexible Thermoelectric Modules Enabled by a Reticulate Carbon Nanotube Architecture. *Nat. Commun.* **2017**, *8* (1), 14886. https://doi.org/10.1038/ncomms14886.

(117) Wang, S.; Wu, J.; Yang, F.; Xin, H.; Wang, L.; Gao, C. Oxygen-Rich Polymer Polyethylene Glycol-Functionalized Single-Walled Carbon Nanotubes Toward Air-Stable n-Type Thermoelectric Materials. *ACS Appl. Mater. Interfaces* **2021**, *13* (22), 26482–26489. https://doi.org/10.1021/acsami.1c04786.

(118) Suzuki, D.; Nonoguchi, Y.; Shimamoto, K.; Terasaki, N. Outstanding Robust Photo- and Thermo-Electric Applications with Stabilized n-Doped Carbon Nanotubes by Parylene Coating. *ACS Appl. Mater. Interfaces* **2023**, *15* (7), 9873–9882. https://doi.org/10.1021/acsami.2c21347.

(119) Fukumaru, T.; Fujigaya, T.; Nakashima, N. Development of N-Type Cobaltocene-Encapsulated Carbon Nanotubes with Remarkable Thermoelectric Property. *Sci. Rep.* **2015**, *5* (1), 7951. https://doi.org/10.1038/srep07951.

(120) Nakashima, Y.; Nakashima, N.; Fujigaya, T. Development of Air-Stable n-Type Single-Walled Carbon Nanotubes by Doping with 2-(2-Methoxyphenyl)-1,3-Dimethyl-2,3-Dihydro-1 H -Benzo[d]Imidazole and Their Thermoelectric Properties. *Synth. Met.* **2017**, *225*, 76–80. https://doi.org/10.1016/j.synthmet.2016.11.042.

(121) Suzuki, H.; Kametaka, J.; Nakahori, S.; Tanaka, Y.; Iwahara, M.; Lin, H.; Manzhos, S.; Kyaw, A. K. K.; Nishikawa, T.; Hayashi, Y. N-DMBI Doping of Carbon Nanotube Yarns for Achieving High n-Type Thermoelectric Power Factor and Figure of Merit. *Small Methods* **2024**.

(122) Liu, Y.; Villalva, D. R.; Sharma, A.; Haque, M. A.; Baran, D. Molecular Doping of a Naphthalene Diimide–Bithiophene Copolymer and SWCNTs for n-Type Thermoelectric Composites. *ACS Appl. Mater. Interfaces* **2021**, *13* (1), 411–418. https://doi.org/10.1021/acsami.0c16740.

(123) Horike, S.; Wei, Q.; Akaike, K.; Kirihara, K.; Mukaida, M.; Koshiba, Y.; Ishida, K. Bicyclic-Ring Base Doping Induces n-Type Conduction in Carbon Nanotubes with Outstanding Thermal Stability in Air. *Nat. Commun.* **2022**, *13* (1), 3517. https://doi.org/10.1038/s41467-022-31179-6.

(124) Pasquarelli, R. M.; Ginley, D. S.; O'Hayre, R. Solution Processing of Transparent Conductors: From Flask to Film. *Chem. Soc. Rev.* **2011**, *40* (11), 5406. https://doi.org/10.1039/c1cs15065k.

(125) Lu, Y.; Wang, J.-Y.; Pei, J. Achieving Efficient N-Doping of Conjugated Polymers by Molecular Dopants. *Acc. Chem. Res.* **2021**, *54* (13), 2871–2883. https://doi.org/10.1021/acs.accounts.1c00223.

(126) Wei, P.; Oh, J. H.; Dong, G.; Bao, Z. Use of a 1H-Benzoimidazole Derivative as an n-Type Dopant and To Enable Air-Stable Solution-Processed n-Channel Organic Thin-Film Transistors. *J. Am. Chem. Soc.* **2010**, *132* (26), 8852–8853. https://doi.org/10/cqh4nh.

(127) Shi, K.; Lu, Z.; Yu, Z.; Liu, H.; Zou, Y.; Yang, C.; Dai, Y.; Lu, Y.; Wang, J.; Pei, J. A Novel Solution-Processable n-Dopant Based on 1,4-Dihydropyridine Motif for High Electrical Conductivity of Organic Semiconductors. *Adv. Electron. Mater.* **2017**, *3* (11), 1700164. https://doi.org/10.1002/aelm.201700164.

(128) Yang, C.-Y.; Ding, Y.-F.; Huang, D.; Wang, J.; Yao, Z.-F.; Huang, C.-X.; Lu, Y.; Un, H.-I.; Zhuang, F.-D.; Dou, J.-H.; Di, C.; Zhu, D.; Wang, J.-Y.; Lei, T.; Pei, J. A Thermally Activated and Highly Miscible Dopant for N-Type Organic Thermoelectrics. *Nat. Commun.* **2020**, *11* (1), 3292. https://doi.org/10.1038/s41467-020-17063-1.

(129) Aniés, F.; Nugraha, M. I.; Fall, A.; Panidi, J.; Zhao, Y.; Vanelle, P.; Tsetseris, L.; Broggi, J.; Anthopoulos, T. D.; Heeney, M. In Situ Generation of n-Type Dopants by Thermal Decarboxylation. *Adv. Funct. Mater.* **2023**, *33* (12), 2212305. https://doi.org/10.1002/adfm.202212305.

(130) Yan, L.; Yang, X.; Yang, M.; Neu, J.; Kashani, S.; Giridharagopal, R.; Olanrewaju, Y.; So, F.; Ginger, D.; Ade, H.; Li, X.; You, W. Air-Stable n-Type Dopant for Organic Semiconductors via a Single-Photon Catalytic Process. *Sci. Adv.* **2025**, *11* (23), eadu8215. https://doi.org/10.1126/sciadv.adu8215.

(131) Bardagot, O.; Aumaître, C.; Monmagnon, A.; Pécaut, J.; Bayle, P.-A.; Demadrille, R. Revisiting Doping Mechanisms of N-Type Organic Materials with N-DMBI for Thermoelectric Applications: Photo-Activation, Thermal Activation, and Air Stability. *Appl. Phys. Lett.* **2021**, *118* (20). https://doi.org/10.1063/5.0047637.

(132) Zeng, Y.; Zheng, W.; Guo, Y.; Han, G.; Yi, Y. Doping Mechanisms of N-DMBI-H for Organic Thermoelectrics: Hydrogen Removal vs. Hydride Transfer. *J. Mater. Chem. A* **2020**, *8* (17), 8323–8328. https://doi.org/10/ghk7jv.

(133) Guo, J.; Chen, P.; Yang, S.; Wei, H.; Liu, Y.; Xia, J.; Chen, C.; Chen, H.; Wang, S.; Li, W.; Hu, Y. Dopant-induced Morphology of Organic Semiconductors Resulting in High Doping Performance. *Small Methods* **2025**, *9* (1). https://doi.org/10.1002/smtd.202400084.

(134) Schlitz, R. A.; Brunetti, F. G.; Glaudell, A. M.; Miller, P. L.; Brady, M. A.; Takacs, C. J.; Hawker, C. J.; Chabinyc, M. L. Solubility-Limited Extrinsic n-Type Doping of a High Electron Mobility Polymer for Thermoelectric Applications. *Adv. Mater.* **2014**, *26* (18), 2825–2830. https://doi.org/10.1002/adma.201304866.

(135) Deschler, F.; Riedel, D.; Deák, A.; Ecker, B.; Von Hauff, E.; Da Como, E. Imaging of Morphological Changes and Phase Segregation in Doped Polymeric Semiconductors. *Synth. Met.* **2015**, *199*, 381–387. https://doi.org/10.1016/j.synthmet.2014.11.037.

(136) Giovannitti, A.; Maria, I. P.; Hanifi, D.; Donahue, M. J.; Bryant, D.; Barth, K. J.; Makdah, B. E.; Savva, A.; Moia, D.; Zetek, M.; Barnes, P. R. F.; Reid, O. G.; Inal, S.; Rumbles, G.; Malliaras, G. G.; Nelson, J.; Rivnay, J.; McCulloch, I. The Role of the Side Chain on the Performance of N-Type Conjugated Polymers in Aqueous Electrolytes. *Chem. Mater.* **2018**, *30* (9), 2945–2953. https://doi.org/10.1021/acs.chemmater.8b00321.

(137) Liu, J.; Qiu, L.; Alessandri, R.; Qiu, X.; Portale, G.; Dong, J.; Talsma, W.; Ye, G.; Sengrian, A. A.; Souza, P. C. T.; Loi, M. A.; Chiechi, R. C.; Marrink, S. J.; Hummelen, J. C.; Koster, L. J. A. Enhancing Molecular n-Type Doping of Donor–Acceptor Copolymers by Tailoring Side Chains. *Adv. Mater.* **2018**, *30* (7), 1704630. https://doi.org/10.1002/adma.201704630.

(138) Li, Z.; Fan, B.; He, B.; Ying, L.; Zhong, W.; Liu, F.; Huang, F.; Cao, Y. Side-Chain Modification of Polyethylene Glycol on Conjugated Polymers for Ternary Blend All-Polymer Solar Cells with Efficiency up to 9.27%. *Sci. China Chem.* **2018**, *61* (4), 427–436. https://doi.org/10.1007/s11426-017-9188-7.

(139) Jacobs, I. E.; Moulé, A. J. Controlling Molecular Doping in Organic Semiconductors. *Adv. Mater.* **2017**, *29* (42), 1703063. https://doi.org/10.1002/adma.201703063.

(140) Pallini, F.; Mattiello, S.; Manfredi, N.; Mecca, S.; Fedorov, A.; Sassi, M.; Al Kurdi, K.; Ding, Y.-F.; Pan, C.-K.; Pei, J.; Barlow, S.; Marder, S. R.; Nguyen, T.-Q.; Beverina, L. Direct Detection of Molecular Hydrogen upon P- and n-Doping of Organic Semiconductors with Complex Oxidants or Reductants. *J. Mater. Chem. A* **2023**, *11* (15), 8192–8201. https://doi.org/10.1039/D3TA00231D.

(141) Pallini, F.; Mattiello, S.; Sassi, M.; Paoli, G.; Mattioli, G.; Rossi, P.; Coco, G.; Scaccabarozzi, A. D.; Kim, B. M.; Mariani, P.; Wakidi, H.; Flagg, S. M.; D'Arienzo, M.; Caironi, M.; Nguyen, T.; Beverina, L. Understanding the Interplay Between Thermal Activation, Diffusion, and Phase Segregation of Molecular Dopants Blended with Polymeric Semiconductors. *Adv. Electron. Mater.* **2025**, 2500170. https://doi.org/10.1002/aelm.202500170.

(142) Rossi, P.; Pallini, F.; Coco, G.; Mattiello, S.; Tan, W. L.; Mezzomo, L.; Cassinelli, M.; Lanzani, G.; McNeill, C. R.; Beverina, L.; Caironi, M. An Iminostilbene Functionalized Benzimidazoline for Enhanced n-Type Solution Doping of Semiconducting Polymers for Organic Thermoelectrics. *Adv. Mater. Interfaces* **2023**, *10* (19), 2202416. https://doi.org/10.1002/admi.202202416.

Chapter 2 - Optimized Syntheses of DMBI Dopants

2. Synthesis and Structure-Property Study of Benzimidazoline Dopants

---

Part of the results presented in this chapter have been published in:
F. Pallini, S. Mattiello, M. Sassi, G. Paoli, G. Mattioli, P. Rossi, G. Coco, A. D. Scaccabarozzi, B. M. Kim, P. Mariani, H. Wakidi, S. M. Flagg, M. D'Arienzo, M. Caironi, T. Nguyen, and L. Beverina. "Understanding the Interplay Between Thermal Activation, Diffusion, and Phase Segregation of Molecular Dopants Blended with Polymeric Semiconductors".
Adv. Electron. Mater. **2025**, 2500170

F. Pallini, G. Garavaglia, G. Paoli, G. Mattioli, F. Porcelli, L. Mezzomo, D. Florenzano, R. Ruffo, M. Sassi and S. Mattiello. "Hitchhiker's guide to the preparation of novel benzimidazoline based n-type dopants".
Chem. Mater. **2025**, 37, 19, 7823–7833

In this works, I have contributed specifically to the synthesis of DMBI derivatives.

This chapter connects the present work to the literature on dopant derivatives based on DMBI, while also relating it with the research framework previously developed by our group. It represents a fundamental basis for understanding and contextualizing the experimental work presented in the following chapters.

In the first part of this chapter, we analyze the main N-DMBI derivatives reported in literature, discussing the rationale behind their design and synthesis. We show that, while these compounds often display superior doping performances compared to the benchmark material, the synthetic protocols employed for their preparation are generally limited in versatility, as they are optimized to produce a single target species and are not easily adaptable to the synthesis of new variants.

Building on this observation, we focused on developing a **more flexible synthetic platform**. We examined the strategies proposed in the literature and combined their most effective aspects to optimize two synthetic routes capable of producing derivatives of different types. The validity of these protocols was then demonstrated by synthesizing a broad set of compounds.

Subsequently, we compared their doping performance using the n-type semiconductor polymer poly(N,N'-bis(2-octyldodecyl)-naphthalene-1,4,5,8-bis(dicarboximide)-2,6-diyl-alt-5,5'-(2,2'-bithiophene)) [P(NDI2OD-T2)] (**N2200**).

Most of the content in this chapter has already been reported in the articles cited at the beginning. Since our aim here is uniquely to highlight the **effectiveness** of the new synthetic protocol, as well as to demonstrate that dopants with different structures may exhibit similar energy levels yet markedly different doping efficiencies, we do not dwell on the specific synthetic procedures or on characterizations that fall outside this objective.

2.1. DMBI-derivatives in Literature

DMBI derivatives maintain the central molecular scaffold of N-DMBI, but vary in the functional groups bond to the nitrogen atoms. They can essentially be categorized as:

- **derivatives functionalized at the imidazoline nitrogens**, symmetric when the same substituent is introduced at both positions, asymmetric when the groups are different;
- **derivatives functionalized at the aniline nitrogen**, where the substituents differs from the two methyl groups found in N-DMBI. These substituents are usually electron donating groups (-D).

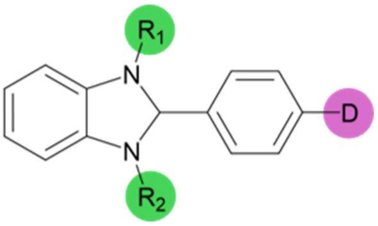

Figure 2.1
Structure of a general DMBI derivatives where the imidazolinic (green) and the anilinic (pink) functionalizations are highlighted.

Derivatives combining **both** types of modification are rarely reported, as it would be difficult to disentangle the individual contributions of each structural change with respect to N-DMBI-H. The main examples of reported DMBI-derivatives are represented in Figure 2.2.

The initial studies on DMBI derivatives focused on the substitution or introduction of alkyl chains at the aniline position of N-DMBI-H, with the goal of improving interactions with the side chains of organic semiconductors, thereby, enhancing mutual compatibility. Saglio et al.[1] reported that increasing the chain length leads to higher conductivity in doped films, although the improvement quickly saturates, reaching a plateau with the DBuBI derivative. A similar strategy was adopted for JLBI, where the alkyl chains were replaced by two cyclohexyl rings.[2] This substitution enhanced lipophilicity while keeping the overall molecular size relatively small.

The situation changes with DPBI, in which the methyl groups are replaced by two aromatic moieties.[3] These do not have a relevant interaction with the alkyl side chains of polymers, but can in principle establish interactions with the semiconductor core. In this case, phase segregation does not result in dopant accumulation at the surface, as observed for N-DMBI-H, but remains confined to the bulk.

Nonetheless, the performance of this derivative is inferior to the benchmark, a behavior in contrast with that of IStBI, a compound previously developed by our group. Both molecules feature

aromatic donor groups, yet IStBI has so far delivered the highest conductivities achieved in the doping of N2200.[4] The reasons behind this discrepancy relies in the flexibility of the substituent, and we will describe this feature in detail at the end of this chapter. Another available derivative, N3-DMBI-H, also contains an aromatic donor group. The design of this molecule was aimed at obtaining a species with a significantly lower HOMO level compared to N-DMBI, since the latter tends to oxidize under ambient conditions and particularly in solution, whereas N3-DMBI-H has been shown to remain stable even in solution. However, the conductivity achieved through doping with this compound **does not surpass** that obtained under the same conditions using N-DMBI.[5]

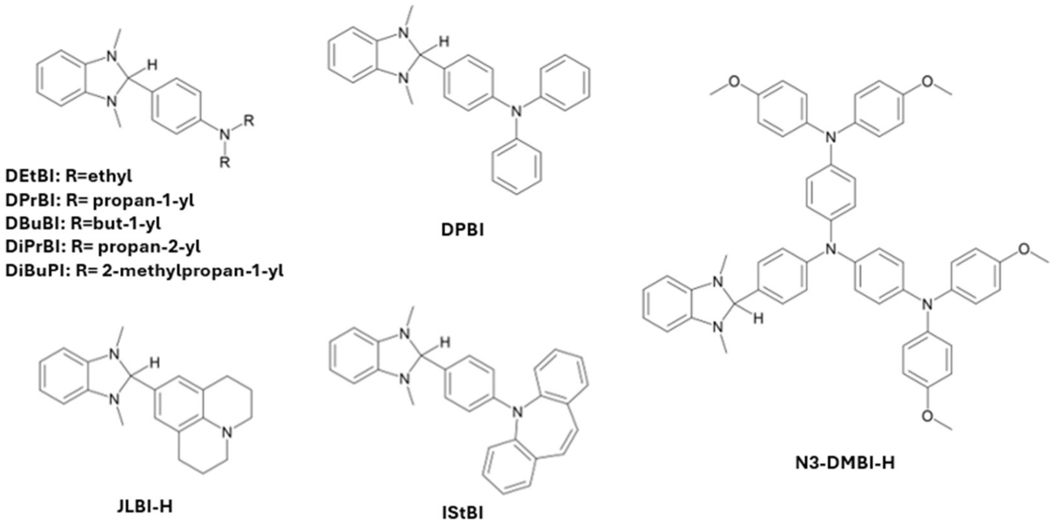

Figure 2.2
Chemical structure of the main monofunctional DMBI derivatives, i.e. derivatives that present only one DMBI core, reported in literature.

The examples discussed illustrate that structural modifications to the DMBI core can influence multiple aspects of the doping process, from **miscibility** and **diffusion** within the host matrix to dopant stability and charge-transfer efficiency. However, no unifying trend clearly emerges from these studies: changes that improve one property often compromise another, and the relationship between molecular structure and electronic performance remains largely empirical.

To enable a more **rational exploration** of DMBI derivatives, it is necessary to access a wider range of molecular structures, which, at the same time, requires a versatile synthetic protocol capable of introducing various substituents.

2.1.1. Traditional synthetic protocols

In literature, two principal synthetic strategies are commonly employed for the preparation of benzimidazoline derivatives:

1. the **acid-catalyzed condensation** of o-phenylenediamines with benzaldehydes (Route 1)
2. the **reduction of benzimidazolium salts** (Route 2)

While both methods are well established and widely applied to the synthesis of DMBI-type dopants, they suffer from intrinsic limitations, such as a limited number of accessible targets, harsh reaction conditions, and moderate atom economy.

A schematic overview of these conventional pathways is shown in Figure **2.3**.

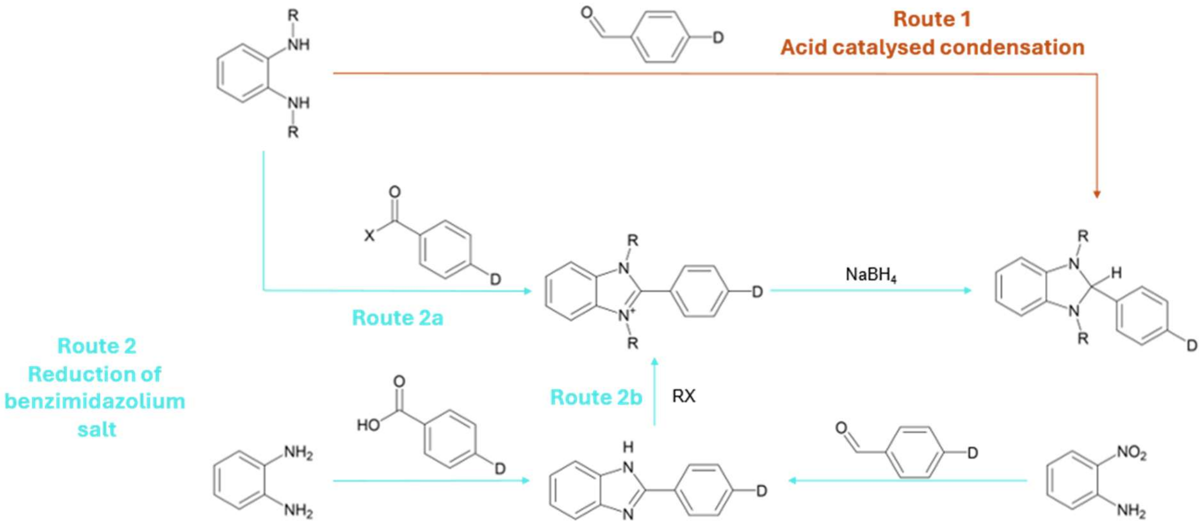

Figure 2.3
Scheme of the reaction mechanisms of the main synthetic routes to obtain DMBI derivatives.

2.2. Optimized Synthetic Protocols

To overcome the limitations of the traditional protocols, our group developed two **optimized synthetic variants**, referred to as **Route 1*** and **Route 2*** (see Figure 2.4).

These improved procedures were designed to enhance overall efficiency, expand the diversity of accessible benzimidazoline derivatives, and enable the synthesis of asymmetric or otherwise challenging structures.

In the following sections, each protocol is described in detail, with emphasis on the modifications introduced, the rationale behind them, and their advantages compared to the conventional methods.

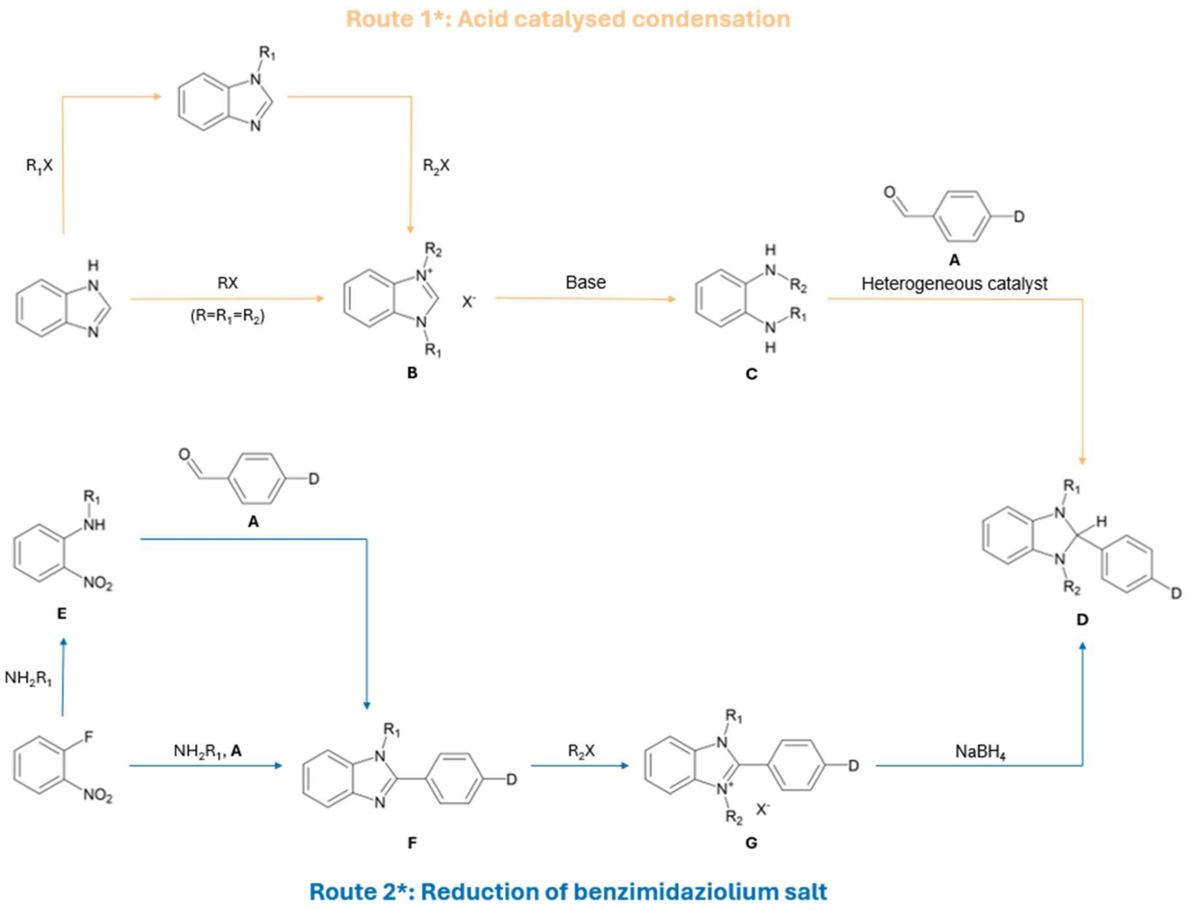

Figure 2.4
Representation of the reaction mechanism of the two optmized routes that compose our synthetic protocol to produce DMBI derivatives.

2.2.1. Synthesis of Benzaldheydes (A)

In both Routes 1 and 2, the synthesis relies on benzaldehydes bearing electron-donating substituents (-D) on para position. These precursors can be obtained either through the formylation of the corresponding aniline via a **Vilsmeier-Haack reaction** or by a **Buchwald-Hartwig amination** starting from 4-bromobenzaldehyde. The product that we have obtained following these strategies are summarized in Figure. In our work, the formylation approach was primarily adopted to access the dialdehyde derivative.

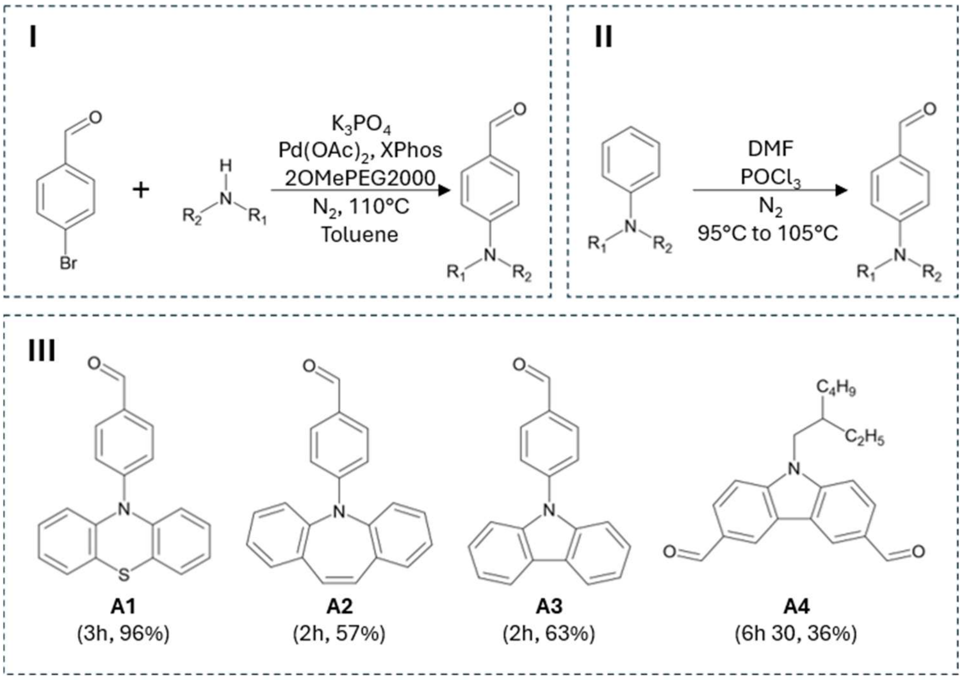

Figure 2.5
I. Vilsmeier-Haack reaction scheme, with the conditions used by our group.
II. Buchwald-Hartwig ammination scheme, with the conditions used by our group.
III. Chemical structure of the benzaldheydes obtained and relative reaction yield.

2.3. Route 1*: Acid catalyzed condensation

2.3.1. Synthesis of N,N'-disubstituted o-phenylenediamines (C)

The **classical** acid-catalyzed condensation route relies on **N,N'-dimethyl-o-phenylenediamine** as a starting material, but its prohibitive commercial cost makes the direct approach unattractive. For this reason, we have considered the reported synthetic strategies to obtain this species. If we consider the synthesis of **N,N'-dimethyl-o-phenylenediamine**, the classical protocol proceeds through tosylation, methylation, and subsequent deprotection of o-phenylenediamine, thereby allowing access to the desired diamine, but with **poor atom economy and limited scalability** (Figure **2.6**).[6]

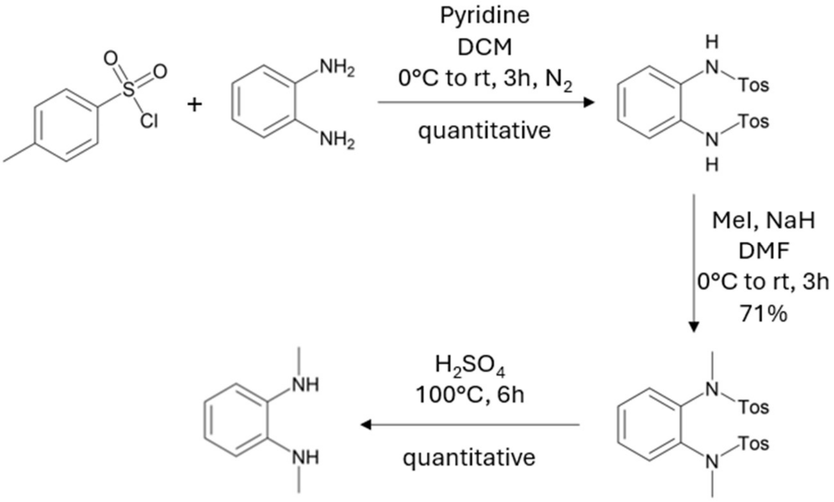

Figure 2.6
Common protocol to synthesize N,N'-dimethyl-o-phenylenediamine.

If we move to the more general synthesis of N,N'-disubstituted o-phenylenediamines, the traditional synthetic approach involves the **alkylation of o-phenylenediamine** with alkyl halides under strongly basic (or occasionally acidic) conditions. Although this method is straightforward, it typically requires harsh reagents and the use of potentially genotoxic reagents (alkyl halides), and it often suffers from limited selectivity and over-alkylation.[7]

More recently, greener and more selective alternatives have been developed based on **the hydrogen autotransfer** (HA), or **borrowing hydrogen** (BH), mechanism. In this transformation, primary alcohols, which are not strong electrophiles by themselves, serve as alkylating agents.

Through the borrowing hydrogen cycle (Figure 2.7), two hydrogen atoms are abstracted from the alcohol to form a more reactive species, such as an aldehyde, which subsequently reacts with an amino group to yield an imine intermediate that is finally reduced to the secondary amine.[8,9] In these processes, the presence of a transition-metal catalyst is crucial.[10,11]

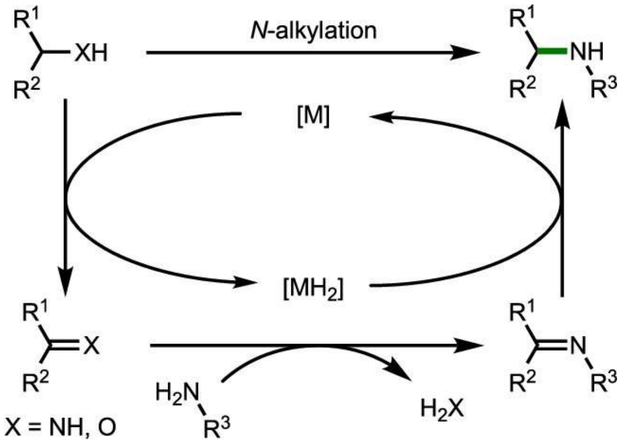

Figure 2.7
Generalized Transition-Metal-Catalyzed Borrowing Hydrogen Reaction. Reported with permission from the work of Reed-Berendt et al.[9] License CC-BY-NC-ND 4.0.

A relevant example of this approach was reported by Michlik et al.[12], who employed an **iridium-based** catalyst to obtain both symmetrical and unsymmetrical N,N'-disubstituted o-phenylenediamines via the reaction of o-phenylenediamine with primary alcohols, achieving excellent yields under mild conditions. However, iridium is considered a **rare and expensive metal**, which limits its large-scale applicability.

Contemporary to the development of our work, other studies demonstrated that the same class of compounds could be synthesized under similarly mild conditions and high yields using **more abundant and affordable transition-metal catalysts**, such as those based on cobalt,[7] nickel,[13] or manganese.[14]

2.3.1.1. Our strategy

The approach that we have employed for the isolation of N,N'-disubstituted o-phenylenediamines starts from the benzimidazole, which can be selectively alkylated with the desired substituent. Performing this first step under **micellar conditions** proved particularly advantageous, as it enables efficient transfer of the released hydrogen halide into the aqueous phase, avoids the use of organic solvents, and affords nearly quantitative yields. A subsequent solvent-free alkylation yields **benzimidazolium salts (B)**, either with two different substituents when the reaction is carried out sequentially, or with symmetric substitution patterns when an excess of alkyl halide is employed to alkylate directly benzimidazole in a single step.

Subsequently, the obtained salts are hydrolyzed under basic conditions to yield the corresponding **N,N'-dialkyl-o-phenylenediamines (C).**

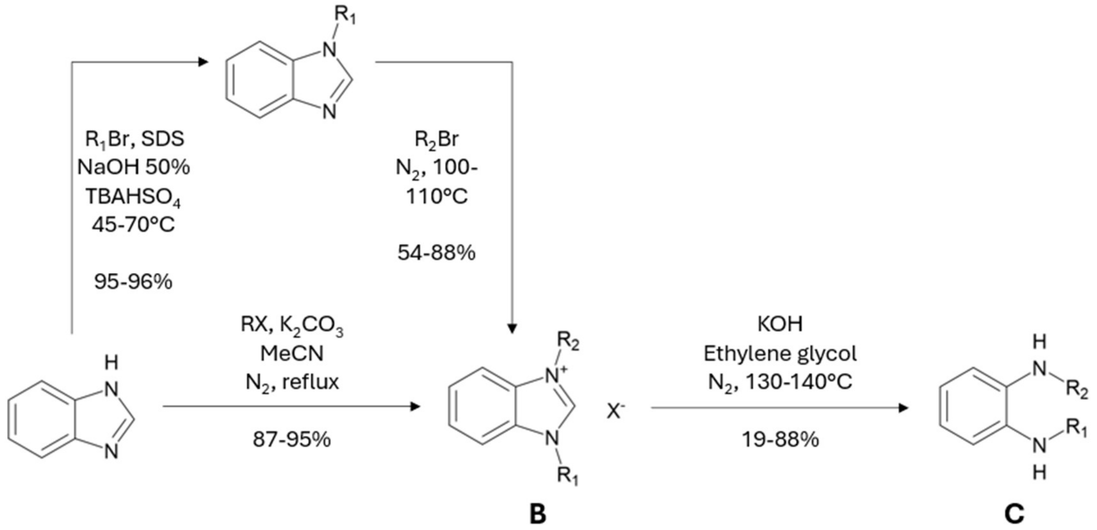

Figure 2.8
Novel and general protocol for the synthesis of N,N'-dialkylbenzene-1,2-diamine.

2.3.1.2. Results and discussion

The structures of the obtained species, compounds B and compounds C, are summarized in Figure **2.9**. Overall, this methodology combines sustainability and efficiency while broadening the available structural diversity, although in some cases issues of selectivity and purification were still encountered.

For instance, compound **B4** could not be purified fully purified. However, this condition did not hinder the subsequent hydrolysis step, from which the corresponding product (**C4**) was successfully obtained and isolated. Moreover, compound **C5** exhibited pronounced instability in solution, leading to a lower yield in respect of the other diamines.

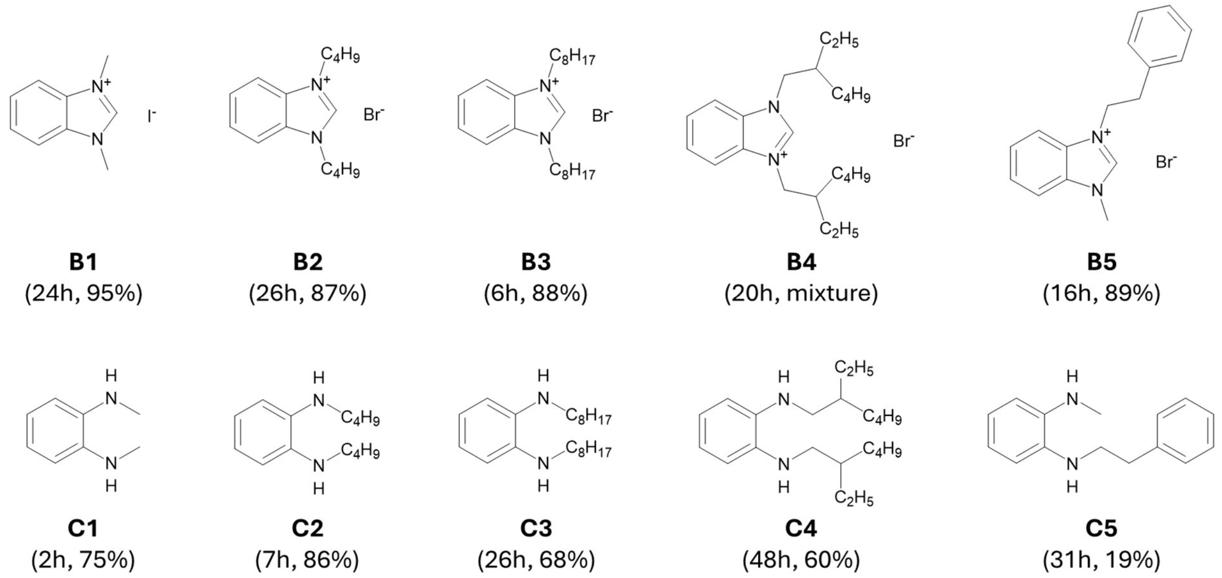
B1 (24h, 95%)
B2 (26h, 87%)
B3 (6h, 88%)
B4 (20h, mixture)
B5 (16h, 89%)
C1 (2h, 75%)
C2 (7h, 86%)
C3 (26h, 68%)
C4 (48h, 60%)
C5 (31h, 19%)

Figure 2.9
Chemical structure and yield of the 1,3-dialkyl-1H-benzimidazol-3-ium salts and the N,N'-dialkyl-o-phenylendiamines obtained.

2.3.1.3. Summary

Our optimized approach to diamine synthesis within Route 1* enhances process efficiency by shortening the reaction sequence and eliminating the need for protecting groups. Nevertheless, the hydrolysis of benzimidazolium intermediates can lead to the formation of the corresponding ureas, persistent impurities that in the case of compounds C3, C4 and C5 has reduced the purity of the products to 90%. In fact, although the target diamines themselves are stable under basic conditions, the **benzimidazolium intermediates** can undergo side reactions that limit the overall yield and reproducibility. Consequently, while this method is effective for obtaining both symmetric and asymmetric diamines, its reliability depends mainly on the **reactivity of the intermediates** and on how well the reaction conditions are tuned to the structural features of the desired products. These considerations highlight the importance of aligning the synthetic strategy with the intrinsic behavior of the intermediates to ensure both reproducibility and scalability.

2.3.2. Condensation - Synthesis of the dopants (D)

The condensation between N,N'-dialkyl-1,2-phenylenediamines and benzaldehydes is conventionally carried out under acidic conditions, typically employing glacial acetic acid (I, Figure **2.10**).[1] This approach is attractive for its simplicity, however, its main limitation lies in the fact that the reaction is **reversible** and establishes an equilibrium between the starting diamine, the imine (or imidazoline) intermediate, and **water**. Consequently, the conversion of the diamine into the desired product is incomplete, and the position of the equilibrium, which depends on the reaction medium and the removal of water, ultimately limits the reaction yield.

2.3.2.1. Our strategy

In this work we adopted and refined the procedure exposed by Bonacci et al.[4,15] In particular, the reported approach relies on the employment of **Montmorillonite K-10** as a heterogeneous catalyst and as a dehydrating agent, thus, it removes the water formed during the condensation leading to quantitative reactions. We further introduced in the procedure molten-state conditions to eliminate solvents and enable higher operating temperatures (II, Figure 2.10).

A practical limitation of this modification is the progressive rise in **viscosity** as product builds up, which in cases of derivatives with higher melting points (notably D5 and D9) hindered reaction progress.

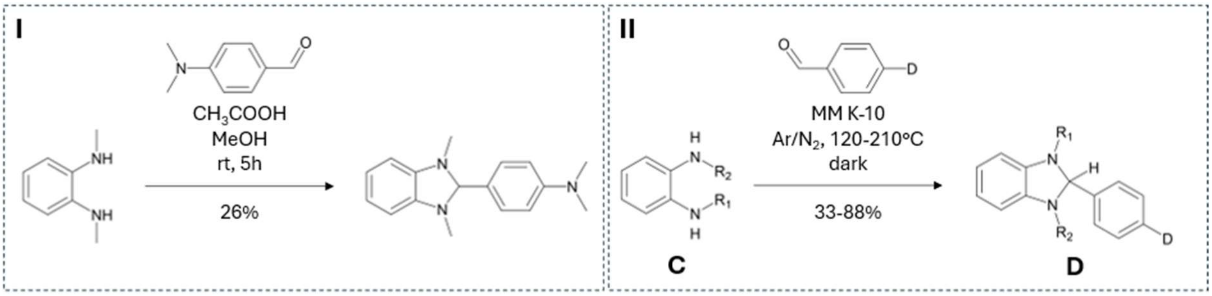

Figure 2.10
I. Reaction scheme of a traditional acid catalysed condensation between N,N'-dimethylbenzene-1,2-diamine and 4-dimethylamino-benzaldehyde.
II. Reaction scheme of the optimized variant of the conventional acid catalysed condensation.

Benzimidazoline-based dopants are intrinsically prone to oxidation when handled either in solution or in the molten state.[6] This **instability** makes work-up particularly delicate, as purification methods such as column chromatography require dissolving the crude mixture and, thus, expose the product to conditions that can lead to degradation. For this reason, all reactions and purifications needed to be carried out as rapidly as possible, under inert atmosphere and with minimal light exposure, to reduce product loss during handling.

2.3.2.2. Results and discussion

The outcomes of this strategy are summarized in Table 2.1.

Table 2.1
Summary of the dopants synthesized with route 1*.

Compound	R_1	R_2	D	T (°C)	Reaction time	Yield (%)
D1	CH_3	CH_3	$N(CH_3)_2$	120	1h	64
D2	C_4H_9	C_4H_9	$N(CH_3)_2$	120	3h	58
D3	CH_3	CH_3	N,N-diphenylamino	120	20'	71
D4	2-ethylphenyl	CH_3	$N(CH_3)_2$	120	40'	33
D5	CH_3	CH_3	carbazol-9-yl	160	50'	54
D6	CH_3	CH_3	dibenzo[b,f] azepin-5-yl	185	1h	64
D7	CH_3	CH_3	julolidine-9-yl	120	4h 30'	78
D8	CH_3	CH_3	phenothiazin-10-yl	120	1h 30'	88
D9	CH_3	CH_3	9-(2-ethylhexyl)-9H-carbazole-3,6-diyl	210	1h 40'	44

Route 1* demonstrates that acid-catalysed condensations can be made more efficient and operationally cleaner through the combination of a solid acid (MM K-10) and solvent-free conditions. Nonetheless, the **rheological limitations** in viscous melts constrain generality for some substrates. Given the intrinsic solution/molten instability of benzimidazoline dopants, the effective processing window can be narrow. Therefore, for sterically demanding donors or highly viscous product mixtures, alternative sequences (e.g., Route 2*) may represent a more reliable pathwat. In conclusion, Route 1* is a valuable option within the synthetic toolbox for DMBI derivatives.

2.4. Route 2*: Reduction of Benzimidazolium Salts

2.4.1. Synthesis of 2-Phenyl-1-Substituted-1H-Benzimidazoles (F)

The standard synthesis of DMBI derivatives by the reduction of the corresponding benzimidazolium salts can essentially proceed through two main approaches. In the first pathway (**Route 2a**), the salt is obtained via condensation of a N,N'-disubstituted benzene-1,2-diamine with an acyl halide. However, this strategy offers limited versatility due to the relatively small number of commercially available acyl halides. The second pathway (**Route 2b**) involves the condensation of N,N'-dimethylbenzene-1,2-diamine with a carboxylic acid, leading to the formation of the benzimidazole core. This intermediate can then be further alkylated with an alkyl halide, thus allowing the introduction of various substituents,[16–18] as like alkyl chains,[19] or benzyl groups.[20]

2.4.1.1. Our strategy

In comparison to these routes, we optimized an alternative synthetic strategy that offers greater **flexibility**. Our approach relies on commercially available N-alkyl-2-nitrobenzen-1-amines, even called o-nitroanilines, which are accessible in a wide range of derivatives. Moreover, when required, o-nitroanilines can be readily synthesized from 2-fluoro- or 2-chloro-nitrobenzene through nucleophilic aromatic substitution with a primary amine, thereby providing access to either N-aryl or N-alkyl derivatives (A, Figure 2.11). The formation of the o-nitroaniline can be either as an isolated reaction or performed one-pot with the subsequent reductive cyclization.

The key step of this synthetic route is the reductive cyclization between an o-nitroaniline and a benzaldehyde, in which sodium dithionite reduces the nitro group in situ to the corresponding o-phenylenediamine, which then condenses with the aldehyde to form a 2-phenyl-1-substituted benzimidazole (B, Figure 2.11).[21]

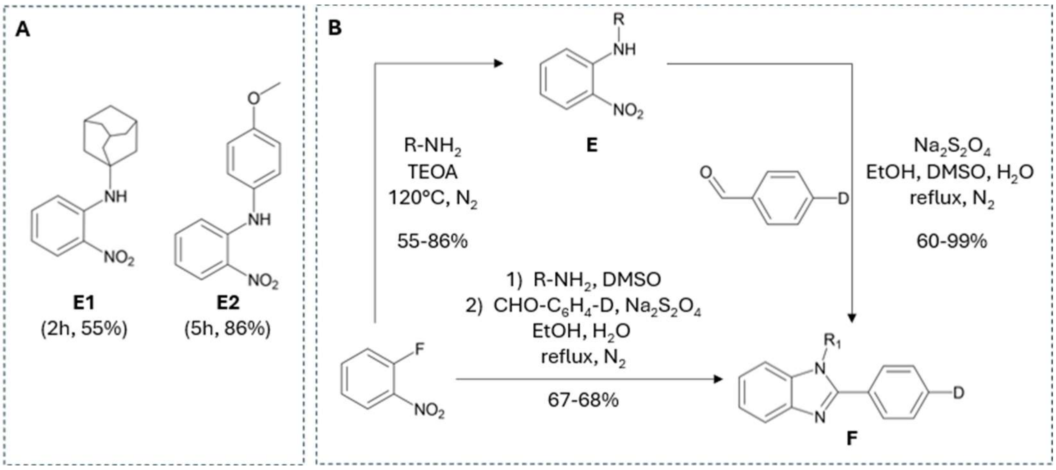

Figure 2.11
A) Chemical structure and reaction yield of the o-nitroanilines isolated.
B) Reaction scheme of the synthesis of o-nitroanilines and of the synthesis of 2-phenyl-1-substituted-1H-benzimidazoles (reductive cyclisation), performed either one-pot or in two steps.

2.4.1.2. **Results and discussion**

Using this approach, we successfully isolated a broad set of derivatives (reported in Table 2.2). Except for F9 and F10, obtained from the isolated o-nitroaniline, most products were produced in one step.

Table 2.2
Summary of the 2-Phenyl-1-Substituted-1H-Benzimidazoles synthesized with route 1*. The substituents, the reaction yield and the reaction time are specified for each species.

Compound	R	D	Yield (%)	Reaction time
F1	CH_3	$N(CH_3)_2$	99	48h
F2	C_4H_9	$N(CH_3)_2$	68	18h
F3	CH_3	N,N-diphenylamino	62	23h
F4	2-ethylphenyl	$N(CH_3)_2$	67	21h
F5	CH_3	carbazol-9-yl	84	4h 30'
F6	CH_3	dibenzo[b,f]azepin-5-yl	92	4h 30'
F7	CH_3	julolidine-9-yl	62	2h 30'
F8	CH_3	phenothiazin-10-yl	88	1h 30'
F9	1-adamantyl	$N(CH_3)_2$	82	16h
F10	p-anisyl	$N(CH_3)_2$	91	18h

This strategy significantly expands the **scope and flexibility** of benzimidazole synthesis compared to classical condensation methods. Its one-pot nature preserves efficiency, while the possibility to access various o-nitroaniline precursors leads to a wide spectrum of N-substituted derivatives. However, the method is not universally applicable, due to the solubility limitations of certain aldehydes.

At this stage we can say that Route 2* constitutes a **robust** and **adaptable** synthetic entry to structurally diverse benzimidazoles, complementing Route 1* by addressing substrates that would otherwise be challenging to access.

2.4.2. Synthesis of 2-Phenyl-1,3-Disubstituted Benzimidazolium Salts (G)

Following the reductive cyclization, the unsubstituted imidazoline nitrogen is **alkylated** with different alkylated agents to afford the corresponding benzimidazolium salt. Conceptually, this step parallels the alkylation employed in the acid-catalyzed condensation protocol, but in practice it presents distinct challenges.

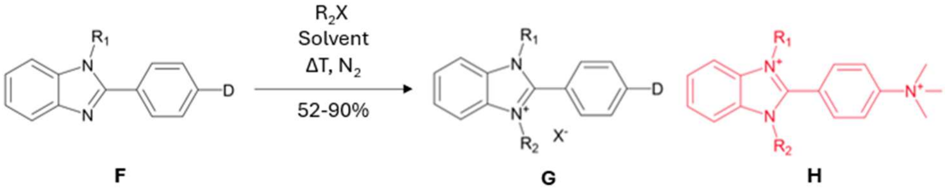

Figure 2.12
Reaction scheme of the alkylation of 2-phenyl-1-substituted-1h-benzimidazoles (f).

The first difficulty lies in the careful choice of **the solvent and the reaction temperature**, both specific for each substrate. Efficient alkylation requires a medium that solubilizes the benzimidazole precursor at the operating temperature while simultaneously allowing precipitation of the benzimidazolium salt, thereby reducing the need for extensive purification.

Then, a more critical issue is the **competing alkylation of the aniline nitrogen**, which, although less nucleophilic than the imidazolic nitrogen, can occasionally undergo reaction. The resulting doubly alkylated species is highly problematic: its structural and electronic similarity to the desired salt makes separation difficult.

This side reaction is strongly substrate dependent. When the substituent on the aniline nitrogen is an **aromatic moiety**, delocalization of electron density reduces the nucleophilic character of the site and suppresses over-alkylation. Whilst, in the case of aliphatic donors, steric hindrance makes the difference. For instance, substituting the methyl groups with isopropyl groups reduces the probability of double alkylation almost to zero. Solvent choice also has an influence in this context: a medium in which the monoalkylated product is poorly soluble inhibits the formation of the undesired by-product.

2.4.2.1. Results and discussion

The results obtained with this strategy are summarized in Figure 2.13. Notably, the use of methyl triflate (MeOTf) in the synthesis of G1 produced significant amounts of the doubly alkylated by-product H. To avoid this side reaction, less reactive alkylating agents (MeI, C_4H_9Br, $C_6H_{13}Br$) were successfully employed in the preparation of G2, G4, and G9-G11. On the contrary, for sterically relevant derivatives (G3, G5-G8), methyl triflate proved to be advantageous, affording high yields and short reaction times without detectable over-alkylation.

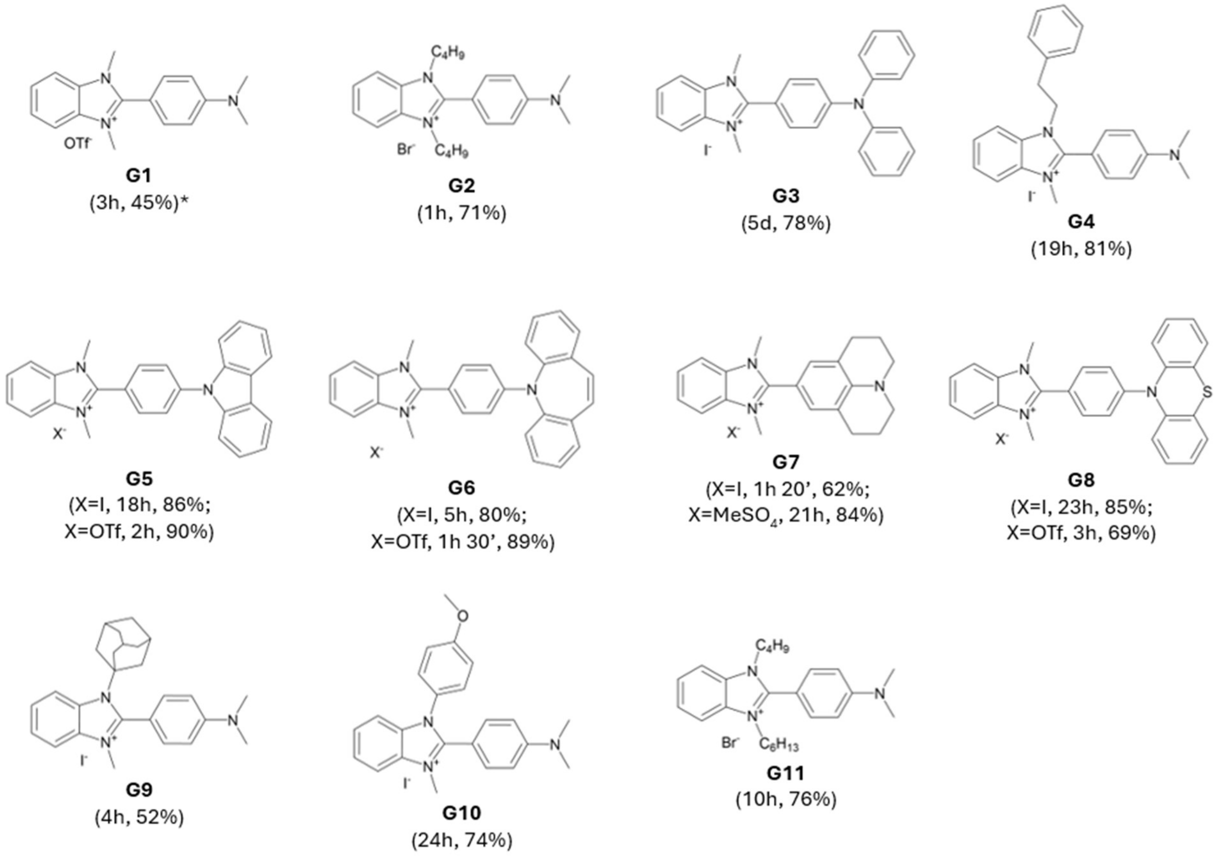

G1 (3h, 45%)*

G2 (1h, 71%)

G3 (5d, 78%)

G4 (19h, 81%)

G5 (X=I, 18h, 86%; X=OTf, 2h, 90%)

G6 (X=I, 5h, 80%; X=OTf, 1h 30', 89%)

G7 (X=I, 1h 20', 62%; X=$MeSO_4$, 21h, 84%)

G8 (X=I, 23h, 85%; X=OTf, 3h, 69%)

G9 (4h, 52%)

G10 (24h, 74%)

G11 (10h, 76%)

Figure 2.13
Chemical structure, reaction yield and reaction time of the 2-phenyl-1,3-disubstituted benzimidazolium salts produced.

This step illustrates the delicate balance between **reactivity and selectivity** in benzimidazole alkylation. Highly reactive alkylating agents accelerate the process but can be responsible of uncontrolled double substitution, whereas milder reagents improve selectivity at the expense of yield and time. Structural features of the aniline substituent are determinant in shifting this balance: electron delocalization or steric hindrance can effectively suppress side reactions. Overall, the method is versatile but requires **substrate-specific optimization** of both reaction temperature and solvent to ensure reliable access to the desired benzimidazolium salts.

2.4.3. Reduction - Synthesis of the Dopants (D)

The final step of Route 2* involves the reduction of benzimidazolium salts (G) to the corresponding benzimidazoline dopants (D). This transformation is typically performed with sodium borohydride in methanol, where the high solubility of most of the compounds G ensures rapid and complete conversion (Figure 2.14). A key advantage of this protocol lies in the poor solubility of the reduced products, which readily precipitate and can often be collected by simple filtration, giving reproducible high yields across a broad range of derivatives.

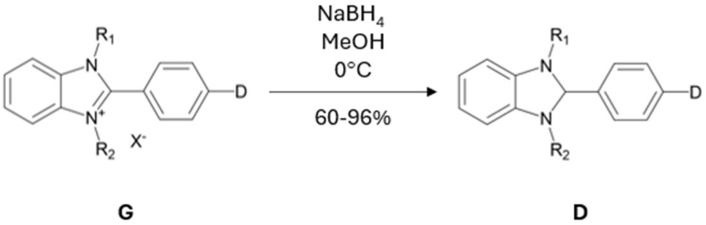

Figure 2.14
Reaction scheme of 2-phenyl-1,3-disubstituted benzimidazolium salts reduction, performed to obtain DMBI-based dopants.

2.4.3.1. Results and discussion

Table 2.3
Summary of the dopants synthesized with route 2*. The substituents, the reaction yield and the reaction time are specified for each species.

Compound	R1	R2	D group	Yield (%)	Reaction time
D1	CH_3	CH_3	$N(CH_3)_2$	93	15'
D2	C_4H_9	C_4H_9	$N(CH_3)_2$	58	20'
D3	CH_3	CH_3	N,N-diphenylamino	62	2h 30'
D4	2-ethylphenyl	CH_3	$N(CH_3)_2$	60	5'
D5	CH_3	CH_3	carbazol-9-yl	93	2h 30'
D6	CH_3	CH_3	dibenzo[b,f]azepin-5-yl	93	1h
D7	CH_3	CH_3	julolidine-9-yl	65	1h 30'
D8	CH_3	CH_3	phenothiazin-10-yl	96	40'
D10	C_4H_9	C_6H_{13}	$N(CH_3)_2$	66	20'
D11	1-adamantyl	CH_3	$N(CH_3)_2$	72	1h 30'
D12	p-anisyl	CH_3	$N(CH_3)_2$	99	1h

Nevertheless, by considering the results obtained in the reduction step, which are resumed in Table 2.3, we can note that this efficiency is **not global**.

For example, when the dopant is in liquid state at room temperature (e.g., D2 and D10), precipitation does not occur, requiring **liquid-liquid extraction** that lowers yields and complicates purification.

Moreover, in certain cases, the benzimidazolium salt is **insufficiently** soluble in methanol, preventing its smooth reduction to the corresponding benzimidazoline. While, in other cases, the dopant itself remains soluble in methanol or other polar solvents, making its isolation particularly difficult. These examples make it clear that the outcome of benzimidazoline reactions strongly depends on how each compound behaves in solution, so the conditions must be tailored accordingly.

While the $NaBH_4$/methanol protocol remains a cornerstone of Route 2*, enabling systematic access to a wide variety of DMBI-based dopants, its reliability ultimately depends on the physical state and solubility profile of the target species.

2.5. Comparison between Route 1* and Route 2*

Both synthetic strategies discussed above have proven to be reliable entries to DMBI-based dopants. However, their applicability differs depending on the **structural** and **physical** properties of the target compounds. A general comparison of the two routes highlights **complementary strengths and weaknesses** rather than a clear superiority of one over the other. In **Figure 2.15** is reported a diagram of the overall yield obtained in the synthesis of the DMBI derivatives, following the two optimized routes.

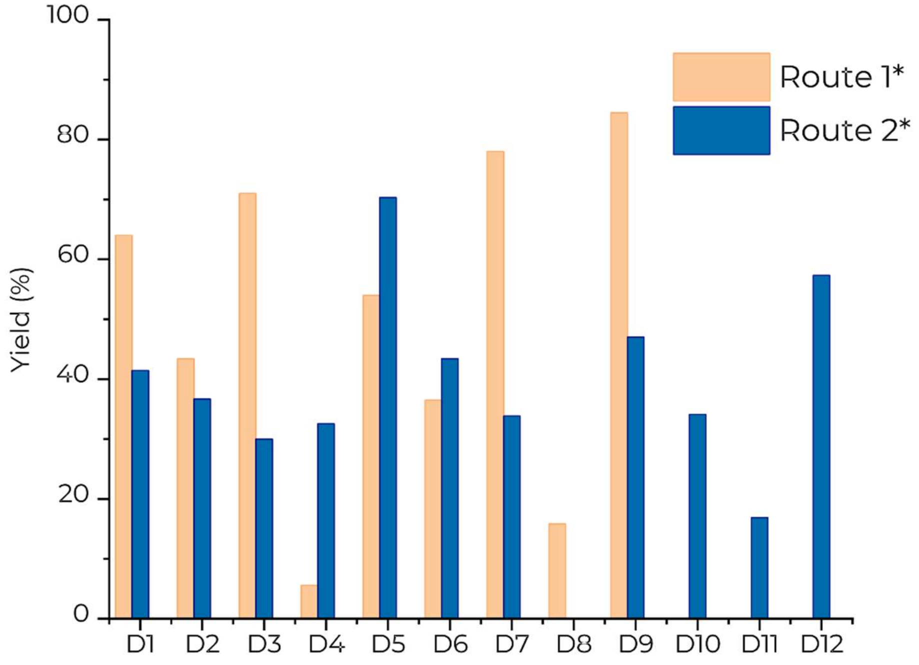

Figure 2.15
Diagram representing the overall yields of the synthesis of the DMBI derivatives, in the two routes. For these calculations, the synthetic steps that lead to a commercial available product are considered to have a 100% yield.

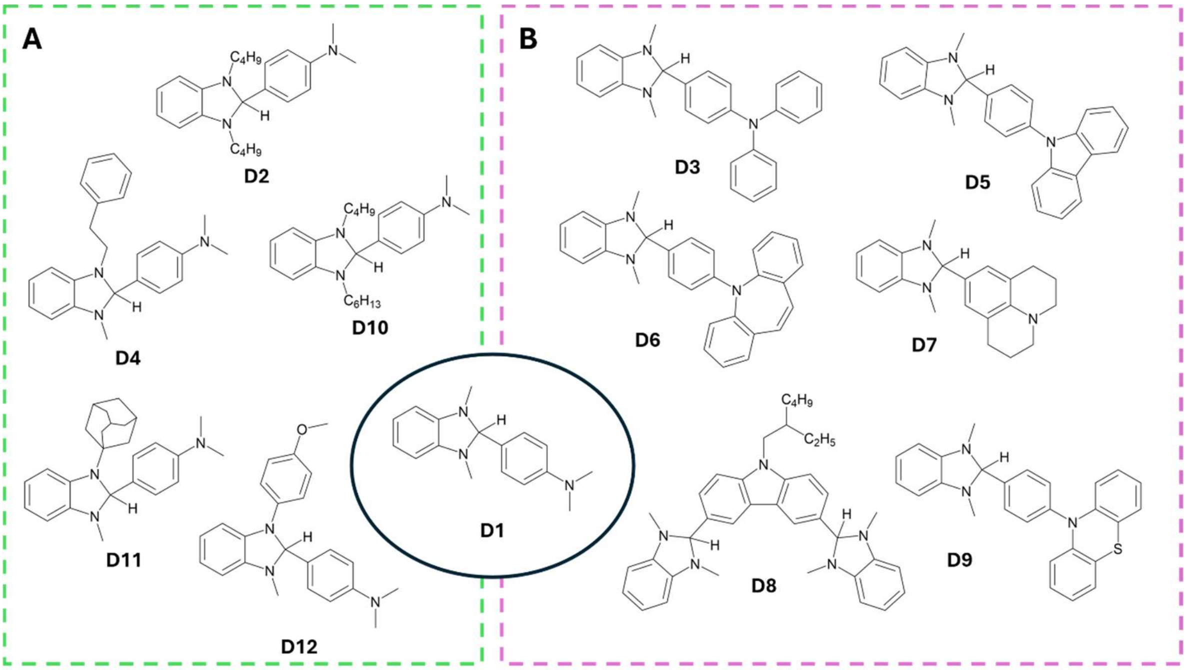

Figure 2.16
Chemical structure of the dopants synthesized, the species are distinguished in derivatives functionalized on the imidazolinic nitrogens (A), and derivatives functionalized on the anilinic nitrogen (B).

When both the N,N'-disubstituted o-phenylenediamine and the aldehyde are **commercially available**, Route 1* provides a short and economical pathway that can be completed in a single step. In such cases, the simplicity of the synthesis leads to greater overall synthetic efficiency and competitive yields. This makes Route 1* particularly advantageous when

1. The derivatives are relatively **symmetric**, thus avoiding the need for **stepwise alkylations** or **selective substitutions**, which are instead required in asymmetric cases (better handled by Route B*)
2. The derivatives are **poorly soluble**. In this situation, purification can rely on the removal of unreacted aldehyde and diamine by washing the product with an appropriate solvent and filtering it. On the contrary, if the product exhibits a solubility similar to that of the reagents, purification requires separation by **chromatography**, which can complicate the isolation of sensitive DMBI derivatives

In contrast, Route 2* involves a longer sequence, composed by three steps when starting from a commercial aldehyde, but compensates with a **broader versatility**. The reductive cyclisation step is based on a wide variety of o-nitroaniline precursors, enabling the preparation of **asymmetric or sterically demanding derivatives** that are less accessible through Route 1*. Moreover, the dopants generated in this route typically precipitate during work-up, simplifying purification and reducing the risk of product oxidation. This feature makes Route 2* especially suitable for **unstable or structurally complex species**, where rapid isolation is essential.

Essentially, Route 1* should be regarded as a **simplified and economical pathway**, most effective when starting materials are readily available and the target derivative is resilient. Route 2*, while synthetically longer, provides **greater flexibility**, especially for challenging substrates. The two strategies should be considered **complementary tools**, each addressing specific synthetic demands.

In parallel to the two optimized synthetic protocols, we explored an **alternative strategy** for accessing N-alkyl-2-arylbenzimidazoles via **nucleophilic substitution** on halogenated intermediates. Although testing various nucleophiles and catalytic conditions, these attempts proved to be largely unsuccessful, highlighting the limitations of this approach. Full details of these exploratory studies are reported in the following section, as they provide useful insight into the reactivity boundaries of this class of intermediates, even though they did not lead to viable synthetic routes.

2.5.1. Alternative Routes to Access N-Alkyl-2-Arylbenzimidazoles

Within the framework of Route 2*, we carried out exploratory studies to probe an alternative pathway toward DMBI derivatives bearing distinct substituents at the aniline position. Conceptually, this strategy was promising, as it could in principle enable access to a broad family of N-alkyl-2-arylbenzimidazoles from a **single fluorinated intermediate (I1)**. However, the experimental outcome highlighted several intrinsic challenges. The general reaction mechanism followed is represented in Figure 2.17.

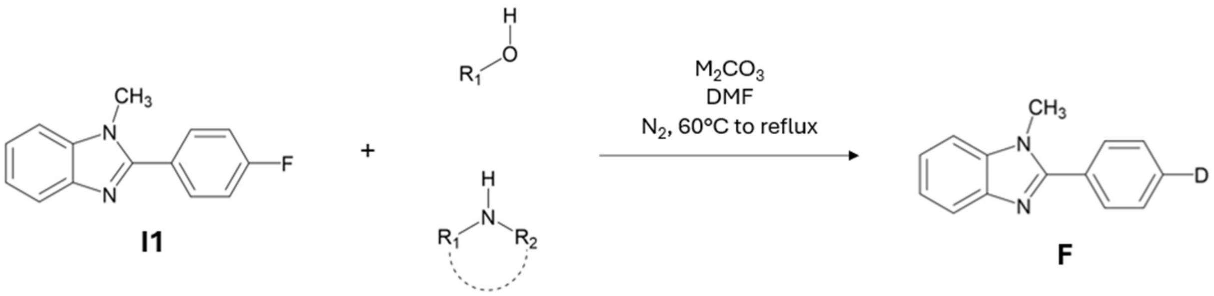

Figure 2.17
General reaction scheme for the synthesis of N-alkyl-2-arylbenzimidazoles through nucleophilic susbstitution operated on an fluorinated intermediate.

Table 2.4
Results obtained during the preliminary tests concerning I1 nucleophilic substitution.

Entry	Reagent	Product	Nucleophile	Base	Catalyst	Time	Yield (%)
1	I1	**F5**	9H-carbazole	Cs_2CO_3	-	5h	70
2	I1	**F6**	5H-Dibenzo[b,f]azepine	Cs_2CO_3	-	-	-
3	I1	**F11**	piperidine	Cs_2CO_3	-	-	-
4	I1	**F12**	4-methoxyaniline	Cs_2CO_3	-	-	-
5	I1	**F13**	2-naphtol	K_2CO_3	18-crown-6	-	-

The results obtained are resumed in Table 2.4.

The direct amination of intermediate **I1** under conventional conditions (Cs_2CO_3 as base, secondary aromatic and aliphatic amines as nucleophiles) proved largely ineffective.[22,23] Product formation was only achieved in the case of carbazole, leading to the isolation of **F5**, while no conversion was evidenced with other substrates. This observation suggests that the reactivity window is extremely narrow, and only highly activated or particularly nucleophilic amines can engage effectively with the aryl halide under these conditions.

To enhance reactivity, we have subsequently introduced **18-crown-6** as a phase-transfer catalyst in combination with K_2CO_3, with the idea of increasing the nucleophilicity of the carbonate anion by sequestration of potassium.[24,25] Nevertheless, this modification did not promote the reaction, indicating that the limiting factor was not related to the basicity of the medium but rather to the inertness of the C-X bond toward nucleophilic substitution.

These trials indicate that the direct amination strategy of the fluorinated intermediate in this system faces substantial thermodynamic barriers. Future work may therefore need to move beyond classical nucleophilic or transition-metal-mediated substitutions, exploring instead alternative activation strategies or the use of **milder** and more **selective catalytic systems**.

2.5.1.1. Synthetic procedures

Reagents were purchased from TCI, BLD pharm, Sigma-Aldrich and Fluorochem. Solvents were bought by Merck, Carlo-Erba and Acros, and used as received unless otherwise stated. Na2S2O8 at 85% wt. was used for synthesis of 2-arylbenzimidazoles.

Composition of solvent mixtures are indicated as volume/volume ratios. Melting points were determined using a Buchi M-560 apparatus. Solution Nuclear Magnetic Resonance (NMR) spectra were acquired with a Bruker Avance 400 NEO Spectrometer. For 1H and 13C NMR of known derivatives, only chemical shifts are indicated.

Synthesis of derivative I1

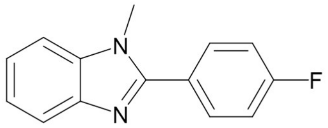

N-methyl-1-nitrobenzene (12.000 g, 78.87 mmol) and **sodium persulfate** ($Na_2S_2O_8$, 43.616 g, 212.9 mmol) are added to a 500 mL round-bottom flask. The system is placed under nitrogen atmosphere. **4-Fluorobenzaldehyde** (9.788 g, 78.8 mmol) is added, followed by EtOH/H_2O (260 mL, 5:1 v/v). The reaction mixture is heated at 85 °C under stirring for 2 h. After cooling to room temperature, the mixture is filtered through a pleated filter and washed with EtOH. The combined filtrates are concentrated to dryness under reduced pressure, a solid is obtained. The solid is suspended in Et_2O (30 mL), filtered on a Hirsch funnel and dried in a vacuum oven at 65°C until constant weight. The resulting solid is crystallized from n-hexane (100 mL). The suspension is cooled to room temperature, filtered on a Hirsch funnel, and the solid is dried in a vacuum oven at 65°C until constant weight, affording the product as a solid (11.870 g, 52.46 mmol, 66.6%).

^{1}H NMR (400 MHz, $CHCl_3$-d): δ [ppm] 7.85-7.80 (m, 1H), 7.80-7.74 (m, 2H), 7.42-7.38 (m, 1H), 7.37-7.30 (m, 2H), 7.27-7.20 (m, 2H), 3.86 (s, 3H).

Synthesis of derivative F5

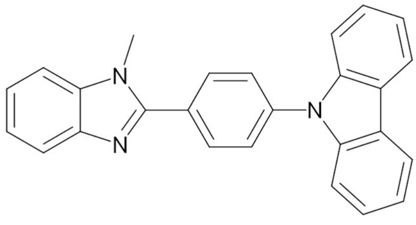

Derivative I1 (1.000 g, 4.42 mmol), **9H-carbazole** (0.817 g, 4.89 mmol), and **Cs_2CO_3** (7.261 g, 22.29 mmol) are added to a 250 mL round-bottom flask: The system is placed under nitrogen atmosphere. Anhydrous, degassed DMF (80 mL) is added, and the mixture is heated at 80 °C. The reaction progress is monitored by TLC (DCM/EtOAc 8:2). After 24 h, the reaction reaches completion. The mixture is filtered through a pleated filter to remove Cs_2CO_3, and the filtrate is poured into water (~300 mL) and acidified with HCl to pH 2. The aqueous layer is extracted with toluene, operation during which a solid precipitates at the interface. The solid is collected by filtration on a Hirsch funnel, washed with water, and dried in a vacuum oven 65 °C to constant weight, affording the product as a solid (1.365 g, 3.65 mmol, 82.6%). mp 174-176 °C.

^{1}H NMR (400 MHz, DMSO-d^6): δ[ppm] 8.29 (d, J = 7.7 Hz, 2H), 8.17 (d, J=8.4 Hz, 2H), 7.86 (d, J = 8.4 Hz, 2H), 7.74 (d, J = 7.6 Hz, 1H), 7.67 (d, J = 7.8 Hz, 1H), 7.55 (d, J = 8.2 Hz, 2H), 7.51-7.45 (m, 2H), 7.38-7.25 (m, 4H), 4.02 (s, 3H).

2.6. Doping efficiency of the novel dopants

To evaluate the efficiency of the newly synthesized dopants, we combined electrochemical measurements (CV and DPV) with DFT calculations, molecular simulations (GFN-FF), and electrical characterization of N2200 doped films. This approach allowed us to distinguish the role of electronic structure from that of intermolecular interactions in determining doping performance. As previously discussed, activation of benzimidazoline-based dopants could, in principle, proceed via direct electron transfer from **the neutral precursor**. In practice, however, this pathway is kinetically and thermodynamically disfavored, making it unlikely to contribute significantly to the overall doping mechanism. Consequently, the HOMO of the neutral benzimidazoline dopant, that is associated with this mechanism, does not directly influence doping performance but it rather represents an indicator of the compound's stability in air. In contrast, the SOMO level of the activated species, which correspond to the DMBI• radical generated upon homolytic cleavage of the C-H aminal bond (activation of the dopant), defines the thermodynamic driving force for electron transfer and, thus, represents the fundamental electronic parameter for evaluating doping capability. In this context, the hydride donor strength of the dopant is directly related to the ionization potential of this radical species.

Alongside the ionization process, the influence of the dopant on the morphology of the doped layer plays a crucial role in determining overall doping efficiency. In particular, the structural features of the dopant determine its interactions with the host semiconductor and thereby influence its **behavior during film processing**, including annealing, diffusion, and phase segregation. For instance, although this effect was not directly investigated in our study, Saglio et al.[1] reported that flexible alkyl substituents increase compatibility with the alkylated side chains of N2200, leading to improved dopant-polymer miscibility, but they do not substantially reduce dopant mobility or diffusivity. By contrast, **rigid heteroaromatic substituents** can in principle promote specific π–π interactions with the conjugated backbone, effectively binding the dopant in proximity of the semiconductor core. Therefore, we expected a different behavior of the mentioned two classes of dopant when mixed with the polymer and let demixing in time.

Finally, by measuring the electrical conductivity of N2200 films doped with the different compounds, we expected to observe a correlation between the obtained values, the FMOs of the dopants, and their respective demixing kinetics.

2.6.1. Results and discussion

The **frontier molecular orbitals levels** of the synthesized dopants are represented in Figure 2.18. In particular, the energy levels reported are the ones obtained by DPV. At the same time, the HOMO and the SOMO values obtained experimentally were in great accordance with the simulated ones, except for a few cases.

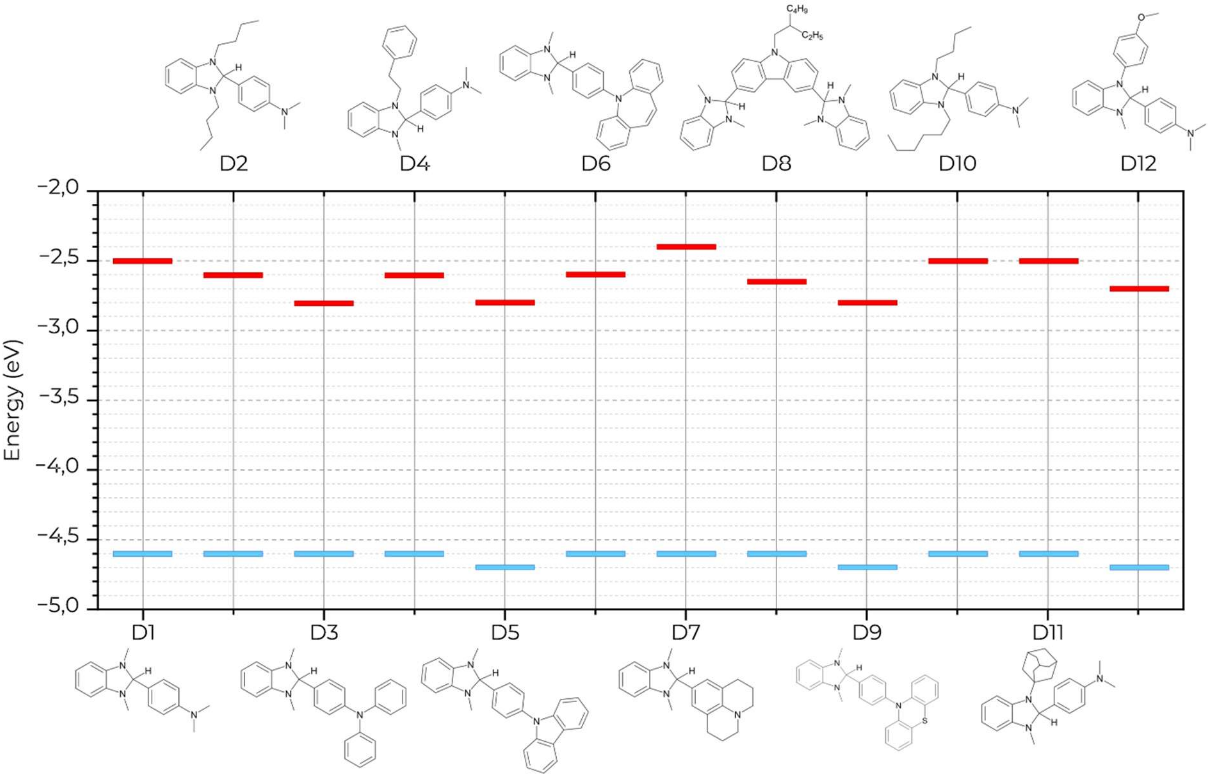

Figure 2.18
Comparison of the HOMO level (blue) of the synthesized dopants and SOMO level (red) of the corresponding activated species. The values considered are the ones obtained by DPV.

Derivatives bearing **alkyl substituents** on the **imidazoline moiety** retained HOMO and SOMO levels comparable to N-DMBI-H, ensuring both stability and effective doping performance. Notably, DFT calculations predicted a slightly lower electron affinity for compound D10 compared to the benchmark (-2.48 eV vs -2.54 eV, respectively). Experimentally, DPV measurements instead revealed a slightly higher value (-2.60 eV), indicating a small deviation between theoretical predictions and experimental observations.

Functionalization of the **anilinic nitrogen**, instead, significantly influenced the SOMO: aromatic donor groups stabilized the energy level (reduction of the SOMO), while strongly electron-donating substituents, such as julolidine, destabilized. Overall, all the species can work as efficient organic n-dopants.

Moreover, we have performed molecular dynamics simulations (GFN-FF at 227 °C) to illustrate the evolution of dopant–polymer interactions over time. Since the initial mixing is imposed in the model, these simulations primarily probe the **kinetics of demixing** rather than the degree of miscibility. Within this framework, alkyl-substituted derivatives exhibit a demixing behaviour comparable to the benchmark, whereas **heteroaromatic derivatives**, such as carbazole- and dibenzoazepine-substituted species, tend to **remain more uniformly distributed** within the polymer matrix throughout the simulation.

Electrical measurements on doped N2200 films reinforced these findings. N-DMBI-H exhibited the expected conductivity reported in literature (~10^{-3} S cm^{-1}).[6,26]

Derivatives designed with **solubilizing chains** reached conductivities in the 10^{-4} S cm^{-1} range. The reduced performance could arise from limited dopant-polymer interaction or partial segregation, although this correlation cannot be directly confirmed from the present data.

In contrast, **rigid heteroaromatic derivatives** achieved significantly higher values, with D9 emerging as the most efficient dopant for this polymer. An exception, however, is represented by compound D5, whose apparent efficiency is lower than that of N-DMBI-H. This anomaly can be rationalized by its particularly high melting point: under the annealing conditions employed, all other dopants were in a molten or near-molten state, which enhanced their mobility and allowed them to more effectively access dopable sites, whereas this was not the case for D5.

In summary, doping efficiency in benzimidazoline derivatives results from a dual interplay: the **SOMO** of the activated species dictates the thermodynamic feasibility of charge transfer, while **structural design,** whether featuring alkyl chains for interfacial entanglement or heteroaromatic groups for π–π anchoring, controls the **morphological stability and dopant retention within the film.** Only by integrating energetics with interfacial interactions can dopant design achieve both high conductivity and long-term stability.

2.7. Conclusion

This study introduces not only two complementary synthetic strategies for benzimidazoline derivatives (Routes 1* and 2*) but also a different conceptual perspective on how to facethe persistent inefficiency of n-type doping in organic semiconductors. The conventional literature approach typically relies on the introduction of solubilizing chains, which represent a rather general solution: such substituents provide nonspecific interactions that are broadly effective across many polymers. In contrast, the route explored in this work emphasizes the fine tailoring of **specific dopant-semiconductor interactions**.

This new perspective carries important implications. While compound D9 clearly emerged as the most efficient dopant for N2200, the fact that its performance is tied to the peculiar π–π interactions with this polymer highlights a limitation: there is no such thing as a truly universal dopant. Instead, dopants should be regarded as **specialized agents**, whose efficiency depends on their ability to establish stable interfacial interactions with a given semiconductor. Such specialization not only enables more stable interfaces but also supports effective doping at higher concentrations. From this standpoint, it becomes justified and indeed necessary to develop a **rich portfolio of dopants**, each optimized for a specific class of semiconductors. The benzimidazoline scaffold represents an ideal starting point for this vision, due to its remarkable structural tunability and the diversity of intermolecular interactions it can establish.

Importantly, dopants that appeared less efficient in respect of the benchmark in the case of N2200 may well prove advantageous in other semiconductor contexts, reinforcing the idea that performance must be evaluated in a system-specific manner rather than against a universal benchmark. In this chapter we focused on **monofunctional dopants** based on a single DMBI core. However, dopants incorporating multiple DMBI units, hereafter referred to as **multifunctional dopants**, are in fact capable of introducing additional types of interactions. Among these is the bifunctional dopant D8, which could only be synthesized via Route 1* and with modest yield. This initial attempt highlights that the optimized approaches (route 1* and route 2*) cannot be directly applied in their current form to access multifunctional species. Nevertheless, given its versatility, Route 2* should provide a solid foundation for the synthesis of such dopants. Building on this insight, the next chapter expands the scope of this research towards **multifunctional dopants**, specifically dimeric and polymeric structures. While these species share essentially the same energy levels as the monomeric DMBI benchmark, they introduce entirely new interaction motifs at the dopant-semiconductor interface. This transition moves the discussion beyond the simple recognition that "dopant structure matters" and towards **the strategic design of interaction-driven doping architectures**. By investigating these multifunctional systems, the thesis seeks to demonstrate how the rational design of benzimidazoline derivatives can combine energetic feasibility with interfacial stability, thereby paving the way toward more efficient and durable n-type doping.

2.8. Bibliography

(1) Saglio, B.; Mura, M.; Massetti, M.; Scuratti, F.; Beretta, D.; Jiao, X.; McNeill, C. R.; Sommer, M.; Famulari, A.; Lanzani, G.; Caironi, M.; Bertarelli, C. *N* -Alkyl Substituted 1 *H* -Benzimidazoles as Improved n-Type Dopants for a Naphthalene-Diimide Based Copolymer. *J. Mater. Chem. A* **2018**, *6* (31), 15294–15302. https://doi.org/10.1039/C8TA04901G.

(2) Li, C.; Wang, W.; Zhan, C.; Zhou, Q.; Dong, D.; Xiao, S. A Julolidine Functionalized Benzimidazoline N-Dopant: Optimizing Molecular Doping in Fullerene Derivatives by Modulating Miscibility. *J. Mater. Chem. C* **2023**, *11* (44), 15599–15607. https://doi.org/10.1039/D3TC03417H.

(3) Schlitz, R. A.; Brunetti, F. G.; Glaudell, A. M.; Miller, P. L.; Brady, M. A.; Takacs, C. J.; Hawker, C. J.; Chabinyc, M. L. Solubility-Limited Extrinsic n-Type Doping of a High Electron Mobility Polymer for Thermoelectric Applications. *Adv. Mater.* **2014**, *26* (18), 2825–2830. https://doi.org/10.1002/adma.201304866.

(4) Rossi, P.; Pallini, F.; Coco, G.; Mattiello, S.; Tan, W. L.; Mezzomo, L.; Cassinelli, M.; Lanzani, G.; McNeill, C. R.; Beverina, L.; Caironi, M. An Iminostilbene Functionalized Benzimidazoline for Enhanced n-Type Solution Doping of Semiconducting Polymers for Organic Thermoelectrics. *Adv. Mater. Interfaces* **2023**, *10* (19), 2202416. https://doi.org/10.1002/admi.202202416.

(5) Uebe, M.; Yoshihashi, Y.; Noda, K.; Matsubara, M.; Ito, A. A Dendritic Oligoarylamine-Substituted Benzimidazole Derivative as a Useful n-Type Dopant. *J. Mater. Chem. C* **2018**, *6* (24), 6429–6439. https://doi.org/10.1039/C8TC01280F.

(6) Pallini, F.; Mattiello, S.; Cassinelli, M.; Rossi, P.; Mecca, S.; Tan, W. L.; Sassi, M.; Lanzani, G.; McNeill, C. R.; Caironi, M.; Beverina, L. Unexpected Enhancement of Molecular N-Doping Efficiency in Polymer Thin Films by a Degradation Product. *ACS Appl. Energy Mater.* **2022**, *5* (2), 2421–2429. https://doi.org/10.1021/acsaem.1c03893.

(7) Siddique, M.; Boity, B.; Rit, A. Control over Borrowing Hydrogen and Acceptorless Dehydrogenative Coupling Process for the Co(III)–NHC Catalysed Chemoselective Alkylation and Cyclisation of 1,2-Phenylenediamine with Alcohols. *Catal. Sci. Technol.* **2023**, *13* (24), 7172–7180. https://doi.org/10.1039/D3CY01235B.

(8) Denjean, A. E. F.; Nova, A.; Balcells, D. Borrowing Hydrogen Mechanism in Amine Alkylation by Single Atom Nickel Catalysts. *ACS Catal.* **2024**, *14* (15), 11332–11342. https://doi.org/10.1021/acscatal.4c02182.

(9) Reed-Berendt, B. G.; Latham, D. E.; Dambatta, M. B.; Morrill, L. C. Borrowing Hydrogen for Organic Synthesis. *ACS Cent. Sci.* **2021**, *7* (4), 570–585. https://doi.org/10.1021/acscentsci.1c00125.

(10) Fujita, K.; Enoki, Y.; Yamaguchi, R. Cp*Ir-Catalyzed N-Alkylation of Amines with Alcohols. A Versatile and Atom Economical Method for the Synthesis of Amines. *Tetrahedron* **2008**, *64* (8), 1943–1954. https://doi.org/10.1016/j.tet.2007.11.083.

(11) Savela, R.; Vogt, D.; Leino, R. Ruthenium Catalyzed *N* -Alkylation of Cyclic Amines with Primary Alcohols. *Eur. J. Org. Chem.* **2020**, *2020* (20), 3030–3040. https://doi.org/10.1002/ejoc.202000167.

(12) Michlik, S.; Hille, T.; Kempe, R. The Iridium-Catalyzed Synthesis of Symmetrically and Unsymmetrically Alkylated Diamines under Mild Reaction Conditions. *Adv. Synth. Catal.* **2012**, *354* (5), 847–862. https://doi.org/10.1002/adsc.201100554.

(13) Donthireddy, S. N. R.; Siddique, M.; Rit, A. N-Heterocyclic Carbene-Supported Nickel-Catalyzed Selective (Un)Symmetrical N-Alkylation of Aromatic Diamines with Alcohols. *J. Org. Chem.* **2023**, *88* (2), 1135–1146. https://doi.org/10.1021/acs.joc.2c02639.

(14) Kaur, B.; Rana, T. R. K.; Rajaraman, G.; Balakrishna, M. S. Base-Tuned Dehydrogenative and Borrowing Hydrogen Strategies for the Synthesis of Benzimidazoles and *N* -Alkylated Derivatives from *o* -Phenylenediamines and Alcohols Using a Cationic Mn^I Catalyst. *Org. Lett.* **2025**, *27* (31), 8434–8439. https://doi.org/10.1021/acs.orglett.5c02197.

(15) Bonacci, S.; Iriti, G.; Mancuso, S.; Novelli, P.; Paonessa, R.; Tallarico, S.; Nardi, M. Montmorillonite K10: An Efficient Organo-Heterogeneous Catalyst for Synthesis of Benzimidazole Derivatives. *Catalysts* **2020**, *10* (8), 845. https://doi.org/10.3390/catal10080845.

(16) Narendra, G.; Raju, B.; Verma, H.; Kumar, M.; Jain, S. K.; Tung, G. K.; Thakur, S.; Kaur, R.; Kaur, S.; Sapra, B.; Silakari, O. Scaffold Hopping Based Designing of Selective ALDH1A1 Inhibitors to Overcome Cyclophosphamide Resistance: Synthesis and Biological Evaluation. *RSC Med. Chem.* **2024**, *15* (1), 309–321. https://doi.org/10.1039/D3MD00543G.

(17) Wang, Y.; Sarris, K.; Sauer, D. R.; Djuric, S. W. A Simple and Efficient One Step Synthesis of Benzoxazoles and Benzimidazoles from Carboxylic Acids. *Tetrahedron Lett.* **2006**, *47* (28), 4823–4826. https://doi.org/10.1016/j.tetlet.2006.05.052.

(18) Huynh, T.-K.-C.; Nguyen, T.-H.-A.; Tran, N.-H.-S.; Nguyen, T.-D.; Hoang, T.-K.-D. A Facile and Efficient Synthesis of Benzimidazole as Potential Anticancer Agents. *J. Chem. Sci.* **2020**, *132* (1), 84. https://doi.org/10.1007/s12039-020-01783-4.

(19) Phan, N.-K.-N.; Huynh, T.-K.-C.; Nguyen, H.-P.; Le, Q.-T.; Nguyen, T.-C.-T.; Ngo, K.-K.-H.; Nguyen, T.-H.-A.; Ton, K. A.; Thai, K.-M.; Hoang, T.-K.-D. Exploration of Remarkably Potential Multitarget-Directed N-Alkylated-2-(Substituted Phenyl)-1 *H* -Benzimidazole Derivatives as Antiproliferative, Antifungal, and Antibacterial Agents. *ACS Omega* **2023**, *8* (31), 28733–28748. https://doi.org/10.1021/acsomega.3c03530.

(20) Arya, C. G.; Chandrakanth, M.; Fabitha, K.; Thomas, N. M.; Allaka, B. S.; Basavoju, S.; Banoth, S.; Banothu, J. Sodium Fluoride-Assisted, Solvent-Controlled Regioselective Synthesis of 2-Substituted and 1,2-Disubstituted Benzimidazoles with Diverse Substituents, and Unveiling Mechanistic Insights. *J. Mol. Struct.* **2024**, *1306*, 137935. https://doi.org/10.1016/j.molstruc.2024.137935.

(21) Naeimi, H.; Alishahi, N. An Efficient and One-Pot Reductive Cyclization for Synthesis of 2-Substituted Benzimidazoles from o-Nitroaniline under Microwave Conditions. *J. Ind. Eng. Chem.* **2014**, *20* (4), 2543–2547. https://doi.org/10.1016/j.jiec.2013.10.038.

(22) Firsan, S. J.; Sivakumar, V.; Colacot, T. J. Emerging Trends in Cross-Coupling: Twelve-Electron-Based L_1 Pd(0) Catalysts, Their Mechanism of Action, and Selected Applications. *Chem. Rev.* **2022**, *122* (23), 16983–17027. https://doi.org/10.1021/acs.chemrev.2c00204.

(23) Fitzner, M.; Wuitschik, G.; Koller, R. J.; Adam, J.-M.; Schindler, T.; Reymond, J.-L. What Can Reaction Databases Teach Us about Buchwald–Hartwig Cross-Couplings? *Chem. Sci.* **2020**, *11* (48), 13085–13093. https://doi.org/10.1039/D0SC04074F.

(24) Houlihan, F.; Bouchard, F.; Fréchet, J. M. J.; Willson, C. G. Phase Transfer Catalysis in the *Tert* -Butyloxycarbonylation of Alcohols, Phenols, Enols, and Thiols with Di- *Tert* -Butyl Dicarbonate. *Can. J. Chem.* **1985**, *63* (1), 153–162. https://doi.org/10.1139/v85-025.

(25) Liotta, C. L.; Harris, H. P. Chemistry of Naked Anions. I. Reactions of the 18-Crown-6 Complex of Potassium Fluoride with Organic Substrates in Aprotic Organic Solvents. *J. Am. Chem. Soc.* **1974**, *96* (7), 2250–2252. https://doi.org/10.1021/ja00814a044.

(26) Wei, H.; Chen, P.; Guo, J.; Liu, Y.; Qiu, X.; Chen, H.; Zeng, Z.; Nguyen, T.; Hu, Y. Low-Cost Nucleophilic Organic Bases as n-Dopants for Organic Field-Effect Transistors and Thermoelectric Devices. *Adv. Funct. Mater.* **2021**, *31* (30), 2102768. https://doi.org/10.1002/adfm.202102768.

Chapter 3 – Multifunctional DMBI Derivatives

3. Synthesis of multifunctional DMBI derivatives

The search for n-type dopants capable of establishing favorable interactions with the host semiconductor has focused largely on monofunctional DMBI derivatives. In this context, we define **monofunctional compounds** as those containing a **single** redox-active benzimidazoline unit, whereas multifunctional derivatives incorporate two or more such units within the same molecular framework. As shown in Chapter 2, these compounds, depending on the type of the substitution, can engage a variety of interactions with the semiconductor. However, by their nature, monofunctional derivatives can only generate a single ion pair with the host. This precludes one specific type of interaction that becomes possible only when **multifunctional dopants** are employed: **ionic crosslinking**. The presence of multiple redox-active centers in multifunctional dopants enable additional electron transfer events, allowing the formation of **multiple ion pairs** that result in crosslinks either within a single polymer chain or between distinct macromolecules. Such interactions are expected to suppress dopant diffusion, reinforce the integrity of doped films morphology, and enhance the long-term stability of multilayer device architectures.

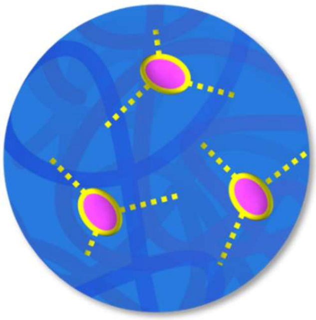

Figure 3.1
Illustration representing the ionic crosslinking formed by multifunctional dopants within the polymer matrix.

In the p-type doping context, the concept of ionic crosslinking can be found in the prototypical Poly(3,4-ethylenedioxythiophene):polystyrene sulfonate **(PEDOT:PSS)** formulation, one of the best performing system.[1,2] It is characterized by the positively charged conducting polymer

PEDOT associated with the negatively charged polyelectrolyte PSS, forming a dense network of electrostatic interactions. As a result, the material is insoluble in most common organic solvents and the dopant does not diffuse within the film, factors that are the basis of its outstanding stability and widespread technological adoption. Solvent resistance is a property of particular relevance in organic electronics field, where device fabrication on large scale relies on layer-by-layer solution-based processes and often suffers from the scarcity of truly orthogonal solvents, in other words solvents that can dissolve the depositing material without degrading the underlying layers.[3]

By similarity, Yang et al.[4] designed the poly(benzimidazobenzophenanthroline):poly(ethyleneimine) **(BBL:PEI)** couple as an n-type analogue of PEDOT:PSS. In this system, PEI dopes BBL through an acid-base reaction, which results in doping that is confined primarily to the surface and does not extend into the bulk of the polymer. Nevertheless, the films exhibit enhanced stability against solvents and environmental exposure. The conductivities achieved, however, remain significantly lower than those of PEDOT:PSS, a limitation that can be attributed to the **insulating nature** of PEI, which hinders efficient electron transport. Despite these drawbacks, the BBL:PEI system represents a promising step toward stable n-type doping strategies.

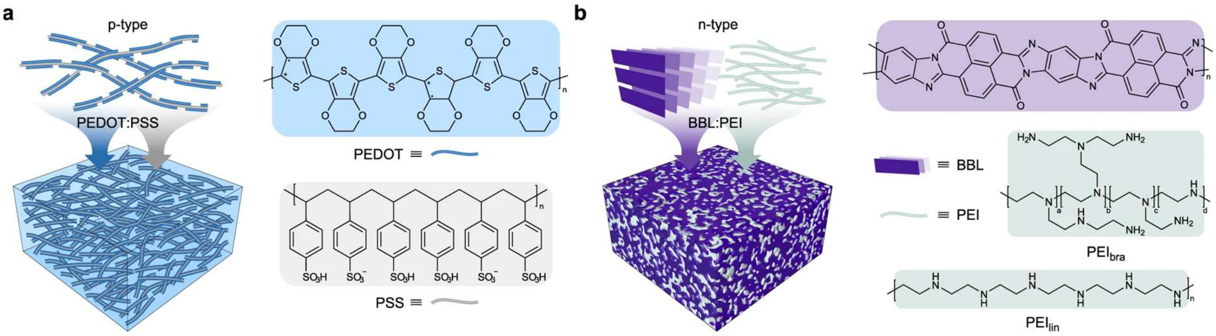

Figure 3.2
a) Schematics of the film structure and chemical structure of p-type PEDOT:PSS.
b) Schematics of the film structure and chemical structures of BBL and PEI, both linear (PEI_{lin}) and branched (PEI_{bra}) polymers.
Reproduced by the work of Yang et al.[4]. License CC BY 4.0.

Even for DMBI derivatives the ionic crosslink concept is not entirely new. Saeedifard et al.[5] first demonstrated it with **tetrakis-O-DMBI-H** (Figure 3.3), a dopant featuring four DMBI cores. Their results showed that ionic crosslinking indeed reduced dopant diffusion and, importantly, rendered the doped semiconductor films more resistant to solvent processing. Notably, while tetrakis-O-DMBI-H enhanced morphological stability, its use did not lead to conductivity values exceeding those obtained with the benchmark N-DMBI-H when measured under inert conditions immediately after doping. This suggests that crosslinking stabilizes the interface but does not necessarily increase the density of free charge carriers.

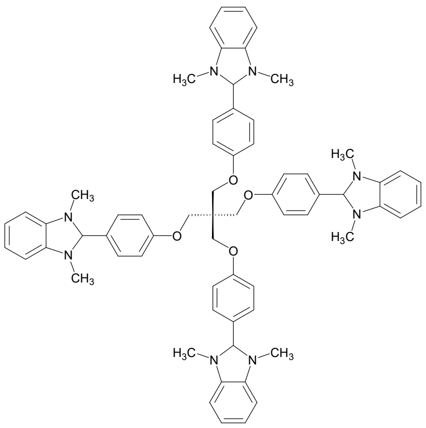

Figure 3.3
Chemical structure of tetrakis-O-DMBI-H.

In conclusion, the development of multifunctional n-type dopants is still at an **early stage**, yet the concept of ionic crosslinking stands out as a particularly appealing strategy. By introducing an additional level of interaction beyond single ion pairing, it offers a means to suppress dopant diffusion and increase the morphological stability of doped organic semiconductor films. In this sense, ionic crosslinking can be regarded as part of a **broader toolbox** of approaches aimed at controlling film microstructure and stability.

Aim of the work and pursued synthetic strategies

These considerations motivated the synthetic direction pursued in this phase of the project. In particular, our goal was to design multifunctional DMBI derivatives capable of integrating multiple redox-active sites within a single molecular or macromolecular framework, thereby enhancing structural stability, limiting dopant diffusion, and promoting controlled charge transport in doped organic semiconductors. To achieve this, three complementary synthetic strategies were developed, differing in their molecular architecture but sharing the same design rationale of controlled connectivity and multifunctionality.

The first approach represents the natural continuation of the work presented in Chapter 2, and specifically of the synthesis of the bifunctional dopant D8. In particular, the strategy that we pursued in these phase was complementary to the synthetic approach to D8: while D8 was obtained via Route 1* by condensing a dialdehyde with two o-phenylenediamine units (a, Figure 3.4), the new design reverses this logic, employing Route 2* to assemble an intermediate bearing two o-nitroaniline moieties that condense with aldehydes to yield aliphatically linked dimeric DMBI structures (b, Figure 3.4).

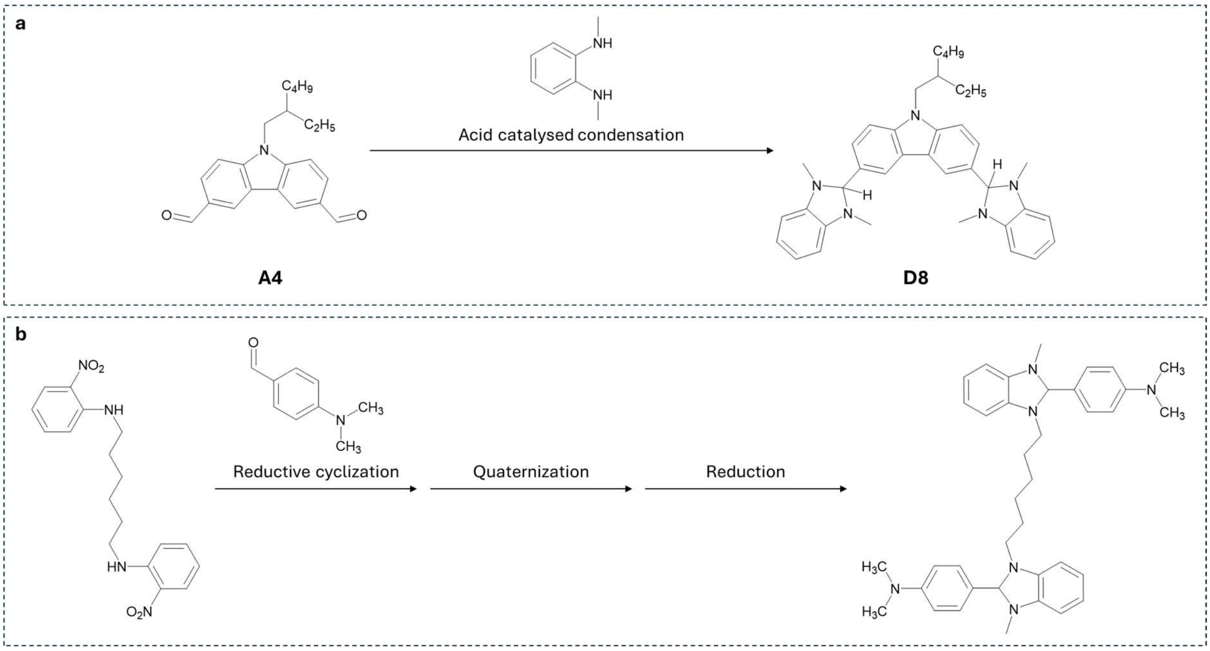

Figure 3.4
(a) Reaction scheme for the acid-catalyzed condensation between compound A4 and N,N'-dimethyl-o-phenylenediamine, affording compound D8.
(b) Conceptual synthetic approach toward aliphatically linked dimeric DMBI derivatives, applying route 2* to a precursor bearing two o-nitroaniline functionalities.

In parallel, a second and conceptually related strategy was developed, focused on the formation of **bis-carbamate dimers** derived from a **hydroxyl-functionalized DMBI intermediate**. In this route, the hydroxyl group served as a bridge for coupling with bifunctional electrophiles, such as diisocyanates, yielding **urethane-linked DMBI dimers**. This polyurethane-based approach offered a highly controllable and chemoselective framework for assembling multifunctional structures and could be readily extended to produce **oligomeric analogues** through the same reaction motif.

Finally, the exploration was broadened toward **polymeric DMBI systems**, embedding the redox-active DMBI units along a macromolecular backbone. The key insight underlying this effort was that, within the **Route 2*** framework, the synthesis of polymeric dopants necessarily requires passing through **benzimidazolium-type intermediates**, which are stable, isolable, and suitable for polymerization prior to their final reduction into benzimidazoline dopants. Consequently, the work in this section focused on developing effective strategies to obtain and process such **benzimidazolium-based polymers**, which can be formally regarded as **poly(ionic-liquid)-like precursors**. Three complementary routes were explored toward this goal:

1. **polyurethane-type polymers**, obtained by step-growth coupling between DMBI-based diols and diisocyanates;
2. **chain-growth polymerization** of DMBI monomers bearing acrylate groups,
3. **post-functionalization (grafting)** of preformed reactive polymers with benzimidazolium-containing DMBI units.

These strategies represent the different synthetic routes explored to extend the DMBI framework toward multifunctional systems, from dimers to polymeric precursors.

Even though only one novel bifunctional compound was successfully isolated in this work, we managed to clarify key synthetic limitations and provide useful insight for future developments.

3.1. Exploratory Work on Alkyl-linked Dimeric Dopants

The investigation of dimeric N-DMBI derivatives originated from the idea of linking two dopant units through an aliphatic bridge, with the goal of generating bifunctional systems capable of multiple and possibly cooperative doping interactions. In continuity with the synthetic strategies developed in Chapter 2, this approach required the preparation of ortho-nitroaniline derivatives bearing two reactive amino groups, designed to undergo intramolecular cyclization into benzimidazole units.

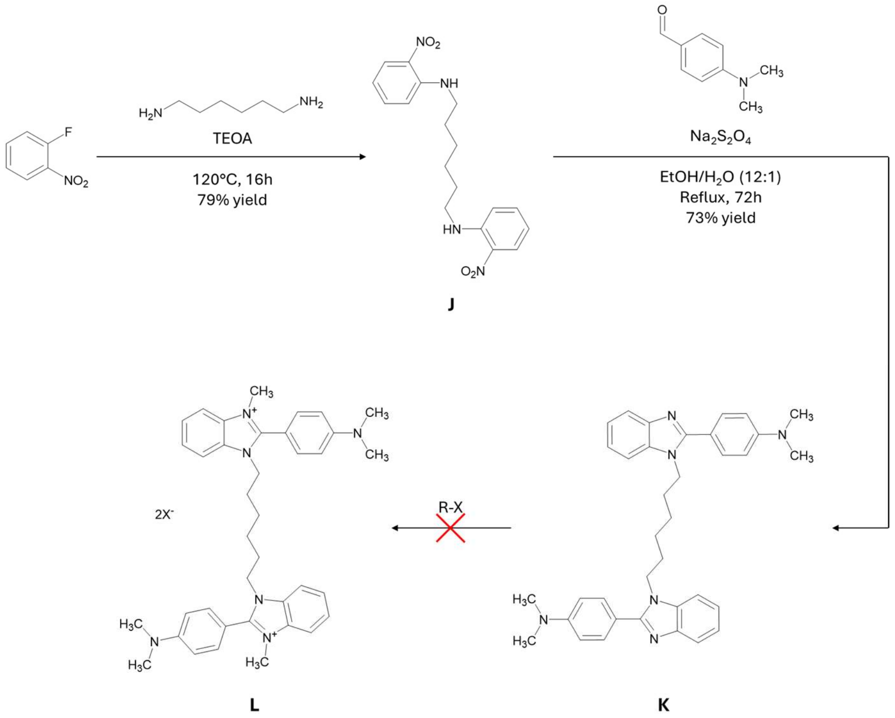

Figure 3.5
Reaction scheme of the approach adopted for the synthesis of a dimer of DMBI with an hexamethylene linker.

The synthetic pathway was explored through the preparation of the intermediate **J**, obtained by nucleophilic substitution of 2-fluoro-1-nitrobenzene with hexamethylenediamine, followed by condensation with p-dimethylaminobenzaldehyde to afford compound **K**, and subsequent methylation to yield the corresponding benzimidazolium salt **L**. Although the condensation proceeded efficiently, the quaternization step proved problematic: methylation with iodomethane resulted in incomplete conversion, while the use of a more reactive alkylating agent, i.e. dimethyl sulfate, led to undesired over-alkylation at the anilinic nitrogen. The resulting mixtures were difficult to purify, preventing the isolation of a clean product.

^{1}H NMR analysis of the crude reaction mixtures indicates preferential alkylation at the benzimidazoline core, consistent with competing alkylation pathways that hindered selective quaternization.

Due to these limitations, this route was not further developed. However, it confirmed the general feasibility of extending the DMBI synthetic framework to dimeric systems and provided new insights into the reactivity of multi-core intermediates. This experience motivated the adoption of a **more controlled coupling** strategy based on urethane chemistry, which will be discussed in the following sections.

3.2. The hydroxyl intermediate: a central building block

The synthetic strategy developed in this work relied on the introduction of a reactive functional group onto the DMBI framework, in order to enable the preparation of multifunctional dopants through subsequent coupling with bifunctional or polyfunctional reagents (e.g., isocyanates or acrylate derivatives). In this context, a hydroxyl-functionalized DMBI intermediate was identified early on as a pivotal building block. Its structural design, consisting of a benzimidazoline-type core bearing a pendant **hydroxyl-functionalized** side chain, provided optimal synthetic flexibility, serving as a versatile platform for the preparation of three different families of derivatives: (i) dimeric dopants, (ii) polyurethane-type linkages, and (iii) polyacrylate-based monomers and precursors. For clarity and continuity, the preparation of this intermediate is presented in a dedicated section prior to discussing downstream chemistry.

3.2.1. Experimental details

The hydroxyl-functionalized intermediate was synthesized following the general DMBI condensation and methylation sequence previously described in Figure 3.6. Condensation of p-dimethylaminobenzaldehyde with 2-[(2-nitrophenyl)amino]ethanol (HC Yellow 2) afforded the substituted benzimidazole (compound F14), which was subsequently methylated with iodomethane to yield the corresponding iodide salt (G12).

Finally, anion exchange was performed to replace iodide with a weakly coordinating and electrochemically inert counterion. The exchange was carried out in aqueous solution, initially at reflux then continued at room temeprature, using an ammonium fluorophosphate salt as the anion source, affording the final compound (G13) in high purity.

To verify the success of the exchange, ^{1}H and ^{19}F NMR spectra were recorded both for the sample alone and after addition of 2,2,2-trifluoroethanol, used as an **internal standard**. By correlating the integrals of the ^{19}F NMR signals of PF_6^- with those of the standard and cross-referencing them with the corresponding ^{1}H NMR integrals of the standard and the target compound, it was confirmed that the ratio between PF_6^- and the molecule matched the expected stoichiometry. The anion exchange was essential to ensure compatibility with future cyclic voltammetry and related electrochemical measurements, as the presence of iodide would otherwise interfere with the analyses.

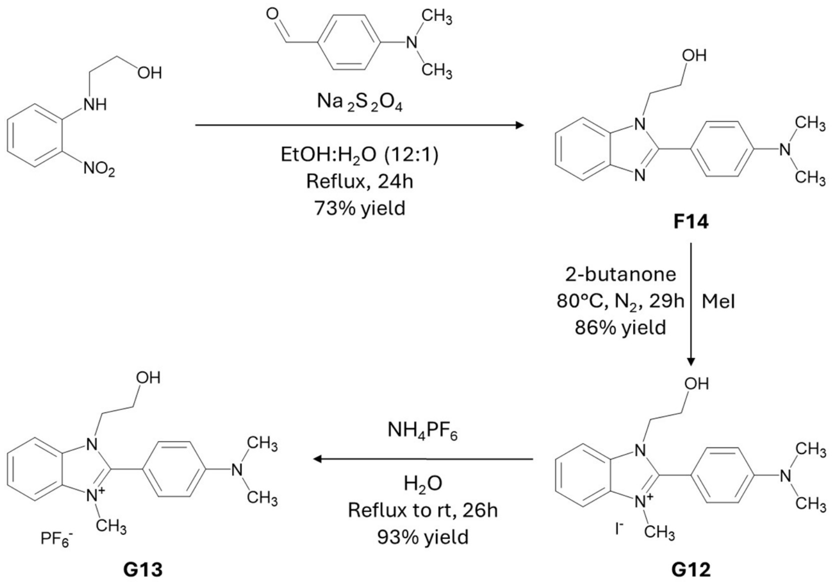

Figure 3.6
Reaction mechanism of the hydroxyl intermediate synthesis.

Among the hydroxyl-functionalized intermediates (F14, G12, and G13), the quaternized derivative G13 was adopted as the preferred starting material for the preparation of multifunctional dopants. Performing the quaternization prior to further functionalization was considered more practical, since post-alkylation of neutral precursors could cause **solubility issues** and **incomplete conversion**.

For these reasons, all subsequent derivatizations were carried out from the pre-alkylated hydroxyethyl intermediate unless otherwise specified.

3.3. Investigation into Bis-carbamate Dimers

Polyurethane synthesis is based on the addition reaction between a polyol and a polyisocyanate, which affords urethane (carbamate) linkages. Although mechanistically an addition reaction, this process follows a step-growth polymerization pathway that is inherently more controlled than the radical chain-growth mechanisms that characterize the free polymerization of vinyl and acrylate monomers.

The central advantage of polyurethane chemistry lies in its remarkable synthetic **versatility**, which originates from a highly efficient transformation: the reaction of an isocyanate with a hydroxyl group. Unlike radical polymerization, this chemistry requires no initiators, harsh conditions, or high temperatures, and it proceeds in a predictable and selective manner under relatively mild conditions.[6,7] Moreover, it offers several additional advantages:

- **Stoichiometric and structural control**: by varying the functionality of the reagents (monoalcohols, diols, triols, polyols, diisocyanates, or polyisocyanates), it is possible to access well-defined small molecules, linear oligomers, or highly cross-linked polymeric networks.
- **Functional group compatibility**: isocyanates react selectively with -OH (and -NH_2) groups, while tolerating many other substituents. In contrast, radical polymerizations of vinyl systems are often hindered by nucleophiles or electron-donating groups that interfere with propagation or induce side reactions.
- **Mild and predictable conditions**: urethane formation occurs readily, often without the need for strong catalysts or energy input, minimizing degradation pathways.
- **Component variability and structural flexibility**: the use of different diisocyanates (aromatic, aliphatic, or cycloaliphatic) and polyols (linear, branched, or functionalized) enables fine control over chain rigidity, polarity, and morphology.

Due to these characteristics, polyurethane chemistry was selected as a versatile and reliable framework for the synthesis of multifunctional DMBI derivatives.

As a first proof of concept, the approach was applied to the preparation of a simple and well-defined **bis-carbamate dimer**. This design served as a model system to demonstrate the feasibility of connecting two DMBI units through urethane linkages, while establishing a foundation for the later development of architectures with higher orders. Specifically, the hydroxyl-functionalized intermediate developed in this work (G13) was reacted with a diisocyanate to form a discrete dimeric structure (bis-carbamate benzimidazolium salt), that was ultimately reduced to form a dimeric dopant.

3.3.1. Dimerization

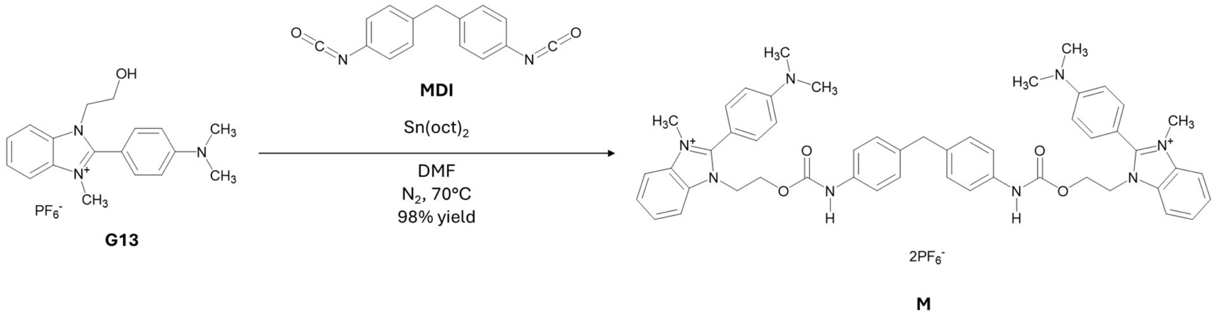

Figure 3.7
Reaction scheme of G13 addition with MDI to obtain a dicationic bis-carbamate dimer (M).

Our first benchmark was the coupling of **GP14** with 4,4'-methylenediphenyl diisocyanate (MDI). In DMF at 70 °C, the reaction proceeded smoothly to near-complete conversion, although in some cases a slight excess of MDI was required to drive the reaction to completion. The desired product could be isolated by precipitation upon addition of toluene, which induced the precipitation of a clean solid, then isolated by filtration. Nonetheless, DMF often proved difficult to remove completely, as traces tended to remain trapped within the precipitated solid. However, repeated washings with toluene allowed complete removal of the solvent, yielding the purified material suitable for characterization.

3.3.2. Reduction

After obtaining compound M, we turned our attention to its reductive conversion into the corresponding neutral DMBI-type dopant, by using different approaches. In all cases sodium borohydride ($NaBH_4$) was employed, while solvent, temperature, and work-up conditions critically determined the reaction outcomes, reported in Table 3.1.

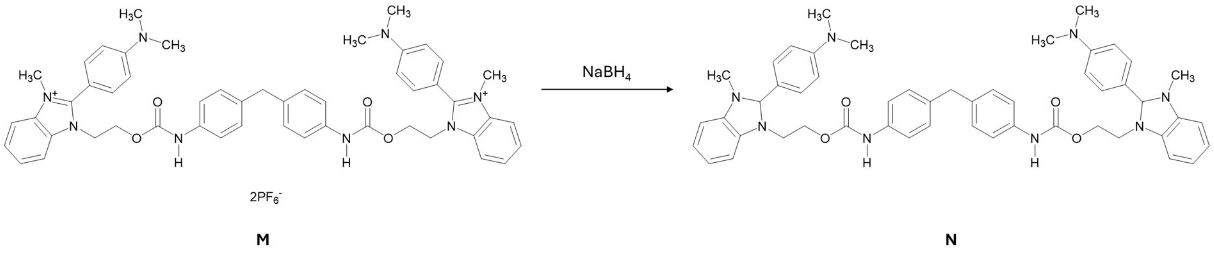

Figure 3.8
Reaction scheme of M reduction to obtain the bis-carbamate dopant N, subsequently called MDI-DMBI$_2$.

Table 3.1
Comparison between the different entries performed to reduce M with NaBH$_4$.

Entry	T (°C)	Solvents	Purification	Reaction time (minutes)	Yield (%)	Comments
1	0	MeOH	Liquid extractions under N$_2$	-	-	-
2	25	MeOH	Liquid extractions under N$_2$	30-120	25-30 per cycle	Incomplete conversion, multiple reduction cycles
3	0	MeOH:DMF 1:1	Precipitation and filtration	30	50	DMF removal problematic
4	0	MeOH:THF 1:1	Precipitation and filtration	30	55	-
5	25	Bulk + Al$_2$O$_3$ (traces of MeOH)	Liquid extractions under N$_2$	10-30	15-20 per cycle	Incomplete conversion, multiple reduction cycles

The first attempts, carried out in **neat methanol** at **0 °C** under ambient atmosphere, showed no detectable product within 30 minutes of reaction time. Performing the reduction at **room temperature** under an inert atmosphere enabled partial conversion, but the process was slow and consistently left unreacted starting material, leading to multiple reduction cycles. Product isolation was also complex, requiring repeated evaporations and extractions, and affording modest yields per reduction cycle.

To improve solubility and facilitate the reduction, methanol was combined with a more polar aprotic co-solvent, i.e. **DMF** (mixture 1:1 v/v MeOH/DMF).[8] Under these conditions, the reaction could be initiated and carried to completion at 0 °C, with clean isolation of the product upon quenching into water. However, in some runs, DMF promoted minor **side reactions**. A similar test using a MeOH/THF mixture gave comparable conversion but higher selectivity, providing a cleaner reaction path.

These comparative trials indicated that solvent polarity and proticity critically affected both the reaction rate and selectivity, guiding the optimization toward mixed MeOH/THF media. Finally, a mechanochemical protocol ($NaBH_4/Al_2O_3$ with catalytic MeOH), analogue to the one proposed by Tabane et al.[9], demonstrated that reduction could proceed under mild, solvent-minimized conditions, though with lower yields and no purification advantage.

As a conclusion, MeOH/THF conditions offered the best compromise between conversion, selectivity, and ease of work-up, establishing them as the optimal protocol.

3.3.3. Summary

The adoption of polyurethane-based chemistry proved to be a decisive step toward achieving well-defined molecular architectures with enhanced synthetic control. By exploiting the high reactivity and selectivity of the isocyanate-hydroxyl coupling, we **successfully** prepared bis-carbamate dimers from the hydroxyl-functionalized intermediate GP14 and 4,4'-methylenediphenyl diisocyanate (MDI). The optimized reduction of the resulting benzimidazolium precursor was carried out in a 1:1 MeOH/THF solvent mixture at 0 °C, conditions that ensured complete conversion and clean product precipitation upon quenching with water, affording the target compound in 54% yield. This protocol proved reproducible and selective, establishing a robust route toward the synthesis of benzimidazoline-based dopants.

The dimer we successfully synthesized, compound N, was designated as **MDI-DMBI$_2$**, a nomenclature that will be consistently adopted hereafter to clearly distinguish it from other derivatives and to provide a more informative terminology. Chapter 4 of this manuscript is entirely devoted to assessing the doping performance of MDI-DMBI$_2$ on semiconducting single-walled carbon nanotubes (s-SWCNTs) and on the polymer N2200.

As discussed at the end of Chapter 2, the introduction of alkyl substituents on the imidazoline nitrogens of DMBI derivatives has only a marginal effect on their electronic properties, with frontier molecular orbital (FMO) levels remaining essentially unchanged. For this reason, the determination of the FMO levels of MDI-DMBI$_2$ was not prioritized, as no substantial deviation from those of the benchmark N-DMBI was expected. Moreover, we plan to perform a complete thermal characterization of the compound.

3.4. Poly(ionic liquid)s: key intermediates for polymeric DMBI dopants

Benzimidazoline-based dopants, although often reported in the literature as air-stable species, are in fact rather **delicate compounds**, especially when dissolved in solution.
A paradigmatic example is N-DMBI, which readily undergoes oxidation: in protic solvents, it forms the cationic species DMBI$^+$, whereas in aprotic solvents (such as chloroform or toluene) it evolves into the neutral DMBI-ox form.[10,11]

Therefore, when aiming to synthesize polymers incorporating DMBI units, it is not feasible to employ synthetic routes where **benzimidazoline intermediates** are involved, as these species are unstable under typical reaction conditions.
A more reliable and cautious approach is to follow route 2* up to the formation of a **benzimidazolium salt**, which represents a stable and well-defined intermediate.
From this point, we developed a variation of route 2* in which the benzimidazolium salt is polymerized, yielding a polymeric intermediate that contains benzimidazolium repeating units. Finally, the synthetic pathway rejoins route 2* during the reduction step with sodium borohydride, which converts the benzimidazolium groups into their reduced benzimidazoline form, thus affording the final DMBI-functional polymeric dopant.

The key challenge of this process lies in obtaining and purifying the **polymeric intermediate**. Once the polymeric intermediate is obtained, the subsequent **reduction** with sodium borohydride is expected to proceed without difficulties, provided that both reagents are dissolved in the reaction medium. In contrast, **obtaining** the benzimidazolium-based polymeric intermediate may represent the true synthetic bottleneck, as its formation and isolation are not guaranteed and may require significant optimization.

The polymeric intermediate consists of repeating benzimidazolium units, forming a polycation whose overall charge is balanced by a mobile counter-anion. Due to structural features, it can be formally classified within the broad family of **poly(ionic liquids) (PILs).**
Although the strict definition of PILs requires that the starting monomers themselves be ionic liquids, the term is used here purely to provide a synthetic framework and contextual reference. [12,13]

Poly(ionic liquids) constitute a broad class of polymeric materials characterized by the presence of covalently tethered ionic groups along the polymer backbone.

Unlike ionic liquids, PILs are **not necessarily** liquid at room temperature: depending on their structural design, they can appear as soft gel-like substances or, more commonly, as solids.
From a synthetic point of view, PILs can be obtained either (i) by **polymerizing ionic monomers**, or (ii) by **chemical modification** of pre-formed polymers.[13,14]

In the first case, radical polymerization is the most widely used approach, applied to acrylate-, styrene-, or ethylene-based monomers functionalized with polymerizable groups. However, such polymerizations are often inhibited in the presence of **bulky substituents** or strong specific interactions, such as hydrogen bonding or Coulombic forces, where the latter are intrinsic to ionic liquid-like monomers.[15]
Alternative polymerization strategies have also been developed.
Among them, click chemistry, and in particular azide-alkyne cycloaddition, has established an entire class of materials known as **1,2,3-triazolium-based PILs (TPILs)**, which represent a well-studied subclass of poly(ionic liquids).[14,16,17] Other examples of alternative approaches include the **thiol-ene hydrotiolation** route, as demonstrated by Wang et al.[18], and the **polyurethane-type PILs** synthesized by Morozova et al.[19] through the reaction of ionic liquids with a diol functionality with various diisocyanates.

Regarding the **post-polymerization modification** of pre-formed polymers, two main synthetic strategies have been established for imidazolium-based PILs:[12,20,21]

1. **Grafting** of the ionic moiety on the polymeric backbone through reaction with a halogenated functionality present on the repeating unit;
2. **Alkylation** (quaternization) of polymers containing nucleophilic heterocycles such as imidazole, pyridine, or tertiary amines.

However, in these processes, complete quaternization of all the units is not guaranteed, as steric hindrance and limited accessibility often limit the extent of conversion.

3.4.1. Our strategy

Taking into account the strategies described in literature for the synthesis of PILs, we chose three different methods to prepare our polycationic polymeric intermediates.
Firstly, building on the successful synthesis of the MDI-DMBI$_2$ dimer, we adopted a polyurethane-based strategy to obtain benzimidazolium polycations by reacting anbenzimidazolium DMBI derivative bearing two hydroxyl functional groups with methylene diphenyl diisocyanate (MDI),

one of the most reactive diisocyanates.

Then, we explored the direct polymerization of an acrylate-functional intermediate derived from the hydroxyl intermediate (G14), and, as a complementary approach, we evaluated the grafting of the same hydroxylated intermediate onto **poly(acryloyl chloride)**, exploiting the high reactivity of its acyl chloride groups.

3.4.2. Investigation into Polyurethane Dopants

The success achieved in the synthesis of the dopant MDI-DMBI$_2$ encouraged us to extend the study to polymeric architectures derived from the same structural motif. To this scope, we aimed to synthesize an intermediate analogous to compound G13, but featuring two hydroxyl groups instead of one, in order to obtain a polyurethane by reaction with the diisocyanate MDI.

Our initial strategy towards the preparation of polyurethane-based dopants involved the modification of derivative **F15**, a DMBI precursor previously synthesized within the group, bearing two hydroxyethyl substituents on the anilinic nitrogen (see Figure 3.9).

However, attempted methylation of this compound under mild conditions resulted in a **hygroscopic and deliquescent material** that could not be purified or reliably characterized. This outcome was not attributed to the chemical instability of the benzimidazolium framework itself, but rather to **difficulties in isolating and purifying the product mixture**, which probably contained partially converted species.

Consequently, we modified the synthetic design and redirected our attention toward more robust precursors through two alternative pathways.

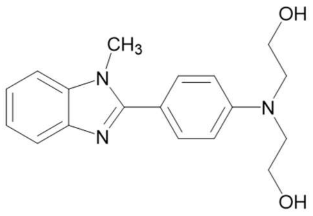

F15

Figure 3.9
Chemical structure of the di-hydroxyl intermediate already synthesized by our group (F15).

3.4.2.1. Pathway A

To circumvent the limitations encountered with F15, we targeted an alternative derivative bearing two hydroxyl substituents on the imidazolic nitrogens. The rationale was that, upon methylation, this scaffold could afford a benzimidazolium salt less prone to deliquescence than F15.

The first step was the synthesis of the o-nitro-aniline derivative **E3**, obtained in satisfactory yield through nucleophilic aromatic substitution with serinol. **E3** was then involved in a reductive cyclization with p-dimethyl benzaldehyde, leading to the benzimidazole **F16**. However, attempts to alkylate **F16** at the imidazolic nitrogen with iodomethane led to undesired **double alkylation**, namely alkylation affecting both the imidazolic and the anilinic nitrogen, despite the mild nature of the electrophile. This result demonstrated the insufficient **steric protection** of the anilinic site.

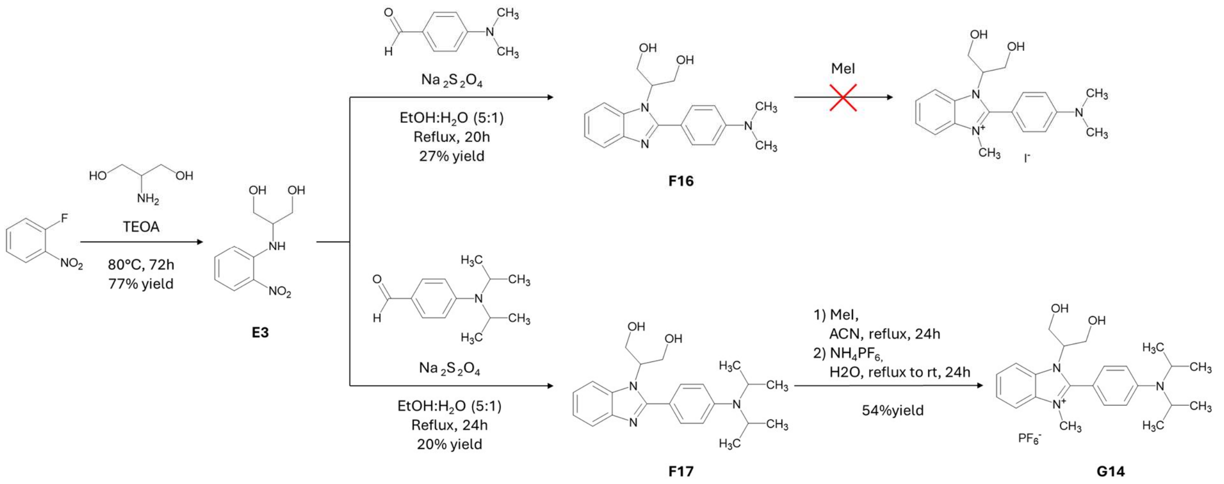

Figure 3.10
Reaction mechanism relative to the synthesis of the o-nitroaniline E3, followed by its condensation with p-dimethylamino-benzaldheyde, leading to F16, and p-diisopropylamino-benzaldheyde, leading to F17. Ultimately, the alkylation of the substituted benzimidazoles is represented.

In response, we pursued an alternative design in which a bulky substituent, i.e. two isopropyl groups, was introduced at the anilinic nitrogen to suppress its nucleophilicity. This strategy led to the synthesis of **F17**, which was subsequently methylated with iodomethane at the imidazolic nitrogen to afford the corresponding benzimidazolium salt. Even though we did not register the formation of the double-alkylated by-product, the product was obtained together with several impurities. In this case, we performed an anion exchange, replacing iodide with hexafluorophosphate, to obtain compound G14. The replacement of the hydrophilic halide anion with the more hydrophobic PF_6^- significantly altered the solubility of the compound.[14] This change enabled the selective precipitation and isolation of the desired product from aqueous solution, effectively separating it from water-soluble impurities. Such a strategy is widely employed in the synthesis and purification of ionic liquids and related ionic compounds.[14]

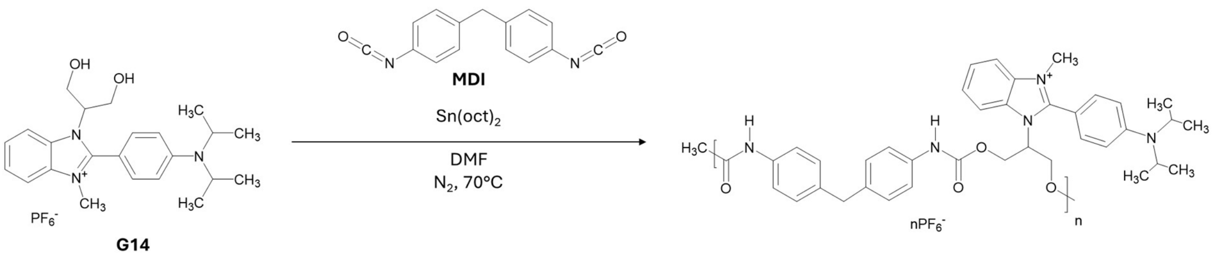

Figure 3.11
Reaction mechanism of G14 polymerization with MDI.

Subsequently, G14 reacted with MDI under tin(II)-catalyzed conditions to afford a polyurethane oligomer. The stoichiometry of the two reagents was set at a 1.25:1 diol-to-diisocyanate ratio, this ratio was chosen to yield OH-terminated chains with an average degree of polymerization of **9**. After 17 h, the reaction flask was dried, affording a solid that was sequentially washed with toluene and diethyl ether, and subsequently dried under vacuum at 65 °C until constant weight was reached.

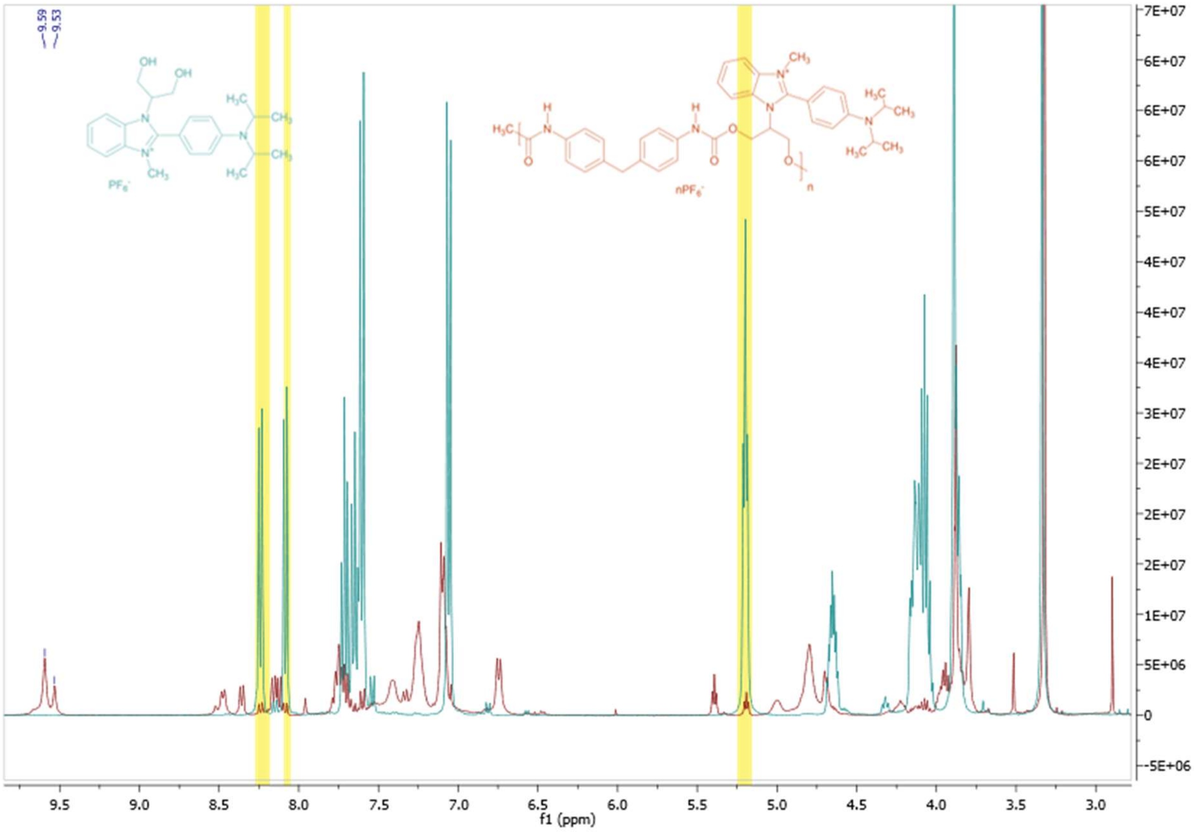

Figure 3.12
Superimposition of the 1H-NMR in DMSO-d$_6$ spectra of compound G14 (blue) and the polymerization product (red). Some of the peaks that the two spectra share are highlighted.

^{1}H NMR spectroscopy of the solid revealed the presence of multiple side products (see the superimposition of the 1H NMR spectra of the di-hydroxyl intermediate and the obtained polymeric material in Figure 3.12.

Nonetheless, two diagnostic resonances at 9.59 ppm and 9.53 ppm, attributable to the urethane NH protons, provide strong evidence for the formation of urethane linkages and thus of polymeric chains.

At the same time, **minor side products may be present**, although their nature could be precisely confirmed from the available data. We hypothesized that these impurities could be related to **residual MDI** and to **secondary condensation products** such as ureas, allophanates, or biurets, which can arise from side reactions of isocyanate groups under the employed conditions. In addition, residual signals associated with the starting material G14 (highlighted in Figure 3.12.) were still detectable.

In a conventional step-growth polymerization, complete consumption of the monomer is expected from the early stages of the polymerization, as chain propagation proceeds in a controlled manner, it is therefore unusual that signals attributable to the monomer are still present. However, this outcome is coherent with the conclusion of Ghoreishi et al.[22], who have reported that the reaction of monomers leading to polyurethanes, in the **presence of a catalyst**, may proceed through either an uncatalyzed step-growth pathway or **a catalyzed chain-growth mechanism**.

The abundance of impurities hindered reliable determination of chain length. An attempt to purify the crude product by washing with diethyl ether proved ineffective, and no alternative purification strategies were successfully implemented. Due to the insufficient purity of the product, **no reduction was attempted**, as the presence of unidentified by-products would have rendered the subsequent step unreliable.

3.4.2.2. Pathway B

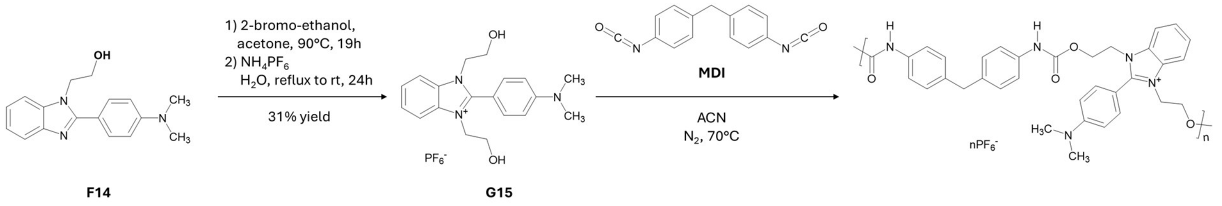

Figure 3.13
Reaction scheme of the synthesis of a symmetrical intermediate bearing two -OH functionalities on the imidazolic core. Followed by its polymerization with MDI.

Approximately simultaneously to pathway A, a second approach was developed starting from the hydroxyl intermediate **F14**. Alkylation with 2-bromoethanol, couple with ion exchange with NH_4PF_6, performed to purify the intermediate and followed by flash chromatography, afforded the di-hydroxyl species **G15**. This intermediate was subsequently reacted with MDI under **catalyst-free conditions**, to be sure that the monomer is completely consumed at the end of the reaction, and using **acetonitrile** as the solvent, while maintaining a 1.25:1 diol-to-diisocyanate ratio.

After 24 h, the reaction flask was dried under reduced pressure, yielding a solid that was washed with n-heptane and further dried under vacuum at 65 °C until constant weight was achieved.

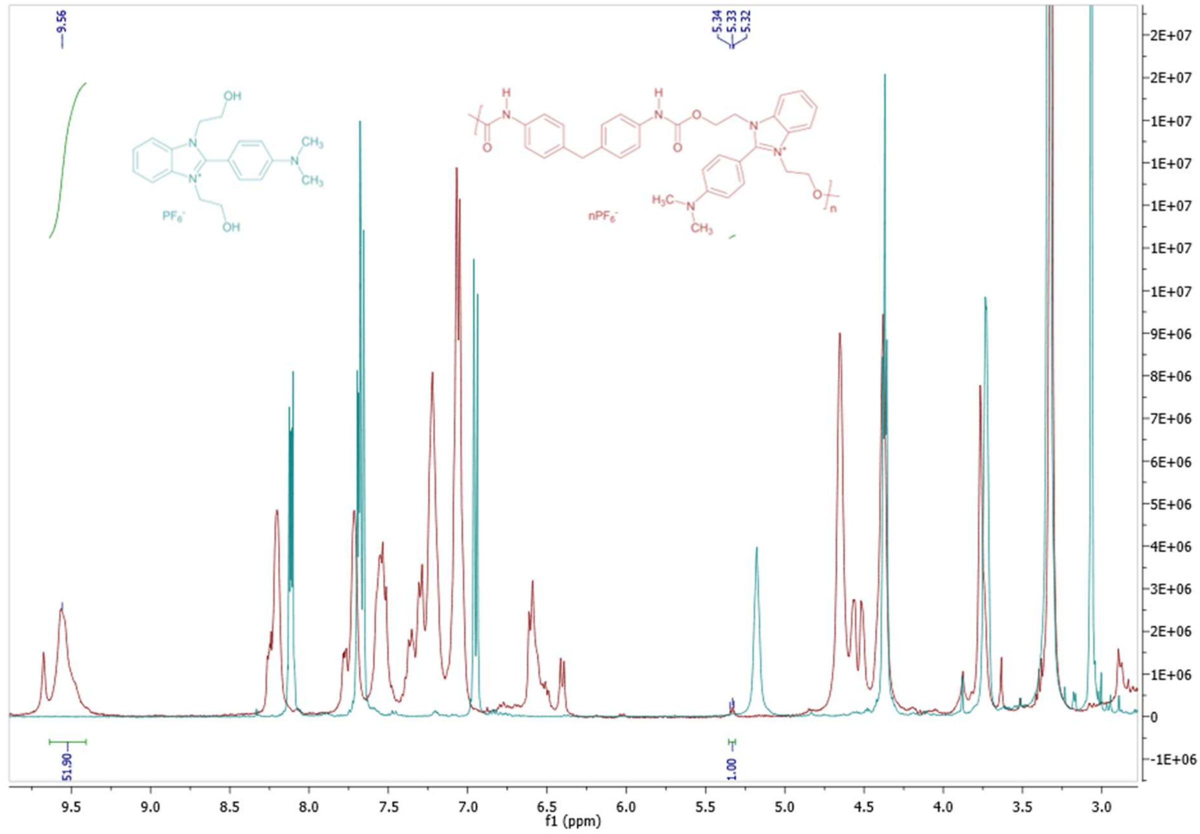

Figure 3.14
Superposition of the 1H-NMR spectra of compound G15 (blue) and its polymerization product (red). Nootably, no significative signals pertaining to the monomer G15 are found in the polymerization product.

^{1}H NMR analysis of the product confirmed the formation of urethane linkages (signals at 9.56 ppm) and showed the complete consumption of the benzimidazolium diol precursor, indicating that the reaction had proceeded even in the absence of a catalyst (see Figure 3.14).

However, the presence of multiple signals observed at similar frequencies suggested the presence of chemically similar environments. This description is coherent, but does not completely prove, the formation of of a complex mixture of oligomeric species of varying chain length and the presence of minor side products derived from isocyanate chemistry (e.g., residual MDI and traces of urea-type species).

Several purification attempts using different solvents (ethanol, anisole, dimethyl sulfoxide, 1,4-dioxane, ethyl acetate, water, and toluene) were ineffective, likely due to the similar solubility of the oligomeric components.

In conclusion, the obtained material can be described as an **urethane-rich product**, containing small amounts of off-spec species, with no evidence of unreacted starting diol.

3.4.2.3. Summary

We have developed two approaches to obtain polyurethane-based chains derived from DMBI-like salts bearing two hydroxyl functionalities. Both approaches confirmed the feasibility of forming urethane linkages, validating the underlying chemical design. Among them, the catalyst-free route in acetonitrile (pathway B) proved to be superior, as it ensured full conversion of the diol precursor under mild conditions.

Despite these advances, the main limitation remains the **isolation and purification** of the resulting oligomers. The coexistence of multiple hydrogen-bonding sites and ionic functionalities leads to strong intermolecular interactions and nearly identical solubility profiles, preventing effective separation of individual species.

Therefore, future work will focus on strategies to **improve the woorkability of the cationic framework**, mainly by developing alternative reaction conditions that facilitate the selective isolation of the desired oligomeric fractions.

3.4.3. Acrylate Monomers as Precursors for Multifunctional Dopants

To obtain a monomer suitable for free-radical polymerization, the acrylate precursor **G16** was synthesized by functionalizing the hydroxylated intermediate **G13** with **acryloyl chloride** under carefully controlled anhydrous conditions. By ^{1}H NMR spectroscopy we have confirmed the presence of the acrylate group in the product, and the absence of the hydroxyl hydrogen.

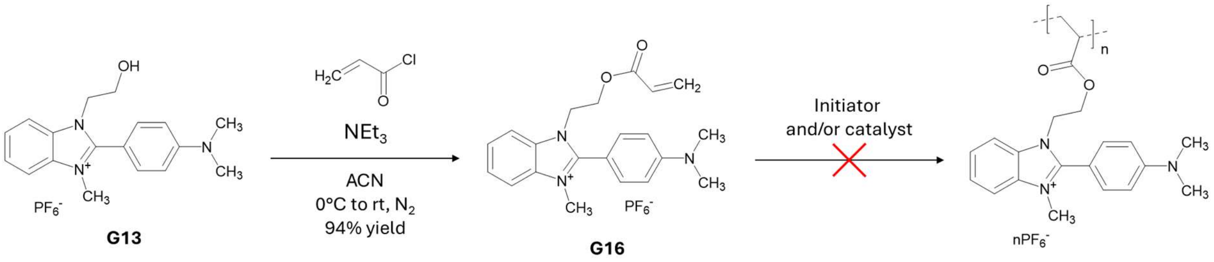

Figure 3.15
Reaction scheme for the synthesis of the acrylate precursor (G16) and the attempted polymerization toward a polyacrylate.

Cobalt-mediated radical polymerization (CMRP) of the acrylate derivative **G16** was first explored, following the conditions reported by **Debuigne and co-workers** for the polymerization of imidazolium-based vinyl monomers.[23]

This approach was particularly appealing, as CMRP represents a living radical polymerization technique capable of providing excellent control over chain length and dispersity, thus potentially enabling the synthesis of **monodisperse ionic polymers** from this type of cationic precursor.

The reaction was carried out under nitrogen atmosphere using **$Co(acac)_2$** (4.4 mol%) as catalyst and **t-BuOOH** as an initiator. A small amount of **anhydrous acetonitrile** was added to ensure solubilization of the ionic monomer, together with degassed water to reproduce the biphasic conditions described in the reference procedure. The mixture was heated to **80 °C** and monitored by ^{1}H NMR spectroscopy over time.

After 20 h, the spectrum of the reaction mixture showed no significant changes relative to the starting monomer, except for a slight broadening of some signals. Even after 42 h, **no polymeric material** could be detected, indicating that cobalt-mediated polymerization did not proceed under these conditions.

To clarify whether the lack of reactivity originated from cobalt deactivation or from the intrinsic nature of the monomer, a **classic free-radical polymerization (FRP)** was subsequently attempted. The reaction was carried out under nitrogen atmosphere using **AIBN** (2.7 mol%) as initiator and **anhydrous, degassed DMF** as solvent. The mixture was maintained at 90 **°C for 72 h**, but **no formation of polymeric material** was detected by ^{1}H NMR analysis, confirming the complete unreactivity of the acrylate monomer under radical conditions.

Collectively, these results clearly demonstrate that the acrylate moiety of G16 is intrinsically unreactive toward radical polymerization, regardless of whether a conventional or cobalt-mediated system is employed. This behavior likely arises from the combination of three factors: the pronounced steric hindrance of the monomer, its ionic nature as a benzimidazolium salt, and a possible interaction between the benzimidazolium core and the radical species, which collectively can deactivate the double bond and suppress radical addition.[24]

Consequently, we decided to pursue the **complementary approach** of **post-functionalizing preformed polymers** with benzimidazolium-based DMBI precursors, thereby introducing the DMBI-like unit through chemical modification rather than direct polymerization of the ionic monomer.

3.4.4. Polyacryloyl chloride functionalization

As an alternative approach, **poly(acryloyl chloride)** was investigated as a reactive backbone for post-functionalization with the hydroxylated benzimidazolium intermediate G13.

Traditionally, two synthetic routes have been reported for the preparation of this polymer:

- **(Path A)** the **radical polymerization of acryloyl chloride** monomer using AIBN as initiator, and
- **(Path B)** the **conversion of sodium polyacrylate** into the corresponding acyl chloride polymer through reaction with thionyl chloride.[25,26]

Both strategies were evaluated in this work (see Figure 3.16).

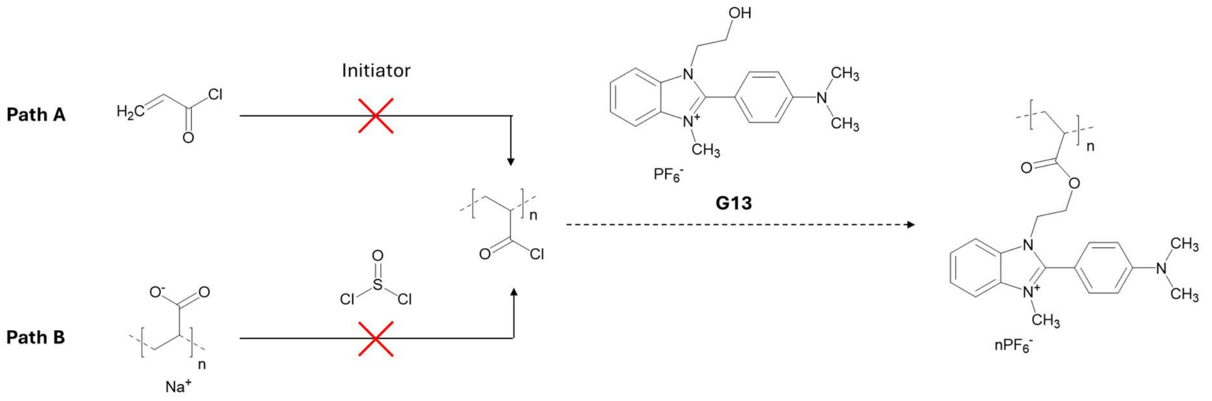

Figure 3.16
Reaction scheme of the synthesis of polyacryloyl chloride starting from the monomer, acryloyl chloride (path A), and starting from the commercial sodium polyacrylate (path B), followed by the functionalization of the chain with compound G13.

3.4.4.1. Path A

Polymerization of acryloyl chloride

The polymerization of acryloyl chloride was attempted following the procedure reported by Buruiana et al.[26], employing AIBN as radical initiator in anhydrous 1,4-dioxane under nitrogen atmosphere at 70 °C for 72 h. After the addition of *n*-hexane, a white solid was isolated and dried under vacuum.

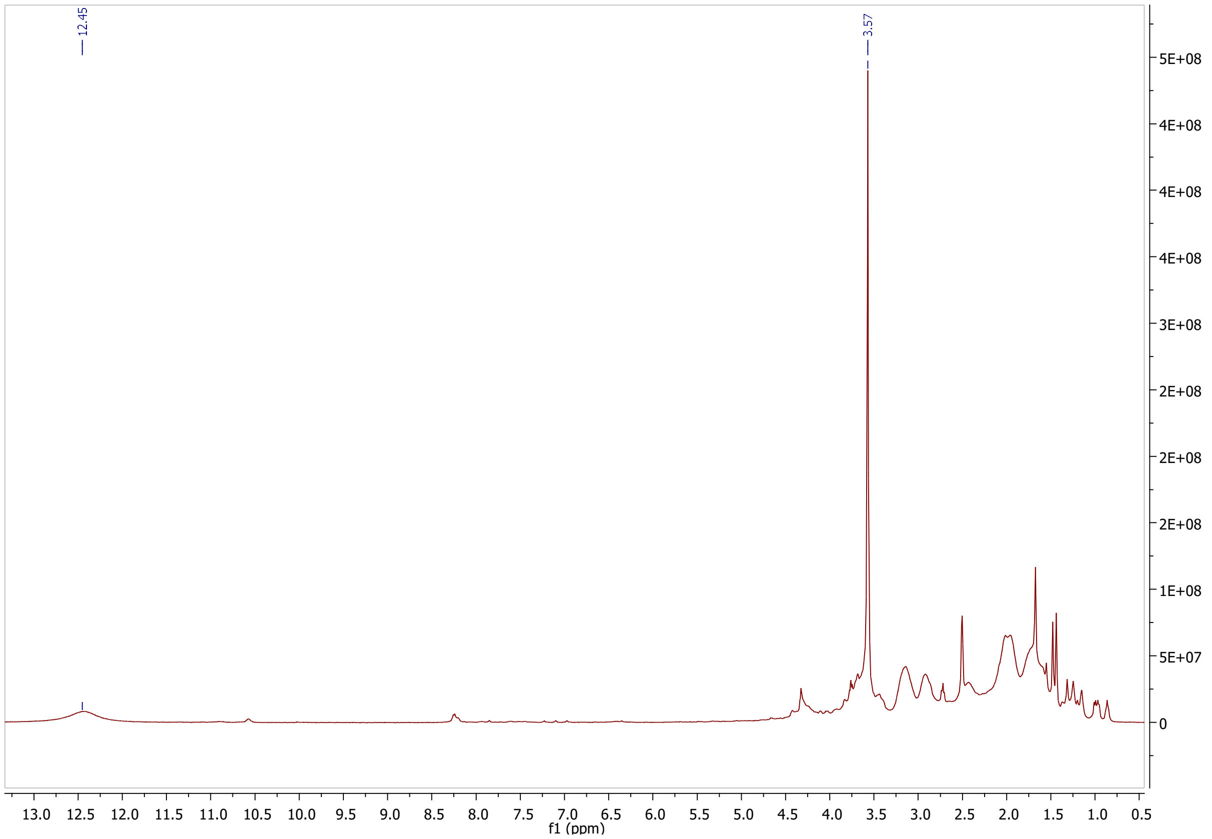

Figure 3.17
^{1}H NMR spectrum (DMSO-d_6) of the polymeric material obtained by the performed polymerization of acryloyl chloride.

The ^{1}H NMR spectrum of the obtained material (Figure 3.17) showed no vinyl resonances (δ = 5.8-6.5 ppm) and displayed a broad signal at 12.5 ppm, attributed to carboxylic **acid protons**. The remaining signals appeared as broad peaks between approximately 4.5 ppm and 1.0 ppm, consistent with the presence of an aliphatic polymeric backbone. The signal at 3.57 ppm was identified as residual solvent (1,4-dioxane).

The data suggested that a polymeric material was indeed obtained. However, it may have undergone **extensive hydrolysis**, making it unsuitable for further use. Alternatively, the observed spectrum could result from partial hydrolysis to poly(acrylic acid), occurring during NMR sample preparation due to the well-known **moisture sensitivity of acryloyl chloride**.

Functionalization of the obtained polymeric material

To assess whether the isolated polymer retained **any reactive acyl chloride** functionalities, the material was subsequently reacted with the hydroxylated intermediate G13 under anhydrous conditions in the presence of triethylamine.

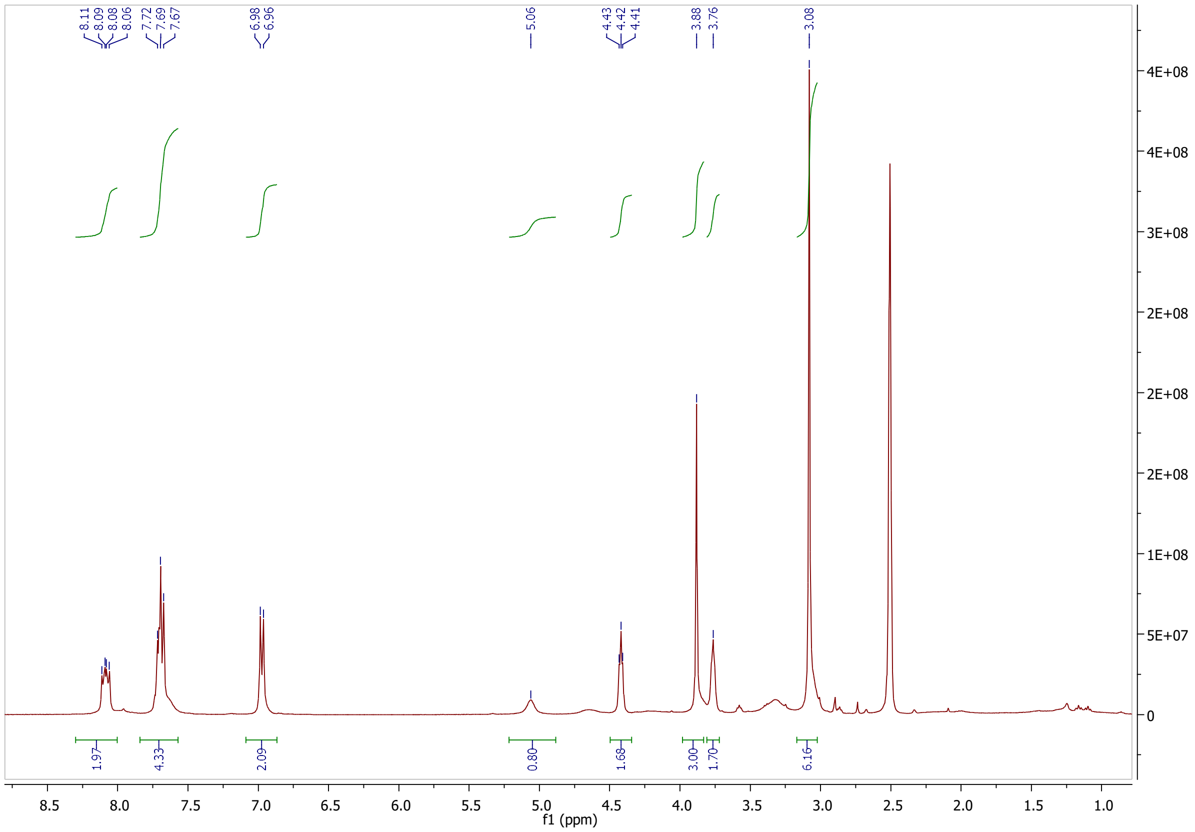

Figure 3.18
^{1}H NMR spectrum (DMSO-d_6) of the solid obtained from the reaction between the polymeric material and G13. Notably, the signals associated with the former species are much less intense than those of the hydroxylated intermediate G13. All integrated and labeled resonances correspond to G13.

The resulting ^{1}H NMR spectrum (Figure 3.18) showed no new resonances relative to the reagents' signals, except for **minor integration deviations**, it matched their superposition. In particular, the signals corresponding to the two nonequivalent methylene groups of the ethylene spacer in G13, N-CH_2- (4.42 ppm) and CH_2-O- (3.76 ppm), integrated to 1.7 H each instead of 2 H, while the hydroxyl proton at 5.06 ppm integrated to 0.8 H instead of 1H. These variations suggest that a small fraction of hydroxyl groups may have reacted, but the overall degree of functionalization was **negligible**, coherent with the loss of acyl chloride functionality in the polymer backbone during the previously performed polymerization.

3.4.4.2. Path B

In a complementary approach, we attempted at **converting** sodium polyacrylate, which was readily available in the laboratory, into poly(acryloyl chloride) via reaction with thionyl chloride. Then, we did not isolate the product but we directly made it react with G13 under anhydrous conditions in the presence of triethylamine.

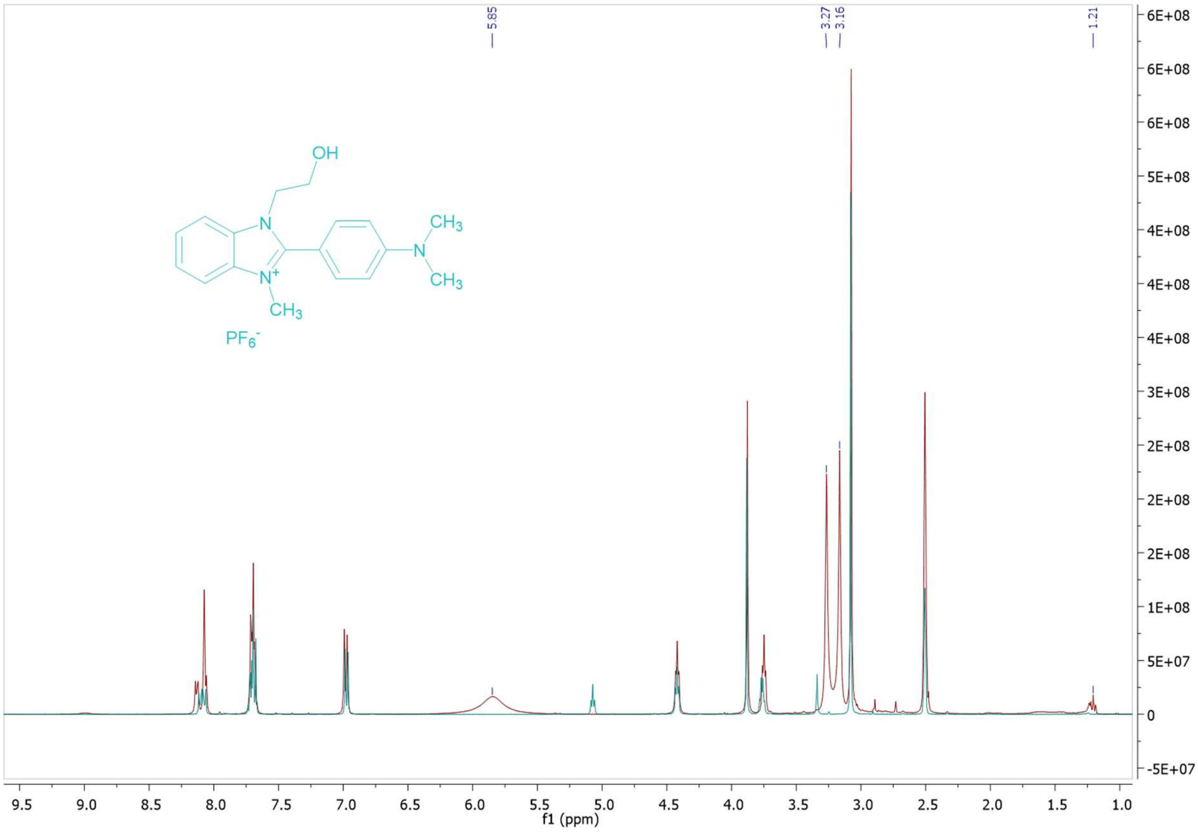

Figure 3.19
Superposition of the ^1H NMR spectra (DMSO-d_6) of the hydroxyl intermediate G13 and the solid obtained by the reaction of the same species with the supposed poly(acryloyl chloride) obtained from sodium poly(acrylate).

The ^1H NMR spectrum of the product of the grafting reaction (Figure 3.19) was essentially identical to that of the sole hydroxylated precursor, except for two signals at 3.27 and 3.16 ppm. These are assigned to residual **H_2O/MeOH** (in DMSO-d_6) and to the CH_2 protons of triethylammonium (**Et_3NH^+**), respectively. At the same time a faint triplet at 1.2-1.3 ppm is coherent with the presence of the Et_3NH^+ methyl group.

Moreover, the broad resonance at 5.85 ppm, is consistent with the presence in trace of **acrylate-type** small molecules. No new resonances indicative of grafting were observed.

It is therefore possible that the reaction of sodium polyacrylate with thionyl chloride ($SOCl_2$) was inefficient. In fact, this reagent is classically effective for **carboxylic acids** (not their carboxylate salts). Moreover, carboxylate salts readily react with acyl chlorides to form **anhydrides,** providing a competing pathway rather than clean activation.[27] These limitations, combined with the unverified nature of the polymeric reagent, are likely responsible for the **absence of detectable grafting** in the subsequent reaction with G13.

3.4.4.3. Summary

Two acrylic-based strategies were explored to obtain functional polymeric backbones suitable for the incorporation of benzimidazolium-type dopant units.

The acrylate monomer G15, derived from G13, was tested under both **cobalt-mediated** and **free-radical polymerization** conditions, but no polymer formation was observed, likely due to the combined effects of steric hindrance, the ionic nature of the benzimidazolium salt, and possible interaction of its extended aromatic core with radical species, which collectively suppress radical propagation. However, this limitation may be specific to radical initiation, and the acrylate intermediate could still participate in alternative polymerization routes, such as **thiol-ene click chemistry**, which represents an outlook of this project.

In parallel, **poly(acryloyl chloride)** was evaluated as a reactive polymer for post-functionalization, but both its direct radical polymerization and its preparation from **sodium polyacrylate** proved unsatisfactory. The main issue appears to be its **excessive reactivity and instability**, indeed, acyl chloride groups on acrylic backbones are known to be highly susceptible to hydrolysis and side reactions that hinder controlled grafting.[28,29]

Future efforts will therefore focus on identifying **more stable and tunable polymer backbones** capable of undergoing efficient grafting reactions.

3.5. Conclusion

This chapter explored the synthesis of **multifunctional DMBI-based dopants**, from dimeric to oligomeric and polymeric architectures. Each step provided original insight into the reactivity and limitations of this molecular framework.

The **hydroxyl-functionalized intermediate** G13 proved to be a key intermediate, enabling three main synthetic directions to our targets: the formation of bis-carbamate dimers, the development of polyurethane-type oligomers, and the preparation of acrylate derivatives for potential polymeric dopants.

Among these, **polyurethane chemistry** proved the most effective, leading to the successful synthesis of the bis-carbamate dimer MDI-DMBI$_2$ and confirming the potential of urethane coupling for producing multifunctional structures. However, the extension of this chemistry to oligomers was hindered by purification difficulties and product heterogeneity.

Acrylate-based strategies were less successful. The **acrylate monomer G16** showed no polymerization activity under either cobalt-mediated or conventional radical conditions, likely due to steric and ionic effects associated with the benzimidazolium core. **Poly(acryloyl chloride)**, on the other hand, was too reactive and unstable, undergoing rapid hydrolysis and preventing controlled grafting.

In summary, polyurethane chemistry stands out as the most robust and selective route for constructing DMBI-based multifunctional systems. Future work should focus on improving the manageability of these **cationic intermediates** and exploring alternative coupling reactions, such **as thiol-ene chemistry on acrylate intermediates**.

3.6. Experimental Section

3.6.1. Synthetic procedures

Reagents were purchased from TCI, BLD pharm, Sigma-Aldrich and Fluorochem. Solvents were bought by Merck, Carlo-Erba and Acros, and used as received unless otherwise stated.

Composition of solvent mixtures are indicated as volume/volume ratios. Melting points were determined using a Buchi M-560 apparatus. Solution Nuclear Magnetic Resonance (NMR) spectra were acquired with a Bruker Avance 400 NEO Spectrometer. For ^{1}H NMR of known derivatives, only chemical shifts are indicated.

3.6.1.1. Synthesis of Dimeric Dopants

Synthesis of compound J

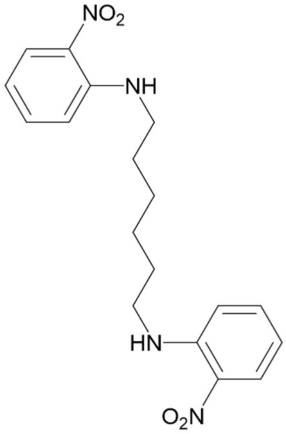

2-Fluoro-1-nitrobenzene (2.247 g, 15.9 mmol), **hexane-1,6-diamine** (0.827 g, 7.12 mmol), and triethanolamine (TEOA, 2.179 g, 14.6 mmol) are added to a 50 mL round-bottom flask. The mixture is stirred and heated to 120 °C. The reaction progress is monitored by TLC using a DCM:AcOEt (1:1) eluent mixture. After 16 h, the reaction is complete. The flask is cooled to room temperature, and water (30 mL) and HCl (37% w/w) are added until the pH reaches approximately 2.0, resulting in the formation of a white precipitate. The solid is collected by filtration on a Hirsch funnel and washed with aqueous HCl (0.2 M, 10 mL). The solid is then refluxed in MeOH (6 mL), filtered, and washed with additional MeOH (10 mL). The resulting solid is dried under vacuum in an oven at 65 °C to constant weight, affording **J** as a white solid (2.030 g, 5.66 mmol, 79% yield). mp 110-112°C.

^{1}H NMR (400 MHz, DMSO-d$_6$): d [ppm] 8.11 (t, J = 5.00 Hz, 2H), 8.05 (d, J = 7.7 Hz, 2H), 7.52 (t, 7.5 Hz, 2H), 7.04 (d, J = 8.7 Hz, 2H), 6.67 (t, J = 7.7 Hz, 2H), 3.34 (q, J = 6.6 Hz, 4H), 1.65 (q, J = 6.2 Hz, 4H), 1.48-1.38 (4H).

Synthesis of compound K

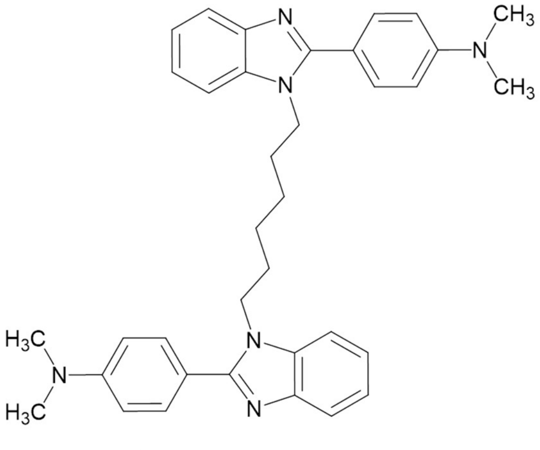

Compound J (502 mg, 1.40 mmol), **4-dimethylamino-benzaldehyde** (420 mg, 2.815 mmol), sodium dithionite ($Na_2S_2O_4$, 1.544 g, 7.54 mmol), EtOH (3.35 mL), and H_2O (0.3 mL) are added to a 50 mL round-bottom flask. The mixture is heated to reflux under stirring, and the reaction progress is monitored by TLC using a DCM:AcOEt (1:1) eluent mixture. After 72 h, the reaction is complete. Aqueous NH_4OH solution (3% v/v, 20 mL) is added to induce precipitation of a white solid. The solid is collected by filtration through a fritted funnel and dried under vacuum at 65 °C to constant weight (722 mg). The crude solid is washed with Et_2O (10 mL), filtered, and dried again under vacuum at 65 °C to afford **K** as a white solid (567 mg, 73% yield). The ^1H-NMR spectrum confirms the formation of the target compound with approximately 3% impurities.

^{1}H NMR (400 MHz, $CHCl_3$-d): d [ppm] 7.83-7.50 (m,2H), 7.57 (d, J = 8.8 Hz, 4H), 7.32-7.22 (m, 6H), 6.76 (d, J = 8.8 Hz, 4H), 4.17 (t, J = 7.51 Hz, 4H), 3.01 (s, 12H), 1.80-1.69 (m, 4H), 1.24-1.14 (m, 4H).

^{13}C NMR (100 MHz, $CHCl_3$-d): d [ppm] 154.36, 151.15, 142.77, 135.54, 130.38, 130.21, 122.18, 122.13, 119.34, 117.2, 112.03, 111.80, 109.75, 44.52, 40.18, 29.53, 26.23, 26.17

3.6.1.2. Synthesis of the hydroxyl intermediate

Synthesis of compound F14

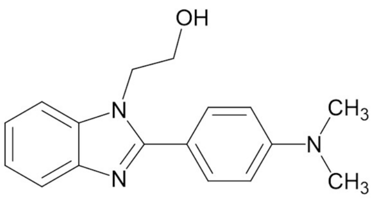

2-((2-Nitrophenyl)amino)ethanol (5.003 g, 27.5 mmol), **4-dimethylaminobenzaldehyde** (4.090 g, 27.4 mmol) and sodium dithionite ($Na_2S_2O_4$, 15.172 g, 74.1 mmol) are placed in a 100 mL round-bottom flask equipped with a magnetic stir bar. Ethanol (33 mL) and water (2.7 mL) are added and the mixture is heated to reflux under stirring. The reaction progress is monitored by TLC (DCM:EtOAc 9:1). After 24 h the reaction is judged complete by TLC. The mixture is cooled to room temperature and a 3% (v/v) aqueous NH_4OH solution (70 mL) is added, causing the formation of a yellow precipitate. The precipitate is collected by filtration on a Hirsch funnel, washed with NH_4OH (3% v/v, 100 mL) and then with water, and dried in an oven at 65 °C to constant weight. The product is obtained as a yellow crystalline solid (5.651 g, 20.0 mmol, 73% yield). mp 180–181 ° C.

^{1}H NMR (400 MHz, DMSO-d$_6$): δ[ppm] 7.74 (d, J = 8.9 Hz, 2H), 7.63-7.56 (m, 2H), 7.24-7.17 (m, 2H), 6.84 (d, J =9.0 Hz, 2 Hz), 5.09 (t, J =5.3 Hz, 1H), 4.32 (t, J = 5.86 Hz, 2H), 3.80 (q, J = 5.7 Hz, 2H), 3.00 (s, 6H).

^{13}C NMR (100 MHz, DMSO-d$_6$): δ[ppm] 154.72,151.42, 143.28, 136.58, 130.87, 122.01, 121.99, 118.93, 117.89, 112.08, 11.25, 59.83, 47.22, 40.28.

Synthesis of compound G12

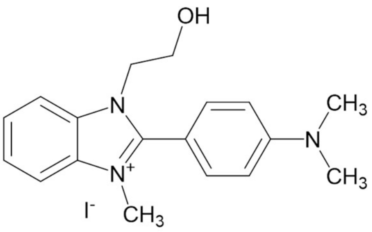

Derivative F14 (1.001 g, 3.56 mmol) is added to a round-bottom flask. The system is put under nitrogen atmosphere. 2-Butanone (16 mL) is added, and the mixture is stirred and heated to 80 °C. **Iodomethane** (0.510 g, 3.59 mmol) is added to the reaction mixture. The reaction progress is monitored by TLC using DCM:AcOEt as eluent. After 29 h, although some starting material appears to remain, the reaction mixture is worked up. A yellow solid forms and is collected by filtration on a Hirsch funnel, washed with 2-butanone (20 mL), and dried in an oven at 65 °C to constant weight. The solid is recrystallized from EtOH (20 mL), collected by filtration on a Hirsch funnel, and dried under vacuum at 65 °C to constant weight, affording the methylated product (1.300 g, 3.07 mmol, 86% yield). mp 169-171 °C.

^{1}H NMR (400 MHz, DMSO-d$_6$): d [ppm] 8.13-8.06 (m, 2H), 7.74-7.67 (m, 4H), 6.98 (d, J = 9.1 Hz, 2H), 5.04 (t, J = 5.6 Hz, 1H), 4.43 (t, J = 5.2 Hz, 2H), 3.89 (s, 3H), 3.77 (q, J = 5.2 Hz, 2H), 3.08 (s, 6H).

^{13}C NMR (100 MHz, DMSO-d$_6$): d [ppm] 152.94, 152.57, 132.37, 131.70, 126.64, 114.27, 113.67, 112.14, 106.47, 58.98, 49.00, 40.10, 33.33.

Synthesis of compound G13

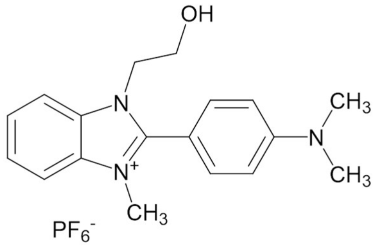

Derivative G12 (5.000 g, 11.8 mmol) is dissolved in water (90 mL) in a 250 mL round-bottom flask equipped with a magnetic stir bar. The solution is heated to reflux under stirring until complete dissolution is achieved. A solution of **ammonium hexafluorophosphate** (NH_4PF_6, 2.885 g, 17.7 mmol) in water (6 mL) is added dropwise to the refluxing solution. The mixture is maintained at reflux for 2 h and then cooled and let at room temperature for 24h. A white precipitate forms, which is collected by filtration on a Hirsch funnel and washed sequentially with NH_4OH (3% v/v, 30 mL) and water (30 mL). The solid is dried in an oven at 65 °C under vacuum until constant weight, affording the PF_6^- salt as a white crystalline solid (4.866 g, 11.0 mmol, 93% yield). mp 182-184 °C.

^{1}H NMR (400 MHz, DMSO-d$_6$): d [ppm] 8.12-8.05 (m, 2H), 7.75-7.65 (m, 2H), 6.97 (d, J = 9.0 Hz, 2H), 5.07 (t, J = 5.6 Hz, 1H), 4.42 (t, J = 5.1 Hz, 2H), 3.88 (s, 3H), 3.76 (q, J = 5.2 Hz, 2H), 3.08 (s, 6H).

^{13}C NMR (100 MHz, DMSO-d$_6$): d [ppm] 152.94, 152.59, 132.34, 131.69, 126.64, 134.24, 113.63, 112.12, 106.46, 58.97, 48.96, 40.06, 33.23.

^{19}F NMR (376 MHz, DMSO-d$_6$): d [ppm] -69.26 (s, 3F), -71.15 (s, 3F).

3.6.1.3. Synthesis of bis-carbamate dimer

Dimerization to M

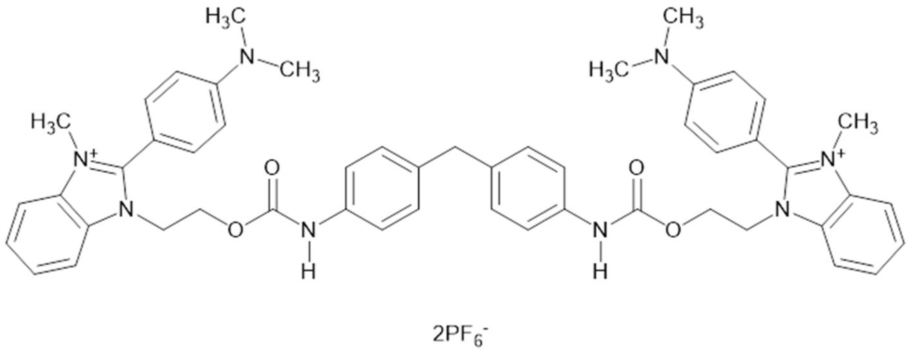

A 25 mL round-bottom flask is put under nitrogen atmosphere. Anhydrous, degassed DMF (5 mL) and tin(II) bis(2-ethylhexanoate) (94 mg, 0.274 mmol) are added, and the system is stirred.

In a second 50 mL round-bottom flask, derivative **G13** (754 mg, 1.71 mmol) and **MDI** (236 mg, 0.943 mmol) are added. The second system is put under nitrogen atmosphere and DMF (anhydrous, degassed, 2.5 mL) is added. 0.5 mL of the catalyst solution is transferred into the second flask. The reaction mixture is heated to 60 °C and stirred.

The reaction progress is monitored by TLC using DCM:EtOAc (8:2) to follow the consumption of the isocyanate and MeOH:$MeNO_2$:NH_4Cl (2 M) (8:1:1) to distinguish G13 from the product. After 24 h, starting material G13 is still observed, and an additional aliquot of **MDI** (43 mg, 0.172 mmol) is added. After a further 24 h, the reaction reaches completion.

The reaction mixture is concentrated to dryness under reduced pressure. The crude is washed in toluene (3x3 mL), in the process a solid is formed, which is subsequently filtered on a Hirsch funnel, and dried in an oven at 65 °C to constant weight, affording the carbamate dimeric salt as a solid (946 mg, 0.838 mmol, 98% yield). mp 169-172 °C.

^{1}H NMR (400 MHz, DMSO-d$_6$): d ppm] 9.38 (s, 2H), 8.52 (s, 2H), 8.20-8.14 (m, 2H), 8.10-8.05 (m, 2H), 7.75-7.68 (m, 4H), 7.58 (d, J = 7.58 Hz, 4H), 7.34 (d, J = 8.4 Hz, 4H), 7.17 (d, J = 7.1 Hz, 4H), 7.10 (d, J =7.8 Hz, 8H), 6.80 (d, J = 8.9 Hz, 4H), 4.70 (t, J = 4.5 Hz, 4H), 4.40 (t, J = 4.5 Hz, 4H), 3.88 (s, 6H), 3.79 (s, 4H), 2.91 (s, 12H).

^{13}C NMR (100 MHz, DMSO-d$_6$): d [ppm] 162.77, 153.05, 152.80, 136.88, 136.31, 132.30, 131.36, 129.36, 129.24, 127.08, 126.91, 118.81, 113.96, 113.80, 112.07, 105.75, 61.67, 45.93, 36.25, 33.33, 31.24.

Representative reduction to N

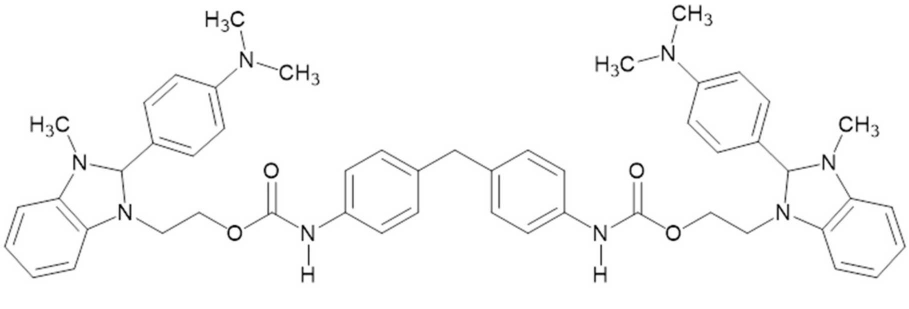

Compound M (187 mg, 0.165 mmol) is added to a 50 mL round-bottom flask, together with THF (1 mL) and methanol (1 mL). The system is cooled to 0 °C under stirring, resulting in complete dissolution of the reagent. Sodium borohydride ($NaBH_4$, 50 mg, 1.320 mmol) is then added. The reaction progress is monitored by TLC analysis, using DCM:EtOAc (95:5) as eluent. After 30 minutes, only the starting material is detected. An additional portion of $NaBH_4$ (100 mg, 2.64 mmol) is added at room temperature. After 30 minutes, a white precipitate is observed, and TLC indicates complete consumption of the starting material along with the formation of several products. Water (10 mL) is added to the mixture, leading to complete precipitation of the product. The solid is collected by Hirsch filtration and washed with water (5 mL). The material is transferred into a vial with septum, dried under vacuum, affording 76 mg (0.0899 mmol, 54.5% yield).

^{1}H NMR (400 MHz, DMSO-d$_6$): d [ppm] 9.47 (s, 2H), 7.40-7.26 (m, 8H), 7.09 (d, J = 8.1 Hz, 4H), 6.69 (d, J = 8.3 Hz, 4H), 6.60-6.50 (m, 4H), 6.45-6.35 (m, 4H), 5.20 (s, 2H), 4.14-4.06 (m, 2H), 4.00 (t, J = 5.2 Hz, 4H), 3.79 (s, 2H), 2.85 (s, 12H), 2.44 (s, 6H).

^{13}C NMR (100 MHz, DMSO-d$_6$): d [ppm] 153.70, 151.43, 142.17, 141.10, 137.39, 136.04, 129.79, 129.26, 125.77, 119.14, 119.00, 118.82, 112.27, 105.57, 104.88, 105.57, 104.88, 91.47, 61.82, 49.07, 45.28, 40.37, 33.00.

3.6.1.4. Synthesis of polyurethanes

Synthesis of compound E3

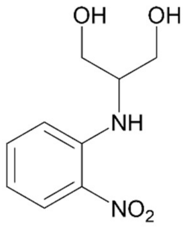

1-Fluoro-2-nitrobenzene (1.545 g, 10.9 mmol), **serinol** (1.008 g, 11.1 mmol), and triethylamine (TEOA, 1.866 g, 12.5 mmol) are added to a 50 mL round-bottom flask. The system is put under stirring and heated to 50 °C. The reaction progress is monitored by TLC using DCM:EtOAc (1:1) as eluent. After 21 h, starting material is still present, so the reaction temperature is increased to 80 °C. The reaction continues for 3 days until complete consumption of starting material is observed. Water (5 mL) is added at 0 °C, resulting in precipitation of a solid. The solid is collected by filtration on a Hirsch funnel and washed with water (20 mL). The solid is recrystallized from water (30 mL), and the supersaturated solution is stored at 0 °C for 5 days, leading to formation of a red precipitate. The precipitate is collected by filtration on a Hirsch funnel and dried under vacuum in an oven at 65 °C to constant weight, affording E3 as a red crystalline solid (1.788 g, 8.40 mmol, 77% yield). mp 101–105 °C.

^{1}H NMR (400 MHz, DMSO-d_6): d [ppm] 8.33 (d, J = 8.0 Hz, 1H), 8.06 (dd, J_1 = 8.6 Hz, J_2 = 1.5 Hz, 1H), 7.56-7.49 (m, 1H), 7.15 (d, J = 8.7 Hz, 1H), 6.70-6.64 (m, 1H), 4.98 (t, J = 5.4 Hz, 2H), 3.72 (hept, J = 4.3 Hz, 1H), 3.65-3.52 (m, 4H).

^{13}C NMR (100 MHz, DMSO-d_6): d [ppm] 145.64, 137.00, 131.37, 126.74, 115.60, 115.54, 60.08, 55.65.

Synthesis of compound F16

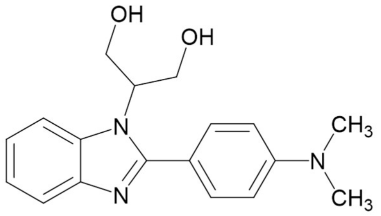

Derivative E3 (747 mg, 3.52 mmol), **4-dimethylaminobenzaldehyde** (644 mg, 4.32 mmol), and sodium dithionite ($Na_2S_2O_4$, 1.961 g, 9.57 mmol) are added to a round-bottom flask. Ethanol (3.7 mL) and water (0.7 mL) are added, and the system is heated to reflux under stirring. After 20 h, the reaction is complete as monitored by TLC. A 3% (v/v) aqueous NH_4OH solution (30 mL) is added, resulting in the formation of a white precipitate. The solid is collected by filtration on a Hirsch funnel and washed with NH_4OH (3% v/v, 20 mL) and water (20 mL). The solid is dried under vacuum in an oven at 65 °C until constant weight. The crude solid is taken up in AcOEt (20 mL), filtered on a Hirsch funnel, and washed with AcOEt (2 × 15 mL), then dried again under vacuum in an oven at 65 °C. The solid still contains minor traces of aldehyde and shows partial solubility in AcOEt. The solid is then taken up in Et_2O (15 mL), filtered on a Hirsch funnel, and dried under vacuum in an oven at 65 °C to constant weight (300 mg, 27.4% yield). mp 192-193 °C.

^{1}H NMR (400 MHz, DMSO-d_6): d [ppm] 7.69 (d, J = 8.6 Hz, 3H), 7.61 (d, J = 7.0 Hz, 1H), 7.22-7.12 (m, 2H), 6.83 (d, J = 8.6 Hz, 2H), 5.04 (t, J = 4.3 Hz, 2H), 4.68 (q, J= 5.2 Hz, 1H), 4.07-3.95 (m, 2H), 394-3.83 (m, 2H), 3.00 (s, 6H).

^{13}C NMR (100 MHz, DMSO-d_6): d [ppm] 156.26, 151.27, 143.78, 134.40, 131.42, 121.69, 119.26, 118.38, 113.11, 112.00, 111.54, 62.24, 59.76, 40.34.

Synthesis of compound F17

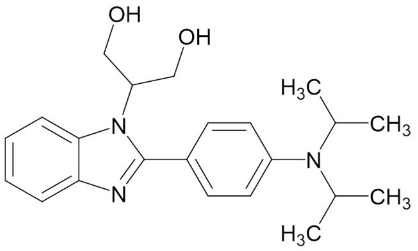

Derivative E3 (748 mg, 3.52 mmol), **4-diisopropylamino-benzaldheyde** (937 mg, 4.56 mmol), and sodium dithionite (Na$_2$S$_2$O$_4$, 1.654 g, 9.50 mmol) are added to a 50 mL round-bottom flask. Ethanol (4.6 mL) and water (0.4 mL) are added, and the system is heated to reflux under stirring. The reaction progress is monitored by TLC using a DCM:AcOEt (1:1) eluent mixture. After 24 h, the nitro reagent is fully consumed. A 3% (v/v) aqueous NH$_4$OH solution (20 mL) is added, and the aqueous phase is extracted with AcOEt (3 × 25 mL). The combined organic layers are dried over MgSO$_4$, filtered through a folded filter, and concentrated under reduced pressure to afford a solid. The solid is washed with n-heptane (5 mL). Minor traces of aldehyde and other impurities remain. The crude product is dissolved in DCM (10 mL), and after 24 h, a white solid precipitates from the red supernatant. The solid is collected by filtration on a Hirsch funnel and dried under vacuum in an oven at 65 °C to constant weight (258 mg, 0.702 mmol, 20% yield).

^{1}H NMR (400 MHz, DMSO-d$_6$): d [ppm] 7.72-7.55 (m, 4H), 7.21-7.11 (m, 2H), 6.91 (d, J = 8.81 Hz, 2H), 5.03 (t, J = 5.1 Hz, 2H), 4.76-4.66 (m, 1H), 4.06-3.86 (m, 6H), 1.28 (d, J =6.8 Hz, 12H).

^{13}C NMR (100 MHz, DMSO-d$_6$): d [ppm] 156.27, 148.88, 143.83, 134.43, 131.06, 121.67, 119.25, 118.19, 115.21, 113.10, 62.18, 59.90, 47.15, 21.30.

Synthesis of compound G14

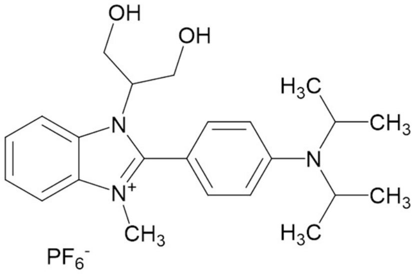

Derivative F17 (203 mg, 0.493 mmol) is added to a 50 mL round-bottom flask. The system is put under nitrogen atmosphere, and anhydrous degassed acetonitrile (1.5 mL) is added. The mixture is stirred and **iodomethane** (116 mg, 0.817 mmol) is added. The system is heated to reflux, under which all reagents dissolve. The reaction progress is monitored by TLC using a DCM:AcOEt (7:3) eluent mixture. After 24 h, the target product forms along with by-products. Water (15 mL) is added, and the reaction mixture is refluxed. The hot mixture is filtered through a folded filter, leaving a precipitate on the filter, while the filtrate appears yellow.

The filtrate contains the product along with other by-products.

An aqueous solution of NH_4PF_6 (239 mg in 4.5 mL water) is prepared, and 3 mL of this solution is added dropwise to the reaction mixture. The mixture is refluxed for 2 h and then allowed to stir at ambient temperature for 22 h, resulting in the formation of a white precipitate. The solid is collected by filtration on a Hirsch funnel, washed with water (10 mL), and dried under vacuum in an oven at 65 °C to constant weight (140 mg, 0.265 mmol, 54% yield). The compound contains minor impurities, yielding an estimated purity of 95%. mp 168–172 °C.

^{1}H NMR (400 MHz, DMSO-d$_6$): d [ppm] 8.24 (d, J = 8.2 Hz, 1H), 8.08 (d, J = 8.2 Hz, 1H), 7.75-7.56 (m, 4H), 7.06 (d, J = 9.0 Hz, 2H), 5.20 (t, J = 5.2 Hz, 2H), 4.65 (hept, J = 4.5 Hz, 1H), 4.19-4.01 (m, 4H), 3.91-3.83 (m, 2H), 3.89 (s, 3H), 1.32 (d, J = 6.8 Hz, 12H).

^{13}C NMR (100 MHz, DMSO-d$_6$): d [ppm] 153.62, 150.86, 132.81, 132.35, 130.05, 126.52, 126.49, 115.59, 114.54, 113.91, 106.13, 65.23, 58.79, 47.28, 20.91.

Synthesis of compound G15

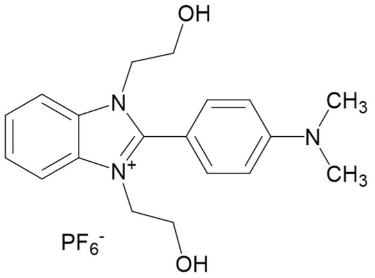

Derivative F14 (502 mg, 1.78 mmol) and **2-bromoethanol** (380 mg, 3.04 mmol) are added to a 50 mL round-bottom flask. The mixture is heated to 90 °C under stirring, and the reaction progress is monitored by TLC using DCM:AcOEt (1:1) as the eluent. After 19 h, starting material is still present, so acetone (1.5 mL) is added and the system is brought to reflux. After an additional 5 h, starting material remains. The reaction mixture is concentrated under reduced pressure to yield a solid containing both product and unreacted reagent. The solid is dissolved in H_2O (30 mL) and heated to reflux. A solution of NH_4PF_6 (653 mg in 4.5 mL H_2O) is prepared, and 3 mL (435 mg) is added dropwise to the refluxing solution. The reaction is maintained for 2 h and then allowed to cool to room temperature, forming a precipitate. The precipitate is collected by filtration on a Hirsch funnel and washed with water. The solid still contains some starting material and is dissolved in AcOEt. Flash chromatography is performed on alumina using a gradient from AcOEt to MeOH as the eluent. Fractions containing the product are combined and concentrated under reduced pressure. The resulting solid is dried under vacuum in an oven at 65 °C to constant weight, affording **G15** as a solid (257 mg, 0.545 mmol, 31% yield). mp 185–188 °C.

^{1}H NMR (400 MHz, DMSO-d$_6$): d [ppm] 8.14-8.09 (m, 2H9, 7.71-7.64 (m, 4H), 6.95 (d, J = 9.0 Hz, 2H), 5.22-5.14 (m, 2H), 4.37 (t, J = 5.1 Hz, 4H), 3.77-3.69 (m, 4H), 3.07 (s, 6H).

^{13}C NMR (100 MHz, DMSO-d$_6$): d [ppm] 153.04, 152.78, 132.32, 131.94, 126.51, 114.36, 112.05, 106.86, 59.04, 49.03, 40.05.

3.6.1.5. Synthesis of polyacrylates

Synthesis of compound G16

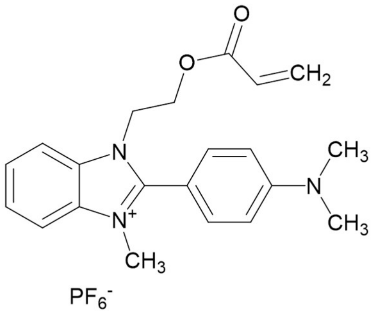

Derivative G13 (4.006 g, 9.08 mmol) is added to a 100 mL round-bottom flask. The system is put under nitrogen atmosphere, and anhydrous, degassed acetonitrile (2.4 mL) is added. The flask is cooled to 0 °C under stirring. Triethylamine (NEt$_3$, 1.475 g, 14.6 mmol), 2,6-di-tert-butyl-4-methylphenol (BHT, 458 mg, 4.54 mmol), and **acryloyl chloride** (92 mg, 1.016 mmol) are added sequentially. The reaction progress is monitored by TLC using MeOH/MeNO$_2$/NH$_4$Cl (2 M) (8:1:1) as eluent. After 24 h, the solvent is removed under reduced pressure to yield a solid residue. The crude product is washed with diethyl ether (20 mL), collected by filtration on a Hirsch funnel, washed with water (20 mL), and filtered again. The resulting solid is dried under vacuum in an oven at 65 °C to constant weight, affording G15 as a white solid (4.257 g, 8.59 mmol, 94% yield). mp 179–181 °C.

^{1}H NMR (400 MHz, DMSO-d$_6$): d [ppm] 8.20-8.15 (m, 1H), 8.10-8.05 (m, 1H), 7.74-7.71 (m, 2H), 7.65 (d, J = 8.9 Hz, 2H), 6.98 (d, J = 9.00 Hz, 2H), 6.19 (d, J = 1.74 Hz, 2H), 6.22–6.14 (AB, 2H, J ≈ 10, 17 Hz), 5.98 (m, 1H), 4.73 (t, J=4.9 Hz, 2H), 4.41 (t, J=4.9 Hz, 2H), 3.87 (s, 3H), 3.08 (s, 6H).

^{13}C NMR (100 MHz, DMSO-d$_6$): d [ppm] 165.44, 153.00, 152.64, 132.77, 132.29, 132.08, 131.56, 128.00, 126.88, 126.81, 113.97, 113.80, 112.23, 106.13, 62.34, 46.18, 45.27, 40.06, 33.30.

3.6.2. NMR spectra

Compound K

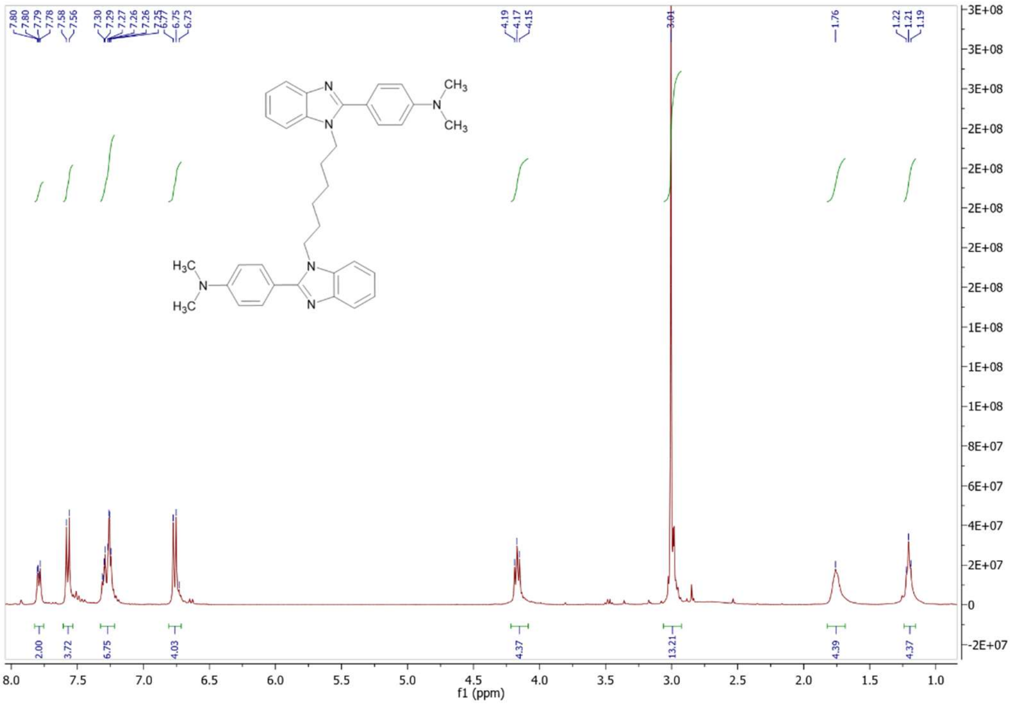

Figure 3.20 ^{1}H-NMR of compound K in CHCl$_3$-d.

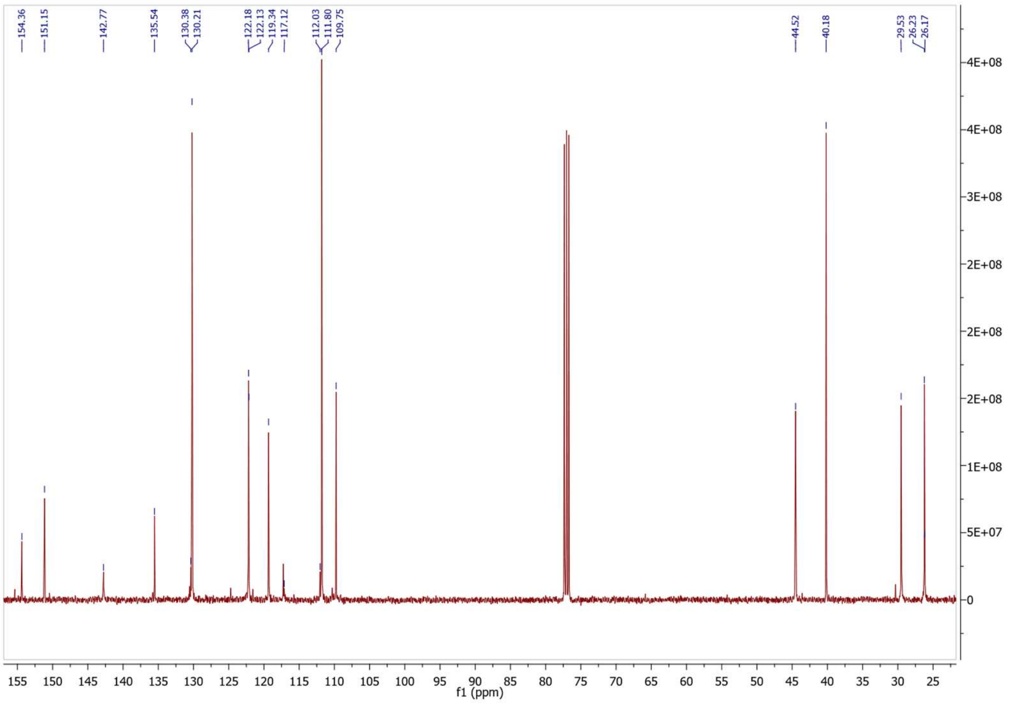

Figure 3.21 ^{13}C-NMR of compound K in CHCl$_3$-d.

Compound F14

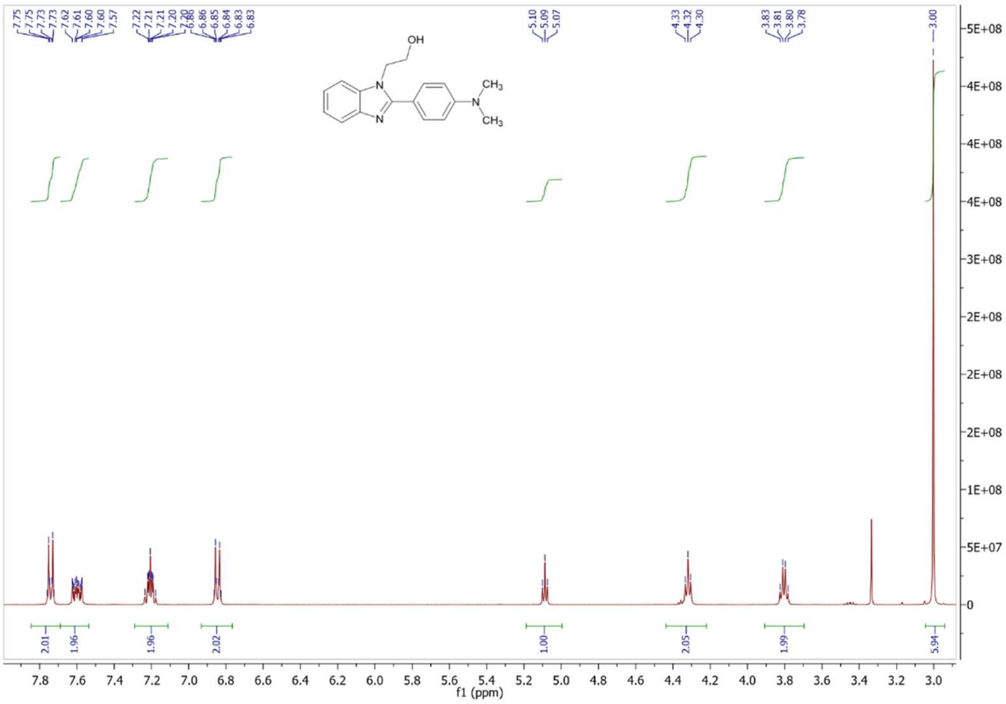

Figure 3.22 ^{1}H NMR of compound F14 in DMSO-d_6.

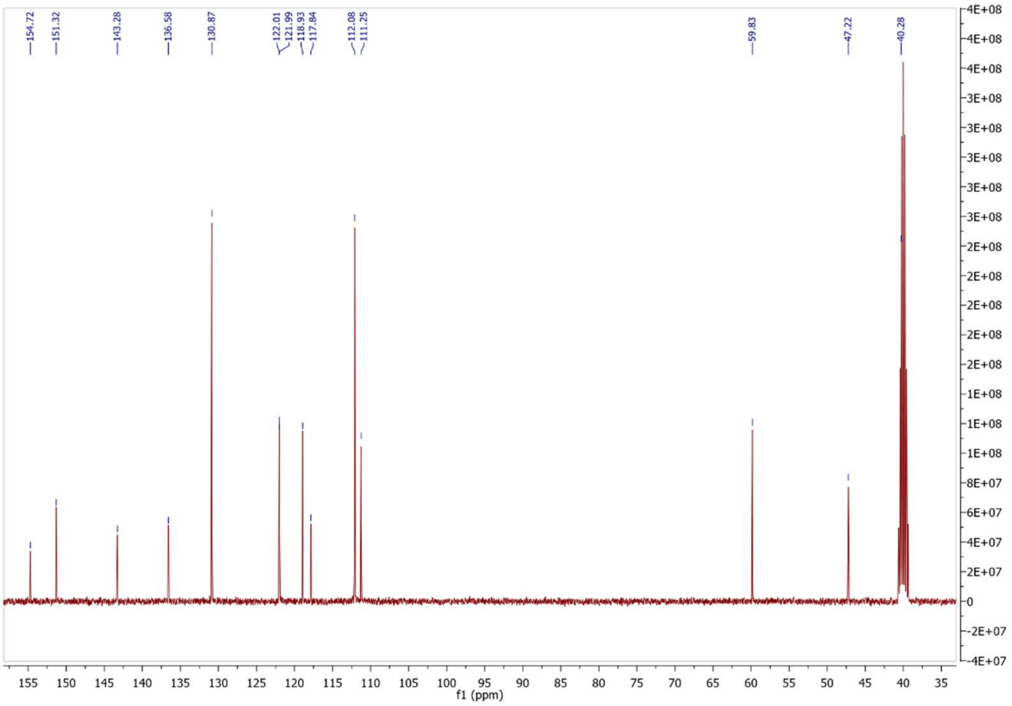

Figure 3.23 ^{13}C NMR of compound F14 in DMSO-d_6.

Compound G12

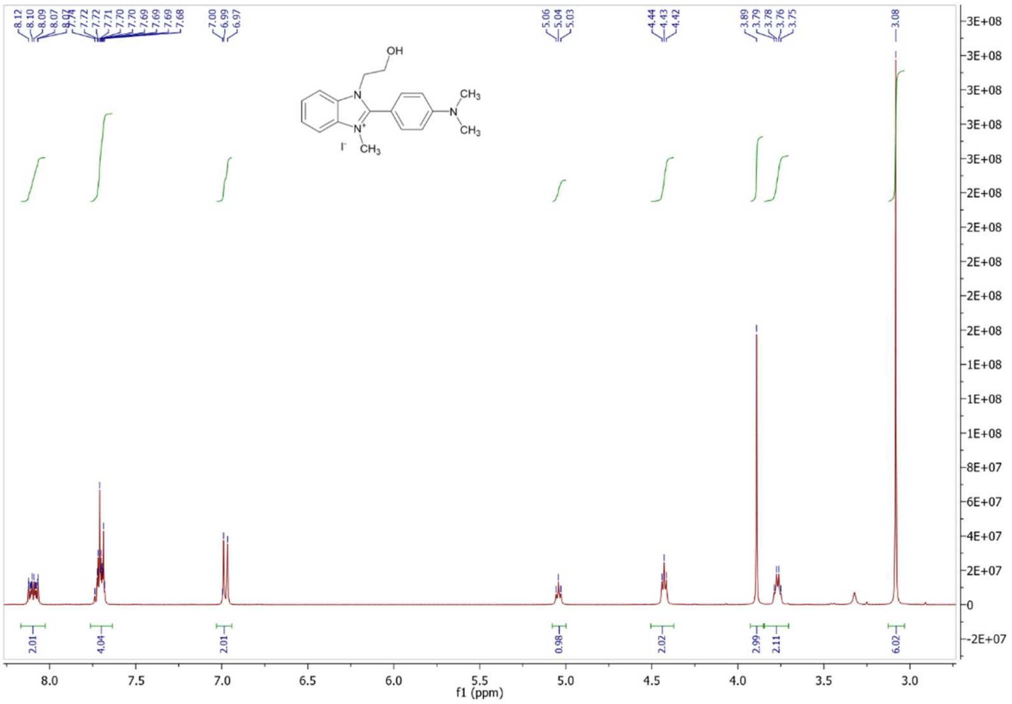

Figure 3.24 ^{1}H NMR of compound G12 in DMSO-d$_6$.

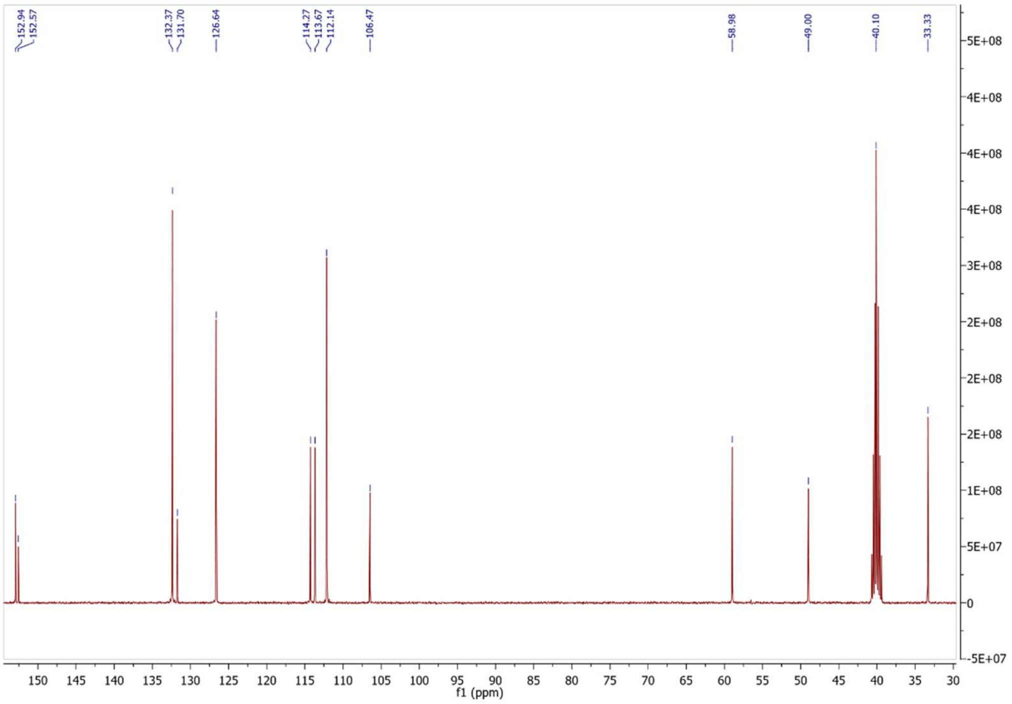

Figure 3.25 ^{13}C NMR of compound G12 in DMSO-d$_6$.

Compound G13

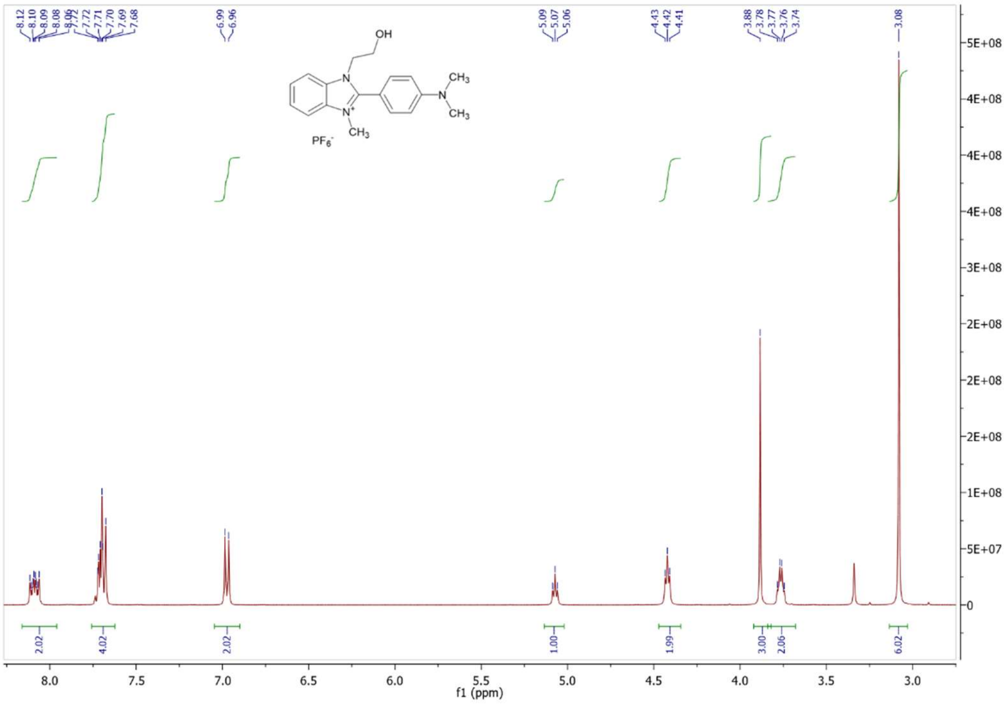

Figure 3.26 ^{1}H NMR of compound G13 in DMSO-d_6.

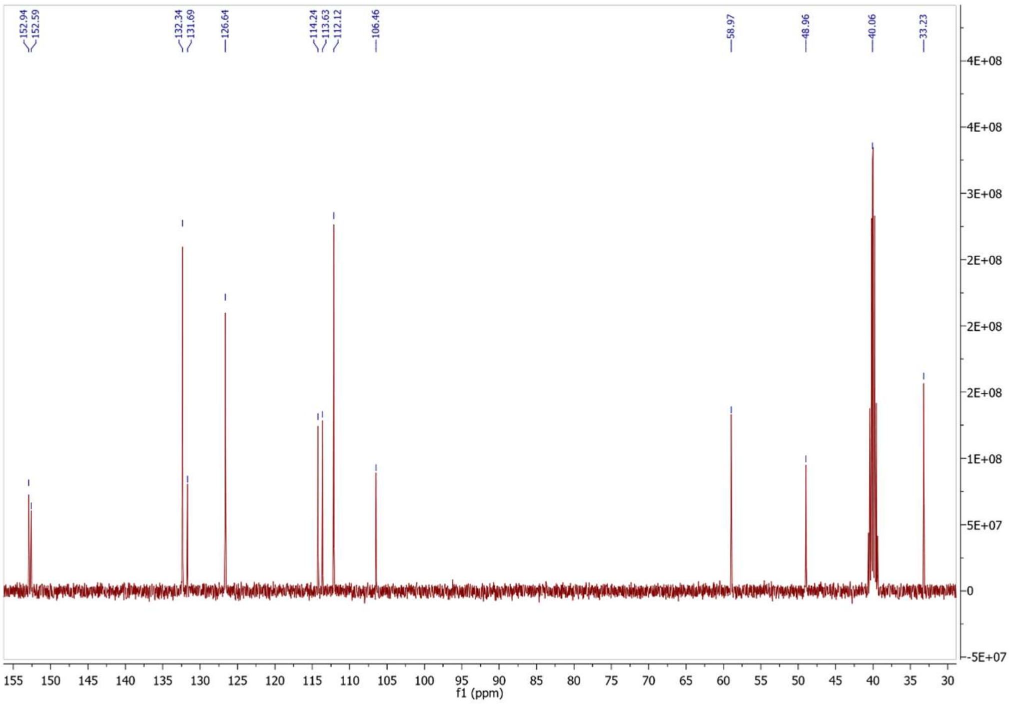

Figure 3.27 ^{13}C NMR of compound G13 in DMSO-d_6.

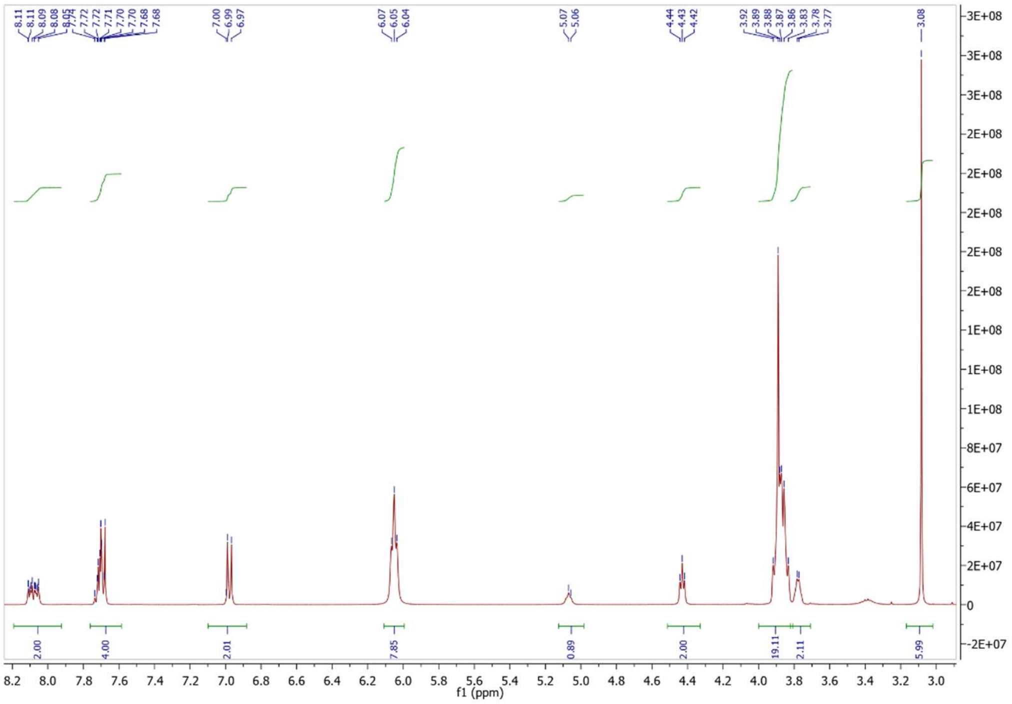

Figure 3.28 ^{1}H NMR of compound G13 + standard of 2,2,2-trifluoroethanol in DMSO-d$_6$.

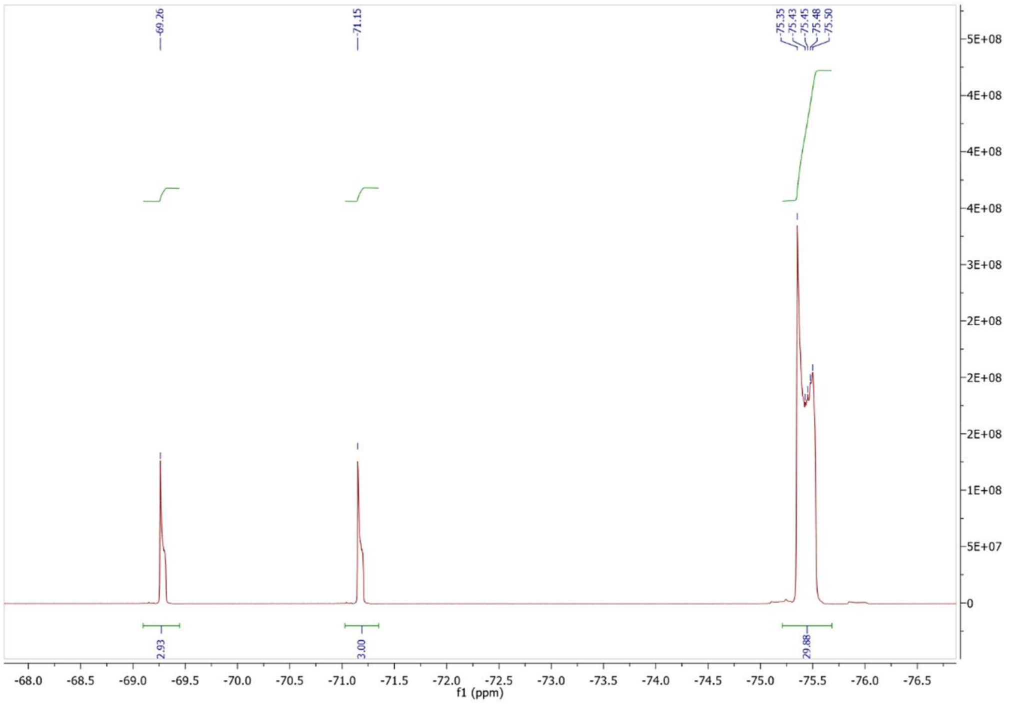

Figure 3.29 ^{19}F NMR of compound G13 + standard of 2,2,2-trifluoroethanol in DMSO-d$_6$.

Compound M

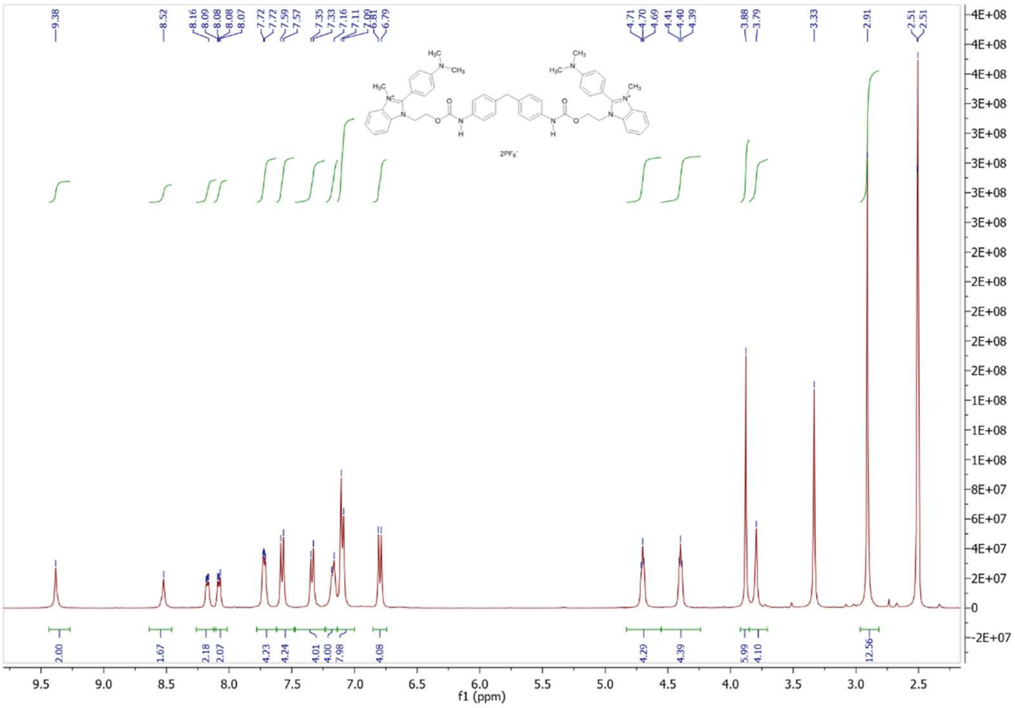

Figure 3.30 ^{1}H NMR of compound M in DMSO-d_6.

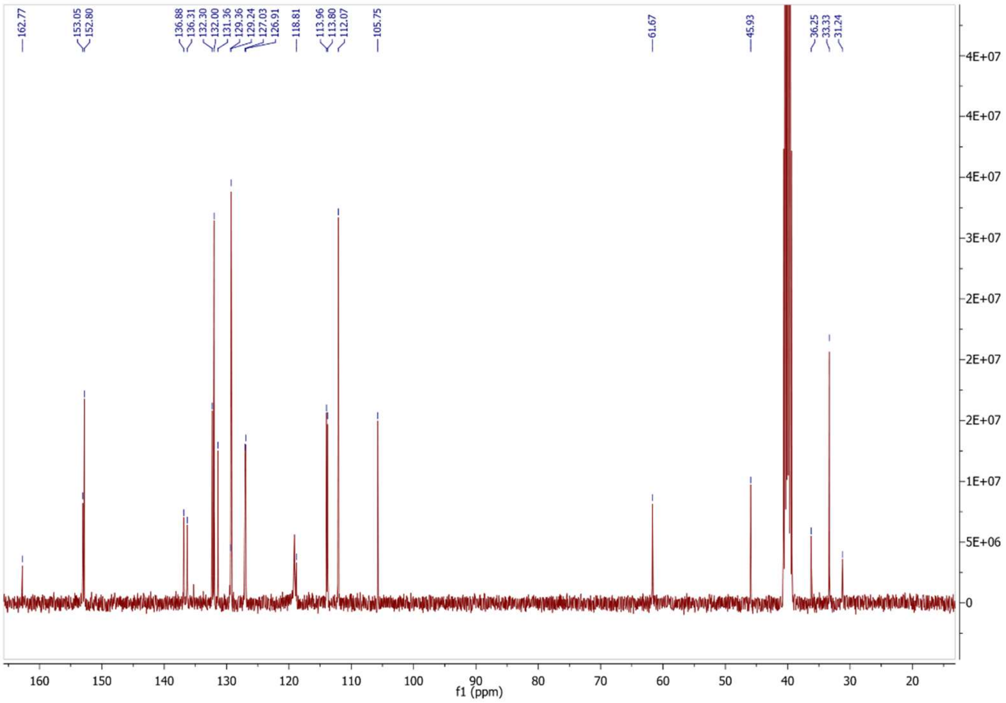

Figure 3.31 ^{13}C NMR of compound M in DMSO-d_6.

Compound N

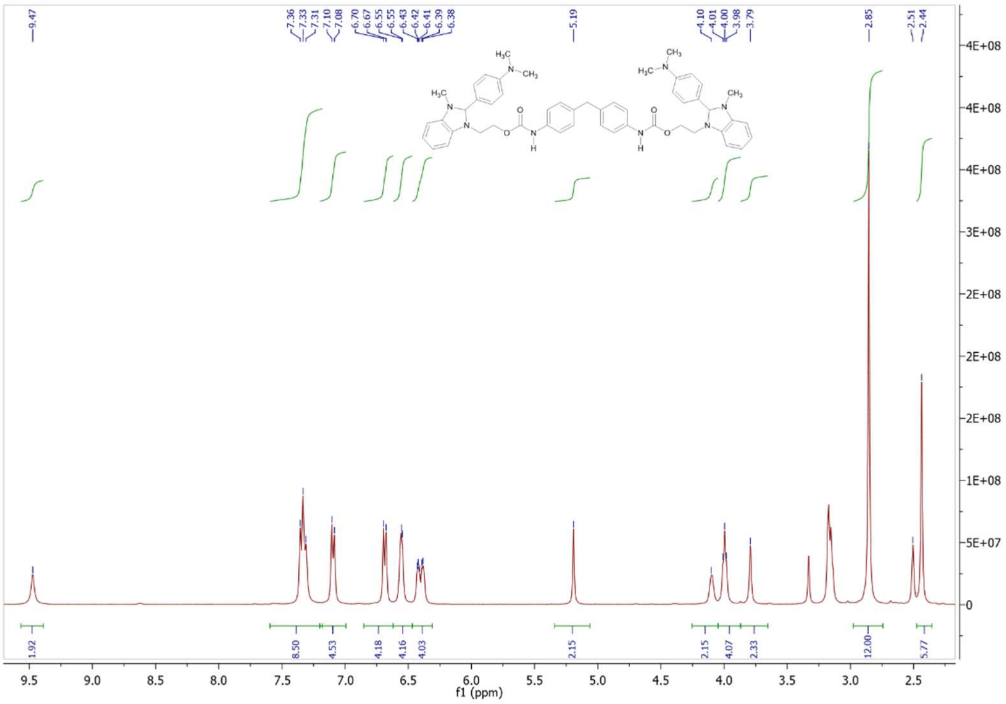

Figure 3.32 ^{1}H NMR of compound N in DMSO-d_6.

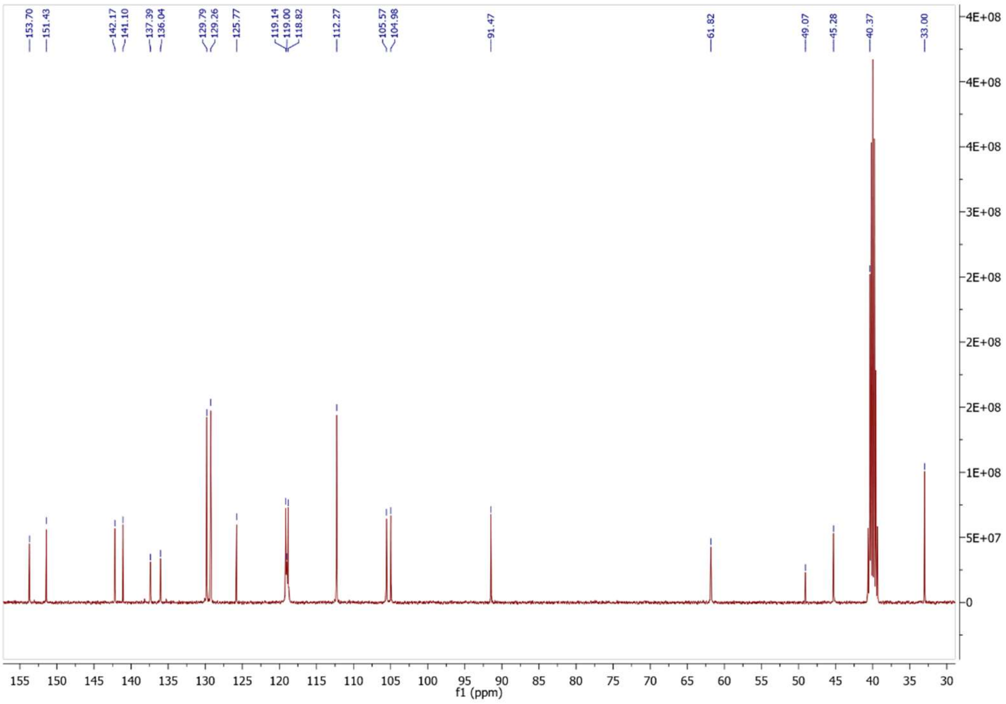

Figure 3.33 ^{13}C NMR of compound N in DMSO-d_6.

Compound E3

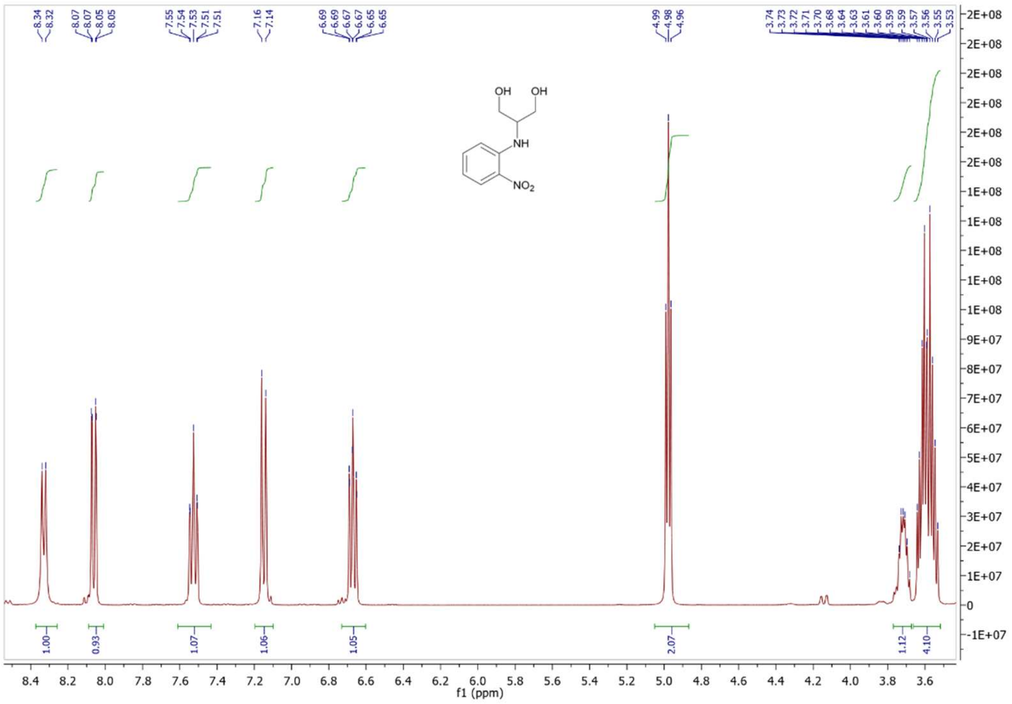

Figure 3.34 ^{1}H NMR of compound E3 in DMSO-d$_6$.

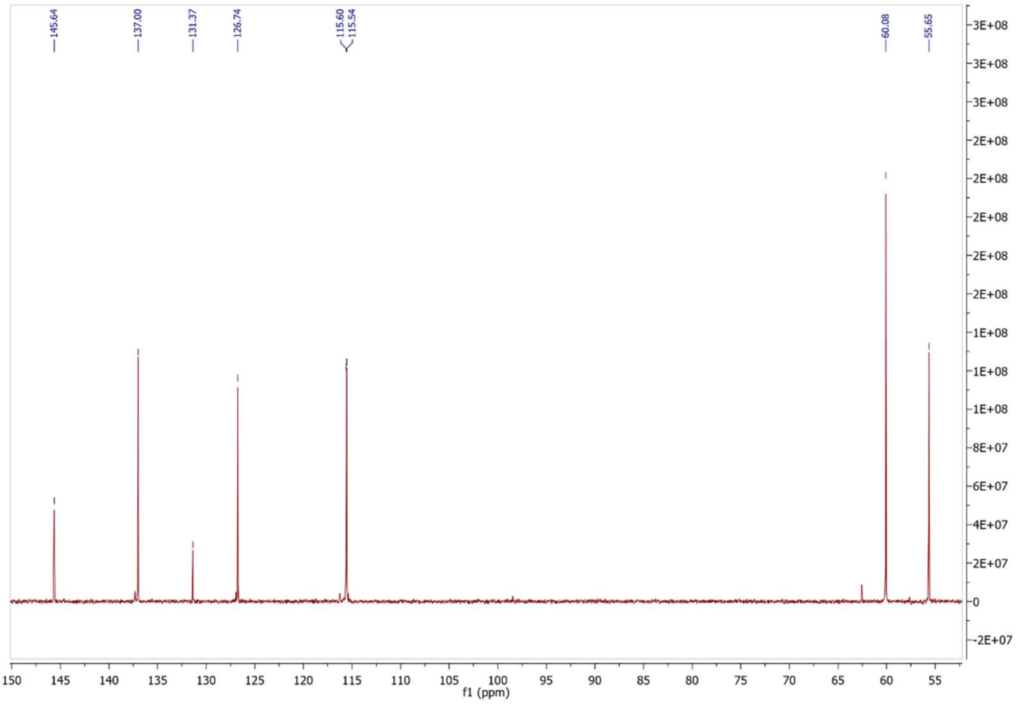

Figure 3.35 ^{13}C NMR of compound E3 in DMSO-d$_6$.

Compound F16

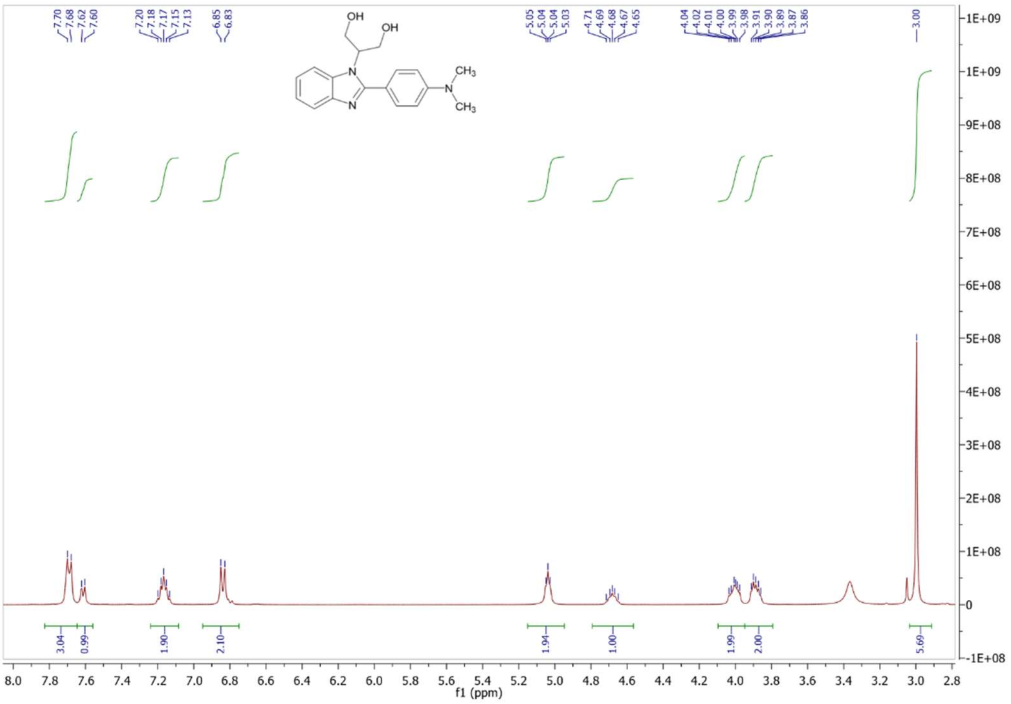

Figure 3.36 ^{1}H NMR of compound F16 in DMSO-d$_6$.

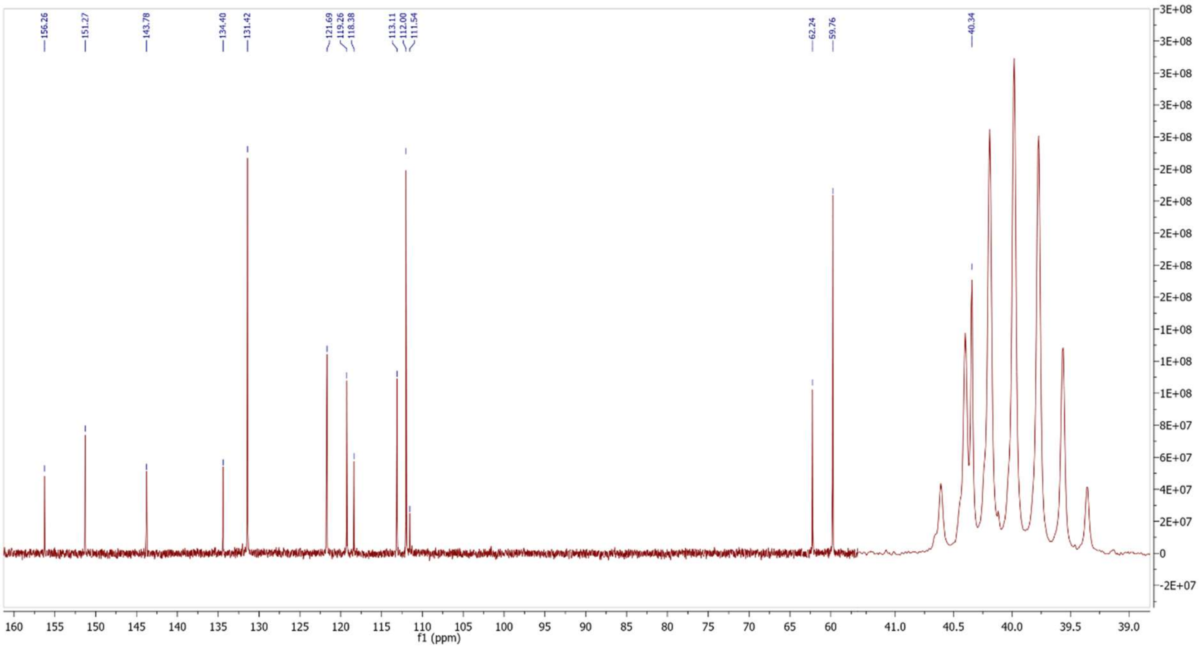

Figure 3.37 ^{13}C NMR of compound F16 in DMSO-d$_6$.

Compound F17

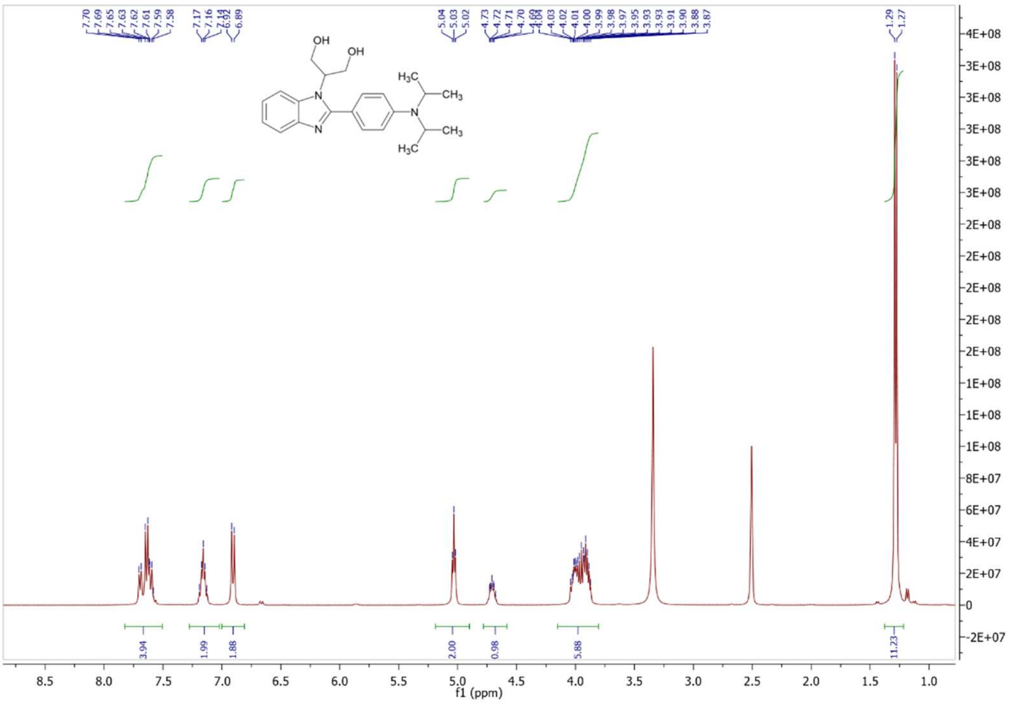

Figure 3.38 ^{1}H NMR of compound F17 in DMSO-d$_6$.

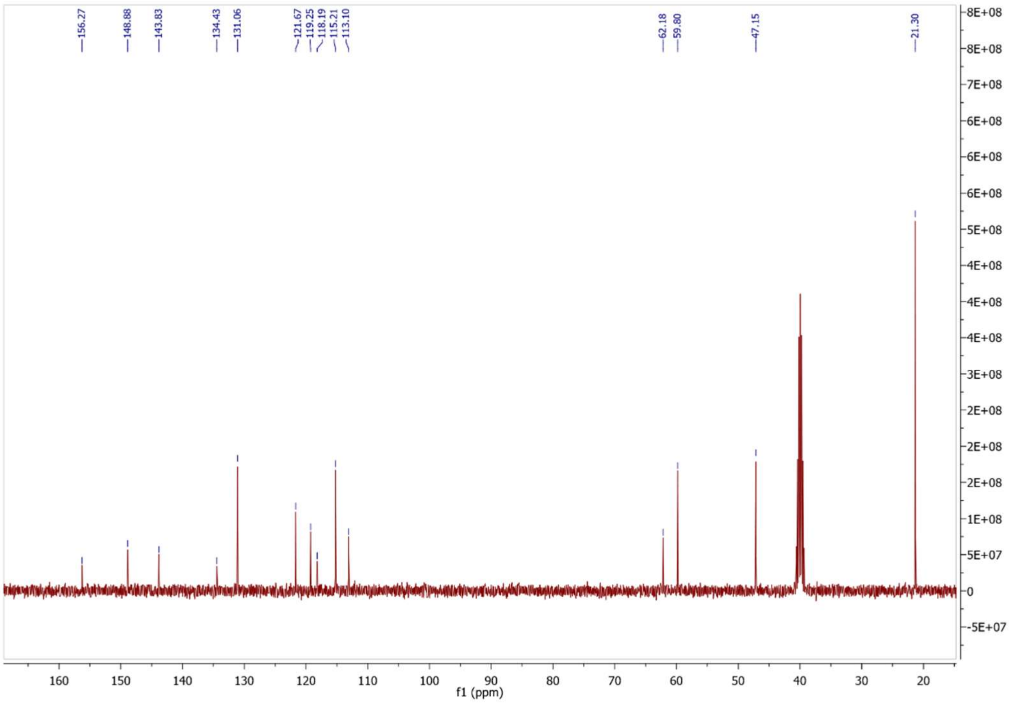

Figure 3.39 ^{13}C NMR of compound F17 in DMSO-d$_6$.

Compound G14

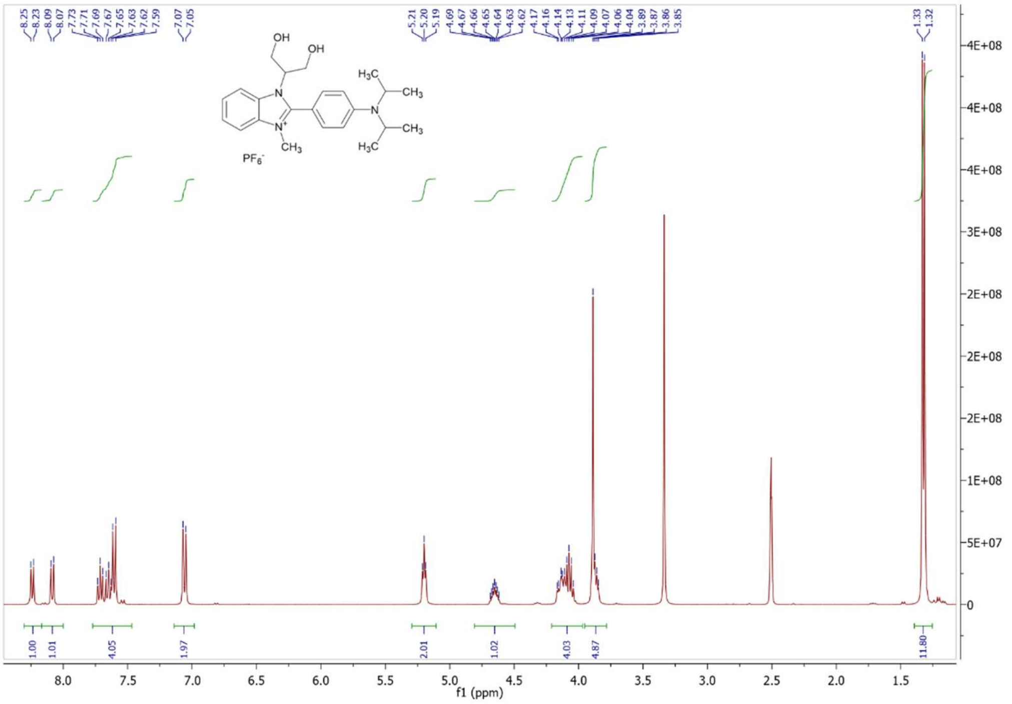

Figure 3.40 ^{1}H NMR of compound G14 in DMSO-d$_6$.

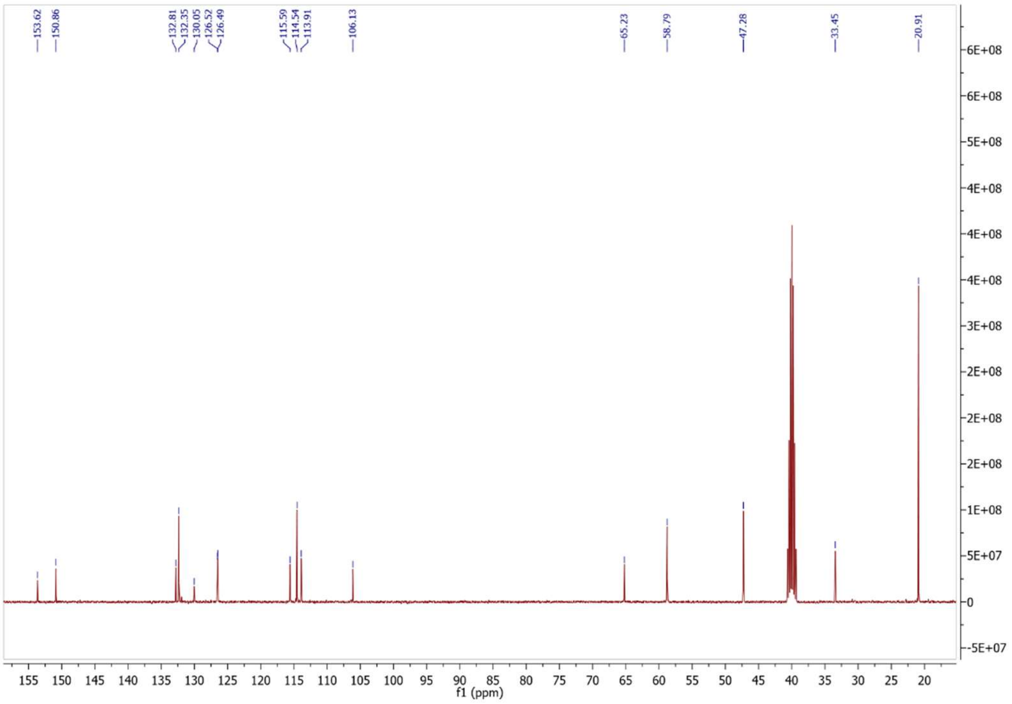

Figure 3.41 ^{13}C NMR of compound G14 in DMSO-d$_6$.

Compound G15

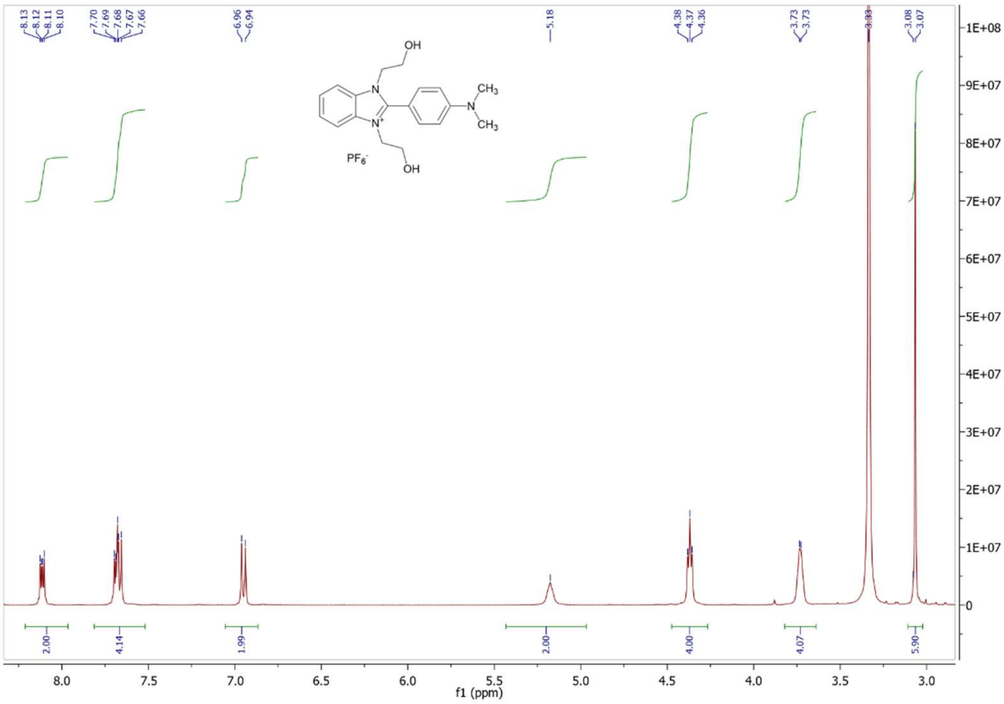

Figure 3.42 ^{1}H NMR of compound G15 in DMSO-d_6.

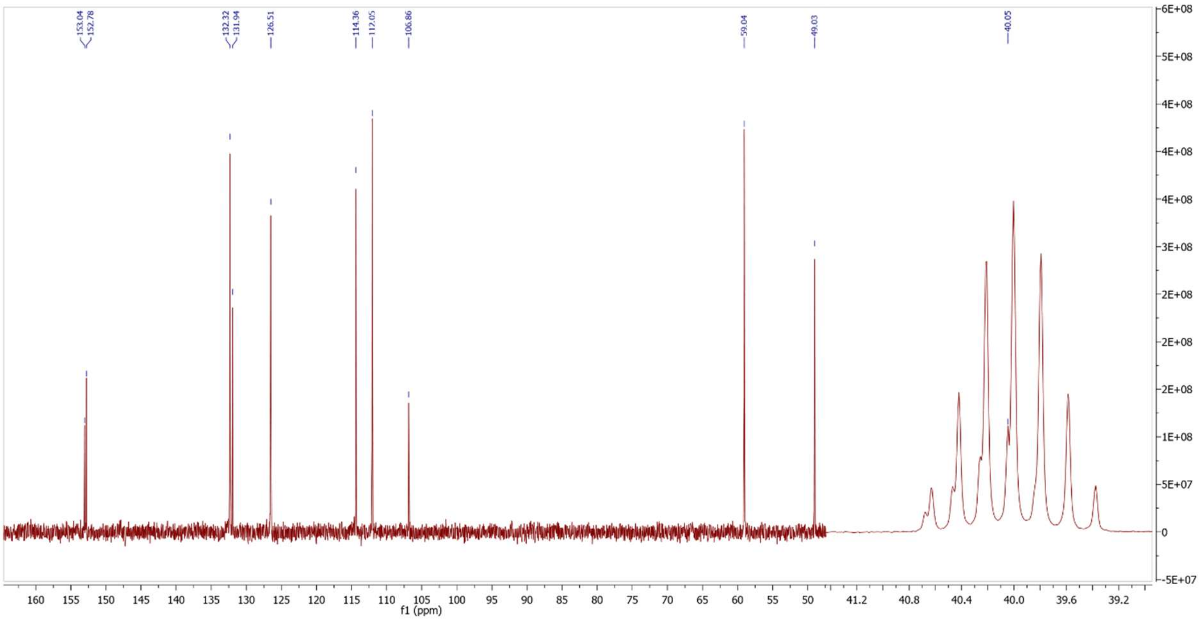

Figure 3.43 ^{1}H NMR of compound G15 in DMSO-d_6.

Compound G16

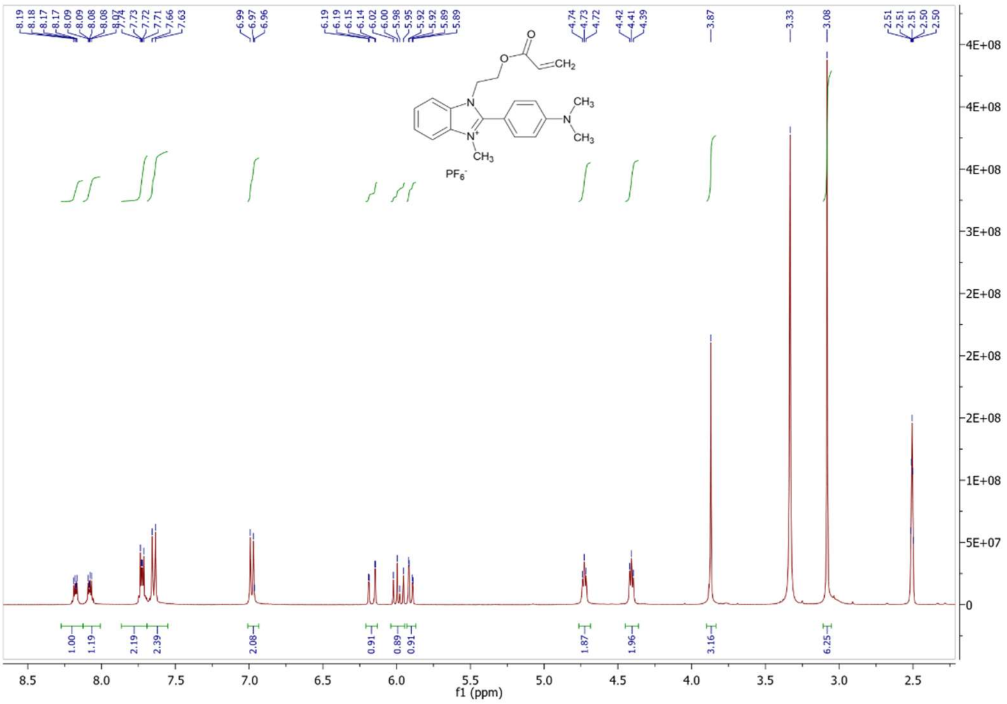

Figure 3.44 ^{1}H NMR of compound G16 in DMSO-d_6.

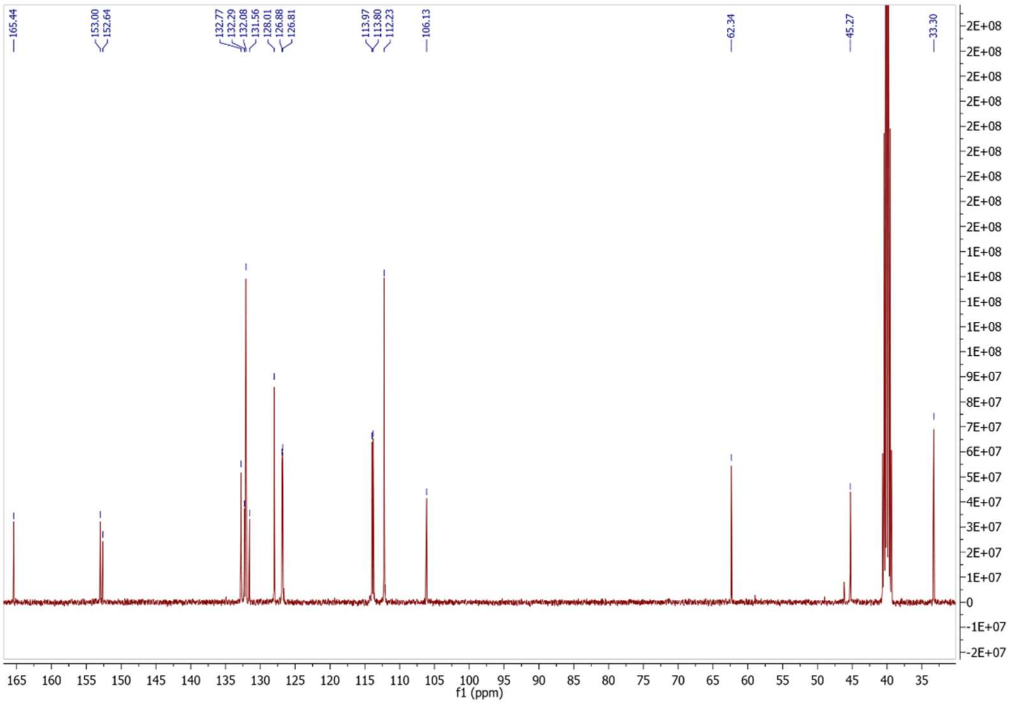

Figure 3.45 ^{13}C NMR of compound G16 in DMSO-d_6.

3.7. Bibliography

(1) Seiti, M.; Giuri, A.; Corcione, C. E.; Ferraris, E. Advancements in Tailoring PEDOT: PSS Properties for Bioelectronic Applications: A Comprehensive Review. *Biomater. Adv.* **2023**, *154*, 213655. https://doi.org/10.1016/j.bioadv.2023.213655.

(2) Chen, S.; Liang, L.; Zhang, Y.; Lin, K.; Yang, M.; Zhu, L.; Yang, X.; Zang, L.; Lu, B. PEDOT:PSS-Based Electronic Materials: Preparation, Performance Tuning, Processing, Applications, and Future Prospect. *Prog. Polym. Sci.* **2025**, *166*, 101990. https://doi.org/10.1016/j.progpolymsci.2025.101990.

(3) Chilvery, A.; Das, S.; Guggilla, P.; Brantley, C.; Sunda-Meya, A. A Perspective on the Recent Progress in Solution-Processed Methods for Highly Efficient Perovskite Solar Cells. *Sci. Technol. Adv. Mater.* **2016**, *17* (1), 650–658. https://doi.org/10.1080/14686996.2016.1226120.

(4) Yang, C.-Y.; Stoeckel, M.-A.; Ruoko, T.-P.; Wu, H.-Y.; Liu, X.; Kolhe, N. B.; Wu, Z.; Puttisong, Y.; Musumeci, C.; Massetti, M.; Sun, H.; Xu, K.; Tu, D.; Chen, W. M.; Woo, H. Y.; Fahlman, M.; Jenekhe, S. A.; Berggren, M.; Fabiano, S. A High-Conductivity n-Type Polymeric Ink for Printed Electronics. *Nat. Commun.* **2021**, *12* (1), 2354. https://doi.org/10.1038/s41467-021-22528-y.

(5) Saeedifard, F.; Lungwitz, D.; Yu, Z.-D.; Schneider, S.; Mansour, A. E.; Opitz, A.; Barlow, S.; Toney, M. F.; Pei, J.; Koch, N.; Marder, S. R. Use of a Multiple Hydride Donor To Achieve an N-Doped Polymer with High Solvent Resistance. *ACS Appl. Mater. Interfaces* **2022**, *14* (29), 33598–33605. https://doi.org/10.1021/acsami.2c05724.

(6) Akindoyo, J. O.; Beg, M. D. H.; Ghazali, S.; Islam, M. R.; Jeyaratnam, N.; Yuvaraj, A. R. Polyurethane Types, Synthesis and Applications – a Review. *RSC Adv.* **2016**, *6* (115), 114453–114482. https://doi.org/10.1039/C6RA14525F.

(7) De Souza, F. M.; Kahol, P. K.; Gupta, R. K. Introduction to Polyurethane Chemistry. In *ACS Symposium Series*; Gupta, R. K., Kahol, P. K., Eds.; American Chemical Society: Washington, DC, 2021; Vol. 1380, pp 1–24. https://doi.org/10.1021/bk-2021-1380.ch001.

(8) Hanson, J. R. Reductions by the Alumino- and Borohydrides in Organic Synthesis. *J. Organomet. Chem.* **1992**, *426* (1), C22–C23. https://doi.org/10.1016/0022-328X(92)83176-I.

(9) Tabane, T. H.; Singh, G. S. A Simple Reduction of Imines to Biologically Important Secondary Amines Using Sodium Borohydride/Alumina in Solid-Phase. *Proc. Natl. Acad. Sci. India Sect. Phys. Sci.* **2014**, *84* (4), 517–521. https://doi.org/10.1007/s40010-014-0130-z.

(10) Tanaka, N.; Ishii, T.; Yamaguchi, I.; Hamasuna, A.; Fujigaya, T. Photoinduced Electron Doping of Single-Walled Carbon Nanotubes Based on Carboxamide Photochemical Reactions. *J. Mater. Chem. A* **2023**, *11* (13), 6909–6917. https://doi.org/10.1039/D2TA08131H.

(11) Pallini, F.; Mattiello, S.; Cassinelli, M.; Rossi, P.; Mecca, S.; Tan, W. L.; Sassi, M.; Lanzani, G.; McNeill, C. R.; Caironi, M.; Beverina, L. Unexpected Enhancement of Molecular N-Doping Efficiency in Polymer Thin Films by a Degradation Product. *ACS Appl. Energy Mater.* **2022**. https://doi.org/10/gpg6sz.

(12) Li, Q.; Yan, F.; Texter, J. Polymerized and Colloidal Ionic Liquids─Syntheses and Applications. *Chem. Rev.* **2024**, *124* (7), 3813–3931. https://doi.org/10.1021/acs.chemrev.3c00429.

(13) Zhu, M.; Yang, Y. Poly(Ionic Liquid)s: An Emerging Platform for Green Chemistry. *Green Chem.* **2024**, *26* (9), 5022–5102. https://doi.org/10.1039/D4GC00202D.

(14) Yuan, J.; Antonietti, M. Poly(Ionic Liquid)s: Polymers Expanding Classical Property Profiles. *Polymer* **2011**, *52* (7), 1469–1482. https://doi.org/10.1016/j.polymer.2011.01.043.

(15) Maksym, P.; Tarnacka, M.; Dzienia, A.; Wolnica, K.; Dulski, M.; Erfurt, K.; Chrobok, A.; Zięba, A.; Brzózka, A.; Sulka, G.; Bielas, R.; Kaminski, K.; Paluch, M. Efficient Metal-Free Strategies for Polymerization of a Sterically Hindered Ionic Monomer through the Application of Hard Confinement and High Pressure. *RSC Adv.* **2019**, *9* (11), 6396–6408. https://doi.org/10.1039/C8RA09242G.

(16) Hirai, R.; Watanabe, T.; Ono, T. Design of Clickable Ionic Liquid Monomers to Enhance Ionic Conductivity for Main-Chain 1,2,3-Triazolium-Based Poly(Ionic Liquid)s. *ACS Omega* **2021**, *6* (15), 10030–10038. https://doi.org/10.1021/acsomega.0c06173.

(17) Hirai, R.; Hibino, T.; Watanabe, T.; Teranishi, T.; Ono, T. One-Pot Synthesis of Poly(Ionic Liquid)s with 1,2,3-Triazolium-Based Backbones *via* Clickable Ionic Liquid Monomers. *RSC Adv.* **2020**, *10* (62), 37743–37748. https://doi.org/10.1039/D0RA07948K.

(18) Wang, A.; Liu, Z.; Xu, L.; Lou, N.; Li, M.; Liu, L. Controllable Click Synthesis of Poly(Ionic Liquid)s by Surfactant-Free Ionic Liquid Microemulsions for Selective Dyes Reduction. *React. Funct. Polym.* **2020**, *147*, 104464. https://doi.org/10.1016/j.reactfunctpolym.2019.104464.

(19) Morozova, S. M.; Shaplov, A. S.; Lozinskaya, E. I.; Vlasov, P. S.; Sardon, H.; Mecerreyes, D.; Vygodskii, Y. S. Poly(Ionic Liquid)-Based Polyurethanes Having Imidazolium, Ammonium, Morpholinium or Pyrrolidinium Cations. *High Perform. Polym.* **2017**, *29* (6), 691–703. https://doi.org/10.1177/0954008317701551.

(20) Nosov, D. R.; Lozinskaya, E. I.; Antonov, D. Y.; Ponkratov, D. O.; Tyutyunov, A. A.; Alaa Eddine, M.; Plesse, C.; Schmidt, D. F.; Shaplov, A. S. Design of Highly Conductive PILs by Simple Modification of Poly(Epichlorohydrin- *Co* -Ethylene Oxide) with Monosubstituted Imidazoles. *ACS Polym. Au* **2024**, *4* (6), 512–526. https://doi.org/10.1021/acspolymersau.4c00051.

(21) Rusli, W.; Halleluyah, P. M.; Jun, L. X.; Lakshminarayanan, R.; Parthiban, A. Synthesis, Characterization and Cell Selectivity of Poly(Quaternary Ammonium Chlorides): Effect of the Degree of Quaternization and Copolymer Composition. *Mater. Adv.* **2023**, *4* (20), 4954–4964. https://doi.org/10.1039/D3MA00661A.

(22) Ghoreishi, R.; Suppes, G. J. Chain Growth Polymerization Mechanism in Polyurethane-Forming Reactions. *RSC Adv.* **2015**, *5* (84), 68361–68368. https://doi.org/10.1039/C5RA10725C.

(23) Cordella, D.; Kermagoret, A.; Debuigne, A.; Riva, R.; German, I.; Isik, M.; Jérôme, C.; Mecerreyes, D.; Taton, D.; Detrembleur, C. Direct Route to Well-Defined Poly(Ionic Liquid)s by Controlled Radical Polymerization in Water. *ACS Macro Lett.* **2014**, *3* (12), 1276–1280. https://doi.org/10.1021/mz500721r.

(24) Matyjaszewski, K.; Xia, J. Atom Transfer Radical Polymerization. *Chem. Rev.* **2001**, *101* (9), 2921–2990. https://doi.org/10.1021/cr940534g.

(25) AL-Salami, F. M. A. Modification of Acrylic Acid and Acryloyl Chloride Polymers. *Baghdad Sci. J.* **2005**, *2* (4), 645–652. https://doi.org/10.21123/bsj.2005.11895.

(26) Buruiana, E. C.; Buruiana, T.; Hahui, L. Preparation and Characterization of New Optically Active Poly(N-Acryloyl Chloride) Functionalized with (S)-Phenylalanine and Pendant Pyrene.

J. Photochem. Photobiol. Chem. **2007**, *189* (1), 65–72. https://doi.org/10.1016/j.jphotochem.2007.01.008.

(27) Lu, M.; Fan, H.; Liu, Q.; Sun, X. A Facile Synthetic Method for Anhydride from Carboxylic Acid with the Promotion of Triphenylphosphine Oxide and Oxaloyl Chloride. *ACS Omega* **2022**, *7* (38), 34352–34358. https://doi.org/10.1021/acsomega.2c03991.

(28) Odian, G. *Principles of Polymerization*, 4th ed.; J. Wiley & sons: Hoboken (N.J.), 2004.

(29) Degtyareva, T. V.; Kudryavtsev, Val. N.; Aliyev, R. E.; Kabanov, V. Ya. Investigation of the Interaction of Thionyl Chloride with Polyacrylic Acid Radiation Grafted to Polymers. *Polym. Sci. USSR* **1991**, *33* (9), 1791–1798. https://doi.org/10.1016/0032-3950(91)90015-I.

Chapter 4 – Doping of N2200 with DMBI Derivatives

4. Doping of N2200 with Dimeric and Monofunctional DMBI Derivatives

---

This work was performed in collaboration with Mariano Campoy-Quiles's group and David Brian Amabilino's group at the Institute of Materials Science of Barcelona (ICMAB-CSIC).

After synthesizing the dimeric dopant MDI-DMBI$_2$, we selected the semiconducting polymer N2200 as the reference system to evaluate its doping behavior. This choice ensures direct comparison with the monofunctional dopants previously studied in Chapter 2, allowing us to isolate the effect of **molecular structure** on the doping process.

The goal of this study was to examine how combining two DMBI units within a single molecule influences the interaction with the polymer matrix and the resulting electronic properties. We aimed to verify whether the presence of two redox centers, connected through urethane linkages, could promote structural stabilization through possible intermolecular crosslinking.

The following sections present the experimental strategy, the results obtained, and their interpretation considering this design hypothesis.

Experimental strategy

Our goal was to draw a comparison between the dimeric dopant **MDI-DMBI$_2$** and two reference molecules: **N-DMBI-H**, used as the benchmark dopant, and **An-DMBI**, a monofunctional analogue sharing the same DMBI core but bearing an aromatic substituent (see Figure 4.1).

Among the monofunctional dopants previously investigated, An-DMBI is the most similar MDI-DMBI$_2$, as both present aromatic and polar substituents capable of dipolar and hydrogen-bonding interactions, which influence their aggregation and doping behavior.

This comparison therefore partially isolates the effect of bifunctionality from that of substituent modification, while also providing a consistency check with previous studies performed under different deposition conditions (i.e. spin-coating).[1]

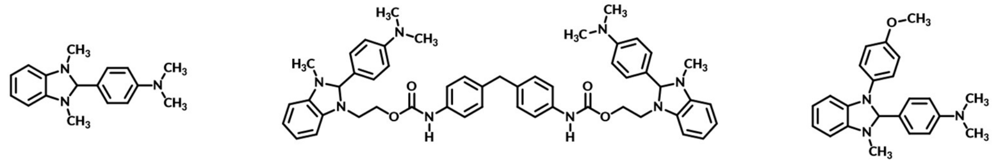

N-DMBI MDI-DMBI$_2$ An-DMBI

Figure 4.1
Chemical structures of the dopants used in this work: N-DMBI, MDI-DMBI$_2$, and An-DMBI.

Our goal was to establish a framework to understand how molecular structure, particularly the presence of two DMBI units and urethane linkages in the dimer, influences the macroscopic properties of doped N2200 films. To this end, we combined **electrical conductivity measurements** with **morphological analysis by atomic force microscopy (AFM)**, correlating changes in conductivity with surface evolution upon thermal activation of the dopant.

We prepared all films via **solution processing using a blade-coating technique**, chosen for its reproducibility and precise control over coating parameters such as thickness. Identical processing and annealing protocols were applied to all samples to ensure comparability.

Before discussing the results, it is thus useful to briefly outline the main aspects of the **solution processing approach**, since the morphology and doping response of N2200 are strongly dependent on the coating conditions. The following section summarizes the most relevant principles from literature, providing the context needed to interpret the experimental observations presented later in this chapter.

4.1. Solution Processing

Solution processing represents a **cost-effective** and **scalable** strategy for the fabrication of thin-film optoelectronic devices.[2] Unlike wafer-scale deposition methods, it enables direct deposition of functional layers from solution, offering compatibility with large-area substrates and mechanical flexibility. The approach is highly **versatile**, supporting the integration of diverse material classes such as organic semiconductors, perovskites, or quantum dots. Moreover, its compatibility with layer-by-layer deposition facilitates the production of **complex device architectures**. From both environmental and economic perspectives, solution processing significantly reduces material waste and energy consumption compared to conventional vacuum deposition.[3,4]

Typical substrates for solution-processed films include glass, metallic foils, and flexible polymeric supports.[2] Prior to deposition, substrates are cleaned and commonly treated, for example with UV-ozone or solvent rinses, to improve wettability and film adhesion. The active material, for example, a mixture of semiconducting polymer and dopant as in this work, is dissolved in an appropriate organic solvent to form a homogeneous solution. This solution can then be deposited by a wide range of **coating methods** (Figure 4.2), among which spin-coating and blade-coating are the most relevant.[5]

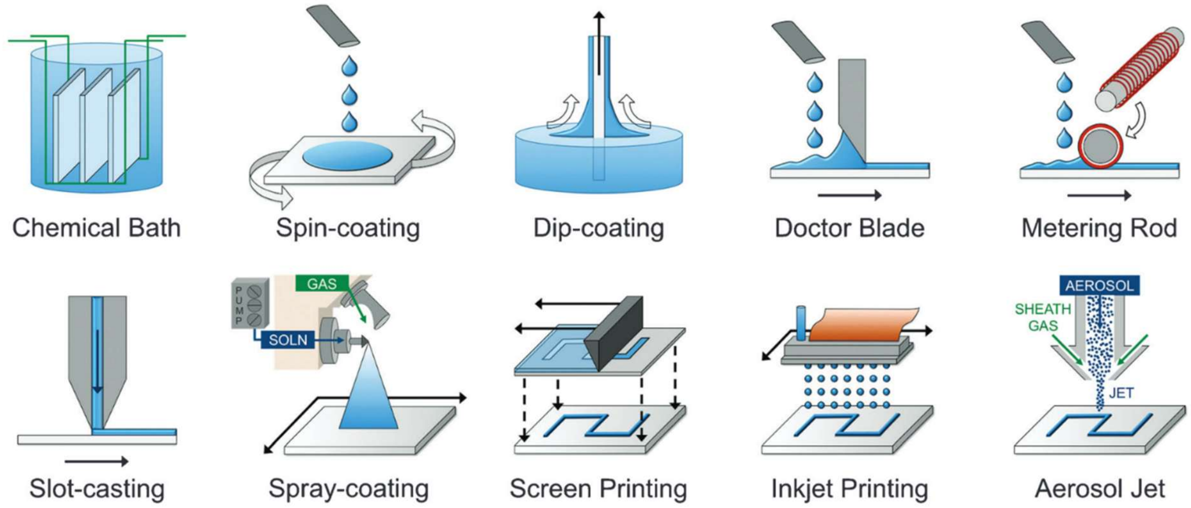

Figure 4.2
Illustration of the most common solution processing methods. Reproduced with permission of the Royal Society of Chemistry from the work of Chiverly et al.[6]

Spin-coating is widely employed at the laboratory scale due to its simplicity, reproducibility, and speed. However, it suffers from relevant material waste and poor scalability, making it unsuitable for large-area manufacturing. In contrast, **blade-coating** is a meniscus-guided deposition method that ensures high material employment, uniform film formation, and straightforward scalability. Its adaptability to both small-area substrates and continuous roll-to-roll processing makes it a promising bridge between lab-scale and industrial-scale device fabrication. For these reasons, blade coating was selected in this work as the primary deposition strategy.

4.1.1. Blade-coating

In the blade-coating process, the solution is dispensed in front of the blade and fills the gap between the blade and the substrate. This geometry gives rise to two menisci: the **advancing meniscus** at the front, which is related to substrate wetting, and the **receding meniscus** at the rear, which determines film quality. The advancing meniscus is characterized by the contact angles with the blade and substrate (θ_1 and θ_2, respectively) and by its height (H), which collectively define the optimal coating speed (U) (Figure 4.3).[7,8]

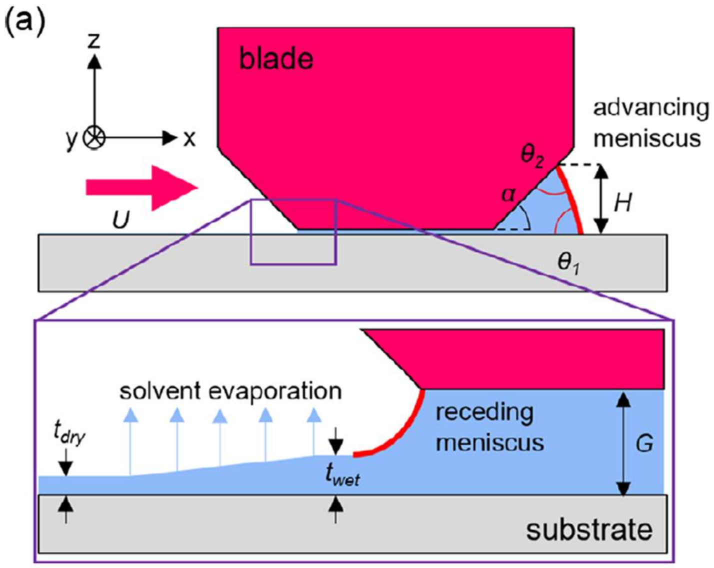

Figure 4.3
Schematical representation of blade coating process, where the geometrical parameters are highlighted. Reproduced from the work of Siegrist et al.[8] License CC BY-NC 4.0.

Two distinct coating regimes are typically observed depending on the coating speed:

1. **Evaporation regime** (low velocities):
   In this regime, solvent evaporation from the meniscus dominates. As solvent evaporates near the contact line, solute accumulates, giving rise to the so-called **coffee-ring effect**. Increasing the meniscus height enhances solvent evaporation, thereby producing thicker films. Moreover, solute transport toward the contact line is affected by **Marangoni flows**, further influencing deposition. Films formed at low coating speeds often exhibit defects referred to as dark spots, corresponding to locally thinner regions.

2. **Landau-Levich regime** (high velocities):
   At higher coating speeds, solvent supply exceeds the evaporation rate. The solidification front is moved further from the deposition front, allowing casting, leveling, and drying processes to occur independently. Here, **viscous drag** dominates over surface tension forces, pulling solution out of the advancing meniscus and generating thicker wet and, consequently, dry films. Film thickness increases with coating velocity under these conditions.

Additionally, there are several secondary factors that influence the final film's thickness and uniformity.[8–10] Among these, the **concentration of the coating** solution plays a central role: higher solute concentrations generally lead to a linear increase in dry film thickness, although excessively concentrated solutions may suffer from increased viscosity, which hinders homogeneous spreading and can introduce morphological defects. The **initial volume** of solution dispensed in front of the blade also affects the process, as it determines the height of the meniscus. A gradual decrease in meniscus height during coating often results in a thickness gradient along the coating direction. However, this issue can be mitigated by dispensing larger volumes or by adjusting the blade angle to stabilize the meniscus.

The substrate **temperature** imposes a critical influence. Elevated temperatures favor solvent evaporation, thereby limiting capillary flows responsible for the coffee-ring effect. Consequently, films formed under these conditions tend to be more homogeneous, though typically slightly thinner due to the reduced time available for solution leveling. Closely related are the intrinsic properties of the solvent itself, such as volatility and surface tension: highly volatile solvents may promote rapid drying but increase the risk of inhomogeneities, while solvents with high surface tension stabilize the meniscus with the effect of impeding uniform spreading. Finally, the **wettability** of the substrate, often tuned through treatments such as UV-ozone or plasma cleaning, strongly impacts film quality: improved wetting facilitates stable meniscus formation and uniform coverage, reducing the probability of formation of pinholes, dark spots, and other local defects.

4.2. Deposition and annealing of doped N2200 films

Doping of conjugated polymers can be performed either **sequentially**,[11–13] e.g., dipping a pre-formed semiconductor layer into a dopant solution followed by thermal annealing, or **by co-deposition**, where semiconductor and dopant are co-dissolved and processed together into a film.[14,15]

In the sequential route, **solvent orthogonality** is required between the polymer deposition solvent and the dopant carrier, when this condition is satisfied, sequential doping is often favored because it preserves the semiconductor morphology.[16,17] Its limitation is that dopants must penetrate and diffuse into the host matrix, thus, bulky dopants frequently yield surface-confined doping and diminished performance.[18] In co-deposition, dopant and polymer already reach **intimate mixing** during the preparation of the solutions, but the dopant have a more relevant influence on microstructure, i.e. the film morphology highly sensitive to host-dopant miscibility. For **N2200/N-DMBI** systems specifically, co-deposition is commonly adopted.[19–22] Halogenated solvents, in particular, 1,2-dichlorobenzene (DCB), chlorobenzene, and chloroform, are commonly used for solution processing .[18,23,24]

Considering the **larger size** of the target DMBI derivatives compared with the benchmark, we adopted **co-deposition** as the processing route most likely to ensure bulk incorporation. We first optimized **blade-coating procedure**, the chosen solution-processing technique, using neat N2200 to establish film uniformity and thickness control. We then deposited polymer-dopant blends of N-DMBI-H, An-DMBI, and MDI-DMBI$_2$ onto substrates with pre-patterned contacts, followed by **thermal annealing** to activate the dopant. For each polymer-dopant pair we applied six annealing temperatures.

4.2.1. Blade coating optimization

The blade-coating trials clearly highlighted how processing parameters determine the quality and uniformity of N2200 films.

In the **first trial** (coating speed = 5 mm s^{-1}, stage temperature = 40 °C, gap = 1450 μm, 100 μL of a 5 mg mL^{-1} N2200 solution in DCB), the process operated within the **evaporation regime**. The slow meniscus velocity and moderate temperature led to high solvent loss at the contact line, and thus, non-uniform solute accumulation. The resulting films exhibited significant inhomogeneities and thinner regions.

By increasing both **velocity** (20 mm s^{-1}) and **stage temperature** (80 °C) in **Trial 2**, while keeping the same solvent and a smaller deposited volume (40 µL), we partially mitigated these defects. The higher velocity shifted the process toward the **Landau–Levich regime**. Consequently, film uniformity improved, and macroscopic coverage became more homogeneous. Nevertheless, material accumulation at the rear edge of the substrate was still present, likely due to the rapid evaporation of DCB at elevated temperature, condition that favors meniscus pinning and relevant thickness gradients.

The best results were obtained in **Trial 3**, where **chloroform** replaced DCB as solvent and both the **polymer concentration** (15 mg mL^{-1}) and **deposited volume** (100 µL) were increased. The process, performed at **room temperature**, with a **20 mm s^{-1} coating velocity** and a **1350 µm gap**, produced the most homogeneous films. Chloroform's higher volatility and better solubility for both N2200 and the dopant permitted rapid but controlled drying, while the higher solution concentration compensated for the rapid evaporation rate. Although no profilometric or microscopic characterization was operated at this point, direct **optical inspection** provided a reliable comparison: films from Trials 1 and 2 showed visible transparency variations, whereas the film obtained from Trial 3 appeared continuous and free of defects. We considered this qualitative assessment sufficient to identify the optimal coating conditions for subsequent doping experiments.

4.2.2. Sample preparation

Once the deposition parameters had been optimized, doped films were prepared from **polymer-dopant solutions** containing either N-DMBI-H, MDI-DMBI$_2$, or An-DMBI. All formulations were based on N2200 at a concentration of 15 mg mL^{-1} in chloroform, ensuring good solubility and uniform film formation under the optimized coating conditions. The **dopant loading** was set in respect of the polymer repeating units, corresponding to **20 mol%** for both **N-DMBI-H** and **An-DMBI**, and **10 mol%** for the dimeric dopant **MDI-DMBI$_2$**. In literature, this dopant concentration for N-DMBI, 20%mol, corresponds to a maximum of electrical conductivity.[25] These concentrations were selected to achieve comparable doping levels while taking in account the bifunctional nature of the dimer.

The deposition of the solution was performed onto **microscope glass slides pre-patterned** with gold electrodes (45 nm) deposited on a thin chromium adhesion layer (5 nm) (A, Figure 4.4). Each substrate comprised three parallel rows of channels (1 mm width, variable length: 30, 40, 50, 60, 80 µm), allowing multiple regions to be exposed to different thermal conditions on the same slide (B, Figure 4.4). This geometry ensured reliable electrical contact and enabled direct comparison of conductivity across distinct annealing temperatures.

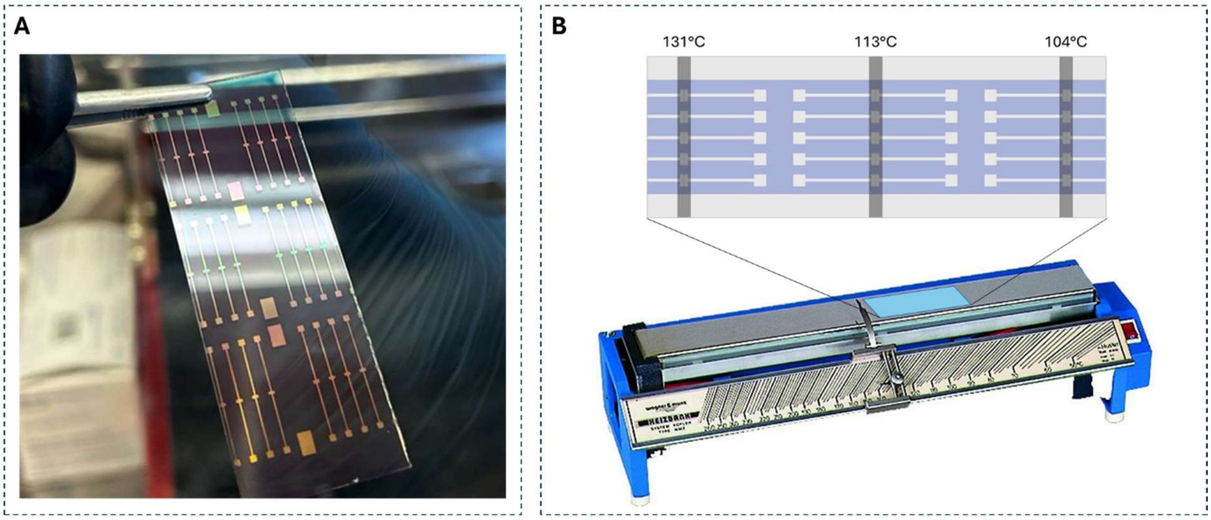

Figure 4.4
(A) Photography of one of the deposited samples.
(B) Schematic of the electrode layout and the Kofler bench used for annealing at different temperatures.The Kofler bench image is reproduced from Equascience: https://www.equascience.com/mesure-chimique/1037-banc-kofler.html.

After deposition, the substrates were placed on a **Kofler bench**, a device that provides a **controlled temperature gradient** along its length. This setup allowed the simultaneous **annealing of different film regions** at progressively increasing temperatures, thereby minimizing sample-to-sample variability and ensuring consistent comparison between dopants under identical processing conditions.
Recent studies have shown that **DMBI-based dopants** can exhibit measurable doping activity even at **room temperature**, indicating that charge transfer may occur without the need for intentional thermal activation.[1,26] This observation challenges the conventional view that elevated temperatures are strictly required to trigger dopant activation.[22]

At the same time, temperature still plays a complex role in defining the final properties of doped films, as exposed in the introduction of Chapter 3. While, on the one hand, thermal annealing can enhance dopant activation and increase charge-carrier generation. On the other, it can also promote **diffusion and phase segregation**, which may deteriorate film homogeneity and stability. Thus, temperature acts as a **double-edged parameter**, simultaneously improving electronic activation and triggering structural reorganization.

4.3. Electrical conductivity

To clarify the interplay between doping and annealing, we characterized the **electrical conductivity** of doped N2200 films both **before** and **after annealing** at various temperatures for 1h. A control sample consisting of pristine N2200 was also prepared. **Notably, all the samples were deposited, annealed and characterized under inert atmosphere, avoiding their oxidation in air**.
Overall, this approach allows us to separate the intrinsic room-temperature activity of the dopants from the effects induced by thermal treatment, providing a complete view of how temperature influences both activation and morphology.

We expected that at higher annealing temperatures, where dopant activation becomes more efficient, the **crosslinking tendency of the dimeric MDI-DMBI$_2$** could permit to achieve **higher conductivities** while maintaining **more stable morphologies**. Testing this hypothesis was one of the main motivations for conducting the temperature-dependent study described in this section.

4.3.1. Results and discussion

The obtained conductivity (σ) values, and the corresponding standard deviations, are reported in Figure 4.5. For each polymer-dopant system, the evolution of conductivity as a function of annealing temperature is shown.
Since the samples showed a high resistance, typically in the range of tens to hundreds of MΩ, thus approaching the upper detection limit of the measurement setup, the measurements errors are relatively high. Coherently, in the case of the **control film,** the electrical resistance could not be measured, as it exceeded the instrument's sensitivity range. This result further confirms that the doping process enhances significantly the conductivity of the N2200 film.

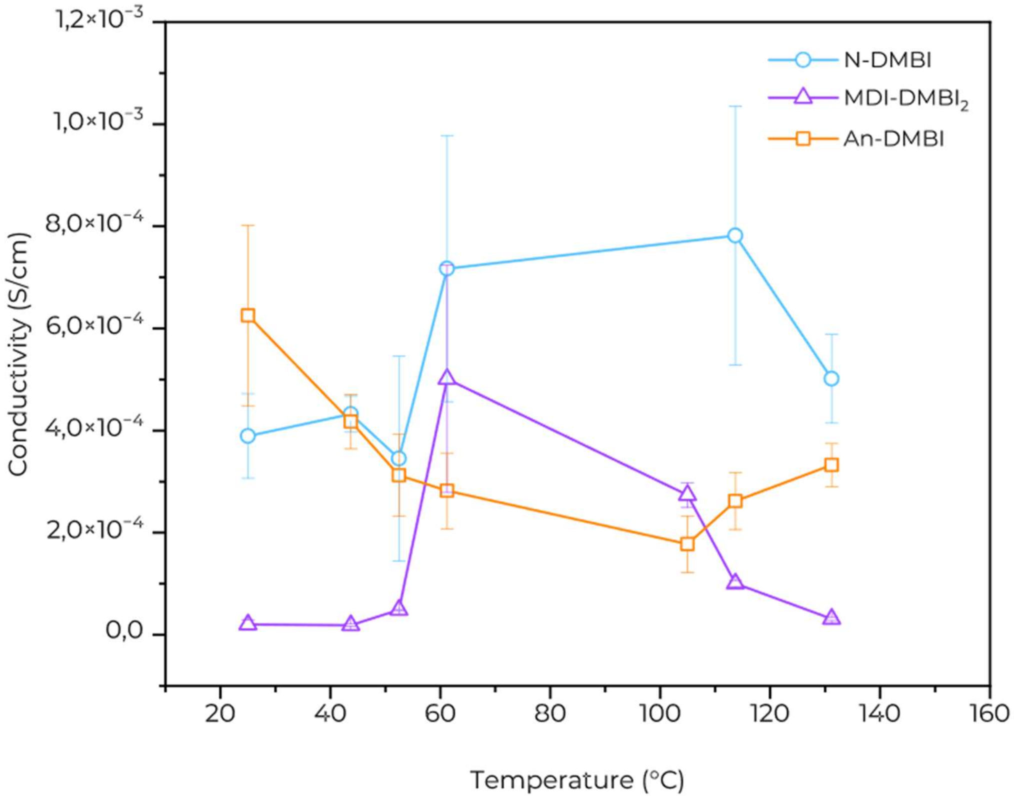

Figure 4.5
Electrical conductivity of N2200 films doped with N-DMBI-H, MDI-DMBI$_2$, and An-DMBI as a function of annealing temperature. Conductivity values were averaged over five electrodes per annealing condition, and error bars represent the standard deviation.

Conductivity is already measurable in the **as-cast films** (25 °C), indicating that charge transfer can occur without thermal activation. Then, upon annealing, each dopant exhibits a distinct response: for N-DMBI-H, σ increases with moderate annealing, reaches a maximum in the ~60-110 °C range, and then decreases at higher temperatures; for MDI-DMBI$_2$, σ displays a narrow maximum around at 61°C followed by a reduction upon further heating; for An-DMBI, σ is highest at room temperature and decreases with annealing, until it with a slight increase again in the range 104-131°C.

Overall, N-DMBI-H delivers the highest conductivities, MDI-DMBI$_2$ yields intermediate values within a narrower thermal window, and An-DMBI shows lower conductivities than the benchmark that decrease upon heating. These trends are consistent with a competition between **dopant activation** at low-to-moderate temperatures and **segregation processes** that dominate at higher temperatures.

The lower doping performance of An-DMBI in respect of N-DMBI is coherent with the results obtained in another work of our group.[1] While overall lower conductivity of MDI-DMBI$_2$ relative to N-DMBI-H is reasonable given its **greater steric bulk** and the presence of a **non-redox-active methylenediphenyl urethane spacer**, which can hinder miscibility and effective charge generation/transport compared to the benchmark.[27]

What is more unexpected is the **drop in σ** at higher temperatures for MDI-DMBI$_2$: if increasing temperature primarily enhanced dopant activation, this would directly translate in a more dense **ionic crosslinking** and, consequently, suppressed phase segregation.

Considering the details of the phenomenon we can say that in the absence of other counter-anions, the cationic dimer (two benzimidazolium sites) pairs directly with polymer polarons (P^-). In a low-ε host such as N2200, **strong ion pairing** is expected, thus, the dication can bridge two P^- segments, acting as an ionic crosslinker that suppresses large-scale phase separation during thermal processing. The same ionic interaction, however, can localize charge (**Coulomb trapping**), reducing the fraction of free carriers and/or the effective mobility.[20] Urethane linkages have N-H···O=C hydrogen-bonding capability, which may further stabilize local associations or promote dopant-rich microdomains that can be triggered by an increase in temperature (nucleation).[28] Therefore, an optimum conductivity is likely reached at moderate annealing temperatures, where ionic crosslinking favors interfacial contact. While, at higher temperatures, conductivity decreases again as **ion-paired clusters form**.

4.4. Morphology Characterization by AFM

Atomic force microscopy (AFM) represents a powerful tool to investigate the **surface morphology** of doped polymer films, providing nanometric resolution and quantitative roughness information.[15,29] As mentioned before, morphology plays a crucial role in determining charge transport, as the disposition and connectivity of **fibrillar domains** directly influence in-plane conductivity. Several examples of this relationship have been reported in the literature for N2200-based systems[24,30] Variations in surface texture, such as **transitions** from a continuous fibrillar network to more granular or segregated structures, are often related to changes in molecular packing or dopant distribution induced by thermal treatment.

For this reason, we employed AFM to correlate the morphological evolution of the doped N2200 films with their electrical performance across the different annealing temperatures. This approach enabled a more comprehensive understanding of how the combination of doping and thermal treatment affects both film structure and charge transport pathways.

4.4.1. Results and discussion

To visualize in a direct way the morphological evolution induced by doping and thermal annealing, both **planar** (Figure 4.6) and **three-dimensional AFM representations** (**Figure 4.7**) are reported. The root mean square (RMS) roughness values, calculated from the height data, are shown alongside the 2D maps, which enable detailed comparison of surface texture across different dopants and annealing conditions. At the same time, the 3D views, emphasize relative height variations and the degree of surface coarsening.

All AFM topographies correspond to **post-annealed states**, except for the topography of the control film constituted by the neat polymer.

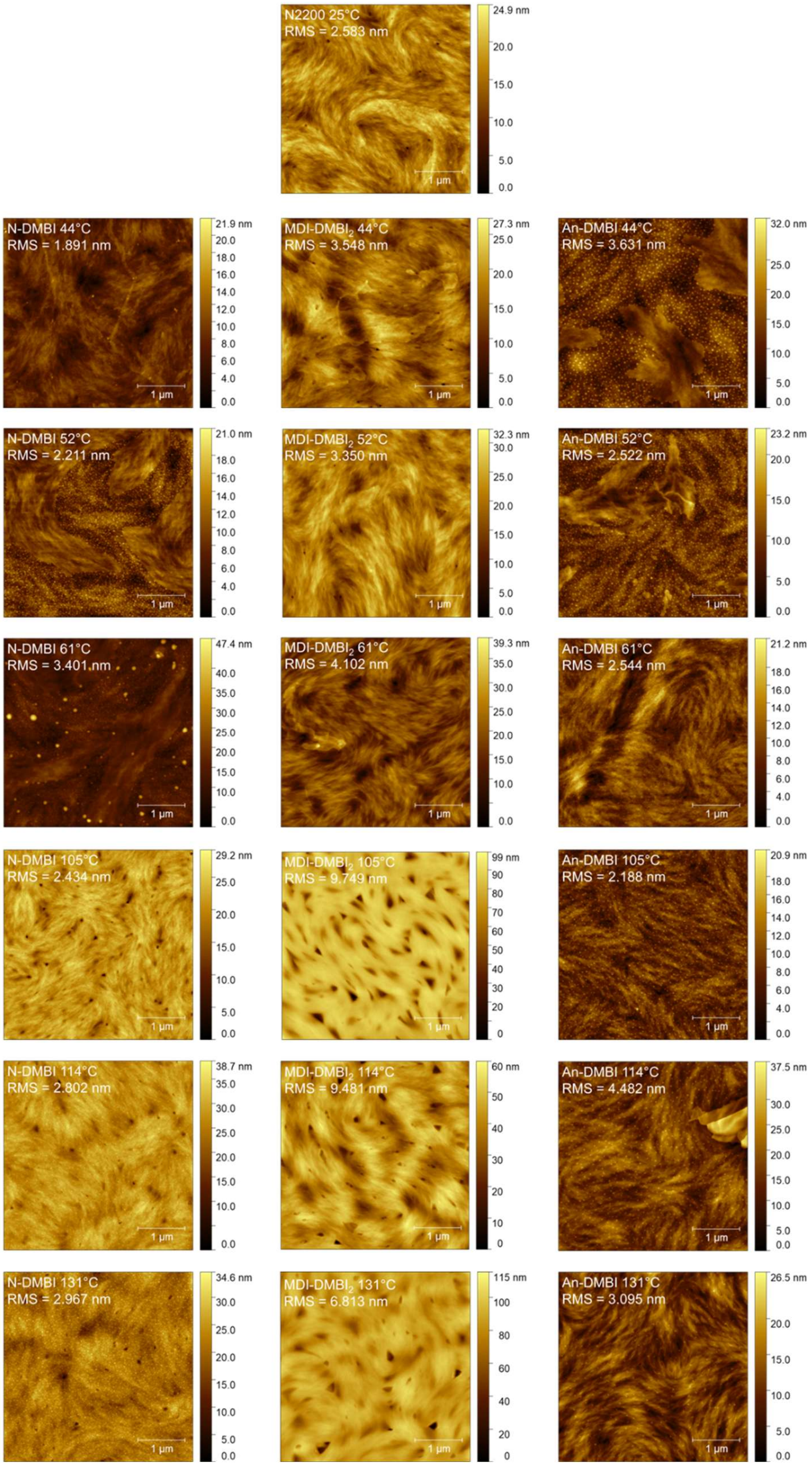

Figure 4.6
2D AFM topography images of N2200 films doped with N-DMBI-H, MDI-DMBI$_2$, and An-DMBI after thermal annealing at different temperatures. RMS roughness values are reported for each condition. The undoped N2200 reference (middle top) provides a comparison for the intrinsic polymer morphology.

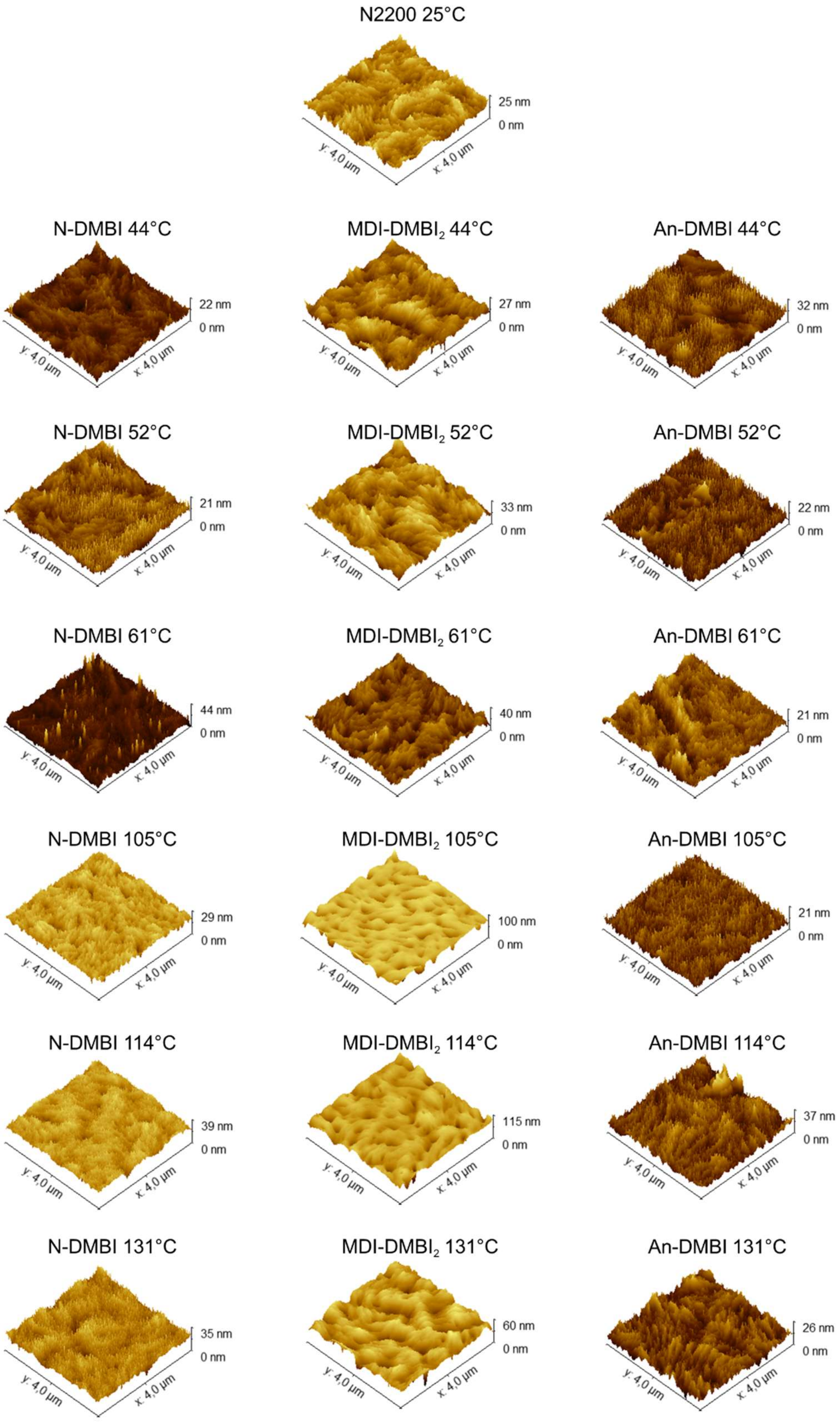

Figure 4.7
3D AFM height maps of N2200 films doped with N-DMBI-H, MDI-DMBI$_2$, and An-DMBI after thermal annealing at different temperatures.

N-DMBI-H

At 44 °C, the film displays a **moderately connected texture** with extended surface features (RMS roughness ~ 1.8-2.4 nm), in agreement with the semicrystalline morphology typically reported for pristine N2200. Upon mild annealing (~60 °C), a slight coarsening occurs, accompanied by the appearance of small granular domains (RMS roughness ~ 3.4 nm). Further heating to 105-114 °C restores a more homogeneous, percolative topography (RMS roughness ~ 2.2-2.5 nm), suggesting **partial reorganization** of the polymer backbone and improved interconnectivity. At the highest annealing temperature (~131 °C), inhomogenities reappear, and the RMS roughness rises again (~3 nm), indicating initial segregation or roughening.

This morphological evolution closely follows the conductivity trend for N-DMBI: σ reaches its maximum at intermediate annealing temperature, where average roughness and good connectivity provide optimal charge transport, and lowers at higher temperatures when excessive diffusion and segregation lead to morphological disruption.

MDI-DMBI$_2$

Already at 44 °C, the film surface exhibits a granular texture (RMS roughness ~ 3.5-4.0 nm), with uniformly distributed nodular domains, suggesting **limited miscibility** between the dimeric dopant and the polymer matrix even before effective thermal activation. Upon mild annealing to ~60 °C, the nodules slightly increase in size, and the RMS roughness increases from ~3.5 nm to ~4.1 nm, consistent with partial dopant activation accompanied by **local aggregation** instead of morphological improvement. Further heating to 105-114 °C results in clear **coarsening** and the formation of **localized voids**, indicative of partial film disruption. At 131 °C, the surface seems to be more homogeneous and more continuous than at intermediate temperatures, and the RMS roughness decreases from ~9.5 nm to ~6.8 nm, possibly due to partial relaxation of the dopant-rich domains. This **morphological** evolution mirrors the conductivity behavior, where the initial activation-driven increase is followed by a decline at higher temperatures as aggregation and local heterogeneity hinder percolation pathways.

An-DMBI

Across the entire temperature range (44-131 °C), the films exhibit a uniform surface morphology with interconnected domains and RMS roughness values between ~2.5 and ~4.5 nm. No clear structural transitions are observed upon annealing, indicating that thermal treatment induces only minor morphological effects.

Therefore, the monotonic decrease in conductivity with temperature that we have registered, is more likely related to changes in dopant-polymer interactions or sub-surface organization rather than from significant morphological coarsening detectable by AFM.

4.4.2. Summary

AFM analysis reveals distinct morphological behaviors among the three dopants.

N-DMBI-H forms films with moderately rough, interconnected textures that reorganize reversibly with annealing, showing an apparent optimum at intermediate temperatures where surface continuity and conductivity are both higher.

In contrast, MDI-DMBI$_2$ films exhibit a granular topography even at low temperature. Upon heating, pronounced coarsening and void formation occur, while a minor recovery of uniformity at the highest temperature likely reflects partial relaxation of dopant-rich areas.

An-DMBI-doped films remain largely unchanged throughout the annealing range, with RMS roughness values comparable to those of the other systems (~2.5-4.5 nm). However, this apparent morphological stability does not coincide with improved conductivity, suggesting that similar roughness values can correspond to different microscopic organizations or dopant distributions.

Collectively, AFM data indicate that **surface continuity** and **nanoscale connectivity**, rather than roughness amplitude alone, tend to correlate with higher charge transport, although sub-surface or electronic factors could play a significant role as well.

4.5. Conclusion

The comparative investigation of N-DMBI-H, MDI-DMBI$_2$, and An-DMBI clarifies how molecular structure affects both the efficiency and the thermal evolution of n-type doped N2200 films. The conductivity measurements performed confirm that charge transfer occurs already at room temperature, demonstrating that DMBI-based dopants can be active without thermal activation. Nevertheless, temperature plays a critical role in the doping process: moderate annealing enhances activation and morphological organization, whereas higher temperatures usually lead to dopant redistribution and conductivity loss.

Among the three systems, **N-DMBI-H** showed the highest conductivity and the broadest activation window.
MDI-DMBI$_2$ exhibited intermediate conductivity within a narrower range. Its granular morphology and the pronounced coarsening with void formation observed upon annealing indicated increasing surface roughness and possible film disruption, which likely hindered charge transport. Although its **bifunctional design** could, in principle, favor ionic crosslinking or interfacial stabilization, the obtained results did not provide clear evidence of such effects.
An-DMBI, instead, displays the lowest conductivities, decreasing gradually with temperature. On the contrary, the surface morphology remains largely unchanged, indicating that its thermal response may be influenced by sub-surface or electronic factors rather than by visible structural rearrangements.

In summary, contrary to our expectations, MDI-DMBI$_2$ did not lead to enhanced doping efficiency in N2200 under the conditions investigated. The combination of strong local interactions and partial incompatibility with the polymer matrix seemed to limit its macroscopic transport properties. However, its **structural rigidity** and the possibility to form **ionic crosslink** may become advantageous in systems where morphology is more robust. The next chapter explores this possibility by investigating MDI-DMBI$_2$ in semiconducting carbon nanotube films, where a percolative conductive network may highlight different aspects of its functional behavior.

4.6. Experimental procedure

Poly[[1,2,3,6,7,8-hexahydro-2,7-bis(2-octyldodecyl)-1,3,6,8-dioxobenzo[lmn][3,8]phenanthroline-4,9-diyl][2,2'-bithiophene]-5,5'-diyl] (P(NDI2OD-T2), N2200) was purchased from 1-Material Inc. (Mw ≈ 130 kDa, Mn ≈ 55 kDa, PDI ≈ 2.4).

All the solvents have been purchased by Sigma-Aldrich or Labkem. All solution preparations and film depositions were performed under inert atmosphere in a nitrogen glovebox, unless otherwise specified.

4.6.1. Blade coating

An initial N2200 solution was prepared by dissolving 5.21 mg of polymer in 521 μL of 1,2-dichlorobenzene (DCB, 10 mg mL^{-1}) inside a GC vial containing a magnetic stir bar. The vial was sealed with Parafilm, wrapped in aluminum foil, sonicated for 5 min at 35 °C outside the glovebox, returned inside, and stirred for 24 h at room temperature (400 rpm), yielding a homogeneous solution. For optimized conditions, a fresh stock was prepared by dissolving 16.66 mg of N2200 in 0.833 mL of chloroform ($CHCl_3$, 20 g L^{-1}). The solution was stirred for 24 h in the glovebox and filtered through a 0.2 μm syringe filter prior to use.

Microscope glass slides were used as substrates, that had been clean before usage by a sequential sonication in organic solvents: acetone (5 minutes), Hellmanex (2% v/v in distilled water, 5 minutes), 2-propanol (5 minutes), NaOH (2M, 10 minutes). Before changing the solution, the substrates were rinsed with distilled water. Successively, substrates were treated by UV-ozone for 15 min. Slides were then transferred to the glovebox.

For blade coating, each slide was fixed onto the coating stage with a small droplet of solvent. Two auxiliary slides were employed: one in front, onto which the solution was initially dispensed, and one at the rear to collect excess solution and mechanically stabilize the substrate. Initial trials of depositions were performed to identify suitable parameters:

- **Trial 1:** velocity 5 mm s^{-1}, stage temperature 40 °C, gap 1450 μm, deposited volume 100 μL, polymer solution 5 mg mL^{-1} in DCB.
- **Trial 2:** velocity 20 mm s^{-1}, stage temperature 80 °C, gap 1450 μm, deposited volume 40 μL, polymer solution 5 mg mL^{-1} in DCB.

- **Trial 3:** velocity 20 mm s^{-1}, room temperature, gap 1350 µm, deposited volume 100 µL, polymer solution 15 mg mL^{-1} in chloroform.

The third condition yielded the most homogeneous films and was therefore selected for subsequent experiments.

Source-drain electrodes were defined on cleaned glass substrates using a Low-Density Linear Channel Mask (Ossila), consisting of 1 mm-wide channels with lengths of 30, 40, 50, 60, and 80 µm (one per substrate). Metal contacts were deposited by thermal evaporation of 5 nm Cr followed by 45 nm Au. Patterned substrates were cleaned again using the same protocol and reintroduced into the glovebox.

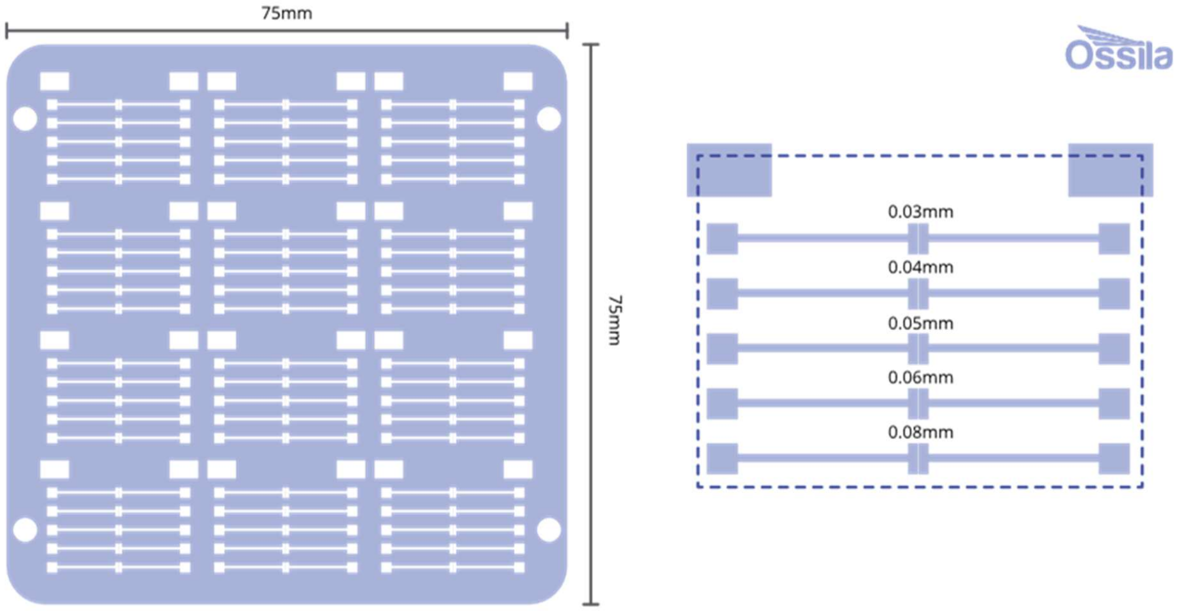

Figure 4.8
Schematic of the Low-Density Linear Channel Mask (Ossila). Source: Ossila (https://www.ossila.com/products/ofet-source-drain-mask-low-density), accessed on 09/10/2025.

Stock solutions of the dopants were prepared right before mixing them with the polymer solution to avoid dopant degradation. N-DMBI-H (4.04 mg), MDI-DMBI$_2$ (6.39 mg), and An-DMBI (5.44 mg) were each dissolved in 0.5 mL of chloroform. This yielded concentrations of 30 mM for N-DMBI-H and An-DMBI, and 15 mM for MDI-DMBI$_2$. The solutions were homogenized by stirring in the glovebox.

For each dopant, a working solution was prepared by mixing 10 μL dopant stock, 75 μL polymer stock (20 g L^{-1} in chloroform), and 15 μL pure chloroform in a GC vial. The mixtures were stirred for 1 h under inert and dark conditions before deposition. Films were blade-coated onto two pre-patterned microscope slides per dopant using the optimized parameters (Trial 3: 20 mm s^{-1}, room temperature, gap 1350 μm, volume 100 μL). The deposited films appeared homogeneous but exhibited a small thickness gradient along the coating direction.

4.6.2. Annealing

Coated substrates were dried in the glovebox and annealed using a Kofler heating bench. The instrument consists of a metal strip with a thermal gradient along its length. Each row of electrodes was positioned at a defined instrumental temperature, and the effective temperature was obtained using a calibration curve. As-cast films were also measured at 25 °C prior to annealing.

4.6.3. Electrical conductivity measurements under inert atmosphere

Electrical characterization was performed after annealing to evaluate the conductivity of the doped N2200 films. Each row of the patterned substrate contained five channels, from which one averaged conductivity value per annealing temperature was extracted. Measurements were carried out using a collinear four-probe configuration adapted to our electrode geometry. A **Keithley 2400 SourceMeter** was operated in **Auto-Ohms (autorange)** mode with **remote sensing (four-wire configuration)** under an inert atmosphere to minimize contact resistance and measurement noise.

Unlike standard collinear setups for continuous thin films, our devices consist of **patterned gold/chromium electrodes** defining channels with known length (L) and width (W). In this configuration, the electrical conductivity (σ) was determined directly from the device geometry and the measured resistance (R) according to:

$$\sigma = \frac{L}{W\, t_z\, R} \tag{4.14}$$

where t_z is the local film thickness determined independently by AFM.

For each dopant-polymer system and each annealing temperature, five resistance values were collected, one from each channel in the corresponding row, and converted into conductivity values using the above expression. The resulting five σ values were then averaged to obtain the mean conductivity, while the corresponding **standard deviation** reflects the variability at a given temperature.

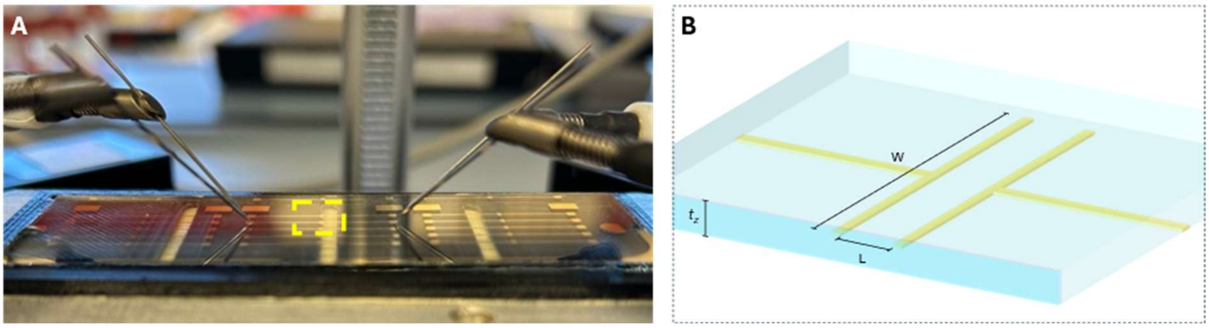

Figure 4.9
(A) Electrical measurement setup showing the collinear four-probe configuration used to determine the conductivity of doped N2200 films.
(B) Schematic representation of a single measurement channel on the patterned substrate, highlighting the geometrical parameters used for conductivity calculation: channel length (L), width (W), and film thickness (t_z).

4.6.4. AFM measurements

The channels within each row were placed perpendicular to the long edge of the glass substrate and thus perpendicular to the blade-coating direction. Under these conditions, we considered intra-row thickness variations negligible relative to the experimental uncertainties, while we took in account thickness variability between the different rows.

AFM measurements were performed using a **Park Systems NX10** operated in **tapping (AC) mode** under ambient laboratory conditions. For all doped samples, AFM images correspond to **post-annealing states**.

Topography within the channels

Morphological characterization was carried out inside the 80-µm-wide channels, away from the gold electrodes, over **4.0 × 4.0 µm^2** scan areas at **512 × 512 pixels** (pixel pitch ~ 7.8 nm/px in both directions). While image processing followed the same workflow for each sample:

1. Plane leveling;
2. Fifth-order polynomial background subtraction;
3. Line-by-line alignment using the median of differences with a first-order polynomial correction.

No height-altering smoothing filters were applied. For each image, the **root-mean-square (RMS) roughness (σq)** was extracted from the Gwyddion statistical analysis tool, using the full scanned area. Since no significant inhomogeneities or drift artifacts were observed, σq was calculated over the entire image. The uncertainty in σq, typically within ±0.1-0.2 nm, was mainly related instrumental noise and residual background subtraction errors.

Film thickness determination.

For each channel row, a controlled scratch was made in a contact-free region of the film to expose the underlying substrate. An AFM image spanning **35.8 × 5.0 µm²** was acquired across the step (fast-scan direction along the long axis) at **512 × 128 pixels**, corresponding to pixel pitches of ≈70 nm/px and 39 nm/px along the long and short axes, respectively.

Film thickness values (t_z) were obtained as the height difference between masked substrate and film regions, selected at least **1 µm** away from the scratch edge to minimize tip-convolution and edge effects. For each image, three height profiles were extracted perpendicular to the scratch direction and averaged to obtain the mean thickness. The measured thicknesses ranged from **160 nm to 550 nm**. The **related error**, varying between **±5 nm and ±50 nm**, was determined as the standard deviation among the three profiles.

4.7. Bibliography

(1) Pallini, F.; Mattiello, S.; Sassi, M.; Paoli, G.; Mattioli, G.; Rossi, P.; Coco, G.; Scaccabarozzi, A. D.; Kim, B. M.; Mariani, P.; Wakidi, H.; Flagg, S. M.; D'Arienzo, M.; Caironi, M.; Nguyen, T.; Beverina, L. Understanding the Interplay Between Thermal Activation, Diffusion, and Phase Segregation of Molecular Dopants Blended with Polymeric Semiconductors. *Adv. Electron. Mater.* **2025**, 2500170. https://doi.org/10.1002/aelm.202500170.

(2) Taylor, D. R. A. *Solution-Processed Solar Cells: Materials and Device Engineering*; IOP Publishing, 2025.

(3) Wang, S.; Peng, L.; Sun, H.; Huang, W. The Future of Solution Processing toward Organic Semiconductor Devices: A Substrate and Integration Perspective. *J. Mater. Chem. C* **2022**, *10* (35), 12468–12486. https://doi.org/10.1039/D2TC02316D.

(4) Eslamian, M. Inorganic and Organic Solution-Processed Thin Film Devices. *Nano-Micro Lett.* **2017**, *9* (1), 3. https://doi.org/10.1007/s40820-016-0106-4.

(5) Zhang, X.; Zhang, H.; Li, S.; Xiao, L.; Zhang, S.; Han, B.; Kang, J.; Zhou, H. Development and Application of Blade-Coating Technique in Organic Solar Cells. *Nano Res.* **2023**, *16* (9), 11571–11588. https://doi.org/10.1007/s12274-023-5425-9.

(6) Chilvery, A.; Das, S.; Guggilla, P.; Brantley, C.; Sunda-Meya, A. A Perspective on the Recent Progress in Solution-Processed Methods for Highly Efficient Perovskite Solar Cells. *Sci. Technol. Adv. Mater.* **2016**, *17* (1), 650–658. https://doi.org/10.1080/14686996.2016.1226120.

(7) Le Berre, M.; Chen, Y.; Baigl, D. From Convective Assembly to Landau−Levich Deposition of Multilayered Phospholipid Films of Controlled Thickness. *Langmuir* **2009**, *25* (5), 2554–2557. https://doi.org/10.1021/la803646e.

(8) Siegrist, S.; Nandi, P.; Kothandaraman, R. K.; Abdessalem, A.; Tiwari, A. N.; Fu, F. Understanding Coating Thickness and Uniformity of Blade-Coated SnO_2 Electron Transport Layer for Scalable Perovskite Solar Cells. *Sol. RRL* **2023**, *7* (14), 2300273. https://doi.org/10.1002/solr.202300273.

(9) Zheng, Z.; Wang, J.; Ren, J.; Wang, S.; Wang, Y.; Ma, W.; Zheng, L.; Li, H.; Tang, Y.; Zhang, S.; Hou, J. Rational Control of Meniscus-Guided Coating for Organic Photovoltaics. *Sci. Adv.* **2023**, *9* (31), eadg9021. https://doi.org/10.1126/sciadv.adg9021.

(10) Gu, X.; Shaw, L.; Gu, K.; Toney, M. F.; Bao, Z. The Meniscus-Guided Deposition of Semiconducting Polymers. *Nat. Commun.* **2018**, *9* (1), 534. https://doi.org/10.1038/s41467-018-02833-9.

(11) Wang, S.; Ruoko, T.-P.; Wang, G.; Riera-Galindo, S.; Hultmark, S.; Puttisong, Y.; Moro, F.; Yan, H.; Chen, W. M.; Berggren, M.; Müller, C.; Fabiano, S. Sequential Doping of Ladder-Type Conjugated Polymers for Thermally Stable n-Type Organic Conductors. *ACS Appl. Mater. Interfaces* **2020**, *12* (47), 53003–53011. https://doi.org/10.1021/acsami.0c16254.

(12) Tang, K.; Shaw, A.; Upreti, S.; Zhao, H.; Wang, Y.; Mason, G. T.; Aguinaga, J.; Guo, K.; Patton, D.; Baran, D.; Rondeau-Gagné, S.; Gu, X. Impact of Sequential Chemical Doping on the Thin Film Mechanical Properties of Conjugated Polymers. *Chem. Mater.* **2025**, *37* (2), 756–765. https://doi.org/10.1021/acs.chemmater.4c03120.

(13) Anderson, M.; Ramanan, C.; Fontanesi, C.; Frick, A.; Surana, S.; Cheyns, D.; Furno, M.; Keller, T.; Allard, S.; Scherf, U.; Beljonne, D.; D'Avino, G.; Von Hauff, E.; Da Como, E.

Displacement of Polarons by Vibrational Modes in Doped Conjugated Polymers. *Phys. Rev. Mater.* **2017**, *1* (5), 055604. https://doi.org/10.1103/PhysRevMaterials.1.055604.

(14) Wheeler, J.; Zozoulenko, I. Computational Microscopy of Spatial Dopant Distribution in Conjugated Polymer. *Adv. Electron. Mater.* **2024**, 2400662. https://doi.org/10.1002/aelm.202400662.

(15) Jacobs, I. E.; Moulé, A. J. Controlling Molecular Doping in Organic Semiconductors. *Adv. Mater.* **2017**, *29* (42), 1703063. https://doi.org/10.1002/adma.201703063.

(16) Wang, S.; Ruoko, T.-P.; Wang, G.; Riera-Galindo, S.; Hultmark, S.; Puttisong, Y.; Moro, F.; Yan, H.; Chen, W. M.; Berggren, M.; Müller, C.; Fabiano, S. Sequential Doping of Ladder-Type Conjugated Polymers for Thermally Stable n-Type Organic Conductors. *ACS Appl. Mater. Interfaces* **2020**, *12* (47), 53003–53011. https://doi.org/10.1021/acsami.0c16254.

(17) Jacobs, I. E.; Aasen, E. W.; Oliveira, J. L.; Fonseca, T. N.; Roehling, J. D.; Li, J.; Zhang, G.; Augustine, M. P.; Mascal, M.; Moulé, A. J. Comparison of Solution-Mixed and Sequentially Processed P3HT:F4TCNQ Films: Effect of Doping-Induced Aggregation on Film Morphology. *J Mater Chem C* **2016**, *4* (16), 3454–3466. https://doi.org/10.1039/C5TC04207K.

(18) Matsuo, T.; Kawabata, K.; Takimiya, K. Highly Electron-Donating Bipyranylidene Derivatives: Potential n-Type Dopants for Organic Thermoelectrics. *Adv. Energy Sustain. Res.* **2021**, *2* (11), 2100084. https://doi.org/10.1002/aesr.202100084.

(19) Yang, C.-Y.; Ding, Y.-F.; Huang, D.; Wang, J.; Yao, Z.-F.; Huang, C.-X.; Lu, Y.; Un, H.-I.; Zhuang, F.-D.; Dou, J.-H.; Di, C.; Zhu, D.; Wang, J.-Y.; Lei, T.; Pei, J. A Thermally Activated and Highly Miscible Dopant for N-Type Organic Thermoelectrics. *Nat. Commun.* **2020**, *11* (1), 3292. https://doi.org/10.1038/s41467-020-17063-1.

(20) Griggs, S.; Marks, A.; Bristow, H.; McCulloch, I. N-Type Organic Semiconducting Polymers: Stability Limitations, Design Considerations and Applications. *J. Mater. Chem. C* **2021**, *9* (26), 8099–8128. https://doi.org/10.1039/d1tc02048j.

(21) Pallini, F.; Mattiello, S.; Manfredi, N.; Mecca, S.; Fedorov, A.; Sassi, M.; Al Kurdi, K.; Ding, Y.-F.; Pan, C.-K.; Pei, J.; Barlow, S.; Marder, S. R.; Nguyen, T.-Q.; Beverina, L. Direct Detection of Molecular Hydrogen upon P- and n-Doping of Organic Semiconductors with Complex Oxidants or Reductants. *J. Mater. Chem. A* **2023**, *11* (15), 8192–8201. https://doi.org/10.1039/D3TA00231D.

(22) Liu, Y.; Villalva, D. R.; Sharma, A.; Haque, M. A.; Baran, D. Molecular Doping of a Naphthalene Diimide–Bithiophene Copolymer and SWCNTs for n-Type Thermoelectric Composites. *ACS Appl. Mater. Interfaces* **2021**, *13* (1), 411–418. https://doi.org/10.1021/acsami.0c16740.

(23) Tang, Y.; Lin, B.; Zhao, H.; Li, T.; Ma, W.; Yan, H. Significance of Dopant/Component Miscibility to Efficient N-Doping in Polymer Solar Cells. *ACS Appl. Mater. Interfaces* **2020**, *12* (11), 13021–13028. https://doi.org/10.1021/acsami.9b21252.

(24) Wei, H.; Chen, P.; Wu, T.; Xia, J.; Ding, J.; Zhang, Y.; Zeng, X.; Gong, Z.; Peng, C.; Xue, J.; Wan, Z.; Shi, W.; Lan, L.; Bai, Y.; Yue, W.; Hu, Y. High-Miscibility n-Dopant for Organic Semiconductors Enabling Highly Stable Organic Transistors. *Adv. Funct. Mater.* **2025**, *35* (36), 2500631. https://doi.org/10.1002/adfm.202500631.

(25) Wei, H.; Chen, P.; Guo, J.; Liu, Y.; Qiu, X.; Chen, H.; Zeng, Z.; Nguyen, T.; Hu, Y. Low-Cost Nucleophilic Organic Bases as n-Dopants for Organic Field-Effect Transistors and

Thermoelectric Devices. *Adv. Funct. Mater.* **2021**, *31* (30), 2102768. https://doi.org/10.1002/adfm.202102768.

(26) Cimò, S.; Denti, I.; Rossi, L.; Cassinelli, M.; Rossi, M.; Castagna, R.; LeCroy, G.; Salleo, A.; Caironi, M.; Famulari, A.; Castiglioni, C.; Bertarelli, C. A Conformationally Driven Mechanism in n-Type Doping of Naphthalene Diimide-Bithiophene Copolymer by 1H-Benzimidazoles. *Adv. Sci.* **2025**, *12* (15), 2402482. https://doi.org/10.1002/advs.202402482.

(27) Saeedifard, F.; Lungwitz, D.; Yu, Z.-D.; Schneider, S.; Mansour, A. E.; Opitz, A.; Barlow, S.; Toney, M. F.; Pei, J.; Koch, N.; Marder, S. R. Use of a Multiple Hydride Donor To Achieve an N-Doped Polymer with High Solvent Resistance. *ACS Appl. Mater. Interfaces* **2022**, *14* (29), 33598–33605. https://doi.org/10.1021/acsami.2c05724.

(28) Li, X.; Lu, Y.; Wang, H.; Pöselt, E.; Eling, B.; Men, Y. Crystallization of Hard Segments in MDI/BD-Based Polyurethanes Deformed at Elevated Temperature and Their Dependence on the MDI/BD Content. *Eur. Polym. J.* **2017**, *97*, 423–436. https://doi.org/10.1016/j.eurpolymj.2017.10.014.

(29) Patel, S. N.; Glaudell, A. M.; Peterson, K. A.; Thomas, E. M.; O'Hara, K. A.; Lim, E.; Chabinyc, M. L. Morphology Controls the Thermoelectric Power Factor of a Doped Semiconducting Polymer. *Sci. Adv.* **2017**, *3* (6), e1700434. https://doi.org/10.1126/sciadv.1700434.

(30) Liu, J.; Qiu, L.; Alessandri, R.; Qiu, X.; Portale, G.; Dong, J.; Talsma, W.; Ye, G.; Sengrian, A. A.; Souza, P. C. T.; Loi, M. A.; Chiechi, R. C.; Marrink, S. J.; Hummelen, J. C.; Koster, L. J. A. Enhancing Molecular n-Type Doping of Donor–Acceptor Copolymers by Tailoring Side Chains. *Adv. Mater.* **2018**, *30* (7), 1704630. https://doi.org/10.1002/adma.201704630

Chapter 5 – Doping of SWCNT with DMBI Derivatives

5. Doping performance of novel DMBI-derivatives on s-SWCNT films

---

This work was performed in collaboration with Mariano Campoy-Quiles's group and David Brian Amabilino's group at the Institute of Materials Science of Barcelona (ICMAB-CSIC). EPR measurements were performed by Pietro Mariani, from Massimiliano D'Arienzo's group at the University of Milano-Bicocca.

The system based on carbon nanotubes represents a clear shift in focus compared to the polymeric N2200 films discussed previously.

In contrast to soluble conjugated polymers, where film morphology and molecular packing strongly influence doping efficiency, single-walled carbon nanotube (SWCNT) networks are **insoluble**, percolative systems in which charge transport and doping processes are determined by interfacial phenomena and the accessibility of dopant molecules within the **nanotube network**.

This structural and physical difference requires a different experimental approach, both in film preparation and in the interpretation of doping behavior.

In this chapter, we have investigated n-type doping of semiconducting SWCNT films using the same family of dopants previously studied on N2200, i.e. N-DMBI-H, An-DMBI, and MDI-DMBI$_2$.

These molecules share the same redox-active DMBI core but differ in their substituents, allowing us to examine how structural modifications influence doping efficiency, adsorption behavior, and long-term stability in CNT-based materials. The CNTs employed are CoMoCAT SG65i, containing about 95% semiconducting tubes and enriched in the (6,5) chirality (~40%).

The study is organized into three main parts:

- **Film preparation and doping:** description of the procedures used for CNT dispersion, film deposition by vacuum filtration, post-treatment steps and doping procedure.

- **Thermoelectric characterization:** analysis of the Seebeck coefficient and electrical conductivity of doped films, including a detailed discussion of thickness-dependent effects and a comparison among the different DMBI-based dopants.
- **Spectroscopic investigation:** combined use of UV–Vis, Raman, and EPR spectroscopies to probe the electronic, structural, and spin-related effects of doping, with particular focus on interfacial adsorption and its role in doping stability.

Throughout this chapter, the Seebeck coefficient and electrical conductivity will be referred collectively as thermoelectric properties.

5.1. Film formation

Single-walled carbon nanotubes (SWCNTs) are insoluble in all solvents. Therefore, film formation relies on dispersing the nanotubes in a liquid medium, rather than dissolving them, followed by deposition through vacuum filtration.[1] CNTs naturally tend to aggregate due to strong π–π interactions among adjacent tubes.[2] Therefore, the key objective of these processes is to obtain mainly homogeneous dispersions free of aggregates, which requires careful selection of the **solvent**, the application of **mechanical dispersion methods**, and the use of effective **dispersants**.

For SWCNTs, chlorobenzene and m-dichlorobenzene have been reported as optimal solvents for achieving uniform dispersions.[3] Among the various mechanical treatments available to reduce aggregation, **ultrasonication** is the most commonly used. In this process, high-frequency sound waves promote CNT debundling. Increasing the amplitude and duration of the ultrasonic pulses generally improves dispersion quality, but, exceeding harsh conditions can lead to structural damage or shortening of the nanotubes, altering their pristine properties.[3]

The addition of dispersing molecules is essential for obtaining stable dispersions over time, while also enabling the use of a wider range of solvents, including water. The search for new functionalized surfactants capable of producing highly stable and concentrated CNT dispersions remains an active research area.[4,5] The performance of such dispersants is typically compared to **sodium dodecylbenzenesulfonate (SDBS)**, which serves as a standard reference. For example, semiconducting polymers, particularly polyfluorenes, can act as selective dispersants by wrapping around specific CNT species and stabilizing them in suspension, while incompatible nanotubes precipitate. This strategy can be used either to separate SWCNTs from MWCNTs[6] or to isolate specific chiralities, for instance obtaining dispersions enriched in (6,5) nanotubes.[7–9]

Despite the use of surfactants and ultrasonication, complete homogeneity is rarely achieved. CNT dispersions are typically **metastable** rather than truly uniform, as a dynamic equilibrium persists between suspended and sedimenting nanotubes. Consequently, the actual CNT concentration in the supernatant is often lower than the nominal one calculated from the initial mass.[10–12]

With regard to doping methods, CNTs can be doped either **co-deposition** (by adding the dopant directly to the dispersion)[13,14] or **sequentially** after the film is formed, the latter being the preferred approach.

Co-deposition allows intimate proximity between dopant and CNTs, facilitating charge transfer during dispersion; however, the simultaneous presence of dopant and surfactant can destabilize the suspension, leading to inhomogeneous films and limiting solvent choice, which must remain compatible with both the dopant and the dispersant.[6]

On the other side, sequential doping enables film preparation under optimal conditions using environmentally safe solvents, though it relies on dopant diffusion through the CNT network, introducing an intrinsic uncertainty about the actual doping level experienced by the nanotubes.[15–18]

In the present study, we adopted a **sequential doping strategy** for two main reasons.

First, the co-presence of dopant and surfactant in the same dispersion would compromise its stability, promoting CNT flocculation and resulting in non-uniform films. Moreover, in this case it is possible to process CNTs using water as a solvent, which is quite a bad solvent for dopants. Second, producing the films independently allows filtration and thermal treatment to be optimized separately, ensuring reproducible samples and enabling reliable comparison among different dopants.

Only after obtaining stable and conductive CNT films is it possible to investigate the dopant's effect and its diffusion within the nanotube network.

Accordingly, in this work the **CoMoCAT SG65i powder** was dispersed in water using SDBS as surfactant, followed by vacuum filtration to form conductive CNT mats/films, even called buckypapers, on PTFE filters.

The resulting films were then transferred onto glass slides for electrical characterization and subsequent sequential molecular doping. The overall preparation and doping protocol are illustrated in Figure 5.1.

The phases of this protocol are here summarized:

a. **Addition of the SDBS(aq)** solution - Dispersion of CoMoCAT SG65i powder (4.5 mg) in aqueous SDBS solution to obtain a stable CNT suspension.

b. **Sonication** – Tip-ultrasonication (pulsed, 3 × 10 min, in ice water) to debundle and homogenize the CNT dispersion.

c. **Filtration under vacuum** - Deposition of the dispersed CNTs onto PTFE filters (25 or 47 mm with 0.1 μm pore size) by vacuum filtration to form homogeneous CNT mats.

d. **Transfer of the film** - Mechanical transfer of the CNT mat from the filter onto cleaned glass slides using a DI-water droplet and mild heating (≈70 °C).

e. **Deposition of the Ag contacts** - Definition of a van der Pauw geometry, placing four silver-paste contacts at the edges of the film.

f. **Annealing at 150 °C (1 h)** - Thermal treatment in nitrogen to reduce adsorbed oxygen and the correlated p-type doping.

g. **Drop-casting of the dopant solution** - Deposition of the dopant (typically 40 mM in toluene) onto the CNT film under inert atmosphere.

h. **Dopant diffusion (5 min)** - Allowing the dopant to diffuse through the CNT network at room temperature before activation.

i. **Annealing at 150 °C (1 h)** - Activation of the dopant and stabilization of the n-type doping state.

At the same time, we report a complete description of the experimental procedure in Paragraph 5.9.1.

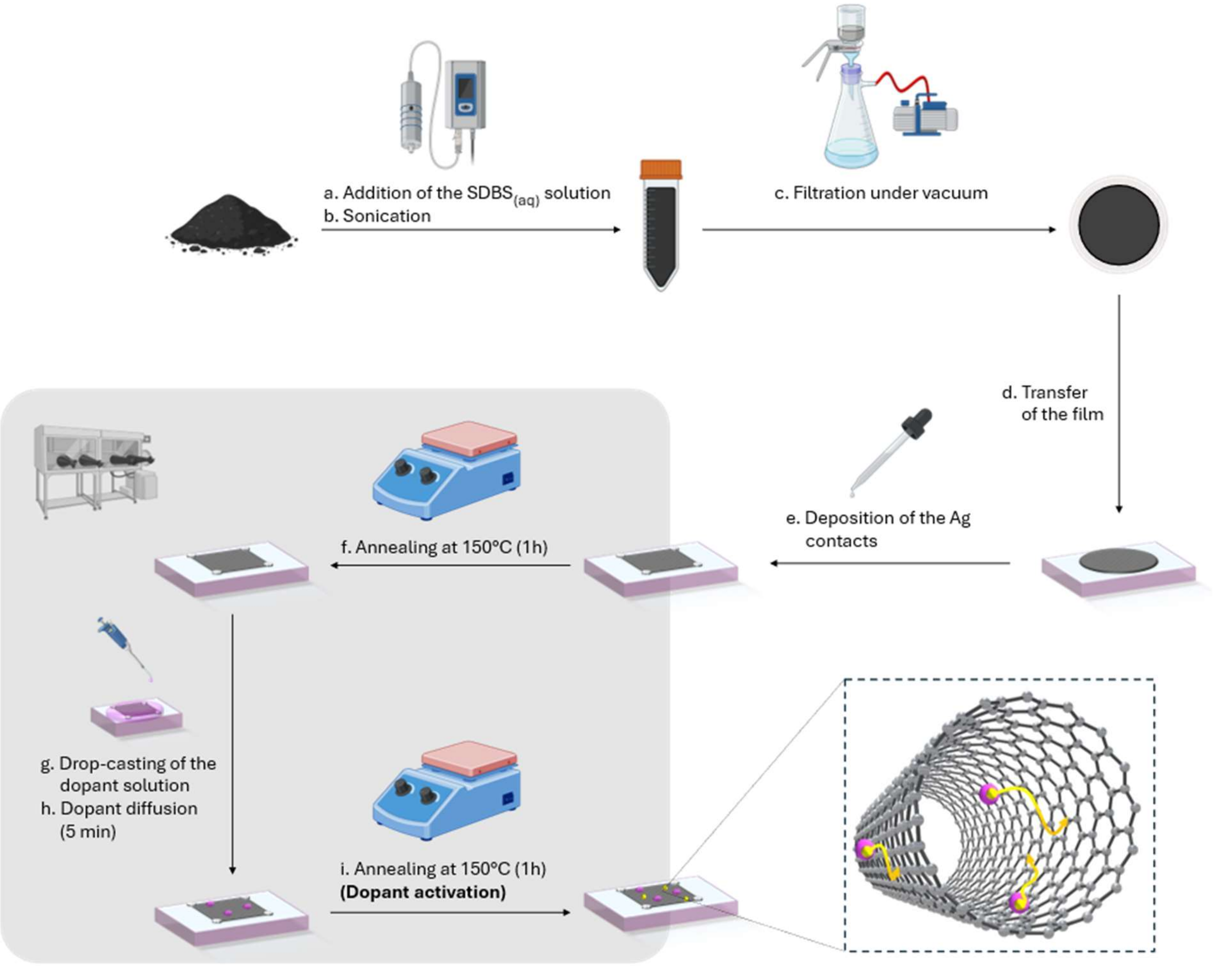

Figure 5.1
Schematical representation of the steps performed in order to obtain and dope the CNT films. The schematic illustration was created using BioRender.com.

5.2. Influence of Film Thickness on the Stability of the Thermoelectric Properties of Doped CNT Films

To ensure meaningful comparison among different dopants and processing conditions, it was first necessary to define a **reference film thickness**.

Previous studies, such as that by Dörling et al.[19], have shown that thicker CNT films tend to exhibit higher conductivity and improved temporal retention of the doping state. This relationship underscores the importance of controlling film thickness and maintaining it within a reproducible range across all samples.

For the thickness choice we had to firstly take in account that accuracy of both **van der Pauw** and **Seebeck** measurements is maximized when the **sheet resistance** of the sample lies within an intermediate range. If the sample resistance is **too low**, it becomes comparable to that of the measurement cables, contacts, and other conductive components typically of the order of 1 Ω. In such cases, the sample contributes only a small fraction (~50%) of the total measured resistance, and variations induced by doping may be confused with changes in contact quality or wiring. Conversely, if the sample resistance is **too high**, it approaches the internal resistance of the measuring instrument (~1 GΩ), leading to significant measurement artefacts.[20,21] For this reason, the optimal range for reliable measurement lies roughly between 10^2 and 10^4 Ω/sqr, where both contact- and instrument-related errors are minimized.

Secondly, we prepared CNT films with varying thicknesses by adjusting the volume of CNT dispersion used during filtration. The film thickness was therefore primarily controlled by the total CNT mass deposited per unit area, with the dispersion concentration kept constant.

Their resistance was then measured to determine the optimal thickness that minimized material usage while still allowing accurate electrical measurements. The applied vacuum and filter porosity were maintained identical across all trials, ensuring that variations in flow rate were negligible compared to those arising from changes in deposited mass.

The protocol was ultimately stabilized using **2.75 mL of ink** on **47 mm PTFE filters**, yielding films with a **sheet resistance of ~200 Ω/sqr** and a corresponding **thickness of 130-150 nm** as determined by profilometry. The observed variation in thickness is mainly attributed to the intrinsic thickness **gradients** across the buckypaper, typically with the center region being thicker than the edges, and to the local variations in the concentration of the suspension due to its metastability. Therefore, the combined effect of these gradients and sample heterogeneity results in the observed spread of thickness values.[11]

5.2.1. Different thicknesses

To investigate how film thickness affects the doping dynamics and long-term stability of CNT networks, two samples with different thicknesses were prepared from the same CNT dispersion batch:

- Sample A (thin): 130 nm
- Sample B (thick): 1670 nm (~10× thicker than A)

The N-DMBI solution was prepared inside the nitrogen glovebox by dissolving 2.1 mg of N-DMBI in 200 μL of toluene, yielding a 40 mM concentration.

Both films were doped under identical conditions: 50 μL of a 40 mM N-DMBI solution in toluene were drop-cast onto an active area of ~1 cm^2 and left to diffuse for 5 minutes under nitrogen, followed by the standard activation annealing (see Section 5.9.1).

This approach intentionally maintained a **constant dopant dose per unit area**, so that differences in response could be attributed mainly to the film morphology and thickness, rather than to variations in processing. Therefore, the thicker film received a proportionally lower dopant concentration per unit volume: a condition that offers insight into **diffusion-limited** and **volume-dependent** activation processes.

5.2.2. Different thicknesses: evolution of thermoelectric properties

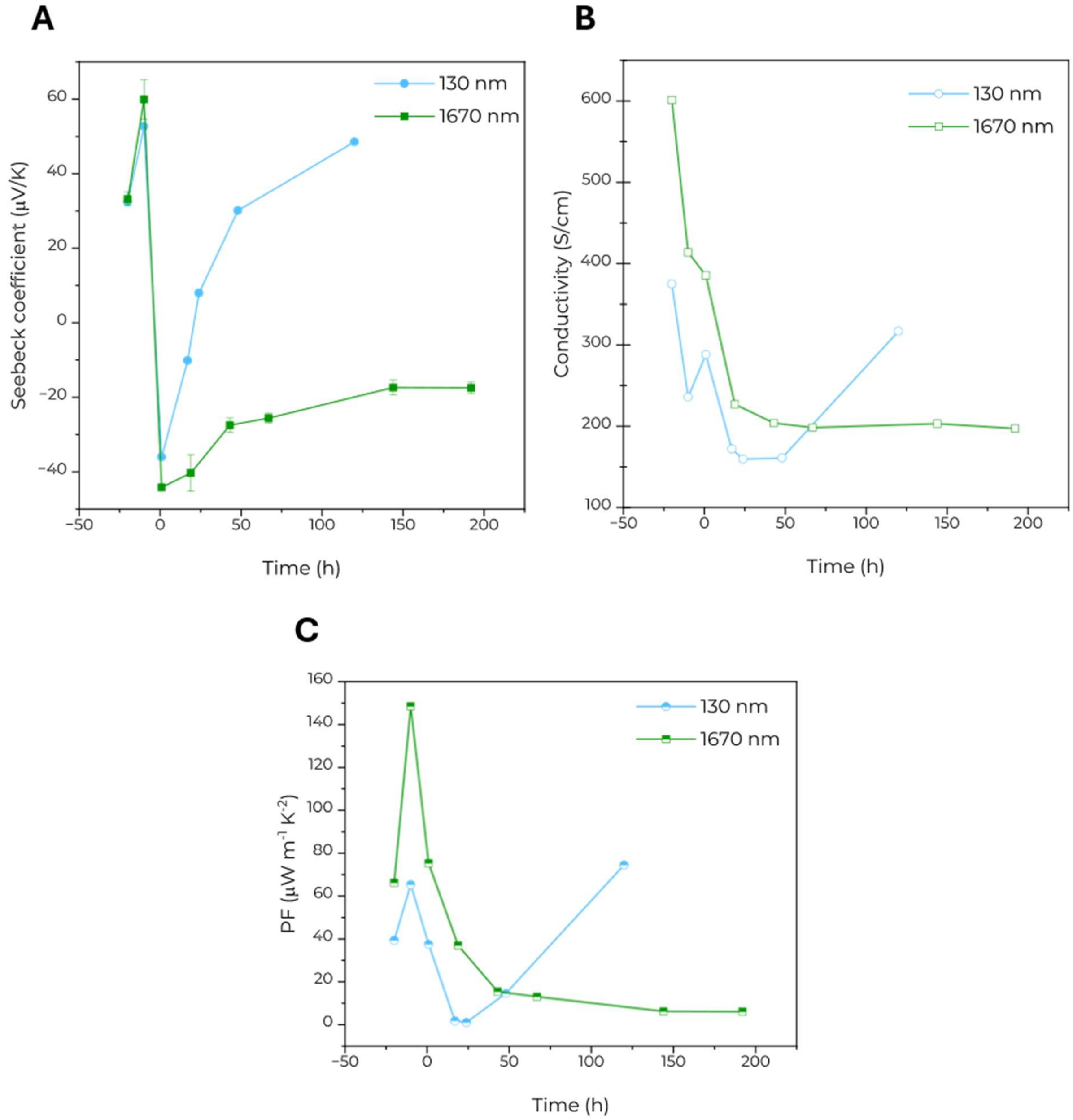

Figure 5.2
Time evolution of the Seebeck coefficient, electrical conductivity, and power factor for the thin film (blue) and the thick film (green). Measurements were performed at three stages: t = –20 h (before the first annealing), t= -10 h (before doping, after the reference anneal for partial oxygen de-p-doping), t = 1 h (first acquisition after doping, requiring ≈1 h), and t > 1 h (subsequent monitoring under ambient air and light for up to ~200 h).

After the reference annealing (t = -10 h), both samples showed a decrease in electrical conductivity (σ) and an increase in the Seebeck coefficient.

This outcome is compatible with **partial desorption of molecular oxygen**, which is known to act as a **p-type dopant** in CNTs by withdrawing electrons from the nanotube π-system.[22]
Thus, its removal decreases the hole concentration, lowering σ while increasing S. Subsequently, we hypothesized that the annealing step thus restored a less oxidized, more intrinsic state of the CNT network, establishing a reliable baseline for subsequent n-type doping. It is worth noting that the annealing conditions employed are not sufficient to completely desorb all oxygen molecules. However, since the same thermal treatment was also applied during the activation of DMBI-type dopants, performing this pre-annealing on pristine CNT films allows us to separate the two contributions: the oxygen dedoping effect and the n-doping induced by the dopant. Without this preliminary step, both effects would overlap, making it difficult to disentangle their individual impact on the final electrical properties.

Immediately after doping (t = 1 h), both films exhibited **negative Seebeck coefficients**, confirming the successful conversion to **n-type conduction** upon reaction with N-DMBI.
However, we registered a different conductivity response in the two samples: σ increased significantly in the **thin film** (130 nm), indicating efficient conversion to n-type transport and enhanced **carrier density**. In contrast, in the **thick film** (1670 nm), σ slightly decreased, suggesting that although n-type doping occurred, the electron density gained from the dopant only partially compensated, rather than exceeded, the residual p-type contribution due to residual oxygen. This contrast can be rationalized by considering the competition between residual O_2-induced p-doping and the efficiency of the n-type charge transfer from N-DMBI to the CNTs. When these opposing effects coexist, the overall carrier balance depends on which mechanism prevails.[16]
In thinner films, oxygen removal and dopant diffusion are more effective, leading to a net increase in electron carriers and thus in conductivity. In contrast, in thicker films, a larger fraction of CNTs remains partially inaccessible to the dopant due to limited penetration depth, while residual oxygen near the surface can still compensate injected electrons.[23]
Additionally, since the same dopant dose per unit area was applied to both samples, the effective dopant concentration per unit volume was lower for the thick film, further reducing the extent of charge transfer.

After ambient exposure (t ≤ 200 h), the **Seebeck coefficient of the thin film** gradually shifted back toward its initial positive value, suggesting a progressive loss of n-type character. Since N-DMBI remains stable after activation in its cationic form, this evolution is more likely due to re-oxidation of the CNT network, triggered by the capture of injected electrons by ambient species.

The **thick film**, however, preserved a **stable negative Seebeck coefficient** throughout the monitoring period, reflecting improved retention of the n-type state.

5.2.3. Summary

In both samples, the evolution of conductivity with air-exposure time is in great accordance with that of the Seebeck coefficient. In the thin film, σ is highest immediately after doping, then decreases as the injected electrons are progressively compensated, reaching a minimum when S approaches zero (point of carrier compensation). As S turns positive, σ rises again, reflecting the partial recovery of p-type transport.

In the thick film, the same trend occurs more slowly, coherent with delayed oxygen penetration and, consequent, reaction within the thicker network. Even in this case we assist to a gradual re-equilibration between injected electrons and ambient oxygen, but on a lower timescale due to film thickness.

Collectively, these results show that **thicker CNT films** retain their n-type character for **longer**, in line with previous observations for N-DMBI-based systems.[19]

5.3. Thermoelectric Stability of CNT Films Doped with DMBI Derivatives

After defining the role of film thickness in the stability of n-type doping, the study then focused on the comparative evaluation of different dopants under identical conditions.

For this purpose, a single CoMoCAT SG65i film (thickness ~130 nm by profilometry) was divided into equal sections to ensure uniform morphology and composition across all samples. Each section was transferred onto glass substrates and sequentially doped under inert atmosphere following the established procedure, using 50 µL of dopant solution in toluene. The **dopant concentrations** were calculated to maintain the same equivalents of redox units: 40 mM for N-DMBI-H and An-DMBI (corresponding to 1.43 mg dissolved in 0.10 mL of toluene), and 20 mM for the bifunctional MDI-DMBI$_2$ (3.38 mg in 0.20 mL of toluene). Following drop-casting and thermal activation, all samples were characterized by electrical conductivity (σ) and Seebeck coefficient (S) measurements, both before and after doping, and subsequently monitored over time while being kept at ambient conditions (light, air-exposure, room temperature).

The resulting σ, S and PF trends for the three dopants are presented in the following section.

5.3.1. Results and discussion

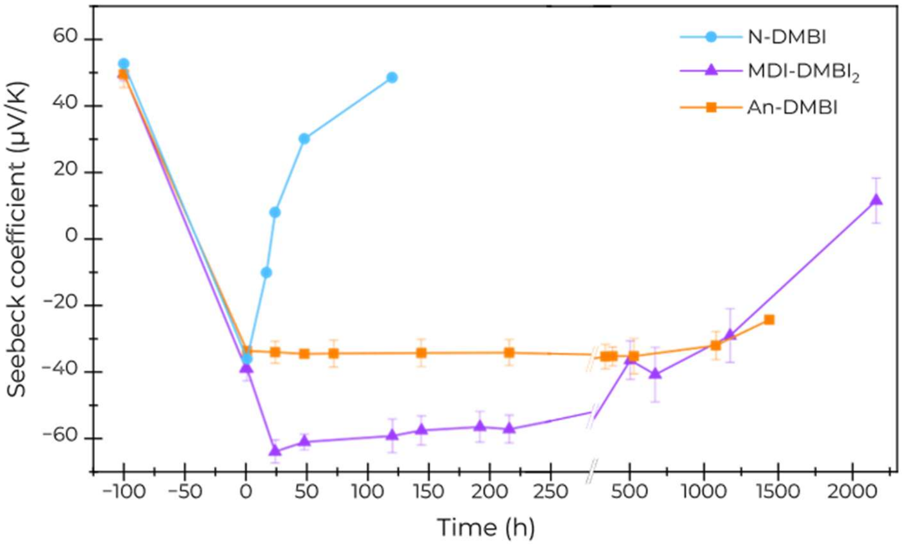

Figure 5.3
Seebeck coefficient evolution in time for the CNT films doped with N-DMBI (blue), MDI-DMBI$_2$ (violet) and An-DMBI (orange).

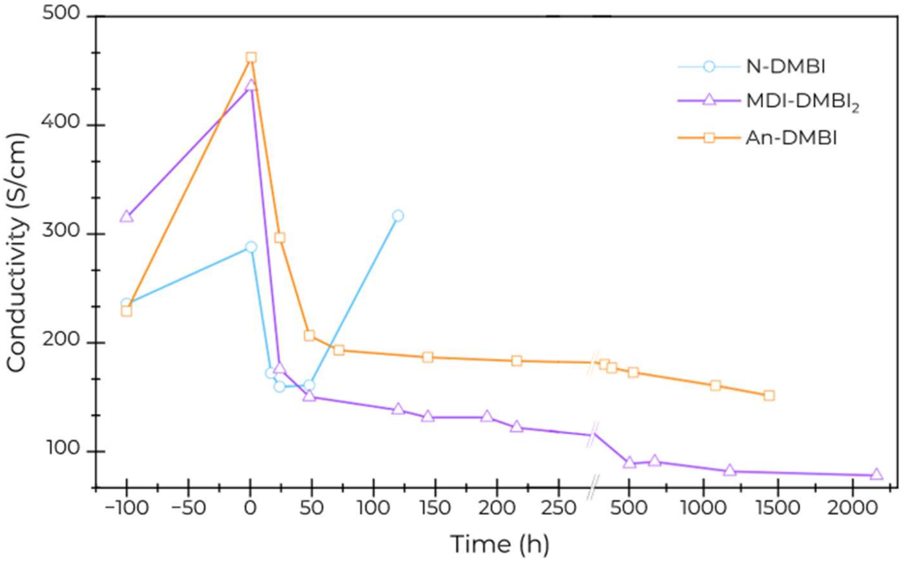

Figure 5.4
Electrical conducitvity evolution in time for the CNT films doped with N-DMBI (blue), MDI-DMBI$_2$ (violet) and An-DMBI (orange).

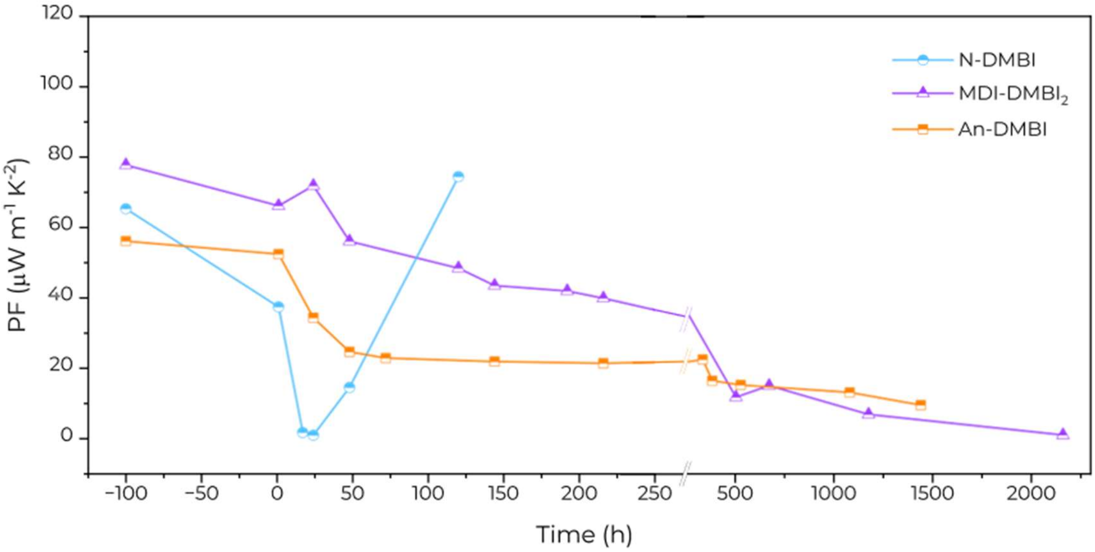

Figure 5.5
Power factor evolution in time for the CNT films doped with N-DMBI (blue), MDI-DMBI$_2$ (violet) and An-DMBI (orange).

Immediately after doping (t = 1 h), the Seebeck coefficient of the three doped films presents a similar value (~ -40 µV K^{-1}), showing a clear inversion from positive to negative values, confirming successful **n-type conversion**. However, the three dopants exhibit markedly different temporal evolutions in both the magnitude and stability of their thermoelectric properties.

In the case of **MDI-DMBI$_2$** doping, after 24h from the doping the Seebeck coefficient decreases further, reaching a value of -64 µV K^{-1}, the most negative of the ser*ies*. This delayed maximum suggests that the film was initially **overdoped**. As the n-doped state partially reduces within the first day, the carrier concentration approaches a more optimal regime, leading to a larger |S|. This behavior is analogue to the trend observed during oxygen de-p-doping of undoped CNTs, where the removal of excess p-type charge decreased electrical conductivity but increased |S| in magnitude.

Nevertheless, MDI-DMBI$_2$ maintains a negative Seebeck coefficient for nearly 2000 h, indicating that the electronic nature of the n-type state remains largely preserved even as the overall conductivity reduces. Part of this decrease may result from **repeated handling** and mechanical wear during measurements. Moreover, in principle, as S gradually shifts toward positive values, σ could rise again, but such recovery is unlikely to approach the initial state, due to the presence of an impurity within the network, i.e. dopant cation.

In general, in CNT networks, σ is highly sensitive to external factors such as mechanical degradation induced by repeated four-point probe measurements.[24,25] On the contrary, the Seebeck coefficient is primarily determined by the electronic doping state, as it reflects shifts in the Fermi level rather than changes in the physical integrity of the film.[26,27] Therefore, the Seebeck coefficient is specifically influenced the electronic drift from n- to p-type, while conductivity is also dependent on the physical wear.

The film doped with **An-DMBI** exhibits the highest initial conductivity (~450 S cm^{-1}), followed by a rapid decrease to intermediate values (~200 S cm^{-1}) that remains relatively stable over time. The Seebeck coefficient preserved the initial value after doping (-37 µV K^{-1}) with only minor variations even after extended aging, while the power factor stabilizes around ~20 µW m^{-1} K^{-2}. This behavior indicates that the An-DMBI-doped system is highly resistant to oxidative dedoping, maintaining its n-type character over prolonged air-exposure.

In contrast, **N-DMBI-H** exhibits the least stable behavior: the Seebeck coefficient rapidly returns to positive values within the first 100 h, and conductivity follows a similar trend, consistent with the rapid capture of the injected electrons by oxygen.

From this comparative analysis, we conclude that MDI-DMBI$_2$ exhibits the most marked n-type behavior and significant oxidative stability, An-DMBI presents the most stable n-type doping, while N-DMBI-H rapidly restores the p-type character under ambient conditions.

These observations demonstrate that subtle **structural modifications** within the DMBI framework can deeply affect both charge-carrier density and the long-term electronic stability of

CNT-based n-type materials.

Following these results, our investigation focused on determining the reasons for the enhanced stability observed in CNT films doped with the newly synthesized DMBI derivatives.

5.4. UV-Visible Analysis on doping residual solutions

Previous reports have proposed that, once activated, N-DMBI$^+$ can remain adsorbed on the CNT surface, forming a **passivating multi-layer structures** that slows reoxidation by atmospheric oxygen. However, this protection is effective only above a critical surface coverage, while below this threshold, oxygen can still penetrate through defects in the layer.[15,28–30]

As seen in the previous section, under our experimental conditions, i.e relatively thick CNT films and moderate dopant concentrations, N-DMBI-H did not provide such stabilization, whereas both An-DMBI and MDI-DMBI$_2$ maintained their n-type character for much longer times.

Therefore, we hypothesized that this difference arises from a stronger and more persistent interaction between the oxidized dopant species (An-DMBI$^+$ and MDI-DMBI2^{2+}) and the reduced CNT surface.

5.4.1. Our strategy

To test this hypothesis, we designed the following strategy.

CNT films are immersed in dopant solutions at room temperature. Since benzimidazoline-based dopants can activate even without annealing, the dopant oxidizes to his cationic form (for instance N-DMBI to N-DMBI+), while at the same time reducing the CNT. After the reaction finishes, the films are removed, and the final cation concentration of the dopant cation in solution is quantified. By comparing the theoretical cation concentration (C$_{th}$) with the measured residual concentration (C$_{res}$), the fraction of dopant retained by the CNTs is obtained as:

$$\text{Retained fraction} = \frac{C_{th} - C_{res}}{C_{th}} \tag{5.15}$$

The theoretical concentration C_{th}corresponds to the number of cations that would be present in solution if none were adsorbed onto the reduced CNT surface. If the doping efficiency were equal to one, C_{th}could be assumed identical to the initial dopant concentration. In practice, however, doping efficiencies are typically below unity.

However, complete activation can be ensured if the doping process is performed with N-DMBI in a polar protic medium, as ethanol, and in presence of oxygen, adsorbed on the CNT or dissolved. This is because in this condition the doping process is interested by an additional **proton-coupled electron transfer (PCET),** as described by Tanaka et al.[31] In this mechanism, the DMBI-type molecule transfer one electron and one hydrogen atom to the CNT network, producing a negatively **doped CNT** and a **hydroperoxyl radical (•OOH)**. The hydroperoxyl radical then oxidizes another neutral DMBI molecule, generating a **DMBI radical** and **hydrogen peroxide (H_2O_2)**. The newly formed DMBI radical can further transfer an electron to the CNT, increasing its electron density. Being excessively negatively charged, the CNT transfers electrons to molecular oxygen or hydrogen peroxide, which act as mild oxidants. In a protic solvent such as ethanol, oxygen is protonated, forming **ethoxide (EtO^-)** as the counterion of the oxidized dopant (**N-DMBI$^+$**). This sequence of coupled redox steps ultimately leads to the **complete conversion of neutral DMBI-type molecules into their oxidized cations**, which can either remain adsorbed on the CNT surface or dissolve in the surrounding solution as ethoxylated salts.

In the following paragraph we give an overview of the experimental conditions, while a complementary description is furnished in section 5.9.4.

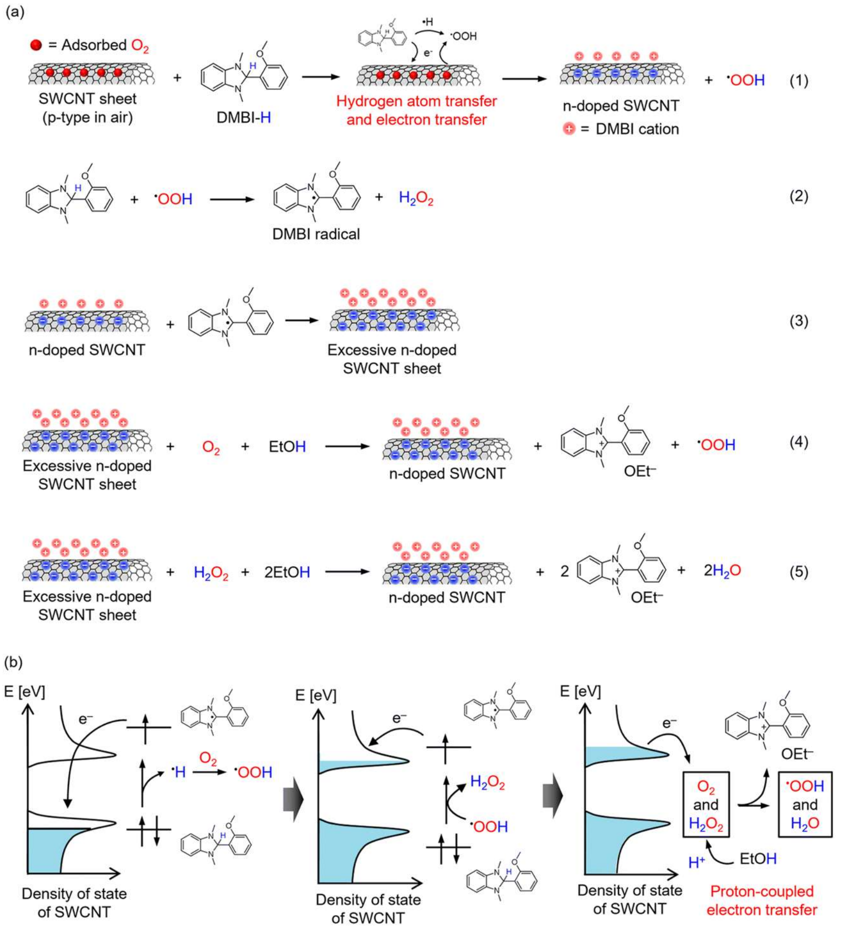

Figure 5.6
(a) Mechanism of the proton-coupled electron transfer reaction. (b) Change in the electric state of SWCNTs, for electron doping of SWCNTs by DMBI-H in ethanol. Reproduced from the work of Tanaka et al.[31] License CC BY-NC 3.0.

5.4.2. Experimental overview

Three CoMoCAT SG65i films (~2 μm thick, measured by profilometry) were immersed in separate dopant solutions of N-DMBI-H, An-DMBI, and MDI-DMBI$_2$, each prepared in a 1:1 (v/v) mixture of methanol and acetonitrile. The addition of acetonitrile to the mixture was necessary to ensure complete dissolution of the dopants. The samples were soaked in the solutions for 50 h at room temperature inside a nitrogen-filled glovebox.

After the reaction, the CNT films were removed, and the resulting solutions, now containing the corresponding oxidized dopant cations, were analyzed by UV–Vis spectroscopy. The cationic species (N-DMBI$^+$, An-DMBI$^+$ and MDI-DMBI$_2^{2+}$) exhibit a characteristic absorption maximum around 340 nm. By comparing the intensity of this band with calibration curves (absorbance vs. cation concentration) constructed from reference solutions of known concentration of N-DMBI-

BF_4, MDI-DMBI-$(PF_6)_2$, and An-DMBI-I salts, the residual concentration of oxidized dopant in each solution was determined. Using this value, the **retained fraction** of dopant on the CNT films was calculated according to equation (5.15).

DMBI-like dopants when dissolved in alcohol tend to spontaneously oxidize to the cationic form, even though with a kinetic much slower than the cation formation during our doping process.[28] To evaluate this phenomenon we characterized by UV-Vis spectroscopy two samples of dopants solutions, one kept in ambient conditions for three days and the other one under inert atmosphere for the same amount of time, and in the absence of the CNT films.

5.4.3. Results and discussion

The observed adsorbed fractions, approximately **6% for N-DMBI-H**, **15% for An-DMBI**, and **35% for MDI-DMBI$_2$**, define an order in dopant-nanotube affinity that is coherent with the trend in electronic stability observed during long-term conductivity and Seebeck monitoring.

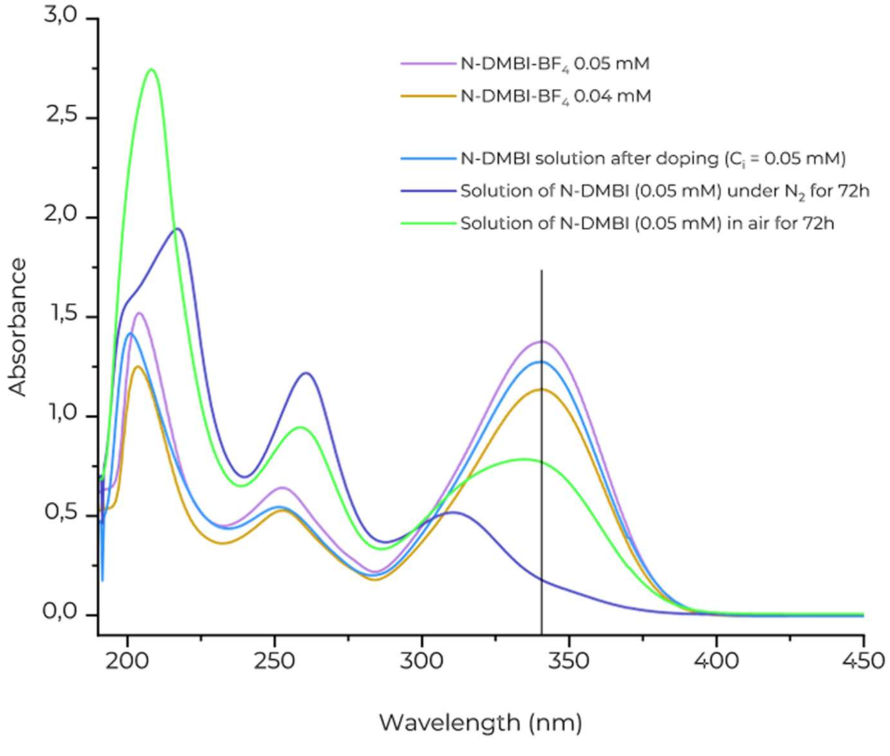

Figure 5.7
UV–Vis spectra of the residual N-DMBI solution after contact with CNT films, compared with the most representative standard solutions, and control solutions stored for three days in air or in the glovebox.

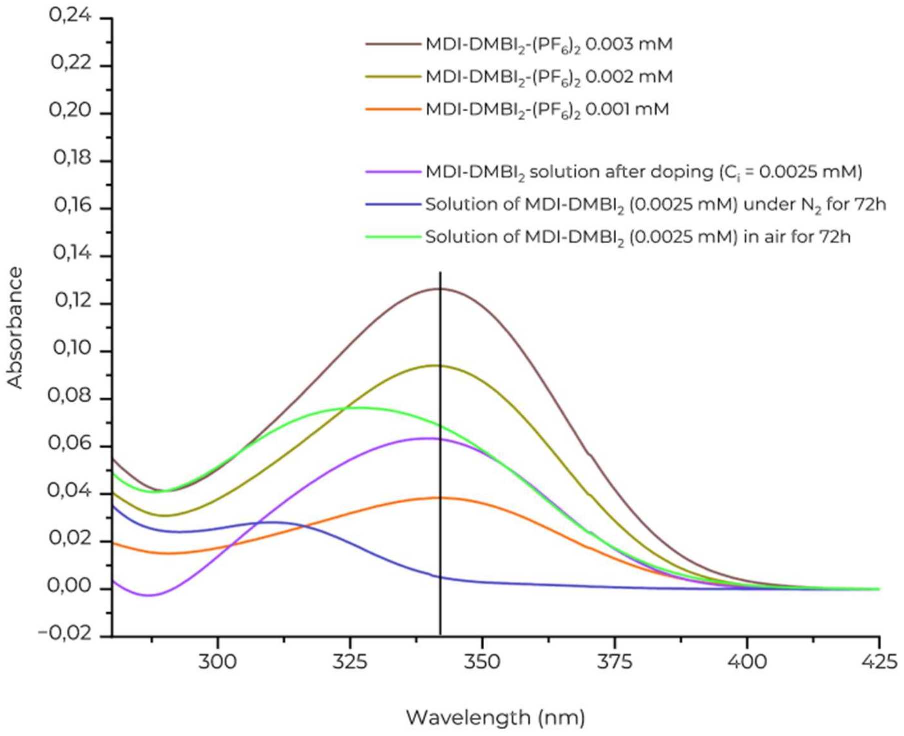

Figure 5.8
UV–Vis spectra of the residual MDI-DMBI$_2$ solution after contact with CNT films, compared with the most representative standard solutions, and control solutions stored for three days in air or in the glovebox.

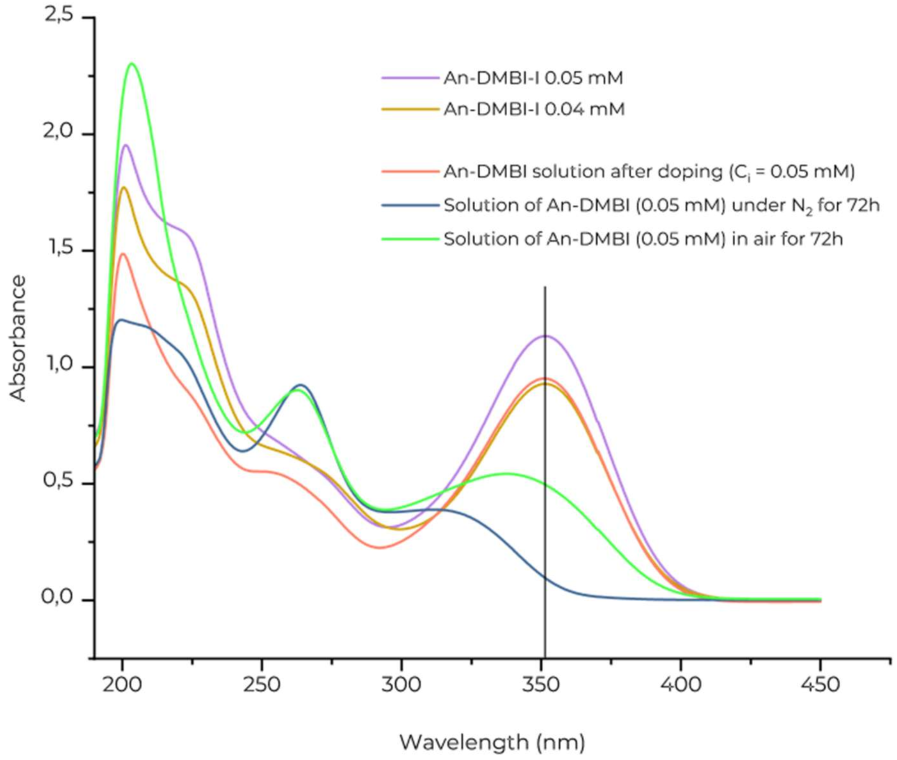

Figure 5.9
UV–Vis spectra of the residual An-DMBI solution after contact with CNT films, compared with the most representative standard solutions, and control solutions stored for three days in air or in the glovebox.

As expected, the dopants solutions that did not react with the CNT exhibit **gradual oxidation** of the dopants over time; however, the process was significantly **slower** than in the presence of CNTs. This confirms that the spontaneous degradation or oxidation of the dopants in solution is not competitive with the CNT-mediated activation, and that the subsequent observed conversion to the cationic form predominantly arises from the doping process itself.

The observed differences in stability can be rationalized by considering the interactions between the oxidized dopants and the reduced CNT network.
All cationic species form **ion pairs** with negatively charged CNTs, but the strength and persistence of these interactions depend on the cumulative intermolecular interactions that the cations can build. N-DMBI$^+$, being a small and relatively weakly polarizable cation, establishes relatively labile ion pairs that can easily dissociate, facilitating reoxidation by oxygen. In contrast, An-DMBI$^+$ and MDI-DMBI$_2^{2+}$ possess larger π-conjugated and more polarizable moieties, which can in principle enhance electrostatic coupling and π–π stabilization with the CNT surface. Moreover, in the case of MDI-DMBI$_2^{2+}$, its bifunctional architecture may further promote double binding across adjacent nanotubes, reinforcing the stability of the doped state over time.

However, stronger adsorption does not necessarily equate to higher conductivity: especially when forming multilayers, may become electronically inactive, immobilized dopant molecules can in principle work more as a **passivating shell** than as an efficient doping stabilizers. Therefore, the most effective dopants may be those that achieve a balance between **surface adhesion and electronic accessibility**.

5.4.4. Summary

Dopant cation retention follows the order N-DMBI$^+$< An-DMBI$^+$ < MDI-DMBI$_2^{2+}$. Compared to the benchmark N-DMBI$^+$, An-DMBI$^+$ contains an additional aromatic moiety capable of π–π interactions, while MDI-DMBI$_2^{2+}$ features extended aromatic groups and two cationic centers, allowing for double ionic anchoring to the CNT network. Consequently, we suggest that CNT films doped with An-DMBI and MDI-DMBI$_2$ exhibit greater resistance to oxidation, because a larger number of cationic species can remain adsorbed, forming more persistent passivation layers that hinder reoxidation of the reduced CNT network.

5.5. UV-Vis-NIR Analysis on doped CNT films

UV-Vis-NIR spectroscopy was employed to investigate how molecular doping affects the **characteristic optical transitions** (E_{11} and E_{22}) of CoMoCAT SG65i CNT films.

For each dopant, three samples were analyzed - annealed (undoped), freshly doped (after 24 h in N_2), and aged doped (after 72 h in air), to assess both the initial modification of the electronic structure and its temporal evolution. Complementary experimental description is reported in Paragraph 5.9.5.

5.5.1. Results and discussion

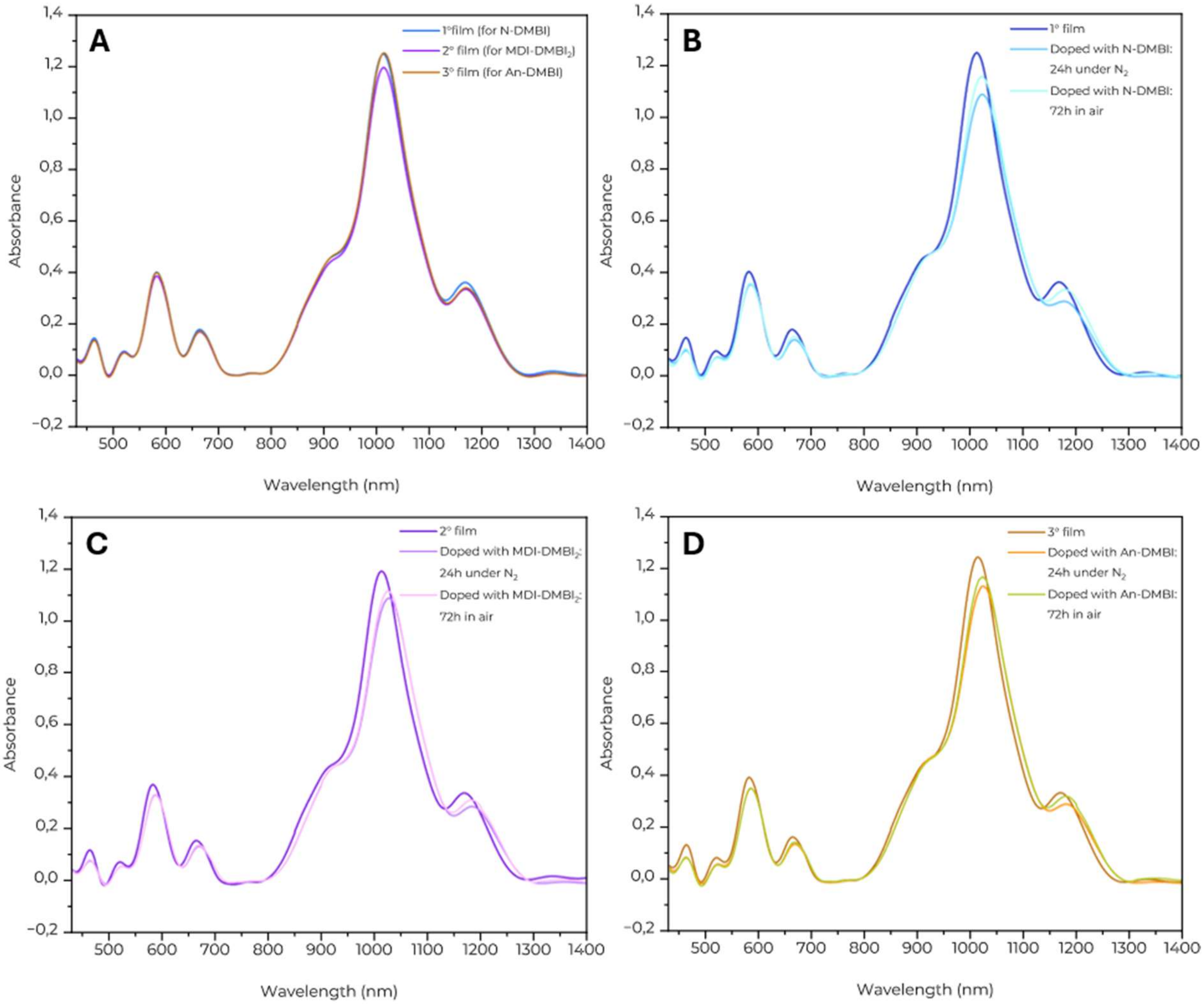

Figure 5.10
UV-Vis-NIR absorption spectra of CoMoCAT SG65i SWCNT films before and after n-type doping with N-DMBI-H (B), MDI-DMBI$_2$ (C), and An-DMBI (D). The spectra were collected in transmission mode, averaging measurements along two orthogonal directions to minimize local inhomogeneities.

Figure 5.10 reports the collected spectra. In panel A, the comparison among the UV–Vis absorption spectra of the **undoped films**, later doped with N-DMBI, MDI-DMBI$_2$, and An-DMBI, shows that the spectra are essentially identical in terms of peak positions, with only minor intensity variations. These slight differences may arise from minor variations in the amount of adsorbed oxygen or small film inhomogeneities.

Therefore, any changes observed after doping can be attributed to the doping process itself rather than to initial differences in the pristine films. The main features related to the graphs are summarized in Table 5.1 and in Table 5.2, to facilitate the discussion.

Table 5.1
Wavelengths of the maximum UV-Vis absorption peaks corresponding to the E$_{22}$ and E$_{11}$ transitions of CoMoCAT SG65i SWCNT films before and after doping with N-DMBI, MDI-DMBI$_2$, and An-DMBI. The table also reports the shifts of these peaks relative to those of the corresponding undoped films.

N-DMBI

	E$_{22}$ (peak)		**E$_{11}$ (peak)**	
	λ (nm)	Shift (nm)	λ (nm)	Shift (nm)
1° film (undoped)	583	**0**	1013	**0**
Doped: 24h, N$_2$	586	**3**	1024	**11**
Doped: 72h, air	586	**3**	1023	**10**

MDI-DMBI$_2$

	E$_{22}$ (peak)		**E$_{11}$ (peak)**	
	λ (nm)	Shift (nm)	λ (nm)	Shift (nm)
2° film (undoped)	583	**0**	1014	**0**
Doped: 24h, N$_2$	588	**5**	1026	**12**
Doped: 72h, air	588	**5**	1027	**13**

An-DMBI

	E$_{22}$ (peak)		**E$_{11}$ (peak)**	
	λ (nm)	Shift (nm)	λ (nm)	Shift (nm)
3° film (undoped)	583	**0**	1015	**0**
Doped: 24h, N$_2$	586	**3**	1024	**9**
Doped: 72h, air	586	**3**	1023	**8**

For CoMoCAT SG65i SWCNTs enriched in the (6,5) chirality, the main optical transitions are expected at ~985 nm and ~570 nm, corresponding to the E_{11} and E_{22} excitonic transitions, respectively.[32] In our films, these peaks are located at 1013 nm and 583 nm, showing red-shifts of ~28 nm and 13 nm. Such **displacements** are related to inter-tube coupling, bundling, and dielectric screening due to residual SDBS and the glass substrate. Analogue peaks are reported in the work of Ferguson et al.[33] for films of the same material.

Upon doping with N-DMBI-H, An-DMBI, or MDI-DMBI$_2$, all spectra display a reduction in the intensity of both excitonic bands, most notably E_{11}, together with a red-shift of 3-13 nm. These features are compatible with **electron injection** into the CNT network: the filling of electronic states reduces excitonic absorption, while increased dielectric screening causes a slight red-shift of the transitions.[22,32–35]

Notably, the sample doped with N-DMBI exhibits the most pronounced quenching of the E_{11} transition (the band intensity is reduced to a 87% of its initial value, while for MDI-DMBI$_2$ and An-DMBI is reduced to a 91% in both cases), which may indicate a stronger **local perturbation** or a **higher effective doping level**.

When comparing the sample doped and stored under inert atmosphere for 24 h with the one exposed to air for 72 h, both the E_{22} and E_{11} peak intensities increase upon aging, indicating **oxidative dedoping**, although to different extents depending on the dopant (see Table 5.2). For the N-DMBI-H-doped film, the E_{22} and E_{11} intensities increase by 1.4% and 6.4%, respectively, whereas these variations are significantly smaller for the other two systems: 0.6% and 2.5% for MDI-DMBI$_2$, and 0.3% and 3.3% for An-DMBI. However, the spectral positions remain nearly unchanged, suggesting that while some charge carriers are lost, the dopant residues or local structural disorder remain, indicating partial but **not complete reversibility** of the doping process.

Table 5.2
Intensities (I) of the maximum UV-Vis absorption peaks corresponding to the E_{22} and E_{11} transitions of CoMoCAT SG65i SWCNT films before and after doping with N-DMBI, MDI-DMBI$_2$, and An-DMBI. Reported values include: (i) the ratio between each intensity and that of the corresponding undoped film (I/ $I_{undoped}$ (%)) and(ii) the ratio between each intensity and that of the same peak for the film stored under inert atmosphere for 24 h after doping (I/ $I_{doped24h}$ (%)).

N-DMBI

	E_{22} (peak)			**E_{11} (peak)**		
	I	I/ $I_{undoped}$ (%)	I/ $I_{doped24h}$ (%)	I	I/ $I_{undoped}$ (%)	I/ $I_{doped24h}$ (%)
1° film (undoped)	0.402	**100.0**	-	1.250	**100.0**	**-**
Doped: 24h, N_2	0.353	**88.0**	**100.0**	1.088	**87.0**	**100.0**
Doped: 72h, air	0.358	**89.0**	**101.4**	1.158	**93.0**	**106.4**

MDI-DMBI$_2$

	E_{22} (peak)			**E_{11} (peak)**		
	I	I/ $I_{undoped}$ (%)	I/ $I_{doped24h}$ (%)	I	I/ $I_{undoped}$ (%)	I/ $I_{doped24h}$ (%)
2° film (undoped)	0.369	**100.0**	-	1.192	**100.0**	-
Doped: 24h, N_2	0.328	**89.0**	**100.0**	1.089	**91.0**	**100.0**
Doped: 72h, air	0.330	**90.0**	**100.6**	1.116	**94.0**	**102.5**

An-DMBI

	E_{22} (peak)			**E_{11} (peak)**		
	I	I/ $I_{undoped}$ (%)	I/ $I_{doped24h}$ (%)	I	I/ $I_{undoped}$ (%)	I/ $I_{doped24h}$ (%)
3° film (undoped)	0.391	**100.0**	-	1.244	**100.0**	-
Doped: 24h, N_2	0.348	**89.0**	**100.0**	1.131	**91.0**	**100.0**
Doped: 72h, air	0.349	**89.0**	**100.3**	1.168	**94.0**	**103.3**

5.5.2. Summary

From these results, we conclude that the stronger decrease in excitonic intensity upon doping with N-DMBI-H suggests a slightly higher initial doping efficiency compared with An-DMBI and MDI-$DMBI_2$, which display comparable but milder effects. However, the more pronounced recovery of absorption intensity upon air exposure in the N-DMBI-H-doped film is an indicator of a **faster oxidative dedoping**. Conversely, the smaller spectral recovery observed for An-DMBI and MDI-$DMBI_2$ confirms their superior robustness to reoxidation. Finally, the persistence of small spectral shifts even after prolonged air exposure suggests that residual dopant species or induced structural disorder continue to perturb the CNT electronic transitions, even after partial reoxidation of the network.

5.6. Raman spectroscopy

The Raman spectrum of single-walled carbon nanotubes (SWCNTs) provides rich information on both their structure and electronic properties.

In this section, we analyze how **molecular dopants derived from the DMBI family** (N-DMBI-H, An-DMBI, and MDI-DMBI$_2$) affect the Raman features of SWCNT films. In particular, we recorded the spectra of doped samples that were kept under inert atmosphere until the measurement, typically within one hour after doping. The samples considered include films doped with N-DMBI, MDI-DMBI$_2$, and An-DMBI, prepared following the same protocol used for the thermoelectric property measurements. Additionally, we examined the Raman spectrum of a film doped with MDI-DMBI$_2$ and stored under ambient conditions for **two weeks**, in order to assess the effects of dedoping

To facilitate the discussion, before presenting our results, we furnish an overview of the main Raman features of CNTs films, and their related variations film upon doping.

5.6.1. SWCNTs Raman Features

The most characteristic Raman bands for SWCNT are the **radial breathing mode (RBM)**, the **D band**, the **G band** (split into G^+ and G^- components), and the **G' (or 2D) band**.[36]

The **RBM**, appearing between 100 and 200 cm^{-1}, corresponds to an out-of-plane vibration in which the nanotube diameter periodically expands and contracts. Its frequency is inversely proportional to the tube diameter, providing a direct way to estimate tube dimensions.

The **D band**, centered around 1350 cm^{-1}, is a defect-induced double-resonance Raman feature. It becomes active when the perfect sp^2 hexagonal lattice symmetry is broken, for instance due to functionalization, vacancies, or amorphous carbon contamination. As the defect density increases, the D band broadens and can merge with the G band due to spectral overlap.

The **G band**, at approximately 1585 cm^{-1}, derives from in-plane stretching of C-C bonds in sp^2-hybridized systems. In graphene this mode is isotropic and appears as a single Lorentzian peak. In SWCNTs, however, lattice curvature and confinement effects split the G band into two components: **G^+**, corresponding to vibrations parallel to the nanotube axis, and **G^-**, perpendicular to it.[37] The splitting magnitude increases inversely with the square of the tube diameter and depends on chirality and metallicity. In semiconducting tubes, the G^- mode is usually broader and downshifted compared to G^+.

Finally, the **G' (or 2D) band**, located near 2700 cm^{-1} for a 532 nm excitation, corresponds to a

second-order double-resonance process involving two phonons near the K point.
Its position and intensity are strongly dependent on the laser wavelength and on the Fermi level position, making it highly sensitive to charge transfer phenomena.

5.6.2. Doping-Induced Modifications

Upon doping, all these Raman signals may undergo **frequency shifts**, **broadening**, and changes in **relative intensity**, due to modifications in the electronic structure and electron-phonon coupling. Most of the studies that refer to these variations have been conducted on graphene or electrochemically doped CNTs. Nevertheless, the same physical mechanisms, Fermi level shift, modification of electron-phonon coupling, and bands quenching, are expected to be applicable even on molecular doped SWCNT, since they are characterized by a sp^2 network as graphene and since doping involves the injection of charges in both molecular and electrochemical processes.[38,39]

For **n-type doping**, electron injection into the CNT π-system usually causes phonon softening of the longitudinal optical mode, resulting in a **red-shift of the G^+ band**.[40,41]
However, literature reports are far from unanimous. In some cases, especially for large-diameter tubes, **blue-shifts** have also been observed.[42] This apparent contradiction arises from the competing effects of charge transfer, local strain, and electrostatic screening, all of which influence the effective electron-phonon interaction.
The **G' (2D) band** behaves differently. Because it originates from a double-resonance process that depends strongly on the Fermi level position, both n-type and p-type doping tend to suppress the resonance condition, leading to phonon stiffening and thus a **blue-shift** of the G' frequency.[43] This shift is often combined with a reduction in the **G'/G intensity or area ratio**, attributed to the partial quenching of the resonance as the Fermi level moves away from the Dirac point.[32]
The **D band** provides complementary information on scattering related to the presence of defects. Although less frequently discussed for SWCNTs than for graphene, several studies report a **decrease of the I_D/I_G ratio** after electron doping, possibly due to enhanced screening of defect-induced scattering by charge transfer.[43]
Doping can also lead to **broadening of the Raman bands**, which is typically attributed to an inhomogeneous dopant distribution or to increased electron-phonon coupling at high carrier densities.[32,33]

5.6.3. Results and Discussion

For this analysis, we collected data both on doped films and on an undoped reference film, in order to compare the variations with respect to a baseline. When observed under the microscope, the films displayed two distinct regions: one consisting of **a homogeneous film** and another characterized by **CNT aggregates** (Figure 5.11). We observed that the profile of the Raman spectra varied significantly between these two regions, while remaining consistent when single-point spectra were recorded at different positions within the same region.

Figure 5.11
Microscopic image of the undoped film, where two main types of regions can be distinguished: an aggregated one and a homogeneous one.

For this reason, we chose the homogeneous regions of the undoped film as the **reference**, and all spectra of the doped films were likewise collected from the corresponding homogeneous regions. The obtained curves for the doped samples are shown in Figure 5.12, along with two magnified views of the relevant spectral regions (Figure 5.13, Figure 5.14).

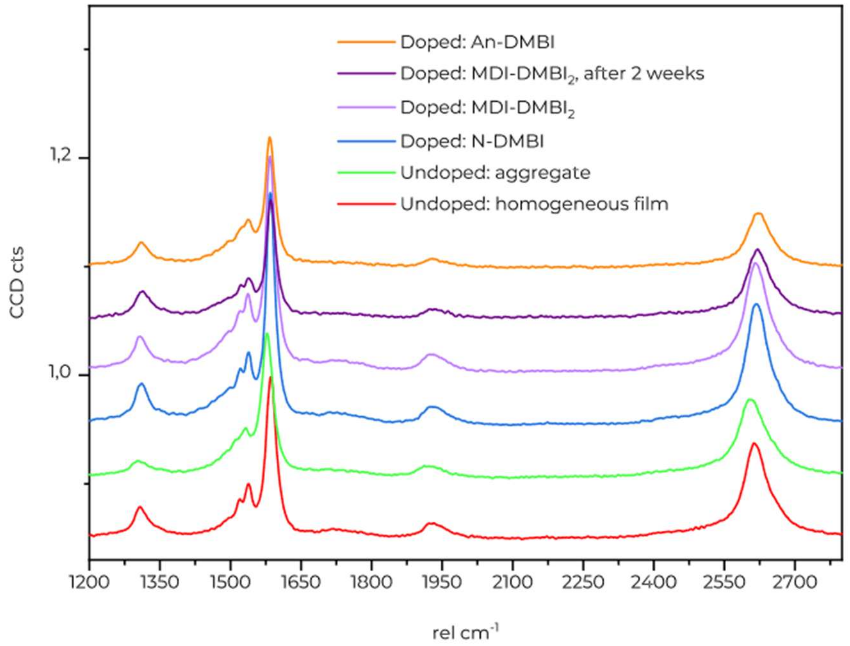

Figure 5.12
Raman spectra of CoMoCAT SG65i films before and after doping with N-DMBI-H, MDI-DMBI$_2$, and An-DMBI. Spectra are vertically offset for clarity.

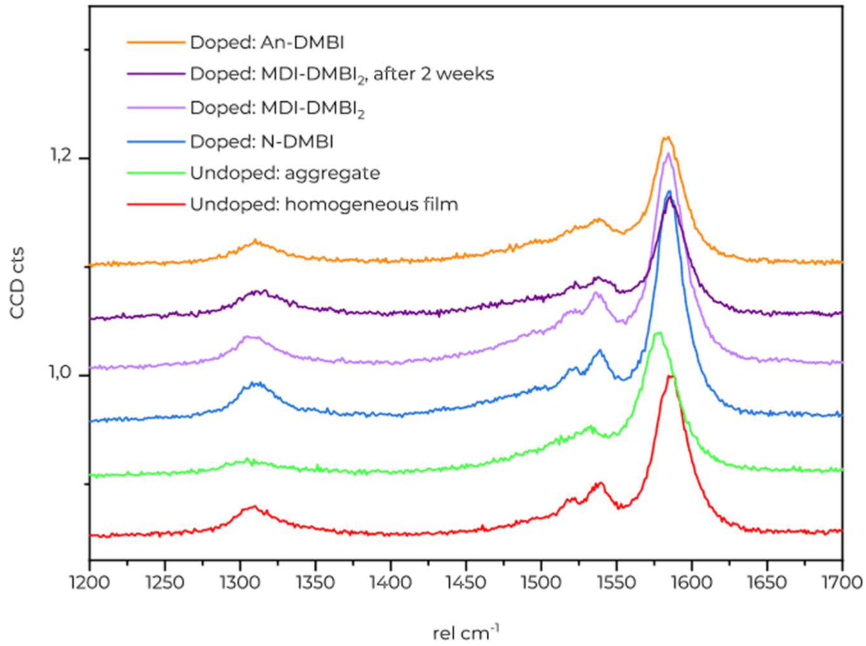

Figure 5.13
Magnified Raman spectra (1200–1700 cm^{-1}) of CoMoCAT SG65i films before and after doping with N-DMBI-H, MDI-DMBI$_2$, and An-DMBI. Spectra are vertically offset for clarity.

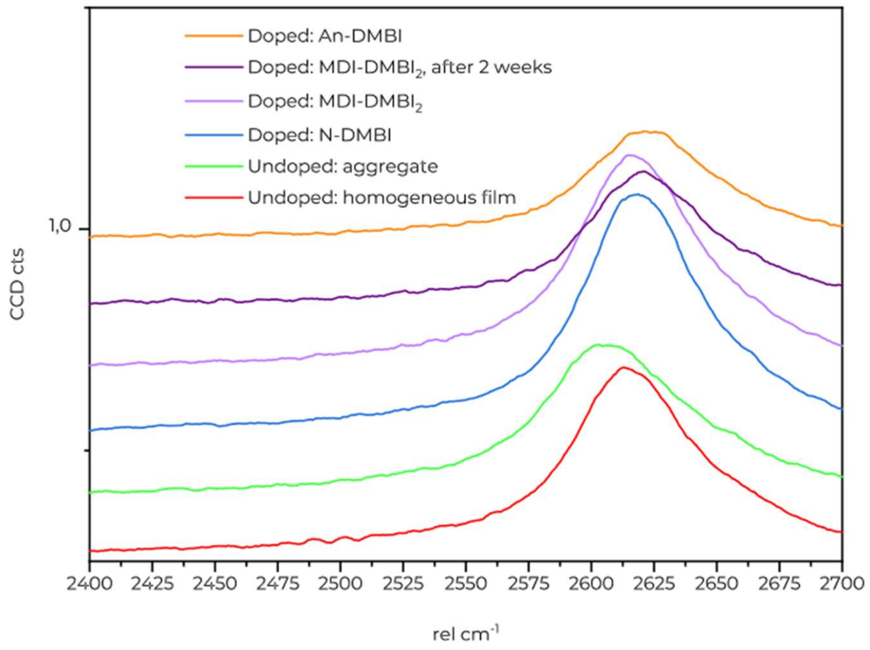

Figure 5.14
Magnified Raman spectra (2400–2700 cm^{-1}) of CoMoCAT SG65i films before and after doping with N-DMBI-H, MDI-DMBI$_2$, and An-DMBI. Spectra are vertically offset for clarity.

The data extracted from the Raman spectra are summarized in three tables to facilitate a clearer discussion: one reporting the bands shifts (Table 5.3), one the peak intensities and their ratios (Table 5.4), and one the integrated band areas and corresponding variations (Table 5.5).

5.6.3.1. Bands shifts

Table 5.3
Raman peak positions of CoMoCAT SG65i films before and after doping with N-DMBI-H, MDI-DMBI$_2$ and An-DMBI. Reported values correspond to the maxima of the D, G$^-$, G$^+$, and G' bands, with relative shifts ($\Delta\lambda$) referenced to the undoped homogeneous film.

	D		**G$^-$**		**G$^+$**		**G'**	
SWCNT treatment	λ_{max} (nm)	**Shift (nm)**	λ_{max} (nm)	**Shift (nm)**	λ_{max} (nm)	**Shift (nm)**	λ_{max} (nm)	**Shift (nm)**
Undoped: homogeneous film	1311.2	0	1536.4	0	1586	0	2616.8	0
Undoped: aggregate	1311.3	0.2	1535	-1.4	1577.7	-8.3	2608.5	-8.2
Doped: N-DMBI	1312.2	1	1538.3	1.8	1584.9	-1.1	2619.8	3
Doped: MDI-DMBI$_2$	1310.4	-0.8	1535.1	-1.4	1584.2	-1.7	2618.6	1.8
Doped: MDI-DMBI$_2$, after 2 weeks	1315.8	4.6	1539.9	3.5	1585.8	-0.2	2622.8	6
Doped: An-DMBI	1312.5	1.4	1537.6	1.2	1583.6	-2.4	2623.3	6.6

The Raman analysis reveals that, in the undoped films, both the G and G' bands are **red-shifted** by approximately 8-10 cm^{-1} in the **aggregated regions** compared to the **homogeneous areas**. Although counterintuitive, since tensile strain typically leads to blue-shifts, this behavior can be justified by the **compressive strain** induced during vacuum filtration.

The literature on CNTs and graphene primarily focuses on **tensile deformation** regimes, [44–47]and no direct data are available regarding the effects of compressive strain. Although the precise origin of this red-shift cannot yet be fully explained, this observation underscores the importance of comparing Raman spectra acquired from regions of similar nature, i.e., either homogeneous domains or aggregates. As mentioned earlier, we therefore chose to refer to the homogeneous regions in our analysis.

In freshly doped **MDI-DMBI$_2$** films, small **red-shifts** are observed for the D (-0.8 cm^{-1}), G$^-$ (-1.4 cm^{-1}), and G$^+$ (-1.7 cm^{-1}) bands, while the **G' band** displays a slight **blue-shift** (+1.8 cm^{-1}). This combination can be related to a strong n-type doping regime, where electron injection softens the longitudinal optical phonon (G$^+$) and stiffens the double-resonance mode (G') due to the suppression of resonance conditions as the Fermi level moves away from neutrality. Such behavior is consistent with observations in electrochemically doped CNTs and graphene.[48,49]

After **two weeks** under ambient conditions, the same **MDI-DMBI$_2$-doped** film exhibits the opposite trend, with **blue-shifts** in D (+4.6 cm^{-1}), G$^-$ (+3.5 cm^{-1}), and G' (+6.0 cm^{-1}), while G$^+$ returns to a value similar to the undoped condition (-0.2 cm^{-1}). This evolution can correspond to **partial dedoping**. As the carrier density decreases, conditions favorable to double-resonance scattering and phonon stiffening are restored.[50–52]

The films doped with **N-DMBI** show similar but slightly limited spectral displacementes, suggesting a lower reducing power and weaker charge-transfer efficiency of this dopant.[53] The D and G$^+$ bands display small blue- and red-shifts (+1.0 cm^{-1} and -1.1 cm^{-1}, respectively), while G' shifts moderately to higher frequencies (+3.0 cm^{-1}). These variations suggest a moderate n-type doping regime, with limited Fermi-level displacement but still evident quenching of the double-resonance process.

On the contrary, the **An-DMBI-doped** film exhibits a distinct behavior.
The G$^+$ band shows the largest red-shift (-2.4 cm^{-1}) among all samples, indicating strong electron injection, while G' undergoes a pronounced blue-shift (+6.6 cm^{-1}), comparable to that observed in the partially dedoped MDI-DMBI$_2$ sample. The D band also shifts slightly to higher frequency (+1.4 cm^{-1}). This combination suggests that An-DMBI induces effective charge transfer, but at the same time it leads to **local structural disorder** or heterogeneous adsorption, which may disturb resonance conditions and lead to an apparently inconsistent Raman response compared to its electrical performance.

In respect of band shifting, G$^+$ remains the most reliable **indicator of doping level**, consistently red-shifting upon electron injection due to phonon softening of the longitudinal optical mode. The G' band serves as a **complementary probe**, because it is influenced by both charge-transfer processes and resonance efficiency. The G$^-$ component exhibits non-monotonic behavior, while the D band, though less sensitive to doping level, becomes a useful indicator for dedoping and **defect-related scattering**.

5.6.3.2. Bands intensities

Table 5.4
Peak intensities of the main Raman bands (D, G, and G') for CoMoCAT SG65i films before and after doping with N-DMBI, MDI-DMBI$_2$, and An-DMBI.

	Peaks Intensities				**Intensities ratios**		
	I_D (a.u.)	**I_{G-} (a.u.)**	**I_{G+} (a.u.)**	**$I_{G'}$ (a.u.)**	**I_D/I_G**	**$I_D/I_{G'}$**	**$I_{G'}/I_G$**
Undoped: homogeneous film	531	544	603	566	0.463	0.938	0.493
Undoped: aggregate	520	533	558	544	0.477	0.956	0.499
Doped: N-DMBI	539	558	648	587	0.447	0.918	0.487
Doped: MDI-DMBI2	533	558	634	579	0.447	0.921	0.486
Doped: MDI-DMBI$_2$, after 2 weeks	533	540	584	555	0.474	0.960	0.494
Doped: An-DMBI	528	539	583	543	**0.471**	**0.972**	0.484

All doped CNT films exhibit a decrease in the **$I_{G'}/I_G$ ratio** compared with the undoped reference, reflecting partial suppression of the double-resonance process as the Fermi level shifts away from neutrality.

For **N-DMBI** and **MDI-DMBI$_2$**, the I_D/I_G ratio slightly decreases, consistent with screening of defect-related scattering at higher carrier densities.

An-DMBI, in contrast, presents a pronounced quenching of the G' band with a slightly higher I_D/I_G ratio, suggesting stronger but less homogeneous interaction with the CNT surface.

In the **MDI-DMBI$_2$** sample aged for two weeks in air, the partial recovery of the G' and G band intensities can be interpreted as progressive oxidative dedoping, while the overall band pattern remains distinct from the undoped film, indicating that some dopant-induced electronic modification persists even after extended air-exposure.

In summary, **An-DMBI** seems to induce the strongest electronic doping, as indicated by the pronounced red-shift of the G^+ band, but also introduces local structural perturbations consistent with less homogeneous adsorption. In contrast, **N-DMBI-H** and **MDI-DMBI$_2$** produce similar, moderate, and more uniform spectral changes in bands intensities.

5.6.3.3. Signals area

Table 5.5
Integrated areas of the main Raman bands (D, G, and G') for CoMoCAT SG65i films before and after doping with N-DMBI, MDI-DMBI$_2$, and An-DMBI.

	Bands areas			**Ratios between the band areas**		
	A_D	**A_G**	**$A_{G'}$**	**A_D/A_G**	**$A_D/A_{G'}$**	**$A_{G'}/A_G$**
Undoped: homogeneous film	1’104	5’851	4’904	0.19	0.23	0.84
Undoped: aggregate	828	6’829	4’180	0.12	0.20	0.61
Doped: N-DMBI	1’331	9’607	6’441	0.14	0.21	0.67
Doped: MDI-DMBI$_2$	1’174	10’097	5’983	0.12	0.20	0.59
Doped: MDI-DMBI$_2$, after 2 weeks	1’125	5’082	3’341	0.22	0.34	0.66
Doped: An-DMBI	784	5’898	2’675	0.13	**0.29**	0.45

The analysis of the integrated band areas confirms the trends observed for the intensity ratios. All doped films show lower $A_{G'}/A_G$ values than the undoped reference (0.84), consistent with reduced double-resonance efficiency as the Fermi level shifts away from neutrality. The decrease is most pronounced for An-DMBI (0.45), followed by MDI-DMBI$_2$ (0.59) and N-DMBI-H (0.67), indicating a doping efficiency trend of An-DMBI > MDI-DMBI$_2$ > N-DMBI-H. The stronger suppression of the G' band in the An-DMBI film suggests more effective electron transfer, although accompanied by greater structural heterogeneity.

For N-DMBI-H and MDI-DMBI$_2$, the **A_D/A_G** and **$A_D/A_{G'}$** ratios slightly decrease, suggesting partial screening of defect-related scattering at higher carrier densities. In contrast, An-DMBI presents a high **A_D/A_G**, supporting, another time, the occurrence of local structural disorder. After two weeks of air exposure, the MDI-DMBI$_2$ film shows a moderate increase in the D-band area, consistent with partial dedoping but incomplete recovery of the pristine structure.

The comparison of these results indicates a doping efficiency trend of An-DMBI > MDI-DMBI$_2$ > N-DMBI-H, with An-DMBI inducing the strongest yet less homogeneous interaction with the CNT network.

5.6.3.4. Summary

Raman spectroscopy provides insight into both the electronic and structural effects of molecular n-doping in SWCNT films.

Upon doping, all samples display red-shifts of the G^+ mode, quenching of the G' band, and moderate D-band changes, features typically associated with electron injection into the CNT π-system and the consequent modification of electron-phonon coupling.[40,42]

MDI-DMBI$_2$-doped film shows clear variations of n-type doping, with red-shifted G bands and blue-shifted G'. After two weeks of air exposure, the G^+ band nearly returns to its initial position while G' continues to blue-shift, consistent with **progressive oxidation** and partial recovery of the **pristine state**.

N-DMBI-H induces slightly weaker but relatively stable spectral changes, suggesting a lower but more uniform doping level. An-DMBI produces the largest G^+ red-shift and the strongest G' suppression, consistent with enhanced electron injection[41,43] but also with the possible contribution of local strain or inhomogeneous adsorption, both of which can lead to apparent variations in Raman trends.[43,44]

The D-band response remains small but provides complementary evidence: the limited reduction of the I_D/I_G ratio observed for N-DMBI and MDI-DMBI$_2$ may arise from defect-screening effects at higher carrier densities,[45] whereas the higher ratio in the An-DMBI sample could reflect **local disorder** induced by less homogeneous surface interactions.

In summary, the data suggest a qualitative trend in apparent doping efficiency (An-DMBI > MDI-DMBI$_2$ > N-DMBI-H). However, given the interplay of charge transfer, strain, and resonance effects, alternative interpretations cannot be excluded. Further in-situ or temperature-dependent Raman studies would be required to decouple electronic from structural contributions.

5.7. EPR analysis

The electrical and spectroscopic analyses presented in the previous sections (conductivity, Seebeck coefficient, UV–Vis absorption and Raman) collectively indicated that molecular doping with N-DMBI affects the electronic structure of the investigated systems. However, these techniques provide indirect information on charge transfer processes. In order to obtain a more direct and independent confirmation of electron injection from the dopant to the host material, **electron paramagnetic resonance (EPR)** spectroscopy was employed.

EPR is uniquely sensitive to the presence of unpaired electrons, making it a valuable probe for detecting paramagnetic species generated upon doping.[54] In particular, molecular dopants such as N-DMBI are known to undergo thermal activation, forming radical intermediates (DMBI•) capable of transferring electrons to the semiconductor or to carbon-based frameworks. The resulting charge carriers or localized spins can produce characteristic EPR signals, thereby offering qualitative evidence of successful doping.[55]

This experiment was therefore designed as a **proof-of-concept measurement** aimed at verifying whether the N-DMBI treatment of SWCNTs indeed produces detectable paramagnetic centers consistent with charge transfer. Given the complexity of EPR measurements on conductive CNT systems and the limited time available, the study was restricted to N-DMBI as a model dopant.[56–58]

Nevertheless, the same procedure will be extended in future work to MDI-DMBI$_2$ and An-DMBI, in order to systematically compare their electronic effects.

The applied experimental procedure was mainly inspired by the protocol reported by Sperlich et al.[7], though several modifications were introduced to adapt it to the available materials and simplify the workflow. In particular, polymer-wrapping steps (e.g., with polyfluorene) were omitted, as the aim was to directly probe the CNT–dopant interaction in powder form. The experimental details are reported in paragraph 5.9.7.

5.7.1. Results and discussion

EPR spectra were recorded for pristine (sample A) and N-DMBI-doped (sample B) SWCNT powders dispersed in chlorobenzene at a concentration of 0.22 mg mL^{-1}, under inert atmosphere and at room temperature. Eventually, both samples were annealed by heating at 60°C for 1h.

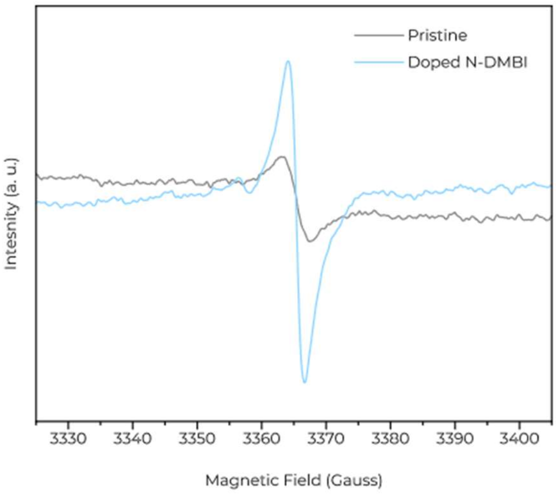

Figure 5.15
EPR spectra of pristine and N-DMBI-doped SWCNT powders.

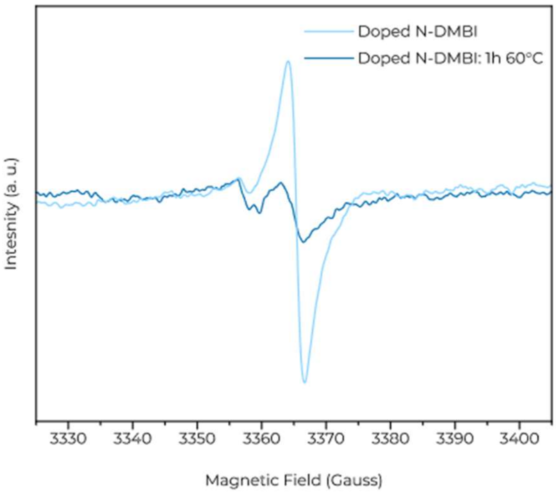

Figure 5.16
EPR spectra of CNT powders doped with N-DMBI before and after thermal annealing (1 h at 60 °C).

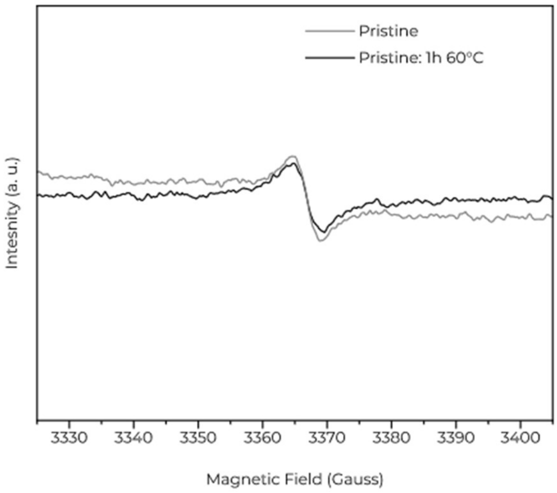

Figure 5.17
EPR spectra of pristine CNT powders before and after annealing at 60 °C for 1 h.

As shown in **Figure 5.15**, both samples before annealing exhibit a resonance feature at **g_1 = 2.0016 ± 0.0009**, attributed to carbon-centered radicals weakly localized on the CNT π-orbitals.[59–61] In addition, the doped sample displays a second component at **g_2 = 2.0069 ± 0.0009**, absent in the pristine CNTs. This additional signal is consistent with the formation of graphitic-type defects or localized unpaired spins generated upon electron transfer from N-DMBI.[62] The overall signal intensity is significantly higher for the doped sample, indicating the creation of unpaired electrons associated with the doping process.

After thermal activation at **60 °C for 1 h**, a different evolution is observed (Figure 5.16, Figure 5.17). The pristine CNTs show negligible changes, whereas the doped sample displays a significant reduction in signal intensity, particularly at g_1. This behavior reflects the activation mechanism of N-DMBI. Heating promotes the activation of the dopant, generating additional DMBI• radicals and enhancing charge transfer to the CNT framework. Therefore, a greater fraction of electrons becomes delocalized along the CNT network, leading to enhanced doping efficiency but fewer localized paramagnetic centers, and thus a weaker EPR signal.

The persistence of the g_2 feature, albeit reduced, suggests **that graphitic-type defects** or spin centers remain partially unpaired even after thermal activation. The observed decrease in intensity can therefore be justified as a signature of more effective electronic delocalization and spin pairing.

By these EPR results, we conclude that N-DMBI doping introduces **new paramagnetic species** into the CNTs. Despite the intrinsic difficulty of performing EPR on conductive CNT systems, the experiment successfully reveals the electronic changes induced by N-DMBI doping.

5.8. Conclusion

The investigation of n-type doping in SWCNT films using N-DMBI-H, An-DMBI, and MDI-$DMBI_2$ reveals a coherent picture linking molecular structure, interfacial adsorption, and long-term thermoelectric stability.
In contrast to soluble polymeric semiconductors such as N2200, doping in CNT networks is dominated by interfacial phenomena. The insoluble, percolative nature of the CNT films makes dopant **accessibility** and **adsorption** the main factors determining both the initial doping efficiency and its persistence under ambient conditions.

Thickness-dependent measurements show that the diffusion and spatial distribution of dopants within the network strongly affect the kinetics of dedoping: thinner films exhibit faster oxidation by oxygen and moisture, while thicker buckypapers retain their n-type character for longer, consistent with slower gas permeation and higher protection of the inner regions.

Moreover, **thermoelectric measurements** reveal that MDI-$DMBI_2$ induces the most significant thermoelectric response after doping, combined with a persistent n-type behavior during air exposure. While An-DMBI yields the most stable long-term doping, N-DMBI-H rapidly reverts to p-type conduction. This trend agrees with the percentage of dopant cation retention determined from UV-Vis analysis (N-$DMBI^+$ < An-$DMBI^+$ < MDI-$DMBI_2^{2+}$), confirming that interfacial adsorption plays a crucial role in stabilizing the doped state. The enhanced resistance to oxidative dedoping observed for An-DMBI and MDI-$DMBI_2$ is consistent with the presence of additional aromatic substituents and increased molecular polarizability, which strengthen π–π and ionic interactions with the CNT surface. These extended interactions likely facilitate the formation of more persistent passivation layers that hinder reoxidation of the doped network.

Spectroscopic analyses support this interpretation.
UV-Vis-NIR spectra indicate comparable initial doping efficiency among the three dopants but a slower spectral recovery for An-DMBI and MDI-$DMBI_2$, reflecting improved resistance to oxydation. **Raman spectroscopy** further confirms electron injection into the CNT π-system through the red-shift of the G^+ mode and quenching of the G' band, with the magnitude of these shifts correlating with the doping strength (N-DMBI < MDI-$DMBI_2$ < An-DMBI).
Ultimately, **EPR data** provide a direct evidence that doping with N-DMBI, and by extension with its derivatives, leads to the formation of paramagnetic species within the CNT network.

Altogether, these results converge toward a unified interpretation: the molecular structure of DMBI derivatives has a predominant effect on environmental stability through interfacial coupling with the CNT network. In particular, the data suggest that introducing additional aromatic units and multiple redox-active functionalities onto the DMBI core enhances adsorption and retards oxidative dedoping, thereby improving the retention of the n-type character.

Rational tailoring of molecular structure to increase dopant-CNT interactions thus represents a promising route to design durable n-type thermoelectric materials based on carbon nanotubes.

5.9. Experimental procedures

5.9.1. Sample preparation

Semiconducting single-walled carbon nanotubes (s-SWCNTs, **CoMoCAT SG65i**, Sigma-Aldrich; semiconducting fraction ≈95%, with ≈40% (6,5) chirality) were used as received. The followed experimental steps for sample preparation are here explained in detail:

a. **Addition of the SDBS(aq) solution** - Since the powder is highly electrostatic, 4.5 mg of CoMoCAT SG65i were weighed on weighing paper and transferred into a 50 mL Falcon tube with the aid of an anti-static gun. A stock solution of SDBS (sodium dodecyl benzenesulfonate, Sigma-Aldrich) was prepared by dissolving 120 mg SDBS in 60 mL of deionized (DI) water, followed by 10 min bath sonication to ensure complete dissolution. Then, 45 mL of this aqueous solution were added to the Falcon tube containing the CNT powder, yielding a nominal CNT concentration of 0.10 mg mL^{-1} and SDBS/CNT = 20:1 (w/w).

b. **Sonication** - Homogenization of the suspension was performed by tip ultrasonication (Sonics Vibra-Cell VC-505) in pulsed mode (3 × 10 min, 10 s on / 10 s off, 15W power) using a broad, flat titanium probe. The tube was immersed in an ice bath, refreshed every 10 min to limit heating and prevent nanotube damage. The resulting dispersion appeared homogeneous; to limit the presence of aggregates, the bottom few milliliters, where sediment occasionally accumulated, were discarded.

c. **Filtration under vacuum** - CNT films were prepared by vacuum filtration using a sintered-glass funnel connected to a Labbox V10 pump. The in-line analog gauge indicated a vacuum of approximately -80 kPa relative to atmosphere (absolute pressure ~20-25 kPa). Filtration continued until a uniform CNT film was formed on PTFE Omnipore filters (0.1 μm pore size, 25 or 47 mm diameter) from Merck. Residual surfactant was removed by rinsing the mat with ~100 mL DI water for 47 mm filters or ~50 mL for 25 mm filters.

d. **Transfer of the film** - The CNT films were then transferred onto cleaned glass slides (previously cleaned with isopropanol and dried with compressed air) by mechanical release. A small DI-water droplet was placed on the glass surface, and the PTFE filter (CNT side facing down) was gently pressed to ensure adhesion. Mild heating at ~70 °C on a hot plate facilitated release of the film from the filter. Films from 47 mm filters were divided in four equal sections and transferred onto four glass sec (~26 × 20 mm), whereas those from 25 mm filters were transferred in one piece. Alternative transfer via dissolvable polycarbonate/PVP filters Nucleopore (0.1 µm, 25 mm) in chloroform or chlorobenzene was also tested but proved reproducible only for thicker films (>1 µm).

e. **Deposition of the Ag contacts** - After transfer, four silver-paste (Sigma-Aldrich) contacts were deposited at the film corners to define a van der Pauw geometry. The contacts were mostly circular and with a diameter of 3 mm. The paste was left to dry in air for 1 h, producing a nearly square film with 10×11 mm^2. Excess CNT film outside this region was removed with scalpels to minimize parasitic current paths.

f. **Annealing at 150 °C (1 h)** - Thermal annealing was carried out inside a nitrogen glovebox ($O_2/H_2O < 10$ ppm) to partially remove adsorbed oxygen and reduce residual p-type doping. Samples were placed on a pre-heated hot plate at 150 °C for 1 h with the film facing upward. After annealing, the slides were moved onto fabric inside the glovebox for a gentle cool-down (~5 min) to room temperature.

g. **Drop-casting of the dopant solution** - Molecular doping was performed by drop-casting the dopant solution (typically 40 mM in toluene) directly onto the CNT film under nitrogen.

h. **Dopant diffusion (5 min)** - The samples were immediately covered with a Petri dish to reduce solvent evaporation and allow the dopant to diffuse through the CNT network for 5 min at room temperature.

i. **Annealing at 150 °C (1 h)** - Finally, doped films were **annealed again** at 150 °C for 1 h and gently cooled as before. This step activates the dopant, which transfer electrons to the CNT network and stabilize the n-type doping state.

5.9.2. Determination of film thickness

Film thickness (t_z) was measured by stylus profilometry (KLA-Tencor Alpha D500) using a 1 mm scan length, 0.1 mm s^{-1} scan speed, 10 µm vertical range, and 5 mg stylus force. For each sample, two scans per side were acquired and averaged.

5.9.3. Determination of electrical conductivity and Seebeck coefficient

The measurement system, described in detail by Dörling et al. [63] consists of two copper blocks acting respectively as heater and heat sink, between which the sample is clamped face-down. Each block contains two Copper-Constantan thermocouples in direct contact with the sample corners.

A 30 W cartridge heater embedded in one copper block generates the temperature gradient, controlled by a PID-regulated solid-state relay (SSR) through pulse-width modulation at 10 Hz. The opposite block acts as a passive heat sink, maintaining a stable ΔT typically between 5 and 10 K.

Electrical connections are managed through a custom relay board, which dynamically switch among the eight thermocouple leads. The board is operated by a Raspberry Pi 3B via GPIO pins and shift registers, which also control the temperature feedback and communicate with the Keithley 2400 SourceMeter used for electrical measurements. Data acquisition and control were automated via Python (PyVISA interface).

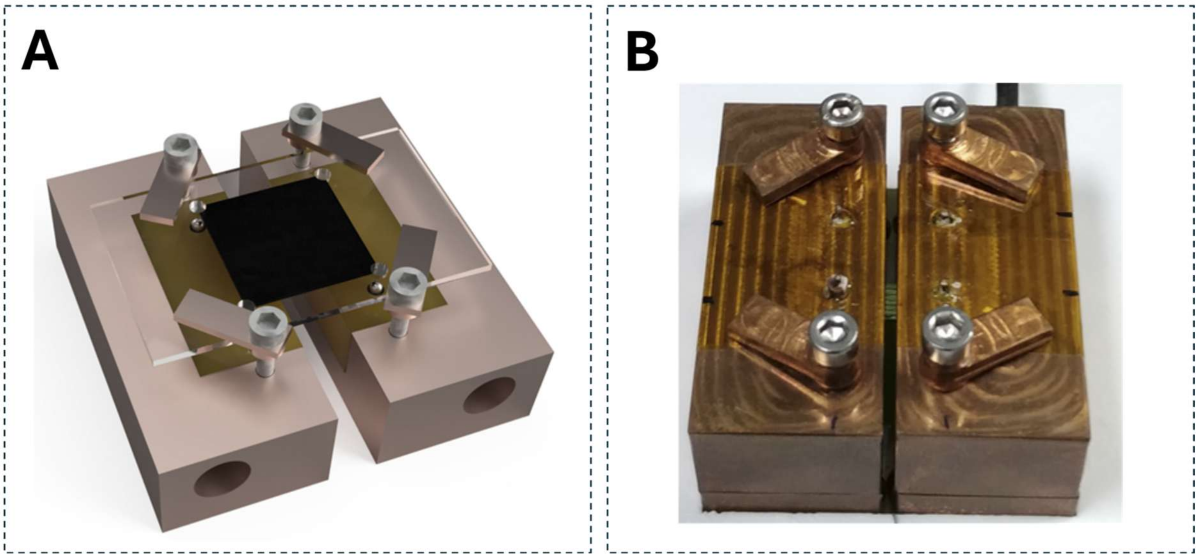

Figure 5.18
(A) Sketch and (B) a photograph of the sample holder. Adapted from the work of Dörling and co-workers.[63] License CC BY-NC 4.0

Thermocouples placed near each contact recorded the effective temperature difference ΔT, accounting for partial heating of the cold side. Measurements were repeated in four contact configurations to minimize systematic errors and were performed at several hot-side temperatures, in the range of 33-37 °C. The Seebeck coefficient was extracted from the slope of the thermoelectric voltage (V_S) as a function of ΔT, while electrical conductivity was measured at room temperature using the van der Pauw method under isothermal conditions, with the heaters switched off and all contacts at approximately the same temperature (room temperature).

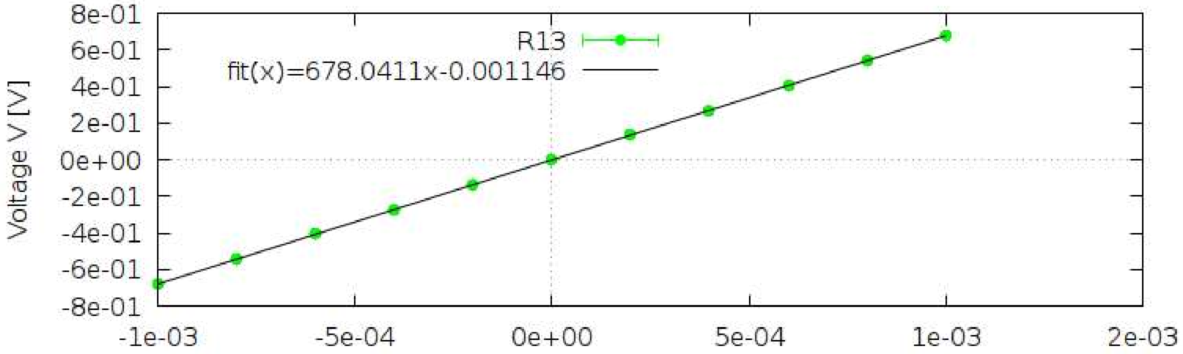

Figure 5.19
Representative current-voltage (I-V) characteristic of a doped CNT thin film measured for resistance extraction using the Van der Pauw method. The linear behavior confirms ohmic transport in the investigated current range, and the resistance was obtained from the slope of the fitted curve.

5.9.4. UV-visible analysis on residual solution

Spectra were recorded using a JASCO V-770 UV/Vis/NIR spectrophotometer equipped with 1 cm quartz cuvettes and operated in photometric (absorbance) mode. Instrumental parameters were: UV/Vis bandwidth 2.0 nm, response 0.96 s, data interval 0.5 nm, and scan speed 1000 nm min^{-1}.

Spectra were acquired in the range 190-450 nm, using the mixture methanol:acetonitrile (1:1 v/v) as solvent and as baseline. Automatic baseline correction was applied via the instrument software.

Calibration curves were constructed using dopant salts, N-DMBI-BF_4, An-DMBI-I, and MDI-$DMBI_2(PF_6)_2$ (see Figure 5.20), over the following concentration ranges: 0.005-0.10 mM for N-DMBI-BF_4 and An-DMBI-I, and 0.001-0.010 mM for MDI-$DMBI_2$-$(PF_6)_2$.

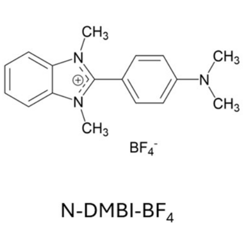
N-DMBI-BF_4

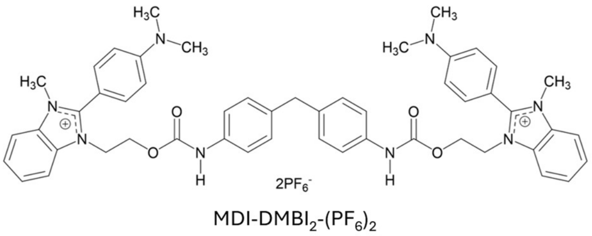
MDI-$DMBI_2$-$(PF_6)_2$

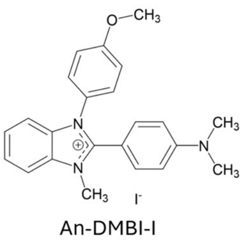
An-DMBI-I

Figure 5.20
Chemical structure of the corresponding cations of the dopants employed.

The absorbance maximum between 340-350 nm was plotted against concentration to generate linear calibration plots ($R^2 \geq 0.99$). The calibration curves and the linear fittings are reported in paragraph 5.10.1.

For adsorption experiments, three CNT films (~2 μm thick, 1 × 1 cm²) were cut from the same CoMoCAT SG65i film and kept on their PTFE supports. The thickness was measured by transferring the remaining parts of the films, left after cutting them to the described dimensions, onto microscope slides, which were then analyzed by profilometry according to the previously described protocol (Paragraph 5.9.2).

Each film was immersed in 2 mL of dopant solution: 5 mM for N-DMBI-H and An-DMBI-H, 2.5 mM for MDI-DMBI$_2$, in 1:1 MeOH:ACN. The sealed 6 mL glass vials were stirred at 400 rpm for 50 h at room temperature in a nitrogen-filled glovebox (O_2, H_2O < 10 ppm). After incubation, aliquots of the residual supernatants were withdrawn and diluted to 0.05 mM (N-DMBI-H, An-DMBI) or 2.5 μM (MDI-DMBI$_2$) before analysis. The measured residual concentrations after 50 h were 0.0468 mM (N-DMBI-H), 0.0427 mM (An-DMBI), and 1.63 μM (MDI-DMBI$_2$), corresponding to adsorbed fractions of ~6 %, 15 %, and 35 %, respectively.

To assess the role of oxygen and light exposure, additional control solutions were stored either (i) under ambient air and light, or (ii) under nitrogen inside the glovebox.

5.9.5. UV-Vis-NIR analysis on doped films

The films of CoMoCAT were produced using the standard general procedure. In respect to this, 2.75 mL of CoMoCAT SG65i suspension were filtered on a PTFE filter (d = 47 mm). The film was washed with approximately 100 mL of distilled water. The film thickness after the transfer on glass was determined at 148 nm by standard profilometry analysis.

UV-Vis-NIR spectra were recorded using a JASCO V-770 UV/Vis/NIR spectrophotometer in transmission mode.

The glass slides carrying the CNT films were suspended during acquisition to avoid reflection artifacts. Spectra were measured along both the x and y directions and subsequently averaged to minimize local inhomogeneity. Baselines were acquired using a clean microscope slide and subtracted from each spectrum; a minor linear correction was applied to remove residual drift, and spectra were normalized to zero absorbance at 793 nm.

The scan speed was set to 400 nm/min, while all other acquisition parameters (bandwidth, data interval, and response time) were analogue to those used for the UV-Vis measurements of dopant solutions (see Section 5.9.4).

5.9.6. Raman spectroscopy details

The Raman spectra were obtained on the same samples used for the electrical conductivity and Seebeck coefficient characterization, in order to establish a direct correlation between the transport properties and the structural/electronic changes upon doping.

For MDI-DMBI$_2$, Raman spectra were recorded both immediately after doping and after two weeks of exposure to ambient conditions to monitor the temporal evolution of the doped state. The pristine CNT film served as reference.

Raman spectra were acquired using a WITec Alpha300RA micro-Raman spectrometer equipped with a 531.9 nm excitation laser and a 1200 g/mm grating (BLZ = 500 nm). The system was operated in backscattering geometry with a Zeiss EC Epiplan-Neofluar 10× / 0.25 objective, corresponding to a laser spot size of approximately 2-3 μm. The spectral resolution was about 1 cm^{-1}, and calibration was verified against the Si reference peak at 520.7 cm^{-1}. Each spectrum was acquired using 10 accumulations with an integration time of 0.515 s per accumulation at a detector temperature of -60 °C. The CCD detector (DR316B, 16-bit, 2000 × 256 pixels) was operated in single-track mode with a preamplifier gain of 1 and without inducing detectable laser heating on the sample. All measurements were carried out at room temperature under ambient conditions.

The pristine CNT film was analyzed in six positions: three corresponding to homogeneous regions and three to aggregated areas. The spectra collected within each group were highly consistent, confirming the overall uniformity of the film.

All spectra were normalized to the acquisition time and laser power and are reported in arbitrary units (CCD counts). The displayed spectra were vertically offset for clarity and lightly smoothed using a Savitzky-Golay filter (12 points, polynomial order 2), while all quantitative analyses were performed on the raw data. Peak deconvolution was performed in OriginLab using independent Voigt fits for the D, G$^-$, G$^+$, and G' bands, from which the peak positions and integrated areas were extracted. An example of the fit is reported in the paragraph 0.

For the doped films, one representative spectrum was recorded for each sample under identical conditions. The observed spectral variations were well above the instrumental uncertainty, confirming the statistical significance of the differences among samples.

5.9.7. EPR details

Semiconducting single-wall carbon nanotubes (SWCNTs, CoMoCAT SG65i) were dispersed in chlorobenzene (CB). In a 50 mL polypropylene centrifuge tube (Falcon), 20.4 mg of SG65i powder were combined with 20.4 mL of CB (nominal concentration 1.0 mg mL^{-1}).

Subsequently, the suspension was homogenized by tip ultrasonication (Sonics Vibra-Cell VC-505) in pulsed mode (3 × 10 min, 10 s on / 10 s off, 20% amplitude), using a broad, flat titanium probe. The tube was immersed in an ice bath throughout to prevent overheating.

After sonication, the dispersion was allowed to settle under ambient conditions. Since perfect homogeneous dispersion is not achievable and part of the material tends to remain attached to the tube walls or sediment, only the supernatant was carefully transferred into a glass vial with septum. The vial was sealed with Parafilm® and degassed by introducing a stream of nitrogen through a needle inserted into the vial, while a second needle served as an outlet vent. The nitrogen flow (from the laboratory line) was maintained for one cycle of 20 min to reduce the dissolved oxygen content, known to interfere with EPR measurements.

In parallel, 20 mL of pure CB were degassed using the same procedure. Both vials were then transferred into a nitrogen-filled glovebox (O_2, H_2O < 10 ppm).

The amount of dopant was calculated to achieve a nominal 100% monolayer coverage of N-$DMBI^+$ (cation) on the CNT surface. Based on manufacturer data, the CoMoCAT SG65i SWCNTs have a surface area ≥ 700 m^2g^{-1}. Thus, 1 mg of nanotubes (~ 1 mL of dispersion) exposes about 0.7 m^2 of surface.

The projected area of the N-$DMBI^+$ cation was estimated from the 3D structure of the N-DMBI-I molecule retrieved from the work of Hwang et al.[64]. Using Mercury software, the distances between the most distant pairs of atoms along two perpendicular directions were measured to estimate the molecular length (L) and width (W).

To account for the steric contribution of the outermost hydrogen atoms (which were used as reference points for the measurements), the van der Waals radius of hydrogen (r = 1.20 Å) was added to each side.[65]

The projected molecular area was then approximated according to the following relation:

$$\mathrm{A}_{mol} \sim (\mathrm{L} + 2\mathrm{r})(W + 2r) \tag{5.16}$$

From our measurements ($L = 12.7$ Å and $W = 6.1$ Å), we obtained an approximate A_{mol} of 1.28×10^{-18} m^2.

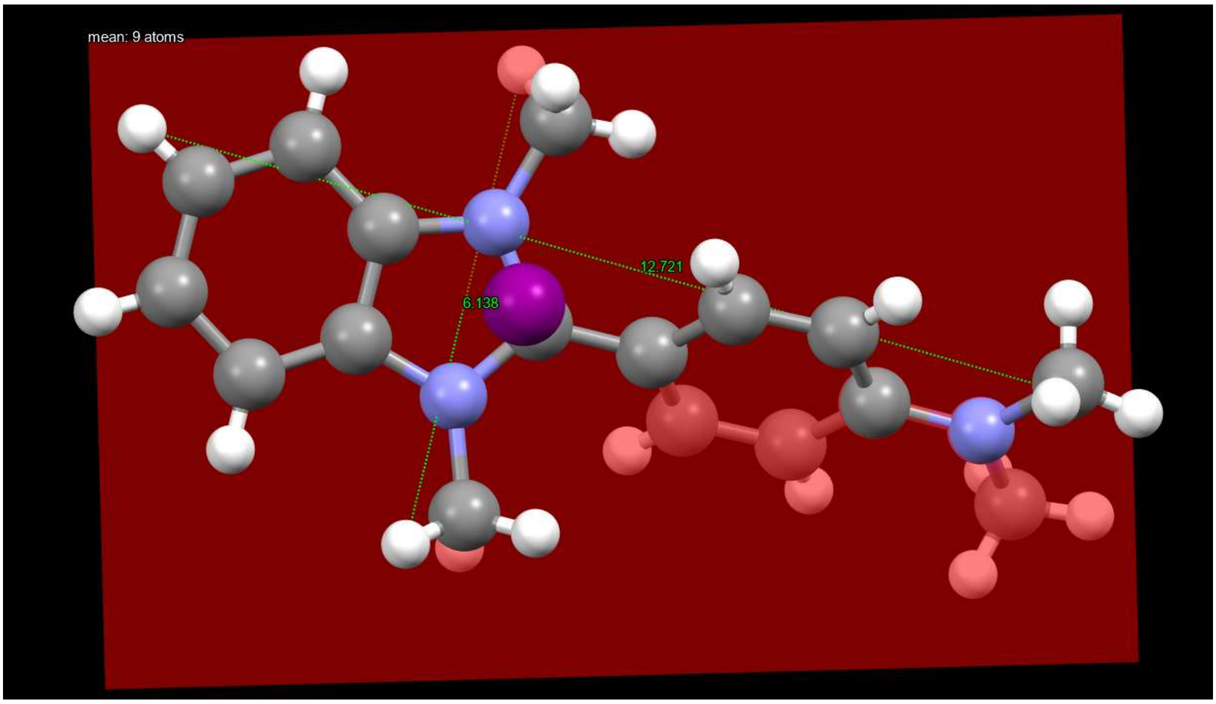

Figure 5.21
3D molecular structure of N-DMBI-I (N-DMBI$^+$ I$^-$). The molecular length and width are highlighted, measured as the distance between the most distant pairs of atoms along two perpendicular directions. The reference plane is also indicated, corresponding to the plane defined by the atoms of the benzimidazolium moiety.

Dividing the total nanotube surface area per 1 mg (0.7 m²) by this molecular footprint yields that 1 mg of SWCNTs could theoretically adsorb ≈ 5.47×10^{17} molecules for full monolayer coverage, corresponding to 9.08×10^{-3} mmol or 0.243 mg of N-DMBI.

Inside the glovebox, a dopant stock solution was prepared by dissolving 3.3 mg of N-DMBI in 0.673 mL of degassed CB, and the solute was completely dissolved under stirring. Subsequently, 0.50 mL of the solution were withdrawn and added to 1.00 mL of SWCNT dispersion to obtain the doped sample (sample B).

Therefore, sample B contained 0.243 mg of N-DMBI, and 1 mg of SWCNT (reaching a concentration of 0.66 mg mL^{-1}).

In parallel, 1.0 mL of SWCNT dispersion (1 mg mL^{-1}) and 0.5 mL of degassed CB were combined in another amber vial (vial A) and stirred overnight, affording a dispersion with a concentration of 0.66 mg mL^{-1}.

Both pristine (A) and doped (B) dispersions were conserved overnight in glovebox. Subsequently both dispersions were diluted with degassed CB to reach a final SWCNT concentration of 0.22 mg mL^{-1} before the characterization.

Then the suspensions were loaded into 4 mm quartz EPR tubes (~ 0.5 mL of suspension per tube), using a needle coupled with a syringe to overcome wetting and adhesion of the dispersion to the tube walls.

The tubes were sealed with Parafilm and covered with silicone sealant to prevent air penetration during storage and measurement.

EPR measurements were performed on a Bruker EMX spectrometer operating at X-band frequency (9.43 GHz), equipped with an Oxford continuous-flow cryostat (4-298 K). Unless otherwise stated, spectra were recorded at the following settings:

- Temperature: 130 K
- Microwave power: 20 mW
- Modulation amplitude: 1 G (100 kHz)
- Sweep width: 100 G (center field ≈ 3365 G)
- Time constant: 40 ms
- Conversion time: 20.48 ms
- Resolution: 10^{24} points
- Receiver gain: 2×10^4
- Averaging: 20 accumulations per spectrum

Calibration of the magnetic field and g-value was performed using a DPPH standard ($g = 2.0036$) measured in the same cavity. Spectra of pure CB and dopant-only solution were also recorded as references to exclude artefacts or direct radical signals unrelated to CNT doping.

All spectra were baseline-corrected and normalized to the same receiver gain before comparison.

Additional treatment

To probe the activation of the dopant, an aliquot of the doped sample was thermally annealed at 60 °C for 1 h prior to EPR measurement.

5.10. Appendix

5.10.1. UV-Vis spectroscopy: calibration curves and linear fittings

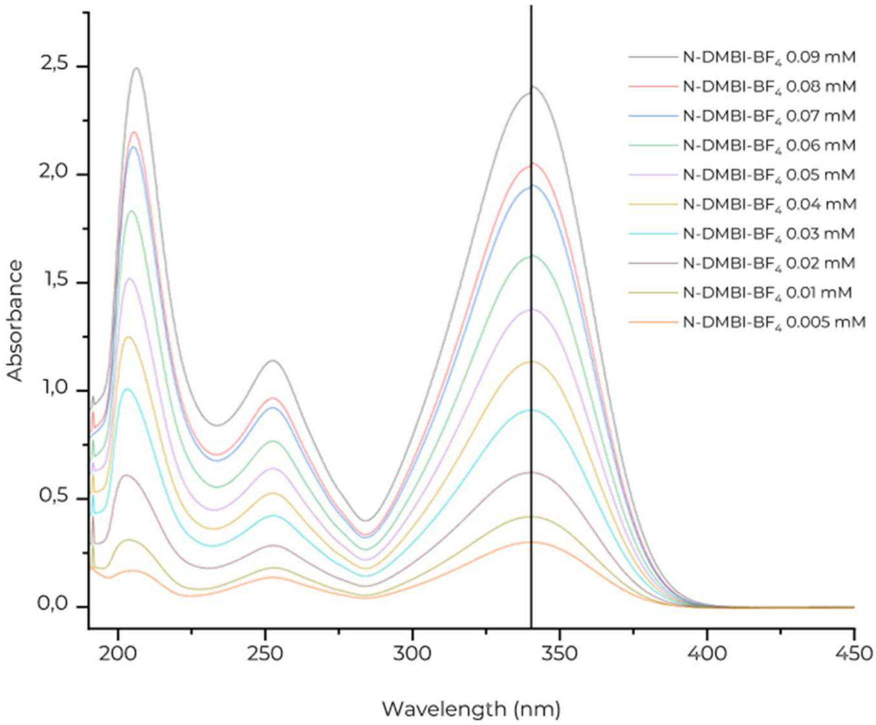

Figure 5.22 UV-Vis spectra of the standard solutions of N-DMBI-BF$_4$.

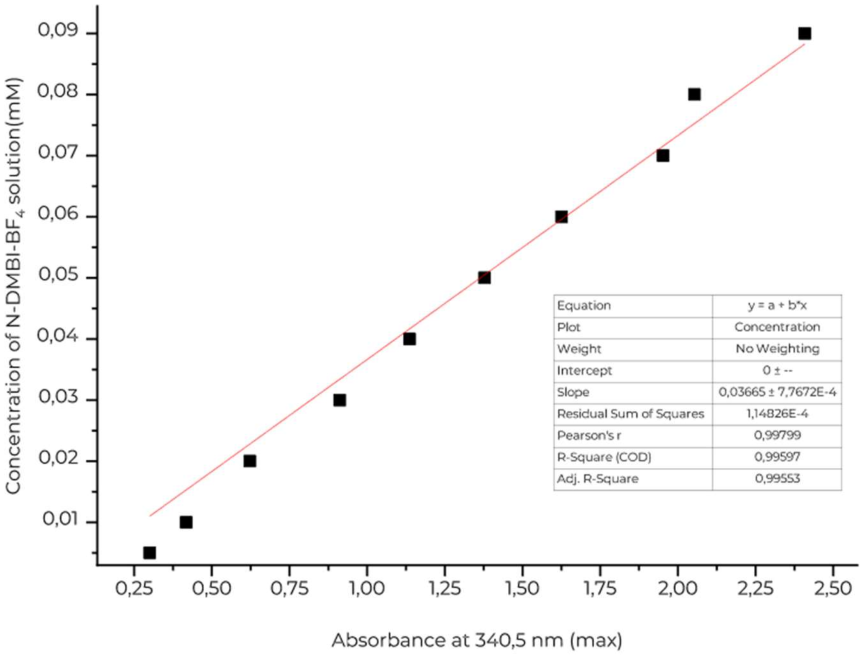

Equation	y = a + b*x
Plot	Concentration
Weight	No Weighting
Intercept	0 ± --
Slope	0,03665 ± 7,7672E-4
Residual Sum of Squares	1,14826E-4
Pearson's r	0,99799
R-Square (COD)	0,99597
Adj. R-Square	0,99553

Figure 5.23 Linear fit of the standard concentrations of N-DMBI-BF$_4$ versus the UV-Vis absorption peak intensity at 340.5 nm (absorption maximum).

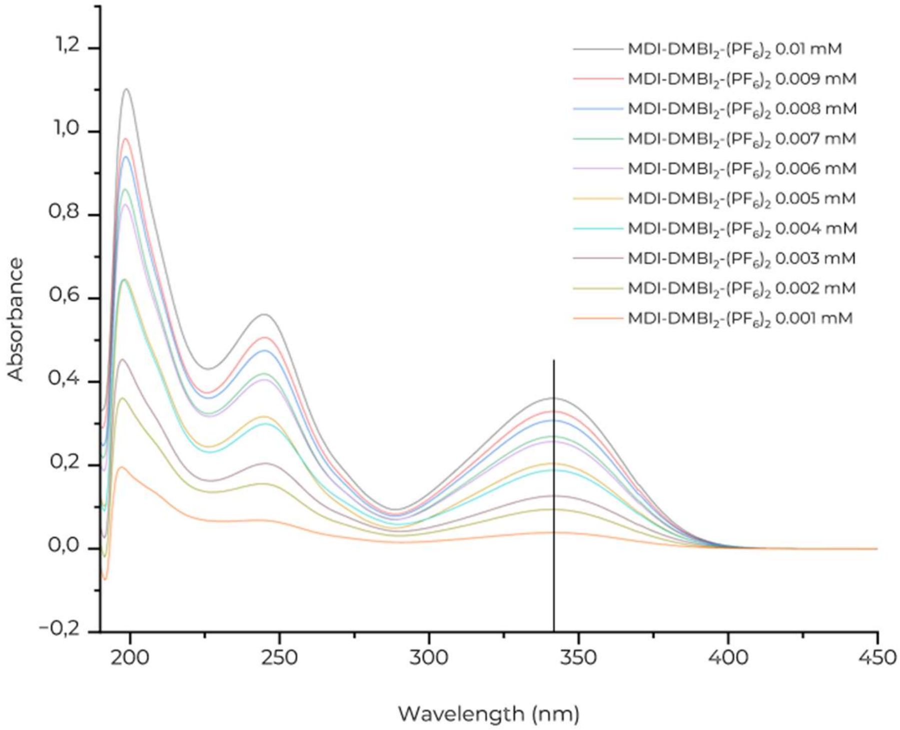

Figure 5.24 UV-Vis spectra of the standard solutions of MDI-DMBI-$(PF_6)_2$.

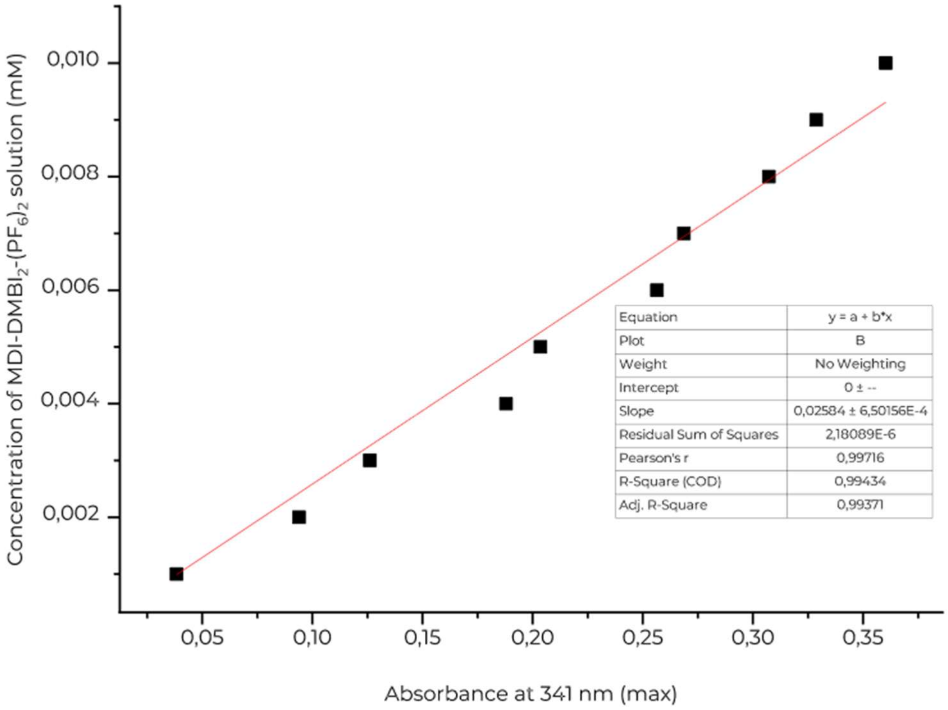

Equation	y = a + b*x
Plot	B
Weight	No Weighting
Intercept	0 ± --
Slope	0,02584 ± 6,50156E-4
Residual Sum of Squares	2,18089E-6
Pearson's r	0,99716
R-Square (COD)	0,99434
Adj. R-Square	0,99371

Figure 5.25 Linear fit of the standard concentrations of MDI-DMBI-$(PF_6)_2$ versus the UV-Vis absorption peak intensity at 341 nm (absorption maximum).

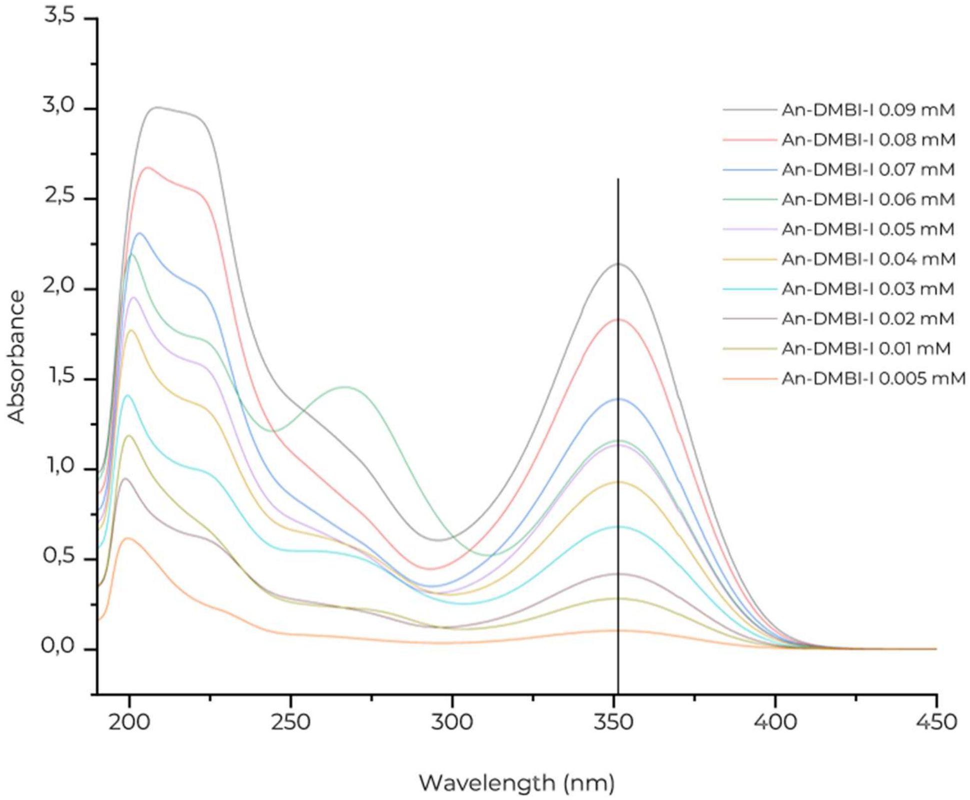

Figure 5.26 UV-Vis spectra of the standard solutions of An-DMBI-I.

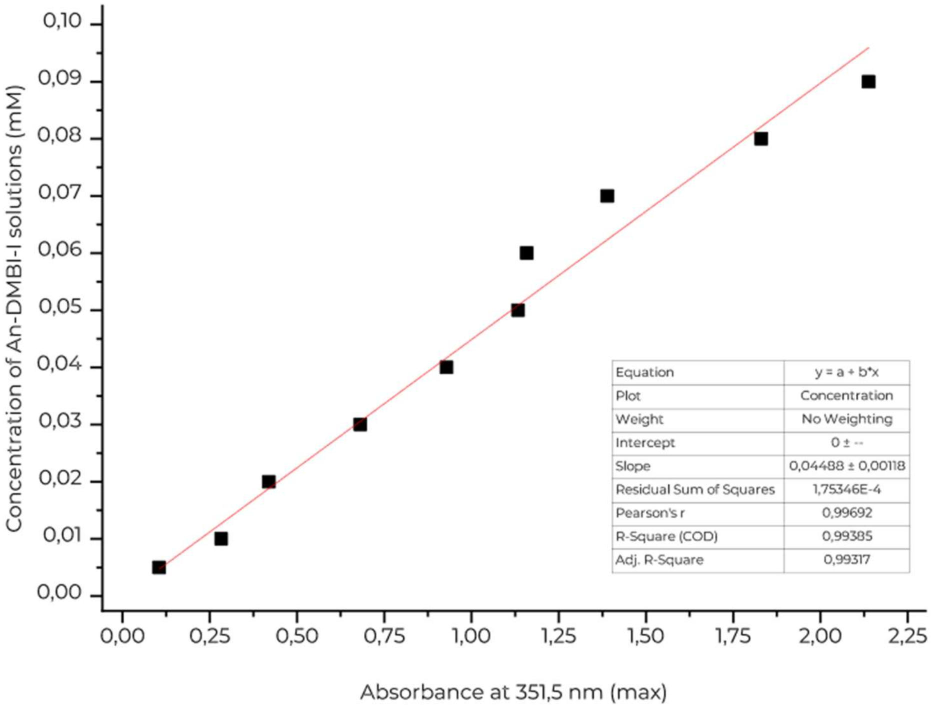

Equation	y = a + b*x
Plot	Concentration
Weight	No Weighting
Intercept	0 ± --
Slope	0,04488 ± 0,00118
Residual Sum of Squares	1,75346E-4
Pearson's r	0,99692
R-Square (COD)	0,99385
Adj. R-Square	0,99317

Figure 5.27 Linear fit of the standard concentrations of An-DMBI-I versus the UV-Vis absorption peak intensity at 351.5 nm (absorption maximum).

5.10.2. Raman spectroscopy: Voigt Fit

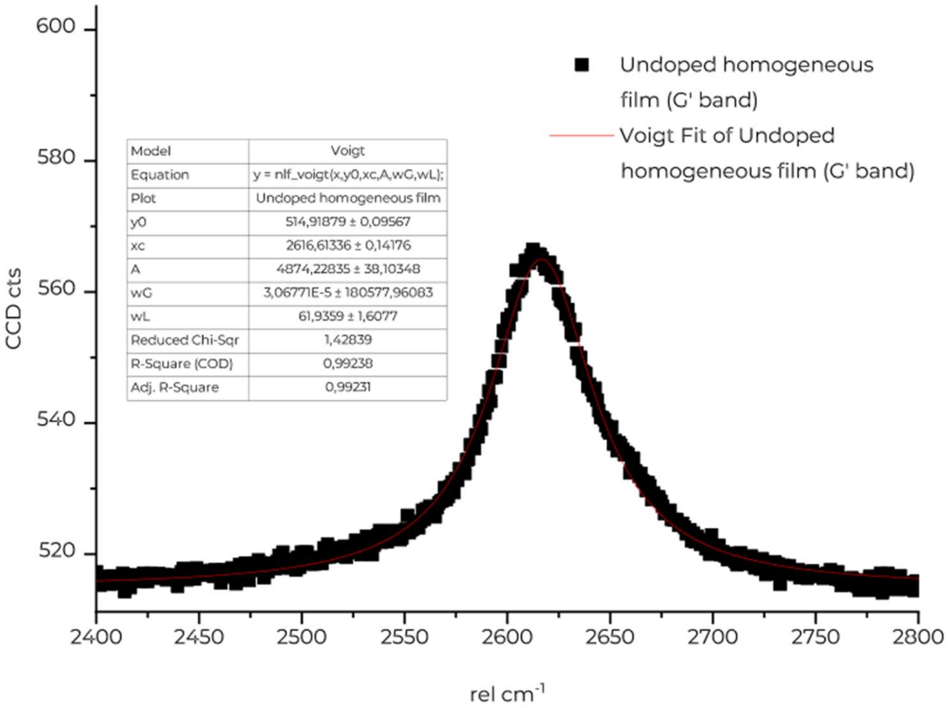

Model	Voigt
Equation	y = nlf_voigt(x,y0,xc,A,wG,wL);
Plot	Undoped homogeneous film
y0	514,91879 ± 0,09567
xc	2616,61336 ± 0,14176
A	4874,22835 ± 38,10348
wG	3,06771E-5 ± 180577,96083
wL	61,9359 ± 1,6077
Reduced Chi-Sqr	1,42839
R-Square (COD)	0,99238
Adj. R-Square	0,99231

Figure 5.28 Raman spectrum of the G' band for the undoped homogeneous SWCNT film, fitted with a Voigt function.

5.11. Bibliography

(1) Yoshida, K.; Kuwahara, Y.; Saito, T.; Nonoguchi, Y. Dopant-Inherent Mechanisms of Atmospheric Stability in Chemically N-Doped Semiconducting Carbon Nanotubes Revealed by Tracking Optical Absorption. *J Phys Chem C* **2024**.

(2) Koh, B.; Cheng, W. Mechanisms of Carbon Nanotube Aggregation and the Reversion of Carbon Nanotube Aggregates in Aqueous Medium. *Langmuir* **2014**, *30* (36), 10899–10909. https://doi.org/10.1021/la5014279.

(3) Choi, Y. J.; Nacpil, E. J. C.; Han, J.; Zhu, C.; Kim, I. S.; Jeon, I. Recent Advances in Dispersant Technology for Carbon Nanotubes toward Energy Device Applications. *Adv. Energy Sustain. Res.* **2024**, *5* (4). https://doi.org/10.1002/aesr.202300219.

(4) Qiao, M.; Ran, Q.; Wu, S. Novel Star-like Surfactant as Dispersant for Multi-Walled Carbon Nanotubes in Aqueous Suspensions at High Concentration. *Appl. Surf. Sci.* **2018**, *433*, 975–982. https://doi.org/10.1016/j.apsusc.2017.10.138.

(5) Hou, J.; Du, W.; Meng, F.; Zhao, C.; Du, X. Effective Dispersion of Multi-Walled Carbon Nanotubes in Aqueous Solution Using an Ionic-Gemini Dispersant. *J. Colloid Interface Sci.* **2018**, *512*, 750–757. https://doi.org/10.1016/j.jcis.2017.10.109.

(6) Stanton, N. J.; Ihly, R.; Norton-Baker, B.; Ferguson, A. J.; Blackburn, J. L. Solution-Phase *p*-Type Doping of Highly Enriched Semiconducting Single-Walled Carbon Nanotubes for Thermoelectric Thin Films. *Appl. Phys. Lett.* **2021**, *119* (2). https://doi.org/10.1063/5.0055837.

(7) Sperlich, A.; Eckstein, K. H.; Oberndorfer, F.; Sturdza, B. K.; Auth, M.; Dyakonov, V.; Mitric, R.; Hertel, T. Onset of Spin Entanglement in Doped Carbon Nanotubes Studied by EPR. *J. Chem. Phys.* **2024**, *160* (23). https://doi.org/10.1063/5.0207502.

(8) Samanta, S. K.; Fritsch, M.; Scherf, U.; Gomulya, W.; Bisri, S. Z.; Loi, M. A. Conjugated Polymer-Assisted Dispersion of Single-Wall Carbon Nanotubes: The Power of Polymer Wrapping. *Acc. Chem. Res.* **2014**, *47* (8), 2446–2456. https://doi.org/10.1021/ar500141j.

(9) Pochorovski, I.; Wang, H.; Feldblyum, J. I.; Zhang, X.; Antaris, A. L.; Bao, Z. H-Bonded Supramolecular Polymer for the Selective Dispersion and Subsequent Release of Large-Diameter Semiconducting Single-Walled Carbon Nanotubes. *J. Am. Chem. Soc.* **2015**, *137* (13), 4328–4331. https://doi.org/10.1021/jacs.5b01704.

(10) Chang, X.; Henderson, W. M.; Bouchard, D. C. Multiwalled Carbon Nanotube Dispersion Methods Affect Their Aggregation, Deposition, and Biomarker Response. *Environ. Sci. Technol.* **2015**, *49* (11), 6645–6653. https://doi.org/10.1021/acs.est.5b00654.

(11) Huang, Y. Y.; Terentjev, E. M. Dispersion of Carbon Nanotubes: Mixing, Sonication, Stabilization, and Composite Properties. *Polymers* **2012**, *4* (1), 275–295. https://doi.org/10.3390/polym4010275.

(12) Li, H.; Qiu, Y. Dispersion, Sedimentation and Aggregation of Multi-Walled Carbon Nanotubes as Affected by Single and Binary Mixed Surfactants. *R. Soc. Open Sci.* **2019**, *6* (7), 190241. https://doi.org/10.1098/rsos.190241.

(13) Rdest, M.; Janas, D. Effective Doping of Single-Walled Carbon Nanotubes with Polyethyleneimine. *Materials* **2020**, *14* (1), 65. https://doi.org/10.3390/ma14010065.

(14) Nonoguchi, Y.; Ohashi, K.; Kanazawa, R.; Ashiba, K.; Hata, K.; Nakagawa, T.; Adachi, C.; Tanase, T.; Kawai, T. Systematic Conversion of Single Walled Carbon Nanotubes into N-Type

Thermoelectric Materials by Molecular Dopants. *Sci. Rep.* **2013**, *3* (1), 3344. https://doi.org/10.1038/srep03344.

(15) Zhou, S.; Shi, X.; Li, L.; Liu, Q.; Hu, B.; Chen, W.; Zhang, C.; Liu, Q.; Chen, Z. Advances and Outlooks for Carbon Nanotube-Based Thermoelectric Materials and Devices. *Adv. Mater.* **2025**, *37* (13), 2500947. https://doi.org/10.1002/adma.202500947.

(16) Brownlie, L.; Shapter, J. Advances in Carbon Nanotube N-Type Doping: Methods, Analysis and Applications. *Carbon* **2018**, *126*, 257–270. https://doi.org/10.1016/j.carbon.2017.09.107.

(17) Hawkey, A.; Dash, A.; Rodríguez-Martínez, X.; Zhao, Z.; Champ, A.; Lindenthal, S.; Zharnikov, M.; Kemerink, M.; Zaumseil, J. Ion-Exchange Doping of Semiconducting Single-Walled Carbon Nanotubes. *Adv. Mater.* **2024**. https://doi.org/10.1002/adma.202404554.

(18) Liu, Y.; Zhao, Z.; Kang, L.; Qiu, S.; Li, Q. Molecular Doping Modulation and Applications of Structure-Sorted Single-Walled Carbon Nanotubes: A Review. *Small* **2024**, *20* (3), 2304075. https://doi.org/10.1002/smll.202304075.

(19) Dörling, B.; Hawkey, A.; Zaumseil, J.; Campoy-Quiles, M. Strong Dependence of Air Stability on Thickness in N-Doped Carbon Nanotube Thermoelectrics. *Appl. Phys. Lett.* **2024**, *124* (11), 113302. https://doi.org/10.1063/5.0198773.

(20) Ono, M.; Nishiyama, A.; Toriumi, A. A Simple Approach to Understanding Measurement Errors in the Cross-Bridge Kelvin Resistor and a New Pattern for Measurements of Specific Contact Resistivity. *Solid-State Electron.* **2002**, *46* (9), 1325–1331. https://doi.org/10.1016/S0038-1101(02)00063-1.

(21) Keithley Instrument Inc. *Low Level Measurements Handbook*, 7th ed.; Tektronix, 2014.

(22) Tey, J. N.; Ho, X.; Wei, J. Effect of Doping on Single-Walled Carbon Nanotubes Network of Different Metallicity. *Nanoscale Res. Lett.* **2012**, *7* (1). https://doi.org/10.1186/1556-276x-7-548.

(23) Nonoguchi, Y.; Takata, A.; Goto, C.; Kitano, T.; Kawai, T. Thickness-Dependent Thermoelectric Power Factor of Polymer-Functionalized Semiconducting Carbon Nanotube Thin Films. *Sci. Technol. Adv. Mater.* **2018**, *19* (1), 581–587. https://doi.org/10.1080/14686996.2018.1500851.

(24) Misak, H. E.; Asmatulu, R.; Sabelkin, V.; Mall, S.; Kladitis, P. E. Tension–Tension Fatigue Behavior of Carbon Nanotube Wires. *Carbon* **2013**, *52*, 225–231. https://doi.org/10.1016/j.carbon.2012.09.024.

(25) Conley, K.; Karttunen, A. J. Bridging the Junction: Electrical Conductivity of Carbon Nanotube Networks. *J. Phys. Chem. C* **2022**, *126* (40), 17266–17274. https://doi.org/10.1021/acs.jpcc.2c03904.

(26) Markov, M.; Rezaei, S. E.; Sadeghi, S. N.; Esfarjani, K.; Zebarjadi, M. Thermoelectric Properties of Semimetals. *Phys. Rev. Mater.* **2019**, *3* (9), 095401. https://doi.org/10.1103/PhysRevMaterials.3.095401.

(27) Abdallah, F.; Ciammaruchi, L.; Jiménez-Arguijo, A.; Duraia, E. M.; Ragab, Hossam. S.; Dörling, B.; Campoy-Quiles, M. Investigating Thermoelectric Stability under Encapsulation Using PEI-Doped CNT Films as a Model System. *Adv. Mater. Technol.* **2020**, *5* (7), 2000256. https://doi.org/10.1002/admt.202000256.

(28) Tanaka, N.; Ishii, T.; Yamaguchi, I.; Hamasuna, A.; Fujigaya, T. Photoinduced Electron Doping of Single-Walled Carbon Nanotubes Based on Carboxamide Photochemical

Reactions. *J. Mater. Chem. A* **2023**, *11* (13), 6909–6917. https://doi.org/10.1039/D2TA08131H.

(29) Suzuki, H.; Kametaka, J.; Nakahori, S.; Tanaka, Y.; Iwahara, M.; Lin, H.; Manzhos, S.; Kyaw, A. K. K.; Nishikawa, T.; Hayashi, Y. N-DMBI Doping of Carbon Nanotube Yarns for Achieving High n-Type Thermoelectric Power Factor and Figure of Merit. *Small Methods* **2024**.

(30) Nakashima, Y.; Nakashima, N.; Fujigaya, T. Development of Air-Stable n-Type Single-Walled Carbon Nanotubes by Doping with 2-(2-Methoxyphenyl)-1,3-Dimethyl-2,3-Dihydro-1 H - Benzo[d]Imidazole and Their Thermoelectric Properties. *Synth. Met.* **2017**, *225*, 76–80. https://doi.org/10.1016/j.synthmet.2016.11.042.

(31) Tanaka, N.; Yamaguchi, I.; Yamaguchi, R.; Fujigaya, T. Study of the Electron-Doping Mechanism in Single-Walled Carbon Nanotubes Using Dimethylbenzimidazole. *Faraday Discuss.* **2024**, *250*, 390–399. https://doi.org/10.1039/d3fd00128h.

(32) Vardeny, S. R.; Phillips, A.; Thurman, K. A.; Vardeny, Z. V.; Blackburn, J. L. Amplitude-Mode Spectroscopy of Chemically Injected and Photogenerated Charge Carriers in Semiconducting Single-Walled Carbon Nanotubes. *Nano Res.* **2023**, *16* (4), 5619–5625. https://doi.org/10.1007/s12274-022-5080-1.

(33) Ferguson, A. J.; Reid, O. G.; Nanayakkara, S. U.; Ihly, R.; Blackburn, J. L. Efficiency of Charge-Transfer Doping in Organic Semiconductors Probed with Quantitative Microwave and Direct-Current Conductance. *J. Phys. Chem. Lett.* **2018**, *9* (23), 6864–6870. https://doi.org/10.1021/acs.jpclett.8b03074.

(34) Ohfuchi, M.; Miyamoto, Y. Optical Properties of Oxidized Single-Wall Carbon Nanotubes. *Carbon* **2017**, *114*, 418–423. https://doi.org/10.1016/j.carbon.2016.12.052.

(35) Hu, Z.; Breeze, B.; Walker, M.; Faulques, E.; Sloan, J.; Lloyd-Hughes, J. Spectroscopic Insights into the Influence of Filling Carbon Nanotubes with Atomic Nanowires for Photophysical and Photochemical Applications. *ACS Appl. Nano Mater.* **2023**, *6* (4), 2883–2893. https://doi.org/10.1021/acsanm.2c05266.

(36) Jorio, A.; Saito, R. Raman Spectroscopy for Carbon Nanotube Applications. *J. Appl. Phys.* **2021**, *129* (2), 021102. https://doi.org/10.1063/5.0030809.

(37) Rao, R.; Pierce, N.; Dasgupta, A. On the Charge Transfer between Single-Walled Carbon Nanotubes and Graphene. *Appl. Phys. Lett.* **2014**, *105* (7), 073115. https://doi.org/10.1063/1.4893698.

(38) Grüneis, A.; Attaccalite, C.; Rubio, A.; Vyalikh, D. V.; Molodtsov, S. L.; Fink, J.; Follath, R.; Eberhardt, W.; Büchner, B.; Pichler, T. Electronic Structure and Electron-Phonon Coupling of Doped Graphene Layers in KC 8. *Phys. Rev. B* **2009**, *79* (20), 205106. https://doi.org/10.1103/PhysRevB.79.205106.

(39) Zhou, W.; Vavro, J.; Nemes, N. M.; Fischer, J. E.; Borondics, F.; Kamarás, K.; Tanner, D. B. Charge Transfer and Fermi Level Shift Inp-Doped Single-Walled Carbon Nanotubes. *Phys. Rev. B* **2005**, *71* (20). https://doi.org/10.1103/physrevb.71.205423.

(40) Xu, J.-L.; Dai, R.-X.; Xin, Y.; Sun, Y.-L.; Li, X.; Yu, Y.-X.; Xiang, L.; Xie, D.; Wang, S.-D.; Ren, T.-L. Efficient and Reversible Electron Doping of Semiconductor-Enriched Single-Walled Carbon Nanotubes by Using Decamethylcobaltocene. *Sci. Rep.* **2017**, *7* (1). https://doi.org/10.1038/s41598-017-05967-w.

(41) Fukumaru, T.; Fujigaya, T.; Nakashima, N. Development of N-Type Cobaltocene-Encapsulated Carbon Nanotubes with Remarkable Thermoelectric Property. *Sci. Rep.* **2015**, *5* (1), 7951. https://doi.org/10.1038/srep07951.

(42) Grimm, S.; Schießl, S. P.; Zakharko, Y.; Rother, M.; Brohmann, M.; Zaumseil, J. Doping-Dependent G-Mode Shifts of Small Diameter Semiconducting Single-Walled Carbon Nanotubes. *Carbon* **2017**, *118*, 261–267. https://doi.org/10.1016/j.carbon.2017.03.040.

(43) Kalbac, M.; Kavan, L. The Influence of Doping on the Raman Intensity of the D Band in Single Walled Carbon Nanotubes. *Carbon* **2010**, *48* (3), 832–838. https://doi.org/10.1016/j.carbon.2009.10.036.

(44) Mohr, M.; Maultzsch, J.; Thomsen, C. Splitting of the Raman 2 D Band of Graphene Subjected to Strain. *Phys. Rev. B* **2010**, *82* (20), 201409. https://doi.org/10.1103/PhysRevB.82.201409.

(45) Huang, M.; Yan, H.; Chen, C.; Song, D.; Heinz, T. F.; Hone, J. Phonon Softening and Crystallographic Orientation of Strained Graphene Studied by Raman Spectroscopy. *Proc. Natl. Acad. Sci.* **2009**, *106* (18), 7304–7308. https://doi.org/10.1073/pnas.0811754106.

(46) Stampfer, C.; Molitor, F.; Graf, D.; Ensslin, K.; Jungen, A.; Hierold, C.; Wirtz, L. Raman Imaging of Doping Domains in Graphene on SiO2. *Appl. Phys. Lett.* **2007**, *91* (24), 241907. https://doi.org/10.1063/1.2816262.

(47) Ding, F.; Jiao, K.; Lin, Y.; Yakobson, B. I. How Evaporating Carbon Nanotubes Retain Their Perfection? *Nano Lett.* **2007**, *7* (3), 681–684. https://doi.org/10.1021/nl0627543.

(48) Das, A.; Pisana, S.; Chakraborty, B.; Piscanec, S.; Saha, S. K.; Waghmare, U. V.; Novoselov, K. S.; Krishnamurthy, H. R.; Geim, A. K.; Ferrari, A. C.; Sood, A. K. Monitoring Dopants by Raman Scattering in an Electrochemically Top-Gated Graphene Transistor. *Nat. Nanotechnol.* **2008**, *3* (4), 210–215. https://doi.org/10.1038/nnano.2008.67.

(49) Casiraghi, C. Doping Dependence of the Raman Peaks Intensity of Graphene Close to the Dirac Point. *Phys. Rev. B* **2009**, *80* (23), 233407. https://doi.org/10.1103/PhysRevB.80.233407.

(50) Attaccalite, C.; Wirtz, L.; Lazzeri, M.; Mauri, F.; Rubio, A. Doped Graphene as Tunable Electron−Phonon Coupling Material. *Nano Lett.* **2010**, *10* (4), 1172–1176. https://doi.org/10.1021/nl9034626.

(51) Beams, R.; Gustavo Cançado, L.; Novotny, L. Raman Characterization of Defects and Dopants in Graphene. *J. Phys. Condens. Matter* **2015**, *27* (8), 083002. https://doi.org/10.1088/0953-8984/27/8/083002.

(52) Jung, N.; Kim, B.; Crowther, A. C.; Kim, N.; Nuckolls, C.; Brus, L. Optical Reflectivity and Raman Scattering in Few-Layer-Thick Graphene Highly Doped by K and Rb. *ACS Nano* **2011**, *5* (7), 5708–5716. https://doi.org/10.1021/nn201368g.

(53) Salzmann, I.; Heimel, G.; Oehzelt, M.; Winkler, S.; Koch, N. Molecular Electrical Doping of Organic Semiconductors: Fundamental Mechanisms and Emerging Dopant Design Rules. *Acc. Chem. Res.* **2016**, *49* (3), 370–378. https://doi.org/10.1021/acs.accounts.5b00438.

(54) Biskup, T. Doping of Organic Semiconductors: Insights from EPR Spectroscopy. *Appl. Phys. Lett.* **2021**, *119* (1), 010503. https://doi.org/10.1063/5.0054685.

(55) Kiefer, D.; Giovannitti, A.; Sun, H.; Biskup, T.; Hofmann, A.; Koopmans, M.; Cendra, C.; Weber, S.; Anton Koster, L. J.; Olsson, E.; Rivnay, J.; Fabiano, S.; McCulloch, I.; Müller, C. Enhanced N-Doping Efficiency of a Naphthalenediimide-Based Copolymer through Polar Side Chains for Organic Thermoelectrics. *ACS Energy Lett.* **2018**, *3* (2), 278–285. https://doi.org/10.1021/acsenergylett.7b01146.

(56) Niklas, J.; Holt, J. M.; Mistry, K.; Rumbles, G.; Blackburn, J. L.; Poluektov, O. G. Charge Separation in P3HT:SWCNT Blends Studied by EPR: Spin Signature of the Photoinduced Charged State in SWCNT. *J. Phys. Chem. Lett.* **2014**, *5* (3), 601–606. https://doi.org/10.1021/jz402668h.

(57) Náfrádi, B.; Nemes, N. M.; Fehér, T.; Forró, L.; Kim, Y.; Fischer, J. E.; Luzzi, D. E.; Simon, F.; Kuzmany, H. Electron Spin Resonance of Single-walled Carbon Nanotubes and Related Structures. *Phys. Status Solidi B* **2006**, *243* (13), 3106–3110. https://doi.org/10.1002/pssb.200669218.

(58) Rice, W. D.; Weber, R. T.; Leonard, A. D.; Tour, J. M.; Nikolaev, P.; Arepalli, S.; Berka, V.; Tsai, A.-L.; Kono, J. Enhancement of the Electron Spin Resonance of Single-Walled Carbon Nanotubes by Oxygen Removal. *ACS Nano* **2012**, *6* (3), 2165–2173. https://doi.org/10.1021/nn204094s.

(59) Barklie, R. C. Characterisation of Defects in Amorphous Carbon by Electron Paramagnetic Resonance. *Diam. Relat. Mater.* **2003**, *12* (8), 1427–1434. https://doi.org/10.1016/S0925-9635(03)00004-9.

(60) Pham, C. V.; Krueger, M.; Eck, M.; Weber, S.; Erdem, E. Comparative Electron Paramagnetic Resonance Investigation of Reduced Graphene Oxide and Carbon Nanotubes with Different Chemical Functionalities for Quantum Dot Attachment. *Appl. Phys. Lett.* **2014**, *104* (13), 132102. https://doi.org/10.1063/1.4870297.

(61) Rao, S. S.; Stesmans, A.; Kosynkin, D. V.; Higginbotham, A.; Tour, J. M. Paramagnetic Centers in Graphene Nanoribbons Prepared from Longitudinal Unzipping of Carbon Nanotubes. *New J. Phys.* **2011**, *13* (11), 113004. https://doi.org/10.1088/1367-2630/13/11/113004.

(62) Dennany, L.; Sherrell, P.; Chen, J.; Innis, P. C.; Wallace, G. G.; Minett, A. I. EPR Characterisation of Platinum Nanoparticle Functionalised Carbon Nanotube Hybrid Materials. *Phys. Chem. Chem. Phys.* **2010**, *12* (16), 4135. https://doi.org/10.1039/b923921a.

(63) Dörling, B.; Zapata-Arteaga, O.; Campoy-Quiles, M. A Setup to Measure the Seebeck Coefficient and Electrical Conductivity of Anisotropic Thin-Films on a Single Sample. *Rev. Sci. Instrum.* **2020**, *91* (10), 105111. https://doi.org/10.1063/5.0021715.

(64) Hwang, J.; Ni, X.; Espenship, M. F.; Tang, K.; Zhang, J.; Basu, A.; Kuila, S.; Barlow, S.; Marder, S. R.; Brédas, J.-L.; Laskin, J.; Mei, J. Elucidating Charge Carrier Reactivity, Conversion, and Degradation in n-Doped Oligo- and Poly(Benzodifurandione). *J. Am. Chem. Soc.* **2025**, *147* (22), 19372–19379. https://doi.org/10.1021/jacs.5c05722.

(65) Bondi, A. Van Der Waals Volumes and Radii. *J. Phys. Chem.* **1964**, *68* (3), 441–451. https://doi.org/10.1021/j100785a001.

6. Conclusion

Summary of Results

This work advances the understanding of molecular n-type doping by investigating how structural modifications of benzimidazoline-based dopants influence their activation, stability, and interaction with different semiconducting hosts. Moving beyond the conventional strategy of enhancing solubility or tuning redox potential, the study focused on designing dopants capable of establishing **defined and persistent interactions** with the host matrix.

The synthetic part of this research set the foundation for this approach. Two synthetic pathways were optimized to access a wide range of DMBI derivatives, expanding the existing portfolio of benzimidazoline based dopants. Among these, a bifunctional dopant, MDI-DMBI$_2$, was successfully obtained through a urethane coupling route, acknowledging polyurethane chemistry as a robust and modular tool for assembling multifunctional molecules.

The comparative characterization of the doping performance of N-DMBI-H, An-DMBI, and MDI-DMBI$_2$ gave insights into the subtle interplay between molecular structure and doping mechanism. In polymeric N2200 films, all dopants were found to trigger charge transfer even at room temperature, yet their thermal evolution exposed the crucial role of miscibility and morphology. In this context, contrary to our initial expectations, MDI-DMBI$_2$ did not provide an enhanced morphological stability of the doped-system upon annealing at high temperature, instead, its limited compatibility with the polymer matrix led to inhomogeneous morphologies and moderate conductivities.

When applied to semiconducting CNT films, the same dopant displayed a completely different behavior. In this case, charge transport is governed by interfacial rather than bulk processes, and the extended aromaticity and multiple redox-active centers, features that characterize MDI-DMBI$_2$, permitted the formation of strong interfacial assemblies and the retainment of the n-type character under long-term monitoring in ambient conditions. The resulting thermoelectric response, comparable to that of An-DMBI and more stable than N-DMBI-H, underscores that persistent doping can be obtained from interfacial adsorption and molecular anchoring.

In summary, this work offers a new perspective on the challenges underlying the limited efficiency of n-type doping in organic semiconductors and carbon nanotubes by examining how dopant structure and host environment jointly determine doping stability and performance. Through the combination of synthetic design and comparative investigation across different materials, this study provides a practical framework for developing benzimidazoline-based dopants that achieve stable and efficient doping via controlled interfacial assembly.

Outlook and Future Perspectives

The results of this thesis suggest that future developments in molecular n-type doping should account for the different physical mechanisms influencing charge transport in polymeric semiconductors and carbon-based materials. In polymer hosts, where transport is strongly influenced by bulk morphology, further work should focus on improving dopant-host compatibility in order to limit phase separation during thermal treatment. This may involve modifying dopant polarity, flexibility, or molecular size to better match the host matrix.

For nanocarbon systems, where charge transport is dominated by interfacial processes, future dopant design should focus on the superficial protection of CNTs against oxidation. Increasing the number of redox-active units or extending the aromatic character of the dopant may enhance the interfacial stabilization of the counterion-CNT ion pair and, in turn, contribute to long-term retention of the n-type character under ambient conditions.

From a synthetic perspective, the modular chemistry employed in this work provides a straightforward route to systematically vary dopant architecture and directly correlate structural features with doping stability and efficiency. Extending this approach to other linker chemistries or dopant backbones could help clarify which molecular parameters most effectively control dopant activation and retention in different hosts.

Finally, further experimental efforts combining electrical characterization with spectroscopic techniques could help refine the interpretation of doping mechanisms and their evolution with temperature and time. Such studies would support the rational optimization of dopant structures for applications where stable n-type doping remains a limiting factor.

List of acronyms

AFM	Atomic Force Microscopy
BCF	Tris(pentafluorophenyl)borane
CB	Conduction Band
CNT	Carbon Nanotube
DCM	Dichloromethane
DMF	Dimethylformamide
DMSO	Dimethyl Sulfoxide
EtOH	Ethanol
FET	Field-Effect Transistor
HOMO	Highest Occupied Molecular Orbital
LUMO	Lowest Unoccupied Molecular Orbital
MeOH	Methanol
OLED	Organic Light Emitting Diode
OPV	Organic Photovoltaic
OSC	Organic Semiconductor
OTEG	Organic Thermoelectric Generator
PF	Power Factor
PMMA	Poly(methyl methacrylate)
RMS	Root-Mean-Square (surface roughness)
SOMO	Singly Occupied Molecular Orbital
THF	Tetrahydrofuran
UV-Vis	Ultraviolet-Visible
VB	Valence Band
EA	Electron Affinity